

**BREATHING RATE AND WORK-OF-BREATHING
ESTIMATION USING REAL BIOMEDICAL SIGNALS**

CHRISTINA KOZIA

Doctor of Philosophy

ASTON UNIVERSITY

January 2020

© Christina Kozia, 2020

Christina Kozia asserts her moral right to be identified as the author of this
thesis

This copy of the thesis has been supplied on condition that anyone who
consults it is understood to recognise that its copyright belongs to its author
and that no quotation from the thesis and no information derived from it
may be published without appropriate permission or acknowledgement.

ASTON UNIVERSITY

Breathing Rate and Work-of-Breathing Estimation using Real Biomedical Signals

CHRISTINA KOZIA

Doctor of Philosophy, 2020

Thesis Summary

Breathing Rate (BR), which is an important indicator of deterioration, has been widely neglected in hospital settings due to the requirement of invasive procedures and skilled nurses for it to be measured. However, BR can be estimated using non-invasive techniques from Electrocardiograms (ECG), Photoplethysmograms (PPG) and Seismocardiograms (SCG) recordings. Nonetheless, the current state of the art non-invasive BR estimation methods have not been broadly evaluated, especially using real data from hospitalised patients, thus are still inaccurate and unreliable in real settings.

Another critical deterioration indicator, especially on paediatric and neonatal wards, is the Work-of-Breathing (WOB). The WOB indicator provides information about the effort expended by a patient while breathing, however its evaluation is largely subjective and until now it has only be assessed by skilled nurses. Regardless of the clinical significance of the WOB, its evaluation from ECG signals has received scant attention in the research literature.

This thesis presents investigations of the standard BR estimation methods in order to develop the theory and implementation know-how around BR extraction from ECG and SCG signals and address the limitations of the current methods with a view to benefit continuous patient monitoring and triage. Advanced signal processing techniques such as Empirical Mode Decomposition (EMD) have been exploited and enhanced, leading to a novel filter-based EMD algorithm for continuous BR monitoring which does not require the identification of ECG features.

In the final part of the thesis the WOB estimation from real ECG signals is explored. A measure based on the R-to-S (RS) amplitude variability due to respiration in the ECG signal was developed in this thesis and it was found for the first time that there is a positive monotonic relationship between the RS variability and the WOB.

All developed methods in this thesis are tested on real children data obtained from Birmingham's Children Hospital. The proposed BR methods in addition to the WOB measure demonstrated good estimation of their corresponding physical indicators on this real data.

Keywords: Electrocardiogram, Seismocardiogram, patient monitoring, respiration, signal processing

Dedication

I dedicate this to my mother and father; ammor magnus doctor est.

Acknowledgements

Firstly, I would like to express my sincere gratitude to my supervisor Dr. Randa Herzallah for the continuous support of my Ph.D study and related research, for her patience, motivation, and immense knowledge. Her guidance helped me in all the time of research and writing of this thesis. I could not have imagined having a better advisor and mentor for my Ph.D study.

Besides my supervisor, I would like to thank Prof. David Lowe, for his insightful comments and encouragement, but also the hard questions which incited me to widen my research from various perspectives.

My sincere thanks goes to Keith Errey, Rory Morrison and Angela Gallego who provided me an opportunity to join their team, and made me a welcome member of the Isansys Lifecare Ltd. Furthermore, thanks are due to Dr. Heather Duncan and Balazs Fule from Birmingham's Children hospital, for assisting me with the work on hospitalised children data.

I would like especially acknowledge my mother and father for their endless support and love. A special thanks to Alexandros for patience and tolerance in the time I spent working on this thesis. Without my family and Alexandros nothing could have been done.

A special thanks to my friends Eleni, Fotini, Giorgos, Kostas and Lida who made my life happier and easier during my Ph.D study. Also I thank my friends Marianna, Thomas and Stefano who always supported my decisions. A shout out is due to my friends in Edinburgh, especially Vassilis.

Thanks also to all past and present members of the research group, Reham Badawy, Ewa Grela, Yazan Qarout, Adam Lowe, Dr. Otte D'Huys, Dr. Jordan Raykov, Dr. Sotos Generalis, Kanchan Patel and Prof. Max Little.

Last but not the least, I would like to thank Black Sabbath, the Spotted Dog and Guliou.

Declaration of Funding

This thesis was jointly funded by Isansys Lifecare Ltd and Aston University. In addition, the supporting company in collaboration with Birmingham's Children Hospital provided real data which have been used in this work.

Contents

1	Introduction	15
1.1	Overview of the Research Problem	15
1.2	Thesis Objectives and Contributions	17
1.3	Thesis Outline	19
2	Literature Review	22
2.1	Clinical Background	22
2.1.1	Importance of Vital Sign Monitoring	23
2.2	QRS Complex Detection	26
2.2.1	Importance of the QRS Complex	27
2.2.2	Single-lead First-derivative-based Methods	30
2.2.3	Hilbert Transform-based Methods	33
2.2.4	Empirical Mode Decomposition-based Methods	35
2.3	Breathing Rate Estimation	37
2.3.1	Respiration Signal Extraction from the ECG	38
2.3.2	SCG-Derived Respiration	51
2.4	Respiratory Distress Estimation	54
2.4.1	Plethysmography-based Estimation	56
2.4.2	ECG Respiratory Artifact	57
3	Breathing Rate Estimation: Methodology and Approaches	59
3.1	Single Methods	60
3.1.1	ECG-Derived Respiration (EDR)	60
3.1.2	RSA-Derived Respiration (RSA)	62
3.1.3	PCA-Derived Respiration (PCADR)	64
3.1.4	ICA-Derived Respiration (ICADR)	66
3.1.5	EMD-Derived Respiration (EMDDR)	68
3.1.6	Frequency domain-based BR estimation	73
3.1.7	Time domain-based BR estimation	75
3.2	Fusion Methods	78

4	QRS Complex Detection	83
4.1	QRS Detection Algorithms	83
4.2	QRS Complex Detection based on Local Signal Energy and EMD . .	92
4.3	Proposed QRS Complex Detector	93
4.4	Statistical Analysis of the proposed QRS Complex Detector	97
4.5	Exploitation of the proposed QRS detector on ECG segmentation . .	112
4.6	Conclusion	113
5	Breathing Rate Estimation from Real Data	116
5.1	Discussion of Investigated Real Databases	117
5.2	Single Methods	119
5.2.1	ECG-Derived Respiration (EDR)	121
5.2.2	RSA-Derived Respiration (RSA)	130
5.2.3	PCA-Derived Respiration (PCADR)	142
5.2.4	ICA-Derived Respiration (ICADR)	151
5.2.5	EMD-Derived Respiration (EMDDR)	158
5.3	Fusion Methods	169
5.3.1	Data Fusion	169
5.3.2	Method Fusion	170
5.4	Conclusion	173
6	Breathing Rate Estimation from Seismocardiograms	177
6.1	Current State of the Art Methods	178
6.2	Advanced Methods	187
6.3	Method Fusion in SCG	196
6.4	Conclusion	198
7	Respiratory Distress Estimation from the ECG	199
7.1	Work-of-Breathing (WOB)	200
7.2	BCH data and reference WOB	201
7.3	R-peak Variance	202
7.4	RS Variability	208
7.4.1	Δ RS Measure	210
7.5	Conclusion	218
8	Conclusions and Directions for Future Work	219
8.1	Research Question Reflection	219
8.2	Direction for Future Research	222
	References	224
	A Results related to Capnobase dataset	236

B	Results related to BCH ECG database	253
C	Results related to BCH EMG database	255
D	Generation of a synthetic ECG signal	258
	D.1 Synthetic ECG signal	258
	D.2 Respiratory-induced Modulations	261
E	Additional information related to Chapter 3	262
	E.1 Additional information related to Chapter 3	262
	E.1.1 BSS Model	262
	E.1.2 Principal Component Analysis	264
F	Additional information related to Chapter 7	265
	F.1 BCH data and reference WOB	265
	F.2 Pearson's correlation coefficient	265
	F.3 <i>K</i> -means clustering	266

List of Figures

2.1	Normal QRS complex	28
2.2	QRS detection algorithms work-flow	31
2.3	ECG respiratory-induced modulations	39
2.4	BR estimation workflow	40
3.1	EDR on a synthetic ECG signal	62
3.2	RSA on a synthetic ECG signal	63
3.3	Data matrix construction II	66
3.4	PCADR signal	66
3.5	ICADR signal	69
3.6	EMDDR signal I	72
3.7	EMDDR signal II	73
3.8	DFT BR estimation	75
3.9	CSD BR estimation	76
3.10	Three-point BR estimation	78
3.11	Pole magnitude method fusion	82
4.1	Pre-processing stage of the QRS detection algorithm of Pan & Tompkins (1985)	88
4.2	Decision stage of the QRS detection algorithm of Pan & Tompkins (1985)	89
4.3	Steps of the QRS detection algorithm of Benitez et al. (2000, 2001)	91
4.4	QRS Complex Detection Flow-Chart	98
4.5	Schematic representation of the buffer's function	99
4.6	The extracted IMFs and their frequency spectra	100
4.7	ECG signal reconstruction	101
4.8	Steps of the proposed QRS complex detector	102
4.9	Comparison of Threshold Estimation	107
4.10	Comparison of averaging segments	108
4.11	Distinction of Q- and R-peaks	110
4.12	Threshold comparison	111

4.13	Q-, S-, T- peaks and QRS onset/offset detection for recording mitdb100	114
4.14	QRS duration and ST segment for recording mitdb100	114
5.1	EMG ICA	120
5.2	ECG extraction from EMG	120
5.3	Noise in ecgch1	125
5.4	EDR method on capno9	126
5.5	DFT analysis of the EDR signal on capno9	127
5.6	FD analysis of the EDR signal on ecgch1	128
5.7	HR Nyquist limit on ecgch9	129
5.8	FD analysis of the EDR signal on emgch2	131
5.9	RSA method on capno16	135
5.10	DFT analysis of the RSA signal on capno16	136
5.11	EDR method on capno16	137
5.12	DFT analysis of the EDR signal on capno16	138
5.13	Frequency Domain (FD) and Time Domain (TD) analysis of the RSA signal on ecgch1	140
5.14	FD and TD analysis of the RSA signal on emgch3	141
5.15	DFT analysis of the PCADR signal on capno9	146
5.16	CSD analysis of the PCADR signal on capno9	147
5.17	3PT analysis of the PCADR signal on capno9	148
5.18	P2T analysis of the PCADR signal on capno9	149
5.19	FD and TD analysis of the PCADR signal on ecgch1	150
5.20	FD and TD analysis of the PCADR signal on emgch3	152
5.21	Cumulative sum of eigenvalues for recording capno15	154
5.22	Extracted ICs for recording capno15	155
5.23	Frequency content of the extracted ICs for recording capno15	156
5.24	FD and TD analysis of the ICADR signal on capno15	159
5.25	EMD analysis of capno9	164
5.26	DFT analysis of IMFs of capno9	165
5.27	FD and TD analysis of the EMDDR signal on capno9	166
5.28	Proposed EMDDR method on ecgch2	168
5.29	PACF of the EDR signal for capno9	172
6.1	S1-peak identification on SCG	179
6.2	DFT and TD analysis of the S1-S1 interval signal on b001	182
6.3	DFT analysis of the intensity methods on b001	188
6.4	DFT analysis of the AM S1 signal for b001	191
6.5	DFT analysis of the IMFs of b001	193
6.6	DFT and TD analysis of the EMDDR signal of b001	195
6.7	Distribution of respiratory windows based on method fusion	198

7.1	Visual inspection of V values for BCH ECG and EMG data	206
7.2	Correlation between reference and estimated WOB with visual inspection	207
7.3	k -means classification of V values for BCH ECG and EMG data	208
7.4	Correlation between reference and estimated WOB with k -means	209
7.5	ΔRS measure for WOB	213
7.6	Visual inspection of ΔRS values for BCH ECG and EMG data	215
7.7	Correlation between reference and estimated WOB with visual inspection	216
7.8	k -means clustering of ΔRS values for BCH ECG and EMG data	217
7.9	Correlation between reference and estimated WOB with visual inspection	217
D.1	Single synthetic ECG beat	258
E.1	Schematic representation of the BSS model	263

List of Tables

2.1	Deaths by age group	26
2.2	Comparison of current state of the art BR Estimation methods	52
4.1	erformance of QRS detection algorithms (reported by the authors)	84
4.2	QRS detection performance using the MIT-BIH database	104
4.3	QRS detection performance using the PICSDB	105
4.4	QRS detection performance using the Capnabase dataset	106
4.5	Comparison of QRS detector performance with other methods for PICSDB and Capnabase	107
4.6	Comparison of Threshold Estimators	108
5.1	Capnabase dataset: EDR performance	123
5.2	ECG children: EDR performance	124
5.3	EMG children: EDR performance	124
5.4	Capnabase dataset: RSA performance	133
5.5	ECG children: RSA performance	134
5.6	EMG children: RSA performance	134
5.7	Capnabase dataset: PCADR performance	144
5.8	ECG children: PCADR performance	145
5.9	EMG children: PCADR performance	145
5.10	Capnabase dataset: ICADR performance	157
5.11	Capnabase dataset: EMDDR performance	162
5.12	ECG children: EMDDR performance	163
5.13	ECG children: Single methods and Data Fusion performance comparison	171
5.14	Capnabase dataset: Method fusion	174
5.15	ECG children: Method fusion	175
6.1	SCG data: S1-S1 interval performance	181
6.2	SCG data: S1 Intensity performance	184
6.3	SCG data: S2 Intensity performance	185
6.4	SCG data: S1/S2 Intensity performance	186

6.5	SCG data: S1 AM performance	190
6.6	SCG data: EMDDR performance	194
6.7	SCG data: Method Fusion performance	197
7.1	WOB reference score	202
7.2	ECG children: R-peak variance measure	204
7.3	EMG children: R-peak variance measure	204
7.4	Distinct bands of each level of WOB (R-peak variance) by visual inspection	206
7.5	Distinct bands of each level of WOB (R-peak variance) by k -means classification	208
7.6	Confusion matrix for R-peak variance measure	209
7.7	ECG children: Δ RS measure	214
7.8	EMG children: Δ RS measure	214
7.9	Distinct bands of each level of WOB (Δ RS measure) by visual inspection	215
7.10	Distinct bands of each level of WOB (Δ RS measure) by k -means classification	216
7.11	Confusion matrix for Δ RS measure	217
A.1	EDR method for Capnabase	239
A.2	RSA method for Capnabase	243
A.3	PCADR method for Capnabase	246
A.4	ICADR method for Capnabase	249
A.5	EMDDR method for Capnabase	252
B.1	Frequency domain analysis for BCH ECG data	254
B.2	Time domain analysis for BCH ECG data	254
C.1	EDR method for BCH EMG data	256
C.2	RSA method for BCH EMG data	256
C.3	PCADR method for BCH EMG data	257
D.1	ECG beat values	259

List of Algorithms

1	EMD Algorithm	71
2	Three-point (3PT) Algorithm	77
3	Pole Magnitude and Phase Angle Criterion	82
4	ECG extraction from EMG	119
5	Proposed EDR	122
6	Proposed RSA	131
7	Proposed PCADR	142
8	Proposed ICADR	151
9	Proposed EMDDR	160
10	Proposed Data Fusion	170
11	Improved Pole Magnitude and Phase Angle Criterion	172
12	R-peak variance	203
13	Δ RS measure	212

Chapter 1

Introduction

1.1 Overview of the Research Problem

Statistics show that 24% of hospital admissions in children are due to the difficulty in breathing (Stewart et al., 1998). Failure to identify the level of illness severity can lead to a number of deaths in children (Pearson, 2008). Moreover, continuous vital sign monitoring is usually neglected in a hospital environment, due to time constraint reasons and lack of reliable measurements (Thompson et al., 2008). All of the triage and warning systems for children, reported by S. Fleming (2010), recommend the measure of breathing rate (BR). The BR plays a key role in patient monitoring as it describes the air in and out of lungs, which can be an indicator of deterioration as the body attempts to maintain oxygen delivery to the tissues (Kelly, 2018). Particularly, it can be used in children triage as a prediction tool of pneumonia (Margolis & Gadomski, 1998) or an indicator of bacterial infections (National Collaborating Centre for Women's and Children's Health (UK), 2013).

There are a number of published methods which investigate non-invasive techniques for BR estimation, incorporating the Electrocardiogram (ECG), the Photoplethysmogram (PPG) (Charlton et al., 2016) and the Seismocardiogram (SCG)

(Zakeri et al., 2016). However, it has been reported that these algorithms have not been broadly assessed, especially using hospitalised children recordings (Charlton, 2017). This means that these approaches are still not tested in real world situations where the monitored recordings are subjected to significant noise effects due to sensor imperfections, patient movements and imperfect sensor-patient contacts. In a hospital environment, there is usually a significant signal processing challenge in extracting such correlated physiological state parameters, such as the BR, reliably for all patient types. Therefore, this thesis will research and develop the theory and implementation know-how of modern techniques for BR estimation derived from hospital recordings based on ECG and SCG signals. To address the limitations of current existing methods for extracting the BR, this thesis will investigate the exploitation of development of advanced signal processing techniques. In particular, the Empirical Mode Decomposition (EMD) and the Independent Component Analysis (ICA) techniques will be investigated and exploited.

However, the ECG signal also reflects other physiological states, not just the BR. Another key parameter used by nurses and clinicians in hospital environment, especially on paediatric and neonatal wards, is the respiratory effort, also known as respiratory distress, or Work-of-Breathing (WOB); a largely subjective measure assessed by skilled nurses on the effort expended by a patient during breathing (Ahrens, 1993; Cohen & Schwartz, 2013). Although electrical and optical sensors can be designed to detect muscle movement, in a hospital setting it is essential to minimise the number of different types of sensor worn by a patient. Therefore extracting measures of WOB from ECG signals that are already being recorded would be very advantageous if it could be performed reliably and trustworthy. Despite its clinical importance, there remains a paucity of evidence on extracting the WOB from

ECG signals. This work will generate fresh insight into developing a WOB measure from the ECG signal by analysing the R-peak variability.

1.2 Thesis Objectives and Contributions

This thesis aims to design a BR monitoring and data fusion system to be used in hospitalised children using ECG and SCG signals in order to improve continuous patient monitoring. Moreover this is the first study to undertake a statistical analysis of the R-peak variability of the ECG signal in order to develop a measure of WOB, which can be later integrated into the ECG/SCG sensors.

The key to these problems is to bring together and apply certain ideas that already exist in classical signal processing and statistics. In support of this aim the main contribution of this thesis to biomedical signal processing include:

1. **The development of a novel QRS complex detection algorithm for all patient types.** A novel QRS patient-specific detection algorithm was designed based on the local signal energy using Empirical Mode Decomposition. The designed algorithm employs an adaptive threshold over a sliding window combined with a gradient-based and refractory period checks. This algorithm was found to provide superior performance compared to existing QRS detectors when tested on adult and children ECG signals (Kozia, Herzallah, & Lowe, 2018a, 2018b, 2018c).
2. **Novel BR estimation algorithms for ECG data.** A novel BR estimation method based on the Empirical Mode Decomposition and a chain of filters was designed which incorporates the age and heart rate levels of the child. This method was found to provide a similar performance compared to existing

BR estimation methods using data from hospitalised children. Moreover this thesis extended the current BR estimation methods in order to improve the BR estimation accuracy using children ECG recordings (Kozia et al., 2018b, 2018c).

3. **Novel BR estimation algorithms for SCG data.** A novel approach which analyses the amplitude modulations, induced by respiration, in the SCG signal was developed in order to estimate the BR from SCG recordings. Moreover, a novel filter-based method which decomposes the SCG signal using the Empirical Mode Decomposition and identifies the respiration component based on a spectral analysis was designed.
4. **Enhanced and new data fusion method for improving BR estimation.** A novel data-oriented fusion method was developed where the BR of one minute window is acquired by averaging BR estimates over 10 sec windows. Additionally, an enhanced fusion technique based on Orphanidou, Fleming, Shah, and Tarassenko (2013) was designed. It uses an Autoregressive (AR) model for the spectral analysis of the respiration signal. The novelty of the proposed technique is that the model order is decided based on the Partial Autocorrelation Function (PACF) of the respiration signal.
5. **A novel WOB measure from the ECG.** A novel WOB measure was created which explores the R-peak variability in the ECG signal over respiratory cycles in order to evaluate the respiratory distress. The measure was applied on hospitalised children ECG signals and achieved a good classification accuracy of patients being at different levels of respiratory distress.

1.3 Thesis Outline

This thesis is structured as follows:

Chapter 2: Literature Review. This chapter presents the clinical background and highlights the importance of the research area. The significance and connection of R-peak detection, BR estimation and respiratory distress are also discussed. A survey of the current BR estimation algorithms is also provided. This chapter further surveys the present respiration distress estimation methods.

Chapter 3: Breathing Rate Estimation: Methodology and Approaches. In this chapter a systematic review of the current BR algorithms is presented, applied on synthetic ECG signals.

Chapter 4: QRS Complex Detection. In this chapter we discuss the two basic QRS complex detection algorithms. Moreover, a novel QRS detection algorithm is presented and compared with the aforementioned detectors. The algorithms are verified by applying them to a well-known ECG database, widely used in R-peak detection. Moreover, the proposed detector is applied for the first time on children and infant ECG recordings.

Chapter 5: Breathing Rate Estimation from Real Data. This chapter constitutes one of the central parts of this thesis. It concerns the exploitation of the BR estimation algorithms on real signals, such as the ECG and EMG, which belong to hospitalised children. Moreover, a novel method for BR estimation from the ECG signal is presented. The developed methods are evaluated using quantitative analysis measures. Furthermore, to obtain a single measure

of BR from multiple estimators, it is necessary to use data and method fusion techniques. This chapter explores fusion approaches to determine which is suitable for improving the estimation accuracy. The results obtained are statistically analysed and compared with the results obtained from each individual method.

Chapter 6: Breathing Rate Estimation from Seismocardiograms. This chapter first reviews current state of the art methods used in the BR estimation from SCG signals. Moreover, two novel methods based on the amplitude variations and the oscillatory modes of the SCG signals are discussed and evaluated in this chapter. Furthermore, data and method fusion techniques are applied on the extracted respiration signals and the performance is evaluated.

Chapter 7: Respiratory Distress Estimation. The evaluation of respiratory distress as Work-of-Breathing (WOB) using the amplitude variations in the ECG signal of sick children is introduced in this chapter. Moreover, a classification of the patients is attempted based on the estimated WOB and compared with the reference WOB levels.

Chapter 8: Conclusion and Future Considerations. This chapter presents a summary of the contributions of this thesis and the obtained results. In addition, suggestions for future research are given and discussed.

Appendix A: Results related to Capnabase dataset. This appendix provides the reference BRs for all Capnabase recordings used, along with the estimated BRs from all the proposed methods discussed in **Chapter 5**.

Appendix B: Results related to BCH ECG database. This appendix provides the reference BRs for all BCH ECG recordings used, along with the

estimated BRs from all the proposed methods discussed in **Chapter 5**.

Appendix C: Results related to BCH EMG database. This appendix provides the reference BRs for all BCH EMG recordings used, along with the estimated BRs from all the proposed methods discussed in **Chapter 5**.

Appendix D: Generation of a synthetic ECG signal. This appendix explains how a synthetic ECG signal is created.

Appendix E: Additional information related to Chapter 3. This appendix provides information on the theoretical background of the PCA method used in **Chapter 3**.

Appendix F: Additional information related to Chapter 7. This appendix provides information about the reference WOB data from the BCH and also discusses an algorithm used in **Chapter 7**.

Chapter 2

Literature Review

In this chapter the clinical background and the importance of the research area is presented. The significance and contribution of R-peak detection in BR estimation and respiratory distress evaluation is also reported. Therefore a survey of the current QRS complex detection algorithms is presented. Moreover, an overview of the state-of-the-art BR estimation methods is also discussed in detail. Finally, this chapter further investigates the present respiration distress evaluation methods. The current methods focus muscle activity related recordings and the respiratory distress has never been extracted from the ECG.

2.1 Clinical Background

There are two primary aims of this thesis: 1) To investigate the development of a BR monitoring and data fusion system that combines ECG and SCG signals in order to improve continuous respiration monitoring in a hospital setting and 2) To ascertain the correlation of the ECG signal with the respiratory distress by conducting a statistical analysis of the R-peak variability in order to develop a measure of

WOB. Initial focus was given on BR estimation. The latter is very difficult, especially in paediatrics, and it is not used routinely due to algorithms being unreliable and due to distress caused by cumbersome devices. The complexity of BR estimation results also from the presence of muscle activities as high frequency components in the ECG signal. The latter are usually filtered out from the ECG signals. Moreover, the importance of vital sign monitoring will be discussed with focus on the respiratory distress which is expressed by the Work-of-Breathing (WOB). Current literature explores respiratory distress in photoplethysmographic signals. However an ECG-derived measure for the WOB has not been investigated. Before describing the methods suggested in the literature for BR extraction and WOB evaluation, it is important to highlight the significance of the research area.

2.1.1 Importance of Vital Sign Monitoring

Breathing Rate (BR) is a crucial vital sign that describes the number of movements indicative of inspiration and expiration per unit time, or in other words it describes the speed that the air goes into and is expelled from the lungs. Abnormalities in BR can be an indicator of deterioration as the body attempts to maintain oxygen delivery to the tissues (Kelly, 2018). A study, investigating early signs of deterioration, has shown that patients in a critical status could have been identified as high risk up to 24 hours previously, indicating that lack of vital signs monitoring can result in poor outcomes for patients (Cretikos et al., 2008). It has also been recommended that all the vital signs should be recorded as soon as a patient has been admitted to the hospital (National Institute for Health and Care Excellence (NICE), 2007). Furthermore an updated version on the National Early Warning Score (NEWS2) has been published recently which indicates that BR is of high interest in patient status

monitoring (Royal College of Physicians, 2017). NEWS2 is a simple scoring system based on six vital signs, where a score is allocated to each sign and an overall score is then produced (Kelly, 2018).

Much of the literature since the mid-1990s emphasises the importance of the respiration signal and especially its derivative, the BR. However, it has been demonstrated that BR is often neglected due to patient's acuity, lack of time, inadequate nursing skills and cumbersome wearable sensors (Cretikos et al., 2008; Elliott, 2016; Mlgaard, Larsen, & Håkonsen, 2016). Traditionally the BR is extracted by measuring body volume changes around the thorax over a period of time, which is proven inadequate and time-consuming especially in case of emergency (Cretikos et al., 2008). Moreover, counting chest movements cannot be carried out continuously by nurses or clinicians and it is carried out unaccurately in paediatrics where patients (children) are hyperkinetic. In addition, most of the electronic methods for BR monitoring require the use of cumbersome devices, such as chest bands for inductance plethysmography, which cause patients to feel discomfort during the recording (Charlton, 2017; Nayan, Risman, & Jaafar, 2015).

A study conducted in hospitals in 1993 indicated that a BR greater than 27 breaths per minute (bpm) is the most important indicator that can predict failure of the heart to contract effectively (Fieselmann, Hendryx, Helms, & Wakefield, 1993). Moreover, the necessity of BR was investigated in another study and it was claimed that 21% of hospitalised patients with a BR of 25-29 bpm assessed by a critical care outreach service die in hospital (Goldhill, McNarry, Mandersloot, & McGinley, 2005). An increase of the rate of mortality has been also reported for patients with higher BR (Goldhill et al., 2005). It has been demonstrated that just over half of the unhealthy subjects suffering a serious event on the hospital wards have a BR

greater than 24 bpm and these subjects could have been identified as high risk up to 24 hours before the event (Goldhill et al., 2005). Furthermore, it has been reported that BR is a better patient status indicator because of its relative greater changes compared to heart rate or blood pressure (Cretikos et al., 2008).

In 2000, it has been highlighted that the diagnostic accuracy of the ECG signal can be improved by removing modulation effects induced by respiration, hence respiration monitoring could be used in improving diagnostic and ECG applications (Forbes & Helfenbein, 2000). Previous research has established that respiration can be used as a screening tool outside the hospital setting of sleep-disorder breathing, a set of dysfunctions characterised by abnormalities of breathing pattern or the quantity of ventilation during sleep (Babaeizadeh, Zhou, Pittman, & White, 2011). There are relatively few studies that focus on how BR could be applied to signal gating but, it has been shown that a removal or adjustment of the respiratory motion effects of the thoracic organs could be achieved. Both respiration and ECG are used for image gating in MRI, CT and PET/SPECT nuclear imaging (Ehman, McNamara, Pallack, Hricak, & Higgins, 1984; E. Helfenbein, Firoozabadi, Chien, Carlson, & Babaeizadeh, 2014).

Evaluation of the respiratory function of a subject can be performed using a range of methods for patients who are mechanically ventilated and also for patients who breath spontaneously (Cohen & Schwartz, 2013). Monitoring the respiratory function can be helpful for optimising the mechanical ventilation process in a clinical setting, regulating the amount of ventilation needed, indicating weaning from ventilation and to which extent, and also defining a suitable ventilation support. Assessment of respiratory distress has a pivotal role in Intensive Care Unit (ICU) as a technique for pulmonary mechanical function appraisalment. A number of techniques have been

proposed for the respiratory effort evaluation (Addison, 2016b) such as the WOB (Pandit, Courtney, Pyon, Saslow, & Habib, 2001) and pulse transit times (Contal et al., 2013).

The significance of respiratory distress monitoring can be also shown by a study conducted in 2014 on behalf of the National Children’s Bureau and the British Association for Child and Adolescent Public Health (Royal College of Paediatrics and Child Death (RCPD), 2014). The study shows that 32% of deaths in childhood are caused by respiratory and circulatory issues. The considered age groups are given in Table 2.1. The statistics point out that the investigation of paediatric ECG and respiration is significant as many diseases are highly connected with the respiratory system. In 2017, a statistical survey from the Department of Education demonstrated that 2,444 of the 3,575 child deaths reviewed occurred in an acute hospital, a fact that enhances the need for a step in the right direction, for a reliable vital sign extraction, such as the BR and WOB, in a hospital environment (Department of Education, 2017).

Deaths by age group	
Age	Deaths due to respiration and circulation issues
1-4 years old	17%
5-14 years old	15%

Table 2.1: Deaths by age group due to respiration and circulation issues in the UK, 2010, as percentage of total (Royal College of Paediatrics and Child Death (RCPD), 2014).

2.2 QRS Complex Detection

The QRS complex is of high interest in computer-based ECG analysis as it is the most distinguishable feature of the heart signal and embodies valuable information which

can be used in Heart Rate Variability (HRV) (Malik et al., 1996) and BR estimation (Moody, Mark, Zoccola, & Mantero, 1985). Signal contamination from various types of noise and the variability of QRS morphology make the detection of the latter more complex. Moreover, the difficulty in differentiating the R-peaks from large P- or T-peaks is another factor that complicates the QRS complex identification (Pan & Tompkins, 1985). Thereupon, for the last forty years a large body of literature has investigated the QRS detection problem. Several methods have been proposed ranging from derivative-based (Pan & Tompkins, 1985; Hamilton & Tompkins, 1986) to neural networks and machine learning methods (Maglaveras, Stamkopoulos, Diamantaras, Pappas, & Strintzis, 1998; Kohler, Hennig, & Orglmeister, 2002; Xiang, Lin, & Meng, 2018). For the purpose of this thesis, three different approaches have been studied. Derived based methods which use digital filters are firstly studied and presented. Then, methods based on the Hilbert transform of the signal were investigated. Finally methods which analyse the signal in different frequency bands using Empirical Mode Decomposition are discussed. A more detailed account of them is given in the following sections.

2.2.1 Importance of the QRS Complex

The ECG is routinely used to monitor heart activities for anomalous behaviour such as tachycardia, bradycardia, atrial flutter and atrial fibrillation and even seizures. In a hospital environment it is used as a vital signs measure where, in addition to coarse time-grained information such as heart rate, it can be used to extract information that an expert diagnostician can exploit to assess the physiological status of a patient and their progress of recovery from trauma. All the heart information is hidden in the morphology of the ECG signal and especially in the QRS complex. The basic

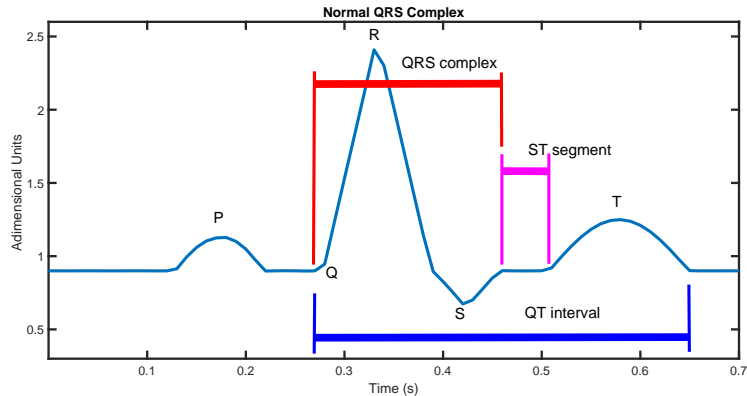


Figure 2.1: Normal QRS complex: The figure also depicts the other ECG components, such as P and T waves.

pattern of a normal ECG, as shown in Figure 2.1, consists of the QRS complex and the P and T waves (Malmivuo & Plonsey, 1995). The QRS complex is the most important among them because it corresponds to the depolarization of the right and left ventricles of the heart (Malmivuo & Plonsey, 1995). Moreover, in the last decades, it has been the research core in computerised ECG signal analysis due to its specific shape and heterogeneity.

The morphology and duration of a QRS complex has been reported as an important prognostic sign in a hospital ward, especially in patients suffering from a heart disease (Brenyo & Zareba, 2011). To determine the effects of QRS duration in patients with myocardial ischaemia, Schinkel et al. (2009) used a large cohort of 1,227 patients where a multivariate analysis was conducted (Schinkel et al., 2009). This study showed that $\text{QRS duration} \geq 120$ ms is significantly correlated to the 4.8% of cardiac deaths in the patient group under research. Moreover, in a study investigating the QRS complex significance, it has been argued that increased mortality was associated with QRS prolongation (Elhendy, Hammill, Mahoney, & Pellikka, 2005). Overall, there seems to be some evidence to indicate that abnormalities in QRS mor-

phology and duration can diagnose individuals with undetected heart diseases and an increased mortality risk (Brenyo & Zareba, 2011).

Furthermore, the shape of the QRS complex recommends the use of the R-peak as a fiducial point for the identification of other ECG components, such as the Q- and T-peaks. In brief, studies have investigated the Q, S, T wave and QRS onset/offset detection after successful extraction of the R-peaks based on the derivative and Hilbert transform of the signal (Mukhopadhyay, Mitra, & Mitra, 2011). The QRS complex is the most important among the ECG components. However, critical information exist not only in the QRS complex, but it can also be embodied in the morphology and the timing of the rest of the ECG signal. For example, the T wave, which represents the repolarization of the ventricles, is generally upright, therefore inverted T waves can be a sign of myocardial ischaemia (Dodd, Elm, & Smith, 2016). The ST segment represents the interval between ventricular depolarization and repolarization. Abnormalities in the ST segment, such as elevation or depression of the latter, could be caused by myocardial ischaemia or infraction (Vogel et al., 2019). Further, abnormalities in the QT interval are significantly associated with ventricular arrhythmias and sudden cardiac death (Rezuş, Moga, Ouatu, & Floria, 2015). Further, the QT interval can be used as an indicator of Obstructive Sleep Apnea (Baumert et al., 2008) and Chronic Obstructive Pulmonary Disease (Sievi et al., 2014). Hence the significance of accurate R-peak detection is evident as a tool for robust identification of the aforementioned ECG components.

There is a large volume of published studies describing the role of the QRS complex in HRV and BR estimation (Moody et al., 1985; Malik et al., 1996; Berntson et al., 1997; E. D. Helfenbein & Forbes, 2007; E. Helfenbein et al., 2014; Tayel & AlSaba, 2015; Charlton et al., 2016). For the evaluation of the HRV a sequence of

heart beats, i.e. R-R intervals, is processed in the frequency domain in order to get information on the activity of the autonomic nervous system. Thus, it is evident that the more accurate the R-peak detection, the more informative the analysis of the HRV. Furthermore, most of the BR estimation methods investigate the amplitude and frequency modulations of the R-peaks induced by respiration in order to extract the respiration signal. To conclude, the QRS complex is an important component in computerised ECG-analysis, especially for the continuous monitoring of vital signs such as the HR and BR. Hence, investigating a QRS complex detector, which is reliable and robust, is a continuing concern in biomedical signal processing. A more detailed account of the most common QRS detectors is given in the following sections.

2.2.2 Single-lead First-derivative-based Methods

Research in the QRS detection has shown that the slope information of the signal can be used to detect the R-peaks (Ahlstrom & Tompkins, 1983). Slope information is obtained by computing the first derivative of the signal, which represents the rate of amplitude change in time. The importance of the first derivative can be explained by the fact that the location of maximum in a peak-type signal, such as the ECG, can be estimated by finding the location of zero-crossings in the derivative. Moreover, methods based on the derivative of the signal were also used in ECG signal segmentation, i.e. identification of the rest of the ECG components, such as the QT segment (Gupta, Mitra, Mondal, & Bhowmick, 2011; Mukhopadhyay et al., 2011). However, approaches of this kind carry various well known limitations. The signal derivative can amplify high frequency noisy components, which will affect the detection accuracy. Furthermore, it has been observed that the abnormal QRS complexes tend to have low R-peak slopes, affecting the accuracy of detection because

these peaks are not identified due to their long durations and large amplitudes.

Several lines of evidence suggest that in order to address the limitations of first-derivative-based QRS detectors, additional QRS complex features should be extracted, such as width, amplitude and energy (Pan & Tompkins, 1985; Hamilton & Tompkins, 1986; Arzeno, Deng, & Poon, 2008). In previous studies the R-peak detection is based on other QRS complex features and not only slope information. It has been observed that these algorithms include two basic stages: pre-processing and decision (Pahlm & Sörnmo, 1984). Figure 2.2 shows the work-flow of these algorithms. In the pre-processing stage the ECG signal is filtered in order to remove noise caused by electrodes during the recording process, chest movements, and baseline wander (Friesen et al., 1990). In addition, the signal is processed in a way to amplify the R-peak slope and width. In the decision stage, the candidate peaks are located by using thresholds and the final decision of real R-peaks is based on some criteria. In this direction Pan and Tompkins (1985) developed a real-time algorithm for QRS complex detection based on the slope, width, and amplitude information of the signal under study (Pan & Tompkins, 1985). The so-called Pan-Tompkins algorithm was a breakthrough in QRS detection and until today it is the most cited paper related to R-peak identification (Álvarez, Penín, & Sobrino, 2013).

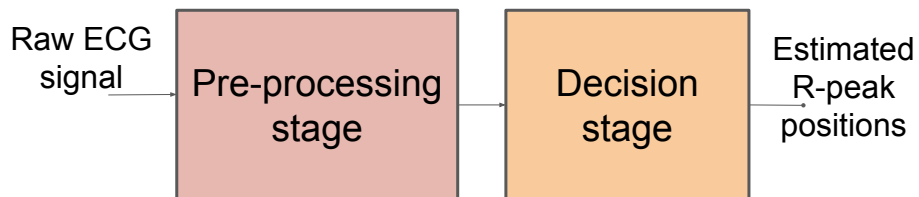


Figure 2.2: QRS detection algorithms work-flow

During the pre-processing stage, the signal is prepared for future use. Initially,

the signal should be smoothed using digital linear filters. For this purpose, the design of a band-pass filter is attempted using a cascade of a high- and low-pass filter. As soon as the signal is passed through the high-pass filter, frequencies above 5 Hz are preserved and as the signal is passed through the low-pass filter, frequencies below 12 Hz are maintained. The low-pass filter facilitates the noise removal and the high-pass weakens the low-frequency components such as P- and T-peaks, and baseline wander. Consequently, in order to derive the slope information of the signal, the first derivative of the latter must be computed, using a five-point derivative. At this instant, the higher frequencies of the signal need to be amplified using a non-linear transformation. A squaring function is used to amplify the ECG frequency components instead of low frequency components, such as noise. The last step of the pre-processing stage is the signal width information acquisition. In order to achieve this, a moving-window integration is used. The width of the window corresponds to the QRS complex duration (150 ms), which though varies from individual to individual.

As soon as the pre-processing stage is completed, the signal is ready to be further analysed in order to extract the R-peaks. The first step of the decision stage is a peak detection approach based on the amplitude of the filtered ECG signal. The latter is divided into blocks of 200 ms, since from a physiological point of view no R-peak can occur in less than 200 ms distance (heart refractory period) (Pan & Tompkins, 1985). Then, the peaks should be classified as signal or noise by thresholding both the filtered ECG and the sequence obtained after the moving-window integration. The fact that thresholds are applied to both sequences increases the algorithm reliability. The threshold estimation relies on a learning step, where an initial threshold is decided and afterwards the threshold is updated. Thus the latter is patient-specific,

and needs to be experimentally determined. The same procedure is followed for the integration sequence. If a peak is above the threshold in both signals, i.e. time domain and moving-window integration signals, it is considered to be a real R-peak.

In 1986, another algorithm was suggested as an improvement of the Pan and Tompkins (1985) algorithm, which has a slightly better performance (Hamilton & Tompkins, 1986). The pre-processing stage remains the same with small changes. For the derivative, a three-point scheme is used instead of five-point and the width of integration window is slightly bigger (160 ms). The idea behind the decision stage is almost the same with Pan and Tompkins (1985). The difference lies in how the thresholds are established, as Hamilton and Tompkins (1986) use different estimators such as median, mean and an iterative estimator. The authors report that the best results were obtained using the median in order to estimate the signal and noise peak levels. Moreover, in order to avoid multiple peak detection due to ripples in the moving-window integrated sequence, the authors established a criterion based on the amplitude of the peaks.

In both algorithms the initial threshold decision is not specified and thus should be further investigated. One main characteristic of Pan and Tompkins (1985) and Hamilton and Tompkins (1986) is that both studies attempt real time QRS detection; a fact that increases the detection error. What follows is an account of methods that attempt to increase the accuracy instead of computation speed.

2.2.3 Hilbert Transform-based Methods

During the last two decades, a considerable amount of literature has been published on QRS detection using methods that maximise the detection accuracy over computation speed. A Hilbert transform based method, proposed by D. S. Benitez,

Gaydecki, Zaidi, and Fitzpatrick (2000); D. Benitez, Gaydecki, Zaidi, and Fitzpatrick (2001), which has drawn the academic attention in the last two decades is related to the methods mentioned in the previous section (Pan & Tompkins, 1985; Hamilton & Tompkins, 1986). The algorithm consists of two stages as before, pre-processing and decision. The pre-processing stage is slightly similar to the Pan and Tompkins (1985) and Hamilton and Tompkins (1986) algorithms. During this stage, the signal should be distinguished from noise, motion and muscle artifacts. For this purpose, previous approaches use a cascade of low- and high-pass filters with a frequency range of 5-12 Hz, whereas D. S. Benitez et al. (2000); D. Benitez et al. (2001) use a band-pass filter which allows frequencies between 8-20 Hz. The next step calculates the first derivative of the signal using a central-difference formula in order to obtain the slope information of the ECG signal. Instead of squaring and averaging the output of the derivative, a Hilbert transform is applied on the latter. The main advantage of the Hilbert transform is that the peaks in the Hilbert sequence represent the zero-crossings of the derivative, e.g. R-peaks in the original ECG signal.

During the decision stage, a primary threshold, which is not patient-specific, is calculated based on the root mean square (RMS) of the Hilbert transform sequence. In fact, the RMS is squaring and averaging the signal, one more similarity with Pan and Tompkins (1985) and Hamilton and Tompkins (1986). As soon as the primary threshold is defined, the peaks are classified as candidate peaks if they exceed this threshold. In order to extract the real R-peaks, a time threshold based on the refractory period of the heart (200 ms) is applied between adjacent candidate peaks and the final decision is made based on the maximum amplitude.

A large and growing body of literature has further investigated the use of the Hilbert transform in QRS detection. Arzeno et al. (2008) analysed the Hilbert trans-

form based method and proposed ways to improve performance by applying secondary thresholds. Another application of the Hilbert transform using Empirical Mode Decomposition has been pointed out by (Yang & Tang, 2008). S- and T-peak extraction (Mukhopadhyay et al., 2011) and, heart rate detection (Prasad & Varadarajan, 2013) are additional applications of the Hilbert transform in computer-based ECG analysis.

2.2.4 Empirical Mode Decomposition-based Methods

The Hilbert-Huang Transform (HHT) has been an object of research since the late 1990s. Since it was first reported by Huang et al. (1998), the HHT has been attracting a lot of interest within the field of data-analysis because it can treat non-linear and non-stationary data while traditional data-analysis methods need linear and stationary assumptions. The HHT consists of two steps: Empirical Mode Decomposition (EMD) and Hilbert Spectral Analysis (HSA). The latter demands the computation of the instantaneous frequency (Huang et al., 1998) which is useful for narrow-band signals and requires the calculation of the analytic signal. Thus, EMD decomposes the signal into a series of narrow-band signals, which are called Intrinsic Mode Functions (IMFs), and fulfil special conditions. The key advantage of the HHT is that it is a data-driven analysis method. Thus, it is adaptive and offers physical information of data.

To date, several studies have considered the use of HHT in ECG signal processing (Nimunkar, Amit J & Tompkins, 2007; Karagiannis & Constantinou, 2009). The ECG represents the electrical activity of the heart. The latter has its own oscillator which is modulated by signals from the brain at every heart beat. Therefore, since the process changes with time, i.e. the way that the heart signal changes at each heart

beat, then it is considered as a non-stationary signal. Consequently, EMD can be applied in computer-based ECG analysis. For example, a contaminated ECG signal can be denoised and then reconstructed by identifying the IMFs after applying EMD (Lu, Yan, & Yam, 2009).

A number of studies have postulated the use of HHT in R-peak detection (Yang & Tang, 2008; Arafat & Hasan, 2009; Zhu, Zhao, & Chen, 2010; Taouli & Bereksi-Reguig, 2011; H. Li, Wang, Chen, & Li, 2014). Most of the proposed algorithms consist of a pre-processing stage before applying EMD and a decision stage based on thresholds. Yang and Tang (2008) suggested a detection algorithm based on the HHT and Wavelet transform. The ECG signal is first denoised using a Wavelet transform. After the signal is filtered, it becomes ready to be decomposed into a set of narrow-band signals, called IMFs. The IMFs can have a variable amplitude and frequency as a function of time. The higher IMFs include the fast oscillations of the signal. Thus, the QRS complex, whose frequency is high about 3-40 Hz (Malmivuo & Plonsey, 1995), corresponds to the first three IMFs. Consequently, the signal is reconstructed by summing these first three IMFs. Once the signal is reconstructed, a different threshold levels method is adopted. In particular, the algorithm calculates a sequence B as follows: $B_i = 2 \cdot (x_i - x_{i-4}) + x_{i-1} - x_{i-3}$, where x is the reconstructed signal, and $i = 1, \dots, N$, where N is the total number of samples. Then, the maximum value of B is identified and the first threshold $Y1$ is calculated as follows: $Y1 = 0.7 \cdot \max(B)$. The next step locates in x the values that exceed threshold $Y1$. For each value greater than $Y1$ and denoted by C , the threshold is modified as follows: $Y = 0.4 \cdot Y1 + 0.4 \cdot C$. If a peak is greater than Y , it is classified as an R-peak. A search back mechanism of ± 12 samples is used in order to find the original position of the R-peak taking the maximum value of this segment. The main point of this method is that the

thresholds are experimentally computed and they are patient-dependent.

A more general setting in defining thresholds can be found in studies conducted by Arafat and Hasan (2009) and Taouli and Bereksi-Reguig (2011). Both studies use different filter implementations in order to reduce high-frequency components and baseline wander. Once the noise is removed from the raw ECG signal, the extraction of IMFs is attempted. Then, the reconstruction of the signal follows by summing the first three IMFs as before. As soon as the signal has been reconstructed, a threshold is established based on the maximum value of the absolute of the reconstructed signal. A possible consideration arises from the fact that a signal can have ectopic peaks which will increase the threshold level and real R-peaks could be missed.

2.3 Breathing Rate Estimation

A summary of the main BR estimation techniques is provided in this section. The idea behind BR estimation algorithms is to extract the BR from non-invasive signals which are modulated by respiration. Two such signals are the ECG and the PPG (Charlton et al., 2017, 2016). This study focuses on the extraction of BR from a single-lead ECG because it is continuously monitored in a hospital setting as it is low-cost using non-invasive equipment. Another key motive is that ECG is easy for retrieval and storage, facilitating sharing and data transmission. Moreover, in recent years there is an increasing body of wearable sensors incorporating ECG measurements for patient monitoring (Gallego, Weir, & Errey, 2019) or wrist-type sensors for monitoring during exercise (Kim et al., 2018). However methods applied on PPG will also be discussed though will not be investigated in this thesis.

It has been reported that ECG demonstrates three types of respiratory-induced modulations based on observations of the QRS complex morphology. These are: am-

plitude modulation (AM), baseline wander (BW), and frequency modulation (FM). AM and BW are related to changes in the cardiac output due to respiration. The QRS complex amplitude and baseline are affected by respiration due to changes in the thoracic impedance and changes in the direction of the heart axis with respect to the ECG electrodes (Moody et al., 1985; Bailón, Sörnmo, & Laguna, 2006). FM is defined as the change in the instantaneous heart rate (IHR) during respiration (Jarchi, Salvi, Tarassenko, & Clifton, 2018). It is observed that IHR tends to increase during inhalation and decrease during exhalation (E. Helfenbein et al., 2014; Berntson, Cacioppo, & Quigley, 1993). The latter is due to the respiratory sinus arrhythmia (RSA), which is controlled by baroreflex sensitivity, where receptors in the main and peripheral arteries respond to slight pressure changes caused by respiration (E. Helfenbein et al., 2014). Therefore the idea behind extracting respiration from an ECG signal is actually to derive a signal controlled by one of the above-mentioned respiratory-induced modulations. The three types of modulation in the ECG signal are shown in Figure 2.3. What follows is an account of the most common BR estimation algorithms.

2.3.1 Respiration Signal Extraction from the ECG

Most of the algorithms which attempt to extract the BR from an ECG signal consist of two stages: respiration signal extraction and BR estimation which can be done either in the frequency or in the time domain. Furthermore, there are some additional stages which are optional, such as fusion of the respiration signals, or fusion of the BR estimates and quality assessment. Figure 2.4 summarises all the BR estimation steps.

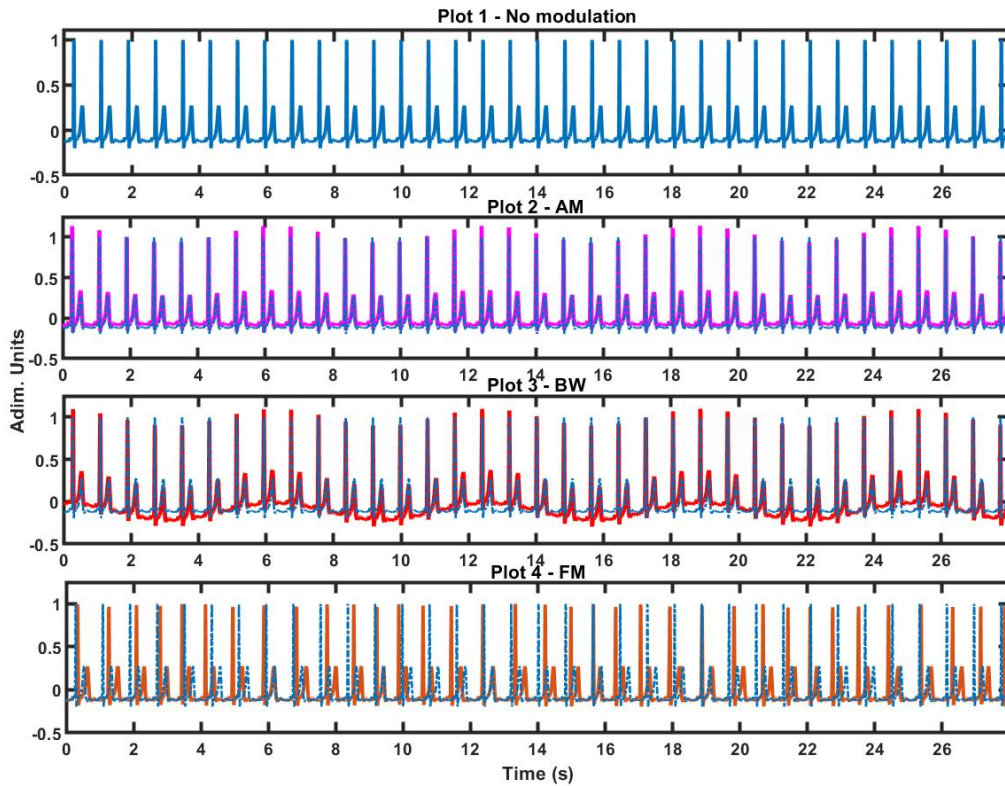


Figure 2.3: ECG respiratory-induced modulations: Plot 1 shows an ECG signal with no modulation. Plot 2 shows an ECG signal dominated by AM (pink line). The periodic amplitude changes with respect to the non-modulated ECG (dashed blue line) are evident. Plot 3 shows an ECG signal dominated by BW (red line). The baseline wander modulation can be easily noticed when comparing with the non-modulated ECG (dashed blue line). Plot 4 shows an ECG signal regulated by RSA (brown line). The R-peaks show a non-periodic pattern affected by the frequency modulation (FM) and occur at different moments when compared to the non-modulated ECG (dashed blue line). The ECG signal generation is described in Appendix D.

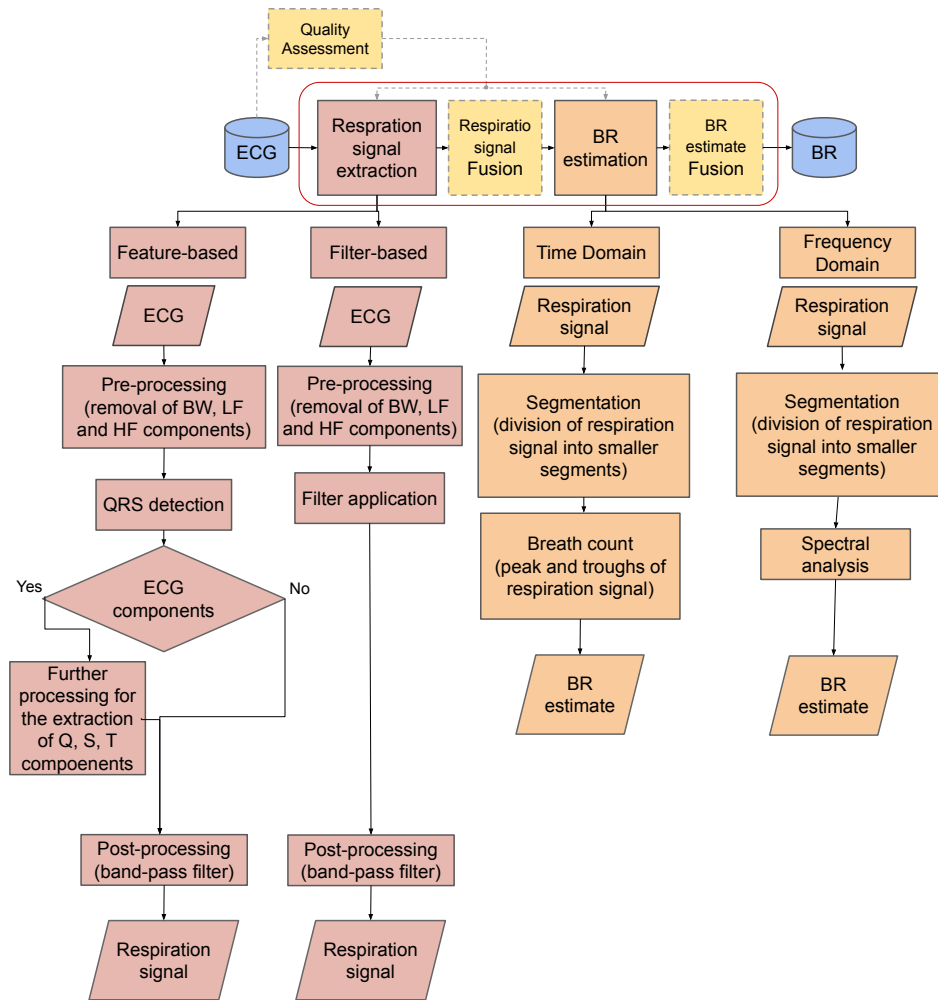


Figure 2.4: BR estimation workflow: The steps required for respiration signal extraction following two different methods: feature-based or filter-based. The work-flow also shows the steps required for BR estimation following two different approaches: time domain and frequency domain. Dashed arrows and boxes represent the optional steps during BR estimation process.

Feature-based Respiration Signal Extraction

The respiration signal can be extracted using feature-based methods, such as the amplitude variability of the QRS complexes, or filter-based methods, where for example the ECG signal can be low-pass filtered in order to extract a signal which is dominated by BW. Prior to respiration signal extraction there is a pre-processing step which is sometimes optional. During the latter, the ECG signal is prepared for future use by eliminating cardiac frequencies, baseline wander and power-line interference. Most commonly used filters are median and high-pass filters with a cut-off frequency of 0.03 Hz or 0.05 Hz (Sharma, Sharma, & Bhagat, 2015; Lázaro, Gil, Bailón, Mincholé, & Laguna, 2013; Campolo et al., 2011; Lázaro, Gil, Bailón, & Laguna, 2011; Sobron, Romero, & Lopetegi, 2010). The powerline interference can be reduced using notch filters at 50 Hz or 60 Hz depending on the continent (Sharma et al., 2015; H. Li et al., 2014; Y. Li, Yan, Zhang, & Yang, 2014; Lázaro et al., 2013; Campolo et al., 2011; Lázaro et al., 2011; Sobron et al., 2010).

Feature-based techniques aim to extract a signal from QRS complex features, such as the amplitude variability of the R-peaks. Therefore a common step in all feature-based methods is the identification of the R-peaks. Babaeizadeh et al. (2011) suggested an algorithm which is based on the variability in the peak-to-trough QRS amplitude in order to extract a signal dominated by AM. A single-lead ECG signal is given as an input to the algorithm. The R-peaks are detected and the peak-to-trough amplitude is measured. A method exploiting the RSA manifestation was proposed by E. Helfenbein et al. (2014). The time locations of the R-peaks are identified in order to compute the R-R intervals. Then, the instantaneous heart rate (IHR) values are computed by taking the inverse of the R-R intervals (time between two consecutive R-peaks).

Much of the recent available literature on feature-based techniques deals with the analysis of beat-to-beat changes using Principal Component Analysis (PCA) or Independent Component Analysis (ICA) (Rajagopalan & Ramachandran, 2017; Sadr & de Chazal, 2016; Tiinanen, Nojonen, Tulppo, Kiviniemi, & Seppänen, 2015; Varon & Van Huffel, 2015; Langley, Bowers, & Murray, 2010). In fact the respiratory-induced variability of the ECG features, such as the R-peaks, can be characterised by PCA. Firstly, the R-peaks are located in order to extract the ECG features. PCA and ICA are both applied to an aligned collection of ECG features. For example, aligned QRS complexes can be seen as observations for PCA or ICA. In order to reduce computational cost, PCA can be performed using Singular Value Decomposition (SVD). Since the application of PCA to an ensemble of QRS complexes describes the degree of morphologic beat to beat variability, the respiration signal is taken to be the first principal component that represents the largest variability caused by this morphologic beat to beat variability that is caused by respiration (Langley et al., 2010). Furthermore, SVD can also be used in ICA-derived respiration for dimensionality reduction, as only the components with the largest eigenvalues will be considered for further analysis. As soon as the independent components (ICs) are estimated, a frequency analysis should be applied in order to identify the component which corresponds to the respiration signal (Tiinanen et al., 2015).

The majority of feature-based methods also contain a post-processing step, where there are alternations from method to method. As soon as the respiration signal is extracted from the ECG signal using one of the aforementioned approaches, it is re-sampled at a constant sampling frequency. This step is essential as the respiratory signal, acquired from the ECG features is unevenly sampled, which will later be processed in the frequency domain where regular sampling is required. Most com-

monly used methods for re-sampling are linear (Orphanidou et al., 2013) or cubic spline interpolation (Birrenkott, Pimentel, Watkinson, & Clifton, 2018). Respiratory signals are usually re-sampled at 4-8 Hz (Varon & Van Huffel, 2015; E. Helfenbein et al., 2014; Karlen, Raman, Ansermino, & Dumont, 2013; Babaeizadeh et al., 2011; Lázaro et al., 2011; Cysarz et al., 2008; E. D. Helfenbein & Forbes, 2007).

Filter-based Respiration Signal Extraction

Filter-based techniques aim to filter the ECG signal in order to maintain only the respiratory frequencies. A filter-based method has been reported by E. Helfenbein et al. (2014) and is called the Electromyogram derived respiration (EMGDR). The idea lies on the fact that ECG contains muscle noise due to intercostal chest muscles and the diaphragm during respiration. It has been observed that EMG contains frequencies between 250 and 500 Hz, therefore the ECG signal is filtered using a high-pass filter with cut-off frequency at least 250 Hz. This reduces low frequency components, such as P or T waves, and enhances EMG. QRS complexes are still present and represented as spikes. Then, in order to compute the power of the muscle activity, the RMS values of the signal is calculated. The derived signal rises above the baseline during respiration. QRS spikes are then removed using a QRS detector. The final signal, which corresponds to respiration, is derived using a moving average filter which smooths out the signal from noisy short spikes. The major drawback of this method is the need of high-sampled ECG recordings in order to have a bandwidth up to 500 Hz.

Another way of extracting the respiration signal using filters can be based on the cepstrum of the ECG signal. Sharma et al. (2015) reported an algorithm based on homomorphic filtering for the respiration signal extraction. Homomorphic filtering

is used in source separation techniques by transforming convolved components into additive, where later a linear filtering scheme can be applied. The cepstrum is defined as the log of the Fourier transform of the signal. Thus, the idea behind homomorphic filtering is to apply a band-pass filter on the cepstrum of the ECG and obtain the respiration signal in the log domain. To recover the respiration signal in its original domain, the exponential of the latter should be taken. The major limitation of homomorphic filtering is that no respiration signal can be reliably retrieved when the respiration frequencies lie outside the cut-off frequencies of the band-pass filter.

Publications that concentrate on filter-based techniques have investigated the use of EMD in respiration signal extraction (Orphanidou, 2017; Gavali & Upasani, 2015; Garde, Karlen, Dehkordi, Ansermino, & Dumont, 2013; Labate et al., 2013; Sierra-Alonso, Sepúlveda-Cano, Bailón-Luesma, Laguna, & Castellanos-Dominguez, 2013; Campolo et al., 2011). It has been already mentioned that EMD decomposes the signal into a series of narrow-band signals, called the IMFs. Thus, EMD can be used to identify covered signals in the ECG, such as respiration (Karagiannis & Constantinou, 2009; Lu et al., 2009). After successful extraction of the IMFs the signal can be reconstructed by summing them. Based on this, Campolo et al. (2011) suggested that the respiration signal can be extracted using the IMFs which are related to respiration. Therefore, a method for identifying the IMFs related to respiration should be established, rather than using visual inspection as in Labate et al. (2013). A recent study of Gavali and Upasani (2015) points out that the IMFs related to respiration could be detected by investigating the frequency range of the respiration signal and the rate at which the ECG signal was sampled. Hence, a spectral analysis of the IMFs is needed.

Another post-processing step common to both feature- and filter-based tech-

niques is the elimination of the non-respiratory frequencies. After successful extraction of the respiration signal, the latter is filtered within reasonable respiration frequencies using band-pass filters. The range of frequencies used in literature varies and sometimes should be adjusted according to the patients, especially for paediatrics (S. Fleming, Tarassenko, Thompson, & Mant, 2008). The minimum cut-off frequency is 0.067 Hz (Karlen et al., 2013), which corresponds to 4 bpm, and the maximum is 1 Hz (Birrenkott et al., 2018; Lázaro et al., 2013), which corresponds to 60 bpm. However, no extensive research has been carried out in order to establish an ideal frequency range. This step completes the respiration signal extraction and the latter is ready to be further investigated in order to estimate the BR.

BR Estimation in the Frequency Domain

Having discussed the respiration signal extraction, the frequency domain methods which aim to analyse the frequency spectra of the respiration signal and identify BR as the most dominant frequency within the range of plausible respiratory frequencies will be discussed here. The mean is first removed from the respiration signal and then the latter is divided into overlapping windows. For each window, the Fourier transform is then analysed in order to identify the maximum spectral peak that corresponds to the BR (Y. Li et al., 2014; Karlen et al., 2013; Sobron et al., 2010). Thus far, previous studies have demonstrated that Power Spectral Density (PSD) can also be used for the frequency domain estimation (Campolo et al., 2011) or the Welch periodogram (Lázaro et al., 2013, 2011). The idea behind these methods is similar to the Fourier transform, what changes is the way to compute the frequency spectra of the respiration signal.

Various studies have assessed the Autoregressive (AR) Modelling in the frequency

domain BR estimation (Shah, Fleming, Thompson, & Tarassenko, 2015; Orphanidou et al., 2013; Nemati, Malhotra, & Clifford, 2010; S. G. Fleming & Tarassenko, 2007; Orphanidou et al., 2009). In 2008 it was reported that the EDR (ECG-Derived Respiration) signal can be modelled as a linearly weighted sum of the preceding p values, where p is the model order. The transfer function, $H(z)$, of the system is evaluated and it is observed that the latter has no zeros, thus the AR model is an all-pole model. The poles define peaks in the frequency spectrum of the signal. The phase angle of each pole results in the frequency of the spectral peak and the pole with the highest magnitude is set to be the BR (S. Fleming et al., 2008). One year earlier, S. G. Fleming and Tarassenko (2007) suggested the pole with the maximum magnitude to be stored and a threshold of 95% of the maximum magnitude is used in order to identify the candidate poles. BR is set to be the candidate pole with the smallest angle. The respiration signal is commonly down-sampled in order to increase the stability of the AR model. Several plausible model orders and model estimation algorithms have been proposed in the literature, with no consensus on the optimal order or estimator. Most commonly used model estimators are the Burg (S. Fleming et al., 2008) and Yule-Walker algorithms (Garde, Karlen, Ansermino, & Dumont, 2014; Orphanidou et al., 2009).

Previous research has established the use of Correntropy Spectral Density (CSD) in frequency domain BR estimation (Garde et al., 2014). CSD is actually based on the Fourier transform of the correntropy of the signal and provides improved spectral resolution compared to power spectral density due to higher-order statistics (Burt, Cinar, & Principe, 2014; Santamaría, Pokharel, & Principe, 2006). The signal is first divided into windows and the CSD is evaluated for each window. The spectral peak which corresponds to the BR can be found as the maximum in the range from 8 to

60 bpm (Garde et al., 2014).

BR Estimation in the Time Domain

Another significant aspect is the time domain BR estimation which aims to detect individual breaths in the respiration signal. In 2012 a simple breath detection method was suggested based on a three-point peak detection algorithm (Shah, 2012), which intends to locate the peaks in the respiration signal and count them as breaths. The mean is first subtracted from the signal and then the latter is divided into windows. In each window, the peak detector is applied. A point is considered as peak if its amplitude is greater than the amplitude of the previous and of the following points. The main drawback of this method is the identification of multiple peaks due to ripples in the signal which will increase the number of breaths and hence affect the accuracy of the estimation. A more sophisticated algorithm for breath detection was proposed by S. Fleming (2010). A point in the respiration signal is set to be a peak if it fulfils some special conditions such as sign change in the derivative of the signal and the least distance between two consecutive peaks.

Additional Approaches: Fusion and Quality Assessment

As indicated previously there are some optional stages in the respiration signal extraction and BR estimation. Several studies have investigated the fusion of respiration signals prior to BR estimation (Lázaro et al., 2013, 2011; Sobron et al., 2010). The general idea is to produce different respiration signals either from both ECG or PPG, or produce several respiration signals following alternative methods. Sobron et al. (2010) extracted four different respiration signals and averaged their spectra in order to attenuate non-respiratory frequencies. The combined spectrum is then later

investigated by a frequency domain estimation method. Alternatively, Lázaro et al. (2011) introduced a peak-conditioned averaging where only the sufficiently peaked spectra are averaged.

A great deal of previous research has focused on fusion of the BR estimates (Orphanidou, 2017; Karlen et al., 2013; Orphanidou et al., 2013; Nemati et al., 2010; S. G. Fleming & Tarassenko, 2007; Orphanidou et al., 2009). A number of BR estimates can be fused by evaluating the standard deviation from all of them and then averaging only those whose standard deviation was lower than 4 bpm (Karlen et al., 2013). Orphanidou et al. (2013) used an AR pole magnitude criterion in order to fuse BR estimates. The fused BR estimate results from the BR pole with the largest magnitude among all the candidate BR poles which came from different respiration signals.

The accuracy of BR estimation can be further improved by introducing a quality assessment step which can be applied on either the ECG signal or the BR estimate or a combination of both (Birrenkott et al., 2018; Birrenkott, Pimentel, Watkinson, & Clifton, 2016; Orphanidou, 2017; Chan, Ferdosi, & Narasimhan, 2013; Karlen et al., 2013; Orphanidou et al., 2013, 2012). The quality of the ECG signal can be assessed by following a number of rules which are based on the HR and R-R interval, combined with a template matching criterion, which is an indicator of signal regularity (Orphanidou et al., 2014, 2012). The quality of the BR estimated was measured by the Fourier transform, autocorrelation function, autoregression, and Hjorth complexity. For each measure, which is later used as a weight, a value between 0 and 1 was obtained. The trustworthy BR estimate is the weighted average of the individual BR estimates (Birrenkott et al., 2016). Nonetheless quality assessment may delay the BR estimation as in order to check the quality of either the ECG

signal or of a BR estimate, we need to investigate a couple of seconds or minutes worth of data.

Assessment Methodologies

Here the assessment methodologies for BR estimation algorithms found in the literature will be discussed. It is observed that ECG is the main non-invasive method used to determine the BR, along with the PPG signal. Moreover, a number of studies have investigated algorithms which use both ECG and PPG signals (Birrenkott et al., 2018; Orphanidou, 2017; Y. Li et al., 2014; Orphanidou et al., 2014; Lázaro et al., 2011). Most of the publications have compared two to three different BR estimation algorithms, meaning that from the same signal different features were extracted and further analysed in order to extract the respiration signal (Birrenkott et al., 2018; E. Helfenbein et al., 2014; Y. Li et al., 2014; Chan et al., 2013; Karlen et al., 2013; Orphanidou et al., 2013). To evaluate the performance of BR estimation algorithms, a number of different datasets has been used. The majority of studies have used recordings which belong to healthy adults. Very few publications have assessed BR estimation algorithms using datasets containing data from hospitalised children (Birrenkott et al., 2018; Shah et al., 2015; Garde et al., 2013; Karlen et al., 2013), which highlights the necessity to broadly evaluate BR estimation methods using recordings which belong to sick children. Moreover, the duration of the recordings varies from 2 m to 12 h (Orphanidou, 2017; Shah et al., 2015) and a number of publications have not indicated the duration of the recordings under study (Varon & Van Huffel, 2015; Chan et al., 2013).

The performance of BR estimation algorithms was evaluated by employing statistical analysis between the estimated and the reference BR. The majority of publi-

cations used the mean absolute error (MAE) for performance evaluation (Birrenkott et al., 2018; Rajagopalan & Ramachandran, 2017; Orphanidou, 2017; Shah et al., 2015). A considerable amount of studies used the root mean squared (RMS) or the percentage error (Garde et al., 2013; Karlen et al., 2013; Orphanidou et al., 2009). Very few publications have investigated the correlation between the extracted and the reference respiration signals, as a statistic for performance assessment (Tiinanen et al., 2015; Varon & Van Huffel, 2015; Sharma et al., 2015; Langley et al., 2010). Moreover, the duration of respiration signal used to estimate a single BR varies between 30 to 90 s and a number of studies have not reported the duration of respiration signal window used.

BR Estimation Performance Comparison

This section briefly discusses the main current state of the art BR estimation techniques found in the literature. The studies that were identified to be further investigated and extended to obtain better BR estimation accuracy are summarised in Table 2.2. All the required techniques and evaluation approaches have been previously stated in this chapter.

In the study presented by Birrenkott et al. (2018), six respiration signals are acquired by extracting the AM, FM and BW modulated signals from both ECG and PPG recordings. Then the authors apply a respiration quality metric, which decides whether to include or exclude a respiration window from the analysis. This method shows a promising performance for the Capnobase dataset after fusing all respiration signals. However, this paper makes no attempt to ascertain whether the suggested approach will produce the same results if applied to children who suffer from a respiratory disease, where it is difficult to define respiration patterns in order

to use quality indices.

Rajagopalan and Ramachandran (2017) and Tiinanen et al. (2015) focused on PCA and ICA which are categorised as feature-based techniques that analyse the beat-to-beat changes in the ECG signal. Both methods appear to adequately estimate the BR of young and elderly subjects, nonetheless Rajagopalan and Ramachandran (2017) fail to specify how the BR estimate was acquired from the PCA-derived respiration signal. On the other hand, the main criticism on the study of Tiinanen et al. (2015) is that their evaluation process finds a correlation between the estimated and reference respiration signals, thus skipping the evaluation of BRs from the respiration signal. Furthermore, Garde et al. (2013), in their interesting analysis of the application of EMD in respiration signal extraction, report a relatively good estimation approach. However, their method was tested only on PPG signals.

The results obtained in the aforementioned literature highlight the importance of applying BR estimation methods on data that belong to sick hospitalised children. Chapter 5 will focus on the BR extraction from ECG and EMG recordings of children with respiratory problems collected in the Birmingham's Children Hospital (BCH). The aforementioned data are not publicly available and they are used for the first time in this thesis. Therefore, a straight comparison of the developed and current state of the art methods is not feasible due to the nature of that data used, as it would be unfair to contrast techniques that have been applied to different datasets.

2.3.2 SCG-Derived Respiration

The existing body of research on BR estimation suggests that the latter can also be extracted by the Seismocardiogram (SCG) signal (Zakeri et al., 2016; Haescher, Matthies, Trimpop, & Urban, 2015; Tadi, Koivisto, Pänkäälä, & Paasio, 2014; Pan-

Study	Sensor	Technique	Dataset	Age	Evaluation
Birrenkott et al. (2018)	PPG, ECG	AM, FM, BW RQIs	Capnobase (Karlén et al., 2013) MIMIC-II (Goldberger et al., 2000)	paed, young, elderly	MAE (0.71±0.89)
Rajagopalan and Ramachandran (2017)	ECG	PCA	Fantasia (Goldberger et al., 2000)	young, elderly	MAE (0.85, 0.5)
Tinanen et al. (2015)	ECG	ICA	Fantasia	young, elderly	correlation
Garde et al. (2013)	PPG	EMD	Capnobase	paed, young, elderly	RSE (3.5)

Table 2.2: Comparison of current state of the art BR Estimation methods

dia, Inan, & Kovacs, 2013; Pandia, Inan, Kovacs, & Giovangrandi, 2012; Reinvuo, Hannula, Sorvoja, Alasaarela, & Myllyla, 2006). SCG is a non-invasive method for recording and analysing heart vibrations which are transmitted to the chest wall. More specifically, SCG measures waves produced by the heart acceleration and deceleration due to the heart wall motion and blood movement (Inan et al., 2014; Zanetti & Salerno, 1991). Moreover, SCG is commonly recorded by accelerometers placed either on the left clavicle or sternum, which makes its acquisition inexpensive and of high quality (Castiglioni, Faini, Parati, & Di Rienzo, 2007). A major advantage of SCG is that the accelerometer can be integrated in the sensor/device that records ECG, hence two respiration signals can be extracted simultaneously and maybe fused, one from the ECG and one from the SCG, with no need for more equipment on the patient (Inan et al., 2018). SCG can play a key role in vital sign monitoring as the heart acceleration waves can provide more details on the heart movement. Moreover, SCG can be a useful indicator of left ventricular malfunctions, such as myocardial infarction (Zanetti & Salerno, 1991). Another important advantage is that if SCG is simultaneously recorded with ECG, the clinicians can have access to information of both mechanical and electrical aspects of the heart and respiration extracted by two different respiratory-modulated signals (Zanetti & Tavakolian, 2013).

A recent study investigated the respiratory phases extraction from the SCG (Zakeri et al., 2016) due to the fact that an accelerometer placed on the sternum or clavicle can capture chest wall movements resulting from the expansion and extraction of the lungs. Haescher et al. (2015) suggested to low-pass filter the SCG signal and then investigate its frequency spectrum in order to obtain respiratory information. As noted by Tadi et al. (2014) SCG-derived respiration can also be used

in nuclear image gating in order to improve the quality and reliability of the image. The SCG signal is passed through a median and a moving-average filter in order to extract respiration. However, the aforementioned methods do not investigate amplitude or morphology-based changes in the SCG due to respiration. Pandia et al. (2012) extracted three respiration-dependent features of the SCG signal including morphology and timing variations between heartbeats (Zakeri et al., 2016), in order to assess SCG-derived respiration. Nonetheless, a more extensive research should be conducted on SCG-derived respiration due to the aforementioned advantages of the SCG signal.

2.4 Respiratory Distress Estimation

As previously mentioned one primary aim of this study is to ascertain the correlation of the ECG signal with the respiratory distress and develop an ECG-based method for the evaluation of the latter as a tool for identifying the ability of a patient to maintain effective respiration. This section discusses the importance of respiratory distress along with the potential methods for its evaluation. Monitoring respiratory distress can be useful for optimising and adjusting the mechanical ventilation process in a hospital ward, regulating the amount of ventilation needed, indicating weaning from ventilation and to which extent, and also defining a suitable ventilation support (Baram & Richman, 2010). Moreover, evaluation of respiratory function plays a key role in the ICU and is one of the most critical components of nurses' assessment abilities (Ahrens, 1993), as it provides information on the function and on injury of the lungs and diaphragm (Bellani & Pesenti, 2014). Several techniques have been used in its estimation including the WOB (Addison, 2016b).

The WOB is an important indicator of a subject's respiratory status (Cohen &

Schwartz, 2013) and it is defined as the change in the airway pressure related to tidal volume (Baram & Richman, 2010). In other words, WOB can be defined as the effort expended by an individual in breathing. The WOB is assessed as a key vital sign by skilled nurses and clinicians especially on paediatric and neonatal wards. In a clinical setting, the WOB can be measured using invasive methods by calculating the esophageal pressure with an esophageal balloon manometer, or transdiaphragmatic pressure with esophageal and gastric balloon manometers (Stoller & Hill, 2012), methods which are often poorly tolerated by patients and cause discomfort, especially during sleep.

In order to avoid the aforementioned invasive methods, nurses usually evaluate increased WOB by observing potential events of anxiety, discomfort, tachypnea, increase in blood pressure or heart rate, nasal flaring, and subcostal and intercostal retractions (Baram & Richman, 2010). Nonetheless, the clinical estimation of WOB is subjective and can lead to false diagnostic conclusions. For example, patients with an increased WOB show they are in comfort or patients breathing at lower BR might have high WOB even if they seem comfortable at the current ventilation support (Cohen & Schwartz, 2013). One of the greater challenges in digital healthcare is the minimisation of different types of sensors worn by a patient and the exclusion of invasive techniques which increase discomfort in a hospital environment. Therefore extracting the WOB for respiratory-modulated signals, such as the ECG, that are already being recorded would be very advantageous if it could be performed reliably and be trustworthy. The following is a brief description of how respiratory distress is currently evaluated using plethysmograph recordings. However there has been no detailed investigation of extracting the WOB from ECG signals. It has been reported that the WOB can be assessed by measuring the work done by the respiratory muscles

(Milic-Emili, Rocca, & D Angelo, 1999), whose frequency range is above 250 Hz. It is evident that in order to capture the respiratory muscled activity, ECG recordings sampled at high rate are required. The latter is not really common as ECG signal are usually sampled between 100 and 200 Hz.

2.4.1 Plethysmography-based Estimation

In recent years, much more has become available on the measurement of the respiratory distress from the PPG signal (Addison, 2017, 2016b, 2016a; Contal et al., 2013). These studies demonstrate a respiratory manifestation in the PPG signal which can be expressed by the period of respiratory modulations. In 2013 Contal et al. (2013) investigated the correlation of pulse transit time (PTT) with respiratory effort. To measure PPT, the R-peak onset and the peak in the PPG signal are identified, then the R-peak time is subtracted from the PPG peak time. To evaluate their assumption, the PPT measure was compared to esophageal pressure and a positive correlation was found between the two, indicating PPT can be used as a measure of respiratory distress. Moreover, it has been shown that the strength of respiratory modulations present in the signal is related to the respiratory effort by indicating changes in the thoracic pressure.

In a preliminary study conducted by Addison (2016a) the PPG baseline modulation was investigated as a measure of respiratory effort. The modulation was extracted by applying a band-pass filter on the PPG signal and then taking the running median of the latter. The baseline modulation was compared to airway pressure signals and a generally increasing trend was found. It has been also argued that there is a positive monotonic relationship between the amplitude changes on the PPG signal over a respiratory cycle and the respiratory distress, by using the PPG fluid

responsiveness parameter, ΔPOP . (Addison, 2016b, 2016a). The latter is defined as follows:

$$\Delta POP = (AMP_{max} - AMP_{min}) / ((AMP_{max} + AMP_{min}) / 2), \quad (2.1)$$

where AMP_{max} and AMP_{min} are the maximum and minimum PPG amplitudes within a respiratory cycle. The ΔPOP measure was compared to an airway pressure signal at the mouth, and it was found that increased respiratory distress is manifested as increase in ΔPOP , hence it can be used in respiratory status monitoring.

2.4.2 ECG Respiratory Artifact

Previous studies have explored the relationship of the respiratory artifact present in the ECG and the respiratory effort (Littmann, 2015; Littmann, Rennyson, Wall, & Parker, 2008; Cheriex, Brugada, & Wellens, 1986; Higgins, Phillips Jr, & Sumner, 1966). Littmann et al. (2008) analysed the ECG signal from 248 patients in order to locate by visual inspection micro-oscillations around the R-peak, which correspond to a sign of increased respiratory distress. In a more recent study (Littmann, 2015) it has been argued that the presence of peaks which are mimicking P waves in the ECG signal manifest increased WOB. However, the main weakness of these studies is the failure to address how these micro-oscillations can be identified from a single-lead ECG using computerised techniques. Moreover, one question that needs to be answered is whether these micro-oscillations are prominent in all leads or it varies for each patient. Furthermore this approach requires ECG signals sampled at a high sampling rate, where in most cases an ECG is sampled between 100 and 200 Hz. These micro-oscillations constitute a high frequency component of the ECG signal, thus a higher sampling frequency is needed due to the Nyquist limitation. Hence the

latter necessitates further investigations given that the existing technology provides sensors/devices which can measure ECG recordings that are sampled at high rate.

Chapter 3

Breathing Rate Estimation: Methodology and Approaches

As previously stated in Chapter 1, one of the main goals of this thesis is to investigate BR estimation from the ECG of hospitalised children. BR plays a key role in medicine and healthcare as it provides early warning for clinicians. Acquisition of the respiration signal can be done physically using spirometry, measurements from nasal thermistors, and plethysmography. However, these methods are expensive in terms of hardware and computational cost. Another drawback of these acquisition methods is that they usually require cumbersome devices which cause patient distress. Since the ECG signal is routinely monitored in many healthcare settings and modulated by respiration as discussed in Chapter 2, a considerable amount of literature has been published on deriving respiratory signals from the ECG. Hence, a more detailed account of respiration signal extraction methods from the ECG is given in the following sections. Here, the estimation of BR from the respiration signal using frequency and time domain analysis will be discussed briefly. Moreover, a method

fusion technique as an attempt to improve the accuracy of the BR estimation will be discussed in this chapter.

3.1 Single Methods

A large and growing body of the literature has focused on the BR estimation using ECG signals because the latter is inexpensive, non-invasive and easy for retrieval and sharing. Furthermore, in the recent years there is an increasing body of wearable sensors incorporating ECG measurements for patient monitoring (Gallego et al., 2019) or wrist type sensors for monitoring during exercise (Kim et al., 2018). As previously mentioned in Section 2.3 the ECG signal demonstrates three types of respiratory-induced modulation: AM, FM and BW, shown in Figure 2.3. What follows is an account of methods which attempt to extract the aforementioned modulations in order to obtain a respiration signal.

3.1.1 ECG-Derived Respiration (EDR)

There are several methods for acquiring respiratory signals from the ECG. EDR (ECG-derived respiration) is a popular technique which takes advantage of the ECG amplitude modulations induced by respiration (E. Helfenbein et al., 2014; Babaeizadeh et al., 2011; Moody et al., 1985). First, the R-peaks are identified and then the peak-to-trough amplitude is computed for each QRS complex. The requirement of the identification of the trough makes the EDR method more complex and time-consuming as it requires the identification of both the R- and S-peaks in the ECG signal. This will be addressed in our enhanced algorithm of the EDR as will be discussed in Chapter 5. Following the computation of the peak-to-trough, the effect of FPs (defined later in Chapter 4) in the R-peak detection on the accuracy of

the BR estimation is minimised by discarding outliers. This contributes to an overall improvement in the performance of the method. The peak-to-trough values are then interpolated in order to derive an evenly sampled waveform. This is required because this waveform will later be filtered in the frequency domain, thus it should be uniformly sampled. The re-sampled waveform is then filtered within reasonable respiration frequencies in order to extract the final EDR signal. To summarise, the conventional EDR method as proposed in E. Helfenbein et al. (2014) is as follows:

1. Extract the QRS complexes from a single-lead ECG signal,
2. For each QRS complex compute the peak-to-trough amplitude,
3. Discard outliers by restricting peak-to-trough values to remain within the range of ± 2 SDs from the average value,
4. Interpolate with a cubic spline and then down-sample the interpolated signal at 8 Hz,
5. Filter the output of step 4 within a reasonable respiration frequencies (0.0666-0.5 Hz) to get the EDR signal.

A synthetic ECG signal was simulated so that it is dominated by AM, meaning that the amplitude of the R-peaks vary over time. The reference BR of the simulated ECG was set to be 4 bpm. The simulated ECG is shown in Figure 3.1 Plot 1. The obtained EDR signal is shown in Figure 3.1 Plot 2. It is evident that the signal is dominated by respiratory-induced amplitude modulations, and in one minute there are 4 breaths, thus indicating a BR of 4 bpm.

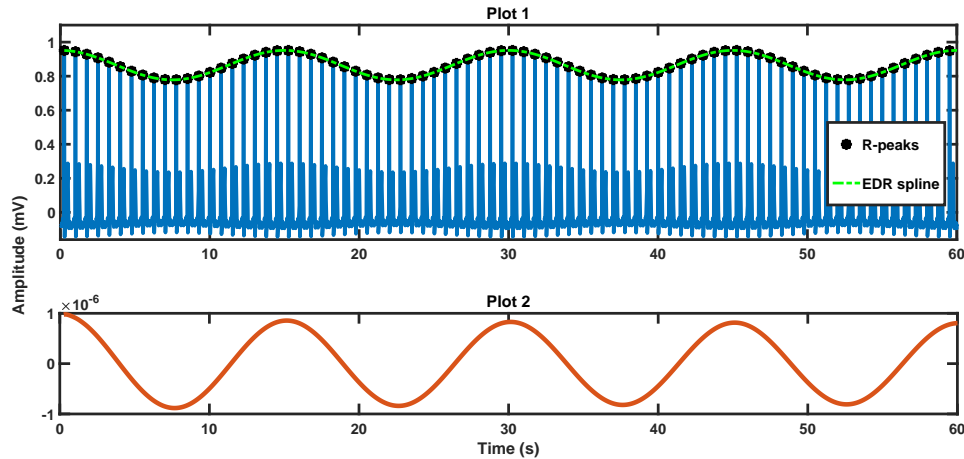


Figure 3.1: EDR on a synthetic ECG signal: Plot 1 shows the proposed EDR method for a small part (60 s) of a synthetic signal dominated by AM. R-peaks are represented by black circles. The output of the EDR interpolation is represented by a green dashed curve. Plot 2 shows the derived respiration signal for one minute window corresponding to the ECG of Plot 1.

3.1.2 RSA-Derived Respiration (RSA)

Another popular method for extracting the respiration signal from the ECG is the Respiratory Sinus Arrhythmia-derived respiration (RSA) (E. Helfenbein et al., 2014). The latter attempts to extract the respiration signal by investigating the frequency modulations induced by respiration in the ECG signal. First the R-peaks are located. Then the R-R intervals are computed, which is the time interval between two consecutive R-peaks. Then the Instantaneous Heart Rate (IHR) values are computed, which are actually the inverse of the R-R intervals. The IHR values are later interpolated and re-sampled in order to get an evenly sampled waveform. The latter is then filtered within reasonable respiration frequencies in order to get the final RSA signal. To summarise, the RSA method is as follows:

1. Extract the QRS complexes from a single-lead ECG signal,

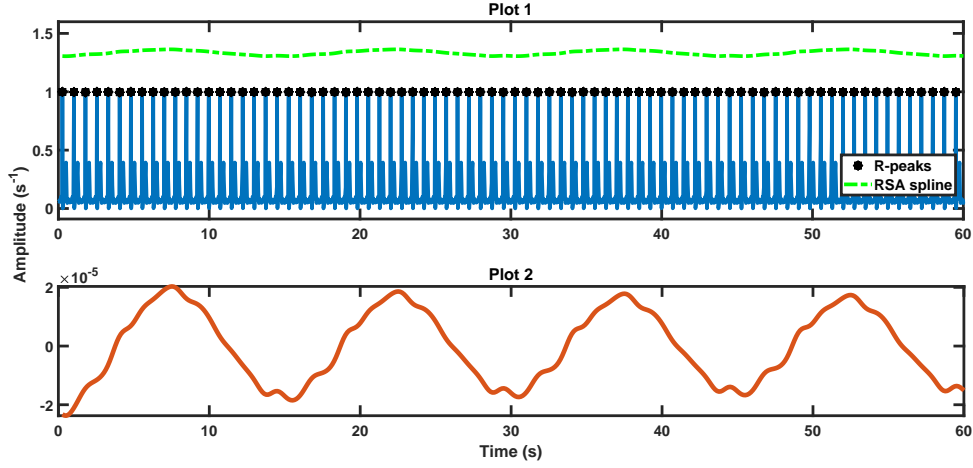


Figure 3.2: RSA on a synthetic ECG signal: Plot 1 shows small part (60 s) of the synthetic ECG signal. R-peaks are represented by black circles. RSA spline is represented by a green dashed curve. Plot 2 shows the derived respiration signal for the one minute window corresponding to the ECG of Plot 1 using the RSA method.

2. Compute the IHR values as follows:

$$\text{IHR}_i = \frac{1}{t_{R_{i+1}} - t_{R_i}}, \quad (3.1)$$

where t_{R_i} is the time of the i -th R-peak and $i = 1, \dots, n$, where n is the total number of identified R-peaks,

3. Interpolate with a cubic spline and then down-sample the interpolated IHR signal at 8 Hz,
4. Filter the output of step 3 within reasonable respiration frequencies (0.0666-0.5 Hz) to get the RSA signal.

A synthetic ECG signal was simulated so that it is governed by FM, meaning that the distances between the R-peaks are not constant. Moreover, the reference BR

was set at 4 bpm. Figure 3.2 shows the RSA method applied on the aforementioned ECG signal (Plot 1). Plot 2 shows the derived respiration signal, which corresponds to the ECG signal of Plot 1. It is observed that there are 4 dominant oscillations in this one minute window, hence indicating a BR of 4 bpm.

3.1.3 PCA-Derived Respiration (PCADR)

In several settings of computer-based ECG signal analysis the respiration signal is unknown. Complications may arise due to uncertainty of the clinical environment and the variability of the biomedical signals due to different pathologies and the inter- or intra-patient variability. Therefore, deterministic signal processing approaches such as frequency filtering, are inappropriate. It has been previously mentioned that the desired signal is unknown but not all its properties. The statistical properties of the signal could be known, thus statistical modelling methods would be more appropriate.

The PCA-derived respiration (PCADR) is based on the assumption that the respiratory-induced variability of the ECG features, such as the QRS complex, can be captured by the PCA. In other words, the ECG signal is the observation in which the respiratory-induced variability which carries information on the respiration signal is unknown. Hence the necessity of methods which can separate the two signals is evident. Further details on PCA can be found in Appendix E, along with information on the Blind Source Separation Problem (BSS), which forms the basis of PCA.

The first step of the PCADR is the generation of a set of observations which contain the ECG features that are affected by respiration. Therefore, a data matrix is constructed by stacking the QRS complexes in the rows of the matrix (Figure 3.3). Then an eigendecomposition of the data matrix is carried out. For computational

reasons the eigenvalues and eigenvectors of the data matrix are computed using SVD. The idea is to keep the component that expresses the greatest variance in the data. Therefore, the first eigenvector which corresponds to the maximum eigenvalue, is kept and then projected on the data matrix in order to get the mixing coefficients. Then the latter projection is filtered by the PCs in order to obtain a linear transformation of the data. To summarise, the PCADR is as follows:

1. Create the data matrix by stacking n QRS complexes of length m in the rows of matrix \mathbf{X} , see Figure 3.3 below, and remove the mean, μ_{x_i} from each row, where $i = 1, \dots, n$,
2. Calculate the eigenvectors and eigenvalues using SVD, $\mathbf{R}_X = \mathbf{U}\mathbf{\Sigma}\mathbf{V}^T$,
3. Keep the first eigenvector \mathbf{v}_1 of length n which corresponds to the maximum eigenvalue, σ_{11}^2 ,
4. Project the eigenvector on the data matrix to get the first PC, $\mathbf{s}_1 = \mathbf{v}_1\mathbf{X}$, where \mathbf{s}_1 is a $1 \times m$ vector,
5. Multiply the PC, \mathbf{s}_1 , with the first eigenvector, \mathbf{v}_1 , in order to obtain the PCADR signal. The first of row of matrix $\hat{\mathbf{X}}$, where $\hat{\mathbf{X}} = \mathbf{v}_1^T \mathbf{s}_1$, is the PCADR signal.

Figure 3.4 shows the derived respiration signal after applying the PCA method to a synthetic ECG signal. It is evident that the BR is accurate as for each one minute window the estimated BR is equal to 4 bpm, which is consistent with the reference respiration.



Figure 3.3: Data matrix construction: The data matrix, i.e. input of PCA, after stacking the QRS complexes in the rows of the matrix.

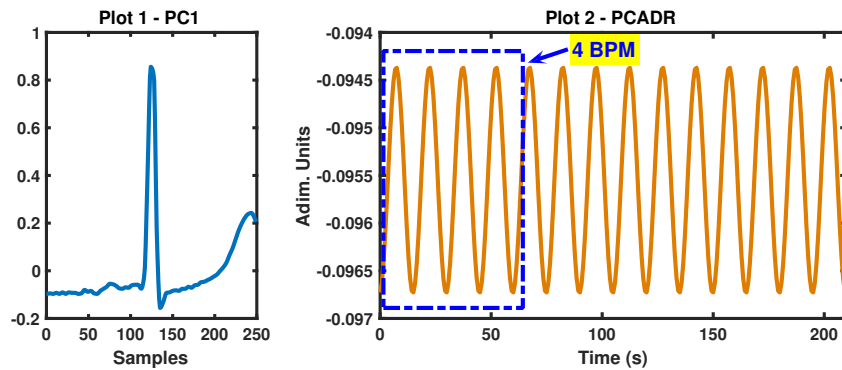


Figure 3.4: PCADR signal: Plot 1 shows the first PC of the synthetic signal under study. Plot 2 shows the PCADR signal extracted. The blue box defines a period of one minute where four oscillations reveal that the BR is 4 bpm, same as the reference BR.

3.1.4 ICA-Derived Respiration (ICADR)

An additional statistical method, which is based on the BSS model, is the Independent Component Analysis (ICA). Since it was reported in 1986, ICA has been attracting a lot of interest in machine learning and signal processing (Tanskanen & Viik, 2012; Herault & Jutten, 1986). ICA is a statistical approach whose main assumption is that the observations are actually linear combinations of source sig-

nals which are statistically independent, whereas PCA assumes that source signals are mutually uncorrelated (Comon, 1994; Jutten & Herault, 1991). Under this assumption the n observations are linear combinations of n unknown independent components (Hyvärinen & Oja, 2000). The source signals are assumed to be mutually independent, zero-mean, $E\{s_i\} = 0$, and of unit variance, $E\{s_i^2\} = 1$. Therefore the problem can be expressed as in Equation E.5. Hence, the main goal of ICA is the estimation of the mixing matrix \mathbf{A} . If the estimation of the latter and its inverse, \mathbf{A}^{-1} was trivial, then the observations could be obtained as follows: $\mathbf{S} = \mathbf{A}^{-1}\mathbf{X}$.

The main ambiguity of ICA is that the order and the variance of the independent components (ICs) cannot be determined, that is why it is assumed that the ICs are of unit variance. Furthermore, the fundamental challenge of ICA is that the observations can be decomposed only to non-Gaussian ICs. There are several algorithms for ICA. For the purpose of this thesis the fastICA algorithm was used, whose core is the kurtosis maximisation as a measure on the non-Gaussianity. For more details please refer to Hyvarinen (1999).

The idea behind ICA-derived respiration (ICADR) is to analyse the beat-to-beat changes in the QRS complex in order to extract the respiration signal using the ICA by attempting to choose the corresponding to respiration IC by making use of its spectral analysis. First the data matrix is constructed, as explained in Section 3.1.3 and PCA is applied in order to reduce the dimensionality of the data. Then the fastICA is applied to the reduced matrix in order to obtain the ICs. Then the ICs should undergo a spectral analysis in order to chose which component corresponds to the respiration signal. To summarise, the ICADR method is as follows:

1. Create the data matrix by stacking n QRS complexes of length m in the rows of matrix \mathbf{X} and remove the mean, μ_{x_i} from each row, where $i = 1, \dots, n$,

2. Apply PCA method in order to reduce the size of \mathbf{X} ,
3. Apply the fastICA algorithm to the reduced matrix, $\mathbf{X}_{\text{tranc}}$ in order to get the source signals as ICs,
4. Analyse the frequency content of the ICs in order to get the ICADR signal.

Figure 3.5 shows the first five ICs derived after applying the fastICA algorithm to the reduced data matrix, along with their frequency spectra. It is evident that there are components which correspond to respiration as they have one dominant frequency at 4 bpm which is the reference BR for the synthetic signal under study.

3.1.5 EMD-Derived Respiration (EMDDR)

It has been already noted in Section 2.3 that the EMD method can be used as a filter-based respiration signal extraction approach because it has been reported that EMD can identify masked signals in the ECG, such as respiration (Karagiannis & Constantinou, 2009). The idea of EMD-derived respiration (EMDDR) is to investigate the IMFs in the frequency domain in order to choose which IMF corresponds to respiration. The BR estimation based on the IMF selection will be demonstrated later in this section, but first the EMD method is discussed which is required for the EMDDR.

Empirical Mode Decomposition

EMD decomposes the signal, $x(t)$, into a series of narrow-band signals, $c_i(t)$, which are called IMFs, and fulfil special conditions. An oscillatory mode of the signal is an IMF exclusively in condition that:

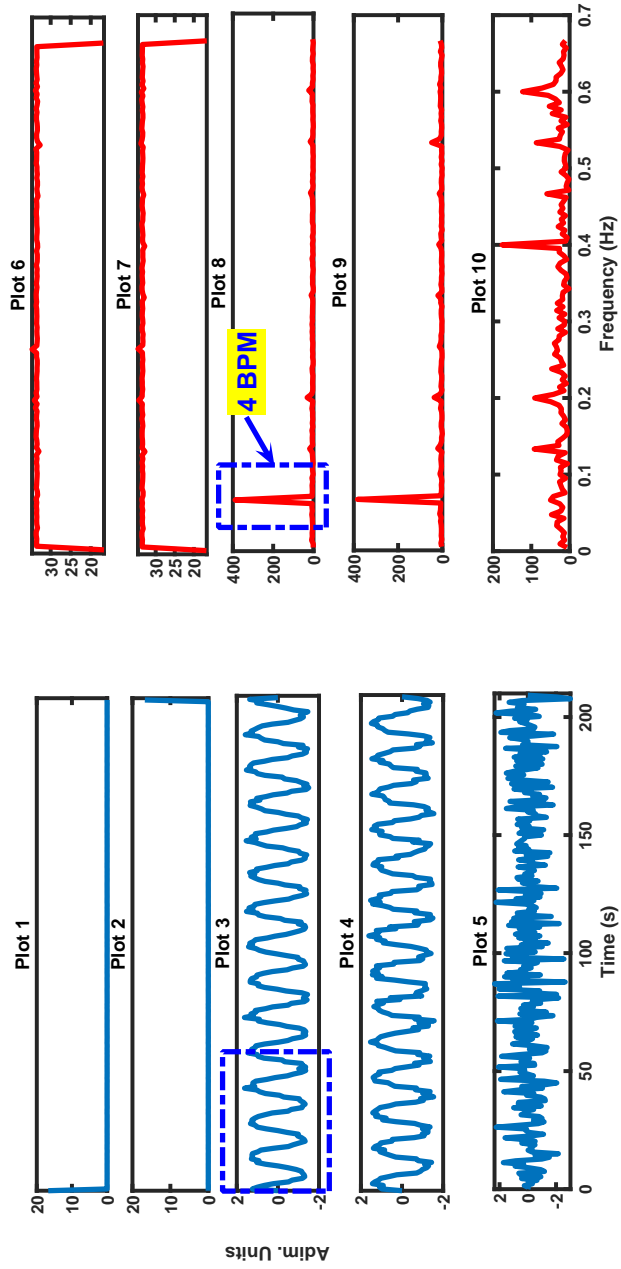


Figure 3.5: ICADR signal: Plots 1-5 show the first five ICs derived after applying the fastICA algorithm to the reduced data matrix, constructed from the synthetic ECG signal under study. Plots 6-10 show the frequency spectra of each component. The blue box indicates the respiration frequency at 4 bpm which is the same as the reference BR.

- (1) In the whole dataset, the number of zero-crossings and the number of extrema are either equal or differ at most by one, and
- (2) At any point, the mean values of maximum and minimum envelope is zero.

The key advantage of EMD is that it is a data-driven analysis method. Thus, it is adaptive, does not require any a priori knowledge and offers a good re-representation of the data (Huang et al., 1998). A brief review of the EMD heuristic algorithm is given in Algorithm 1. The nature of EMD is iterative because the procedure described in Algorithm 1 has to be processed by a *sifting process* (Huang et al., 1998), which includes a number of steps (lines 3 to 9) repeated on the i -th component, $h_i(t)$. The sifting process has to be repeated as many times as required to reduce the extracted signal to an IMF. For our implementations in order to terminate the EMD algorithm, the number of zero-crossings and the number of extrema are checked for equality or whether they differ at most by one. If a residue is a trend line or constant, then EMD algorithm can be terminated, otherwise it means that the residue still has extrema and thus, the EMD scheme should continue. As soon as the EMD algorithm is terminated, the signal $x(t)$ can be written as follows:

$$x(t) = \sum_{i=1}^N c_i(t) + r_N(t), \quad (3.2)$$

where N is the total number of the extracted IMFs and $r_N(t)$ is the final residue.

Regarding the EMDDR approach, the ECG signal is first decomposed into its IMFs using the EMD method. Then a Fourier transform is applied to each IMF in order to get its frequency spectrum (Campolo et al., 2011). The IMF whose frequency content lies between reasonable respiration frequencies is assumed to be the respiration signal. To summarise, the EMDDR method is as follows:

1. Apply the EMD method on the ECG signal in order to extract the IMFs, $c_1(t), \dots, c_N(t)$, where N is the total number of the extracted IMFs,
2. For each IMF $c_i(t)$, where $i = 1, \dots, N$, produced in step 1, compute its Fourier transform $F\{c_i(t)\}$, and choose as respiration signal the IMF whose frequencies lie between reasonable respiration frequencies,

Algorithm 1: EMD

```

1 Initialise:  $i \leftarrow 0, r_i(t) \leftarrow x(t)$ ;
2 while  $r_i(t) \neq \text{trend or constant}$  do
3   Identify extrema in  $r_i(t)$ :
4    $S_{max} \leftarrow \{t : \frac{\partial r_i}{\partial t} = 0 \wedge \frac{\partial^2 r_i}{\partial t^2} < 0\}$ ;
5    $S_{min} \leftarrow \{t : \frac{\partial r_i}{\partial t} = 0 \wedge \frac{\partial^2 r_i}{\partial t^2} > 0\}$ ;
6   Create upper,  $\hat{r}_i(t)$ , and lower,  $\underline{r}_i(t)$ , envelopes:
7    $\hat{r}_i(t) \leftarrow \text{spline}(S_{max})$ ;
8    $\underline{r}_i(t) \leftarrow \text{spline}(S_{min})$ ;
9   Compute mean of envelopes:  $m_i(t) \leftarrow [\hat{r}_i(t) + \underline{r}_i(t)]/2$ ;
10  Find  $i$ -th component:  $h_i(t) \leftarrow r_i(t) - m_i(t)$ ;
11   $n \leftarrow 0$ ;
12  while  $h_i^n(t) \neq \text{IMF}$  do
13    Repeat lines 3 to 9;
14     $n \leftarrow n + 1$ ;
15  end
16  Extract  $i$ -th IMF after  $n$  iterations:  $c_i(t) = h_i^n(t)$ ;
17  Update data and compute the residue:  $r_i(t) - c_i(t) = r_{i+1}(t)$ ;
18   $i \leftarrow i + 1$ 
19 end

```

One of the major reported drawbacks of EMD is the mode mixing issue, which has been defined as an IMF that either consists of signals of differing scales, or a single signal that can be observed in different IMFs (Huang et al., 1998). This might make the physical meaning of an IMF unclear. Considering that the main source of ECG modulations is the BR and HR, information related to respiration and HR

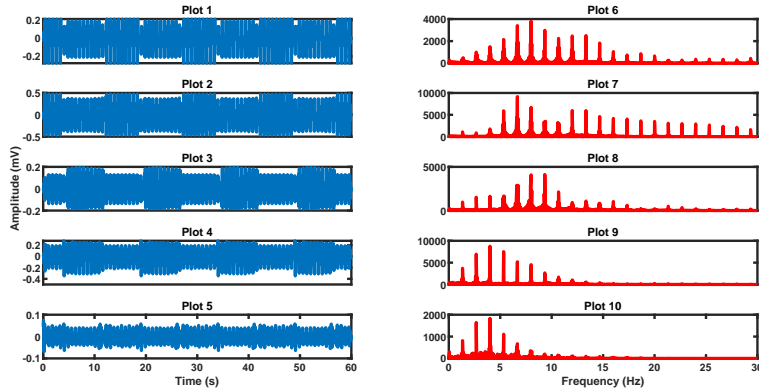


Figure 3.6: EMDDR signal: Plots 1-5 show the IMFs 1-5 after applying EMD on a synthetic ECG signal. Plots 6-10 shows the frequency spectra of Plots 1-5 (DFT points = 30000).

are expected to be identified in the IMFs of the ECG signal. According to the mode mixing issue, the respiration signal could be present in multiple IMFs and might be masked by the HR. However, BR and HR frequency bands are quite different. Thus, it is suggested that a frequency domain investigation of the IMFs could reveal the one that corresponds to the respiration signal, whose frequency would be the most prominent frequency in the IMF, and overcome the limitations induced by the mode mixing issue. This frequency domain based analysis method is proved to be capable of extracting the respiratory signal and accurately estimating the BR as will be demonstrated next.

Figure 3.6 and Figure 3.7 show the first 10 IMFs extracted along with their frequency spectra for the AM synthetic signal under study. In Figure 3.7, Plot 5 and Plot 10 show that the 10th IMF corresponds to the respiration signal, because in the frequency spectrum there is only one dominant frequency at 0.0667 Hz which corresponds to 4 bpm, equal to the reference BR of the synthetic ECG signal.

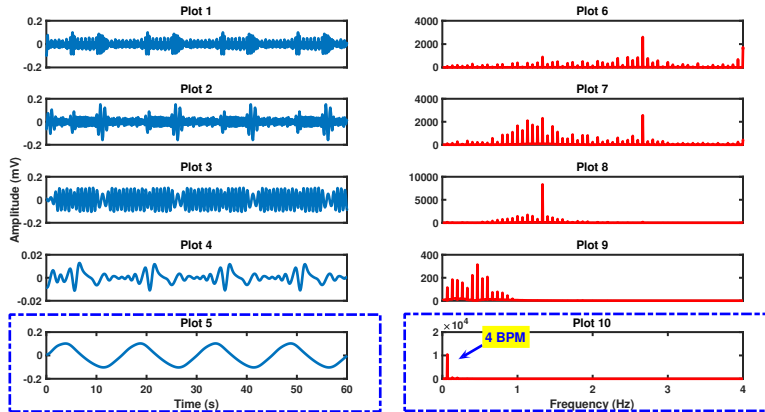


Figure 3.7: EMDDR signal: Plots 1-5 show the IMFs 6-10 after applying EMD on a synthetic ECG signal. Plots 6-10 shows the frequency spectra of Plots 1-5 (DFT points = 30000). The blue box points out that IMF 10 corresponds to the respiration signal giving a BR of 4 bpm, equal to the reference.

3.1.6 Frequency domain-based BR estimation

Thus far, this chapter has shown standard respiration signal extraction methods. As soon as the respiration signal is derived, it can be processed either in the time or in the frequency domain in order to obtain the BR estimates as previously shown in Figure 2.4. According to the methodology followed in this thesis, the respiration signal is divided into one minute windows and each window is further analysed. The main assumption of the frequency domain estimation is that the most dominant spectral peak corresponds to the BR. Under this assumption the most commonly used methods is the Discrete Fourier Transform (DFT) and the Correntropy Spectral Density (CSD). CSD can be defined as a generalisation of the power spectral density and actually is the Fourier transform of the centred correntropy function (Garde et al., 2014):

$$\text{CSD}(\omega) = \sum_{m=-(N-1)}^{N-1} V_c(m) \cdot e^{-j\omega m}, \quad (3.3)$$

where N is the length of the signal and V_c is the centred correntropy function, that is $V_c(m) = V(m) - \bar{V}$, and V and \bar{V} are defined as:

$$V(m) = \frac{1}{N-m+1} \sum_{n=m}^N \kappa(x(n) - x(n-m)), \quad (3.4)$$

$$\bar{V} = \frac{1}{N^2} \sum_{m=1}^N \sum_{n=m}^N \kappa(x(n) - x(n-m)), \quad (3.5)$$

where $\kappa(\cdot)$ is a Gaussian kernel function that is:

$$\kappa(x(n) - x(n-m)) = \frac{1}{\sqrt{2\pi}\sigma} e^{\left[-\frac{(x(n)-x(n-m))^2}{2\sigma^2}\right]}, \quad (3.6)$$

where σ is the kernel parameter which results from the Silverman's rule (Garde et al., 2014).

For the DFT analysis the size of the transform, N , is defined as: $N = 60 * f_{resp}$, where f_{resp} is the sampling frequency of the respiration signal and 60 corresponds to the time duration of the one minute window in seconds. Most of the breathing rate estimation methods discussed in this thesis resample the respiration signal at 8 Hz, which results to an N of 480 DFT points. To avoid repetition, additional information on the DFT analysis will be given when the respiration signal is not resampled and its frequency depends on the frequency of the ECG.

Figure 3.8 shows an example of a DFT analysis of the EDR signal of Figure 3.1. The length of the synthetic signal is 4 minutes thus the corresponding EDR signal is divided into 4 windows. The frequency spectrum of each window is depicted by

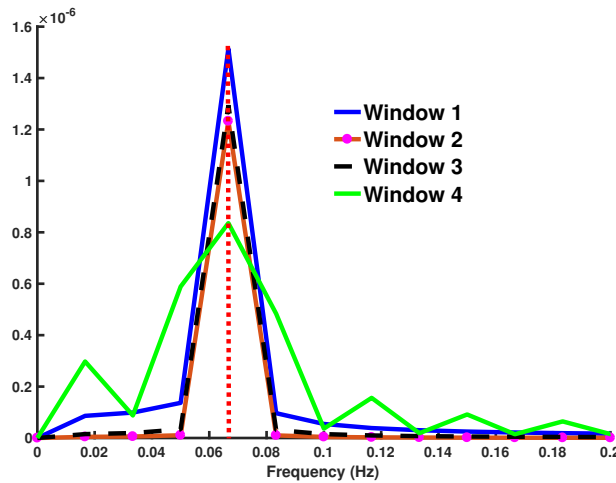


Figure 3.8: DFT BR estimation: Each window is depicted in a different color. It is evident that there is a dominant spectral peak in each window which is located at 4 bpm, which is equal to the reference BR of the synthetic signal.

a different colour line. It is apparent from this figure that a clear dominant peak is present in each window. It can also be observed that the dominant peak is located at 0.0667 Hz which corresponds to 4 bpm which is equal to the reference BR of the synthetic signal.

Figure 3.9 shows an example of a CSD analysis of the same EDR signal of Figure 3.1. Each plot shows the frequency spectrum obtained after applying the CSD analysis. It can be observed that in all windows there is a prominent spectral peak at 4 bpm (0.066 Hz), which is equal to the reference BR of the synthetic signal.

3.1.7 Time domain-based BR estimation

Time domain estimation analysis aims to detect individual breaths in the respiration signal by usually incorporating algorithms which detect peaks in the respiration signal. Shah (2012) proposed a method where the breaths in the respiration signal

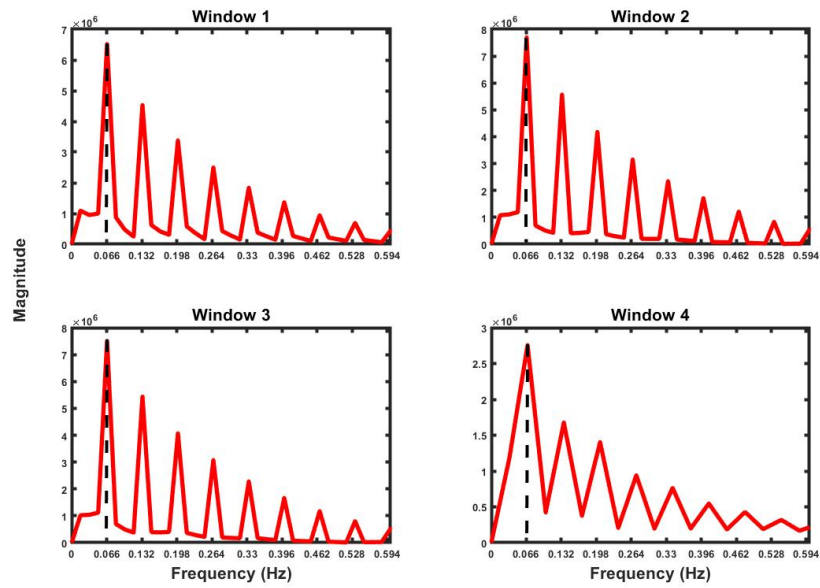


Figure 3.9: CSD BR estimation: Each plot corresponds to a one minute window. It is evident that there is a dominant spectral peak (dashed black line) in each window which is located at 0.066 Hz (4 bpm), which is equal to the reference BR of the synthetic signal.

are identified using a three-point (3PT) scheme, which is given by Algorithm 2.

Algorithm 2: Three-point (3PT)

```

1  $n \leftarrow 1$ ;
2 if  $(x_n > x_{n-1}) \wedge (x_n > x_{n+1})$  then
3   | peak  $\leftarrow n$ 
4 end
5 if  $(x_n > x_{n-1}) \wedge (x_n == x_{n+1}) \wedge (x_n > x_{n+2})$  then
6   | peak  $\leftarrow n$ 
7 else
8   |  $n \leftarrow n + 1$ 
9 end

```

A more complicated method for the time domain BR estimation was suggested by S. Fleming (2010). The idea is to identify peaks and troughs in the respiration signal and then apply a set of rules in order to detect the final peaks which correspond to breaths. This algorithm will be referred from now on as peak-to-trough (P2T). A peak or trough is valid if it fulfils the following four rules:

- a. A point is considered a peak if the gradient change is from positive to negative or a trough if the gradient change is from negative to positive,
- b. A peak must be followed by a trough and vice versa,
- c. The amplitude of a peak should be above the mean of the respiration signal and the amplitude of a trough should be below the mean,
- d. The peak-to-peak or trough-to-trough interval should be greater than 0.5 s,

As soon as the location of the breaths, t_1, t_2, \dots, t_n where n is the total number of breaths, are identified using any of the two methods discussed above, the instanta-

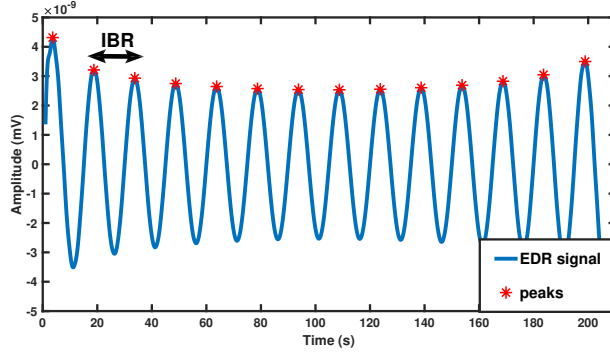


Figure 3.10: Three-point BR estimation: In each window the peaks of the respiration signal are identified and represented by red asterisks. It is evident that in each window 4 breaths are identified.

neous BR (IBR) is computed as follows:

$$\text{IBR}_i = 60 \cdot \frac{1}{t_{i+1} - t_i}, \quad (3.7)$$

where $i = 1, \dots, n - 1$. Then the IBR values are averaged over one minute windows in order to obtain the final BR estimates. Figure 3.10 shows the EDR signal obtained in Section 3.1.1 (Figure 3.1). The three-point detection algorithm is applied at each window, the respiration peaks are located and represented as red asterisks, and then the IBR values are computed. As can be seen from the figure in each window the algorithm identifies 4 breaths, i.e. 4 peaks, which is equal to the reference BR at 4 bpm. The same results are obtained using the P2T method where same peaks are identified from both methods.

3.2 Fusion Methods

It has been already mentioned in Section 2.3 that BR estimation accuracy might be improved by using fusion techniques and also shown in Figure 2.4. The majority of

studies looking at this have investigated techniques that focus on method fusion. The main idea is to generate respiration signals or BR estimates from several methods and fuse them either in the time or in the frequency domain (Orphanidou, 2017; Orphanidou et al., 2013; Sobron et al., 2010). In the above an all-pole autoregressive (AR) model was used for the spectral analysis of the respiration signals and a pole magnitude criterion was developed for the method fusion (Orphanidou et al., 2013; Nemati et al., 2010; S. G. Fleming & Tarassenko, 2007). The idea of this method is based on the fact that the spectral peaks of the signal are represented by the poles of the AR model (Proakis & Manolakis, 1996). Moreover, the frequencies of the spectral peaks are given by the phase angle of the corresponding poles of the model. Before demonstrating the fusion method, a brief discussion on AR modelling is given.

AR modelling

AR modelling can be defined as a linear prediction problem, where the current value of a signal, $x(n)$, can be predicted by a linearly weighted sum of the previous p values (Proakis & Manolakis, 1996). The latter is the order of the AR model, $AR(p)$, and $p < N$, where N is the length of the signal to be modelled. Hence the current value of x can be written as follows:

$$x(n) = - \sum_{k=1}^p a_k x(n-k) + e(n), \quad (3.8)$$

where $e(n)$ is the error term, which is assumed to be normally distributed, with zero mean and a variance of σ^2 . The above AR model can also be seen as a system with input $e(n)$ and output $x(n)$, with the following transfer function:

$$\begin{aligned}
X(Z) &= - \sum_{k=1}^p a_k X(Z) z^{-k} + E(Z), \\
E(Z) &= X(Z) \left(1 + \sum_{k=1}^p a_k z^{-k} \right), \\
\frac{X(Z)}{E(Z)} &= \frac{1}{1 + \sum_{k=1}^p a_k z^{-k}},
\end{aligned} \tag{3.9}$$

where $X(Z)$ and $E(Z)$ are the Z -transforms of the output and input of the system, respectively. This results in:

$$\begin{aligned}
H(z) &= \frac{1}{\sum_{k=0}^p a_k z^{-k}} \\
&= \frac{z^p}{(z - z_1)(z - z_2) \dots (z - z_p)},
\end{aligned} \tag{3.10}$$

assuming that $a_0 = 1$.

It can be seen that the denominator of $H(z)$ can be factorised into p terms, which actually define the roots z_i of the denominator, giving the poles of $H(z)$. Moreover, it can be observed that the transfer function has no zeros away from the origin, making an all-pole AR model. From theory, poles occur in complex-conjugate pairs, defining the spectral peaks in the spectrum. The frequency of each peak is given by the phase angle of the corresponding pole. The phase angle at a frequency f is defined as follows:

$$\theta = 2\pi f \Delta t, \tag{3.11}$$

where Δt is the sampling interval (Proakis & Manolakis, 1996).

Regarding the method fusion for the BR estimation, respiratory signals from different methods were derived. Each respiratory signal was modelled using an all-pole

AR model. A respiratory pole for each signal was selected based on a magnitude and phase angle criterion, described in Algorithm 3. First the poles and phase angles are evaluated. The poles whose phase angle fall within reasonable respiration frequencies are kept and their magnitude is computed. The candidate respiratory poles are selected based on a magnitude criterion and the final BR pole is set to be the pole with the minimum phase angle, which corresponds to the minimum frequency. Hence at this stage different BR poles are derived, one for each generated respiration signal. Finally, the fused respiratory pole is set to be the pole with the highest magnitude, thus the final selection is based on a pole magnitude criterion.

A critical point of AR modelling is the model order selection. The majority of studies decide the model order on an experimental basis by testing orders ranging from 6 to 20. Orphanidou et al. (2013) set the model order at 8 as it gives good results for the database they used. However, the latter is addressed to a specific age and type of patients thus it can affect the BR estimation accuracy for subjects with different characteristics. This drawback will be addressed in our proposed enhanced fusion method as will be discussed in Chapter 5.

Figure 3.11 shows the poles obtained for the EDR and RSA signals (Figures 3.1 and 3.2) discussed earlier in this chapter. The poles in the blue box represent the poles whose phase angle falls within reasonable respiration frequencies (0.1-0.6 Hz). It can be observed that the fusion method selects as the final fused BR based on the pole with the maximum magnitude, which is the EDR pole.

Algorithm 3: Pole Magnitude and Phase Angle Criterion

- 1 Model respiratory signal: $AR(p_1)$, where $p_1 = 8$;
 - 2 Calculate phase angles: θ ;
 - 3 Keep respiratory poles: $\text{poles} \leftarrow \text{poles}(0.1 \text{ Hz} < \theta < 0.6 \text{ Hz})$;
 - 4 Calculate pole magnitudes: $\text{mag} \leftarrow \sqrt{\text{Re}\{pole\}^2 + \text{Im}\{pole\}^2} s$;
 - 5 Find highest magnitude: $\text{mag}_{max} \leftarrow \max(\text{mag})$;
 - 6 Find candidate BR poles: $\text{poles}_{cand} \leftarrow \text{poles}(\text{mag} > 0.95 * \text{mag}_{max})$;
 - 7 Select BR pole: $\text{pole}_{BR} \leftarrow \text{poles}_{cand}(\min(\theta))$;
-

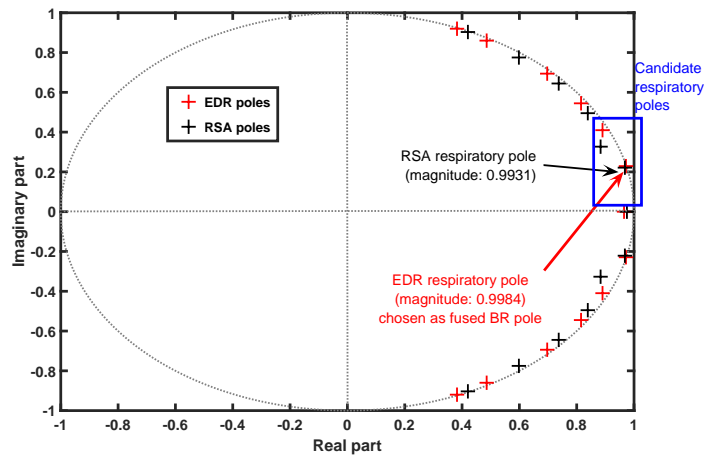


Figure 3.11: Pole magnitude method fusion: EDR poles are represented by red crosses. RSA poles are represented by black crosses. The fusion approach selects as BR the pole whose magnitude is the highest.

Chapter 4

QRS Complex Detection

This chapter discusses the research and experiments conducted over the past three years by the author in order to develop a novel QRS detection algorithm which can be applied to all patients types. For this purpose, an exhaustive review of the most common detectors in the literature was necessary to understand the limitations and strengths of the methods suggested.

4.1 QRS Detection Algorithms

The algorithms reviewed in Chapter 2 on the QRS detection are the most commonly used and have been shown to achieve high levels of accuracy. Thus, they will be implemented, analysed and compared in this chapter. In particular, Pan and Tompkins (1985) and D. S. Benitez et al. (2000) will be discussed in detail. The main reason for further investigating these two algorithms are that both detectors consist of a major finding in the derivative-based QRS identification methods and they have been highly used (Álvarez et al., 2013) due to their high accuracy levels (Ruangsuwana, Velikic, & Bocko, 2010). Another reason why these two methods were selected is that

both algorithms were benchmarked on ECG recordings obtained from the MIT-BIH Arrhythmia database (Goldberger et al., 2000). As we have previously discussed in Chapter 1, this thesis aims to develop a BR monitoring system, thus the verification of the QRS detection algorithms is beyond the scope of this work.

A comparison of the algorithms is shown in Table 4.1, in terms of *Sensitivity* (Se) and *Positive Predictivity* ($+P$), which will be defined later in Section 4.4. It needs to be pointed out that the number of recordings used by the authors is different and that the detection accuracy provided is based on the results reported by the authors. What stands out in the table is that the algorithm suggested by D. S. Benitez et al. (2000) shows the best performance between the two. The following sections describe our findings after implementing these methods, on the same MIT-BIH Arrhythmia database.

Algorithm	Se(%)	$+P$ (%)
Pan and Tompkins (1985)	99.30	-
D. Benitez et al. (2001)	99.94	99.30

Table 4.1: erformance of QRS detection algorithms (reported by the authors)

Hilbert Transform

Before we discuss the Pan and Tompkins (1985) and D. S. Benitez et al. (2000) method, we first discuss the Hilbert transform which will be required for the understanding of the later. The Hilbert transform is an all-pass filter that imparts a 90° phase shift on the signal at its output (Proakis & Manolakis, 1996), thus the zero-crossings in the derivative sequence, which illustrate the peaks in the ECG signal, will be represented as peaks in the Hilbert sequence. Given a continuous time signal

$x(t)$, its Hilbert transform is defined as:

$$\hat{x}(t) = H\{x(t)\} = \frac{1}{\pi} \int_{-\infty}^{\infty} x(\tau) \frac{1}{t - \tau} d\tau. \quad (4.1)$$

It can be observed that the Hilbert transform is an operator that transforms the signal from the time domain to the time domain because the independent variable t does not change. Moreover, $H\{\cdot\}$ is a linear operator because $\hat{x}(t)$ results from the convolution of $x(t)$ with $(\pi t)^{-1}$:

$$\hat{x}(t) = \frac{1}{\pi t} * x(t). \quad (4.2)$$

Applying the Fourier transform, Equation 4.2 can be written as:

$$F\{\hat{x}(t)\} = \frac{1}{\pi} F\left\{\frac{1}{t}\right\} F\{x(t)\}. \quad (4.3)$$

where,

$$F\left\{\frac{1}{t}\right\} = \int_{-\infty}^{\infty} \frac{1}{t} e^{-j2\pi f t} dt = -j \cdot \pi \cdot \text{sgn}(f), \quad (4.4)$$

and where,

$$\text{sgn}(f) = \begin{cases} +1 & f > 0, \\ 0 & f = 0, \\ -1 & f < 0. \end{cases} \quad (4.5)$$

Consequently, the Fourier transform of the Hilbert transform of $x(t)$ can be expressed as:

$$F\{\hat{x}(t)\} = -j \cdot \text{sgn}(f) \cdot F\{x(t)\}. \quad (4.6)$$

It is evident from equation 4.6 that the Hilbert transform can be obtained in the frequency domain by multiplying the spectrum of $x(t)$ by $+j$ ($+90^\circ$) for negative frequencies and $-j$ (-90°) for positive frequencies. In order to obtain the Hilbert transform sequence in the time domain, $x(\hat{t})$, an inverse Fourier transform of $F\{x(\hat{t})\}$ is required.

One of the limitations of the Hilbert transform results from the fact that it makes use of the Fourier transform, as can be seen from equation 4.6. More specifically, the Discrete Fourier Transform (DFT), which is actually used because we are dealing with digital (discrete) signals, assumes that its input signal is one period of a periodic signal, and its outputs are the discrete frequencies of this periodic signal (Proakis & Manolakis, 1996). However, when applying the Hilbert transform on short sequences of data where periodicity is not guaranteed, this periodicity assumption of the DFT introduces discontinuities in the signal which in turn result in a strange behaviour at the ends, known as the edge effect. The latter introduces multiple frequencies, which do not belong to the actual spectral information of the original signal.

Single-lead First-derivative-based Methods

Returning briefly to the QRS detection algorithm of Pan and Tompkins (1985), the method consists of two stages, pre-processing and decision, as previously discussed. During the pre-processing stage the signal is filtered using a cascade of high-pass (at 5 Hz) and low-pass (at 12 Hz) filters. The output of the band-pass filter is denoted as $x(n)$. Consequently, the derivative of the signal, $y(n)$, is computed and its square value, $s(n)$ is evaluated in order to amplify higher frequencies. To be more specific,

the five-point derivative used is as follows:

$$y(n) = \frac{1}{8T}[2x(n+1) + x(n+2) - x(n-2) - 2x(n-1)], \quad (4.7)$$

The output of the derivative is then squared as follows:

$$s(n) = [y(n)]^2, \quad (4.8)$$

for $n = 0, 1, 2, \dots, N - 1$, where N is the total number of recording samples and T is the sampling rate. The final phase of the pre-processing stage considers the integration of the signal, $s(n)$, as follows:

$$m(n) = \frac{1}{M}[s(n - (M - 1)) + s(n - (M - 2)) + \dots + s(n)], \quad (4.9)$$

for $n = 0, 1, 2, \dots, M$, where M is the size of the integration window which depends on the sampling rate and the QRS complex duration. One can observe that the integration process is similar to computing the average of samples from $n - M - 1$ up to n with step -1 , in order to produce the moving-window integrated (MWI) sequence. Following the pre-processing stage, the ECG signal is now ready for further analysis in the decision stage. During the decision stage, two sets of thresholds are applied to both the final output of the pre-processing stage, $m(n)$, and the output of the band-pass filter, $x(n)$. The following discusses our findings as a result of implementing this method on recording 100 from the MIT-BIH database. Figure 4.1 shows the results of our implementation of the different phases of the pre-processing stage.

The results of the decision stage and the identified R-peaks are depicted in Figure

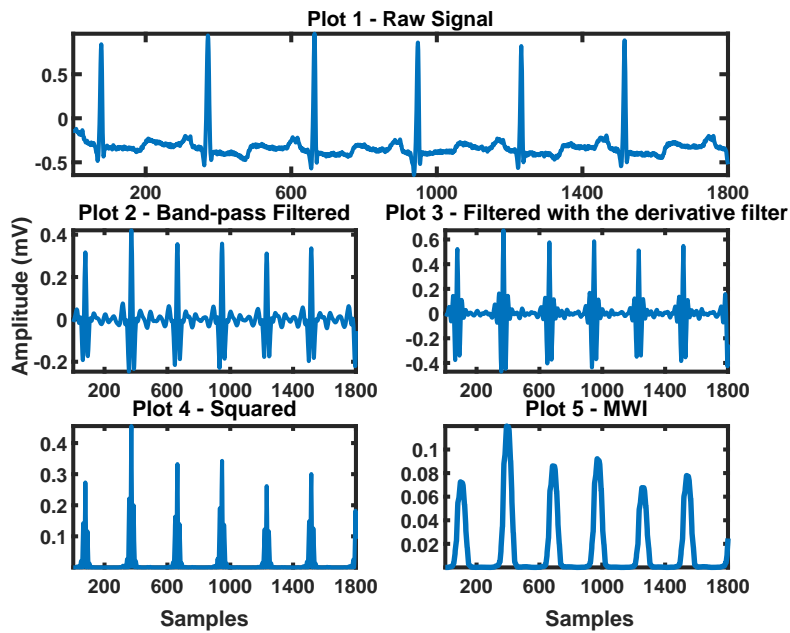


Figure 4.1: Pre-processing stage of the QRS detection algorithm of Pan & Tompkins (1985): Plot 1 shows the raw ECG signal (MIT-BIH recording 100). Plot 2 shows the output of the band-pass filter. Plot 3 shows the output of the derivative filter. Plot 4 shows the squared signal. Plot 5 shows the MWI sequence.

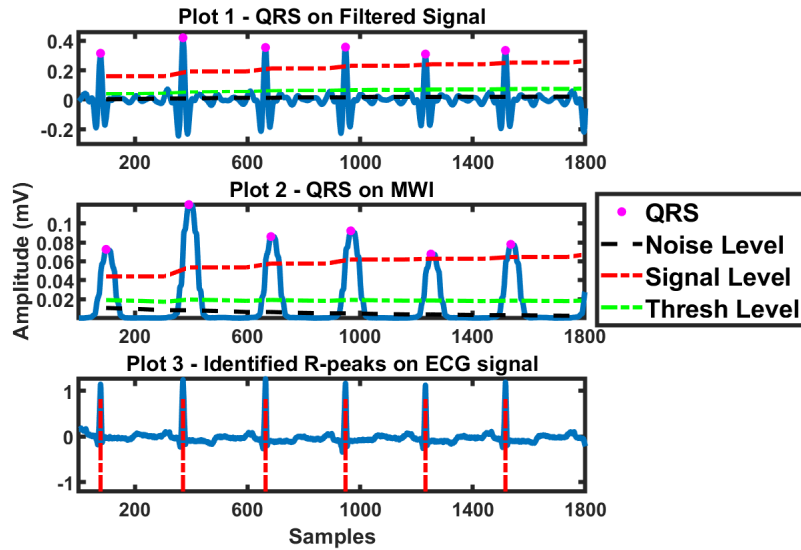


Figure 4.2: Decision stage of the QRS detection algorithm of Pan & Tompkins (1985): Plot 1 shows the decision process applied on the filtered ECG signal (MIT-BIH recording 100). Plot 2 shows the decision process applied on the MWI sequence. Plot 3 shows the identified R-peaks.

4.2. Before applying the thresholds, peaks in the moving-window integration sequence are identified and then thresholds are used in order to classify every peak as noise or signal. A peak is defined as a local maximum within a predefined time interval. For this purpose, we used the MATLAB function `findpeaks` that chooses the highest peak in the signal within a minimum distance. The latter was set to be 200 ms, which corresponds to the heart refractory period. Furthermore, the authors (Pan & Tompkins, 1985) have pointed out that in order to initialise the thresholds a learning phase of 2 s is required.

The thresholds applied on the MWI sequence and the filtered ECG signal are based on estimates of signal or noise levels, which were acquired using the mean or the median of the filtered ECG signal and of the MWI sequence. Following the

decision stage, a search back mechanism is used based on the average of the eight most recent R-peaks. If no R-peak was identified within 166% of the average R-R interval, then a search back is applied and R-peak is set to be the highest peak.

Hilbert Transform-based Methods

It has been already mentioned that the algorithm of D. S. Benitez et al. (2000); D. Benitez et al. (2001) consists of two stages as well, pre-processing and decision. During the pre-processing stage, the signal is filtered with a band-pass filter, which maintains frequencies between the range 8-20 Hz. As the Hilbert transform performs better for short waveforms, at this stage the signal is divided into segments of 1024 samples, which are denoted as $x(n)$. The next step is to calculate the first derivative, $y(n)$, of the signal, in order to obtain the slope information. The derivative is calculated using the central-difference formula as follows:

$$y(n) = \frac{1}{2T}[x(n+1) - x(n-1)], \quad (4.10)$$

for $n = 0, 1, 2, \dots, N-1$, where N is the total number of samples in the segment, i.e. 1024, and T is the sampling rate. In our implementations a derivative filter was designed with a transfer function:

$$H(z) = \frac{1}{2T}(z^1 - z^{-1}). \quad (4.11)$$

Then, the Hilbert transform of the derivative signal, $y(n)$, is computed, based on the work of Todoran, Holonec, and Iakab (2008), where an algorithm is provided for the discrete Hilbert transform implementation.

During the decision stage a primary threshold is calculated based on the RMS

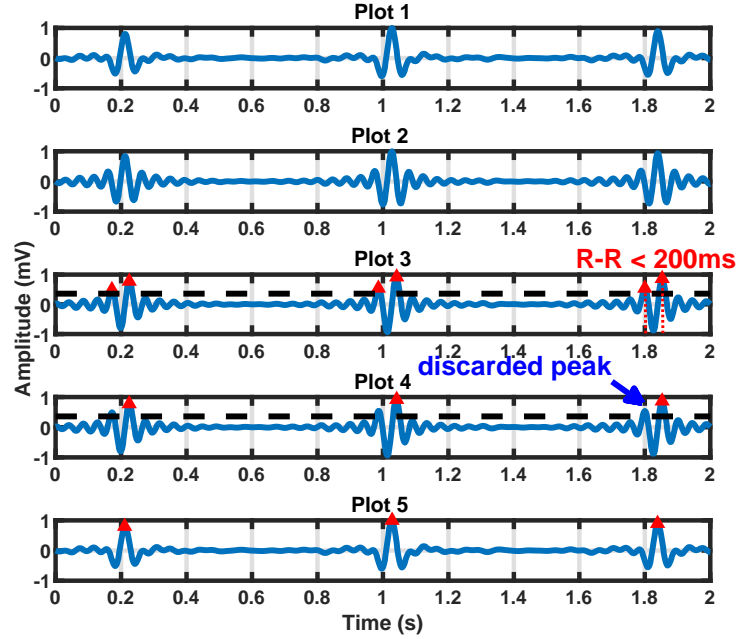


Figure 4.3: Steps of the QRS detection algorithm of Benitez et al. (2000, 2001): Plot 1 shows the filtered ECG signal (MIT-BIH recording 100). Plot 2 shows the output of the first derivative. Plot 3 depicts the Hilbert transform sequence where the dashed black line stands for the RMS threshold, and the red triangles are the candidate peaks. Plot 4 shows the results after the refractory period check. Plot 5 shows the identified R-peaks in the ECG signal.

of the Hilbert transform output, $\hat{x}(n)$, which is calculated as follows:

$$\text{rms}(\hat{x}(n)) = \sqrt{\frac{1}{N}[\hat{x}^2(0) + \hat{x}^2(1) + \dots + \hat{x}^2(N-1)]} = \sqrt{\frac{1}{N} \sum_{n=0}^{N-1} \hat{x}^2(i)}. \quad (4.12)$$

Peaks in the segment are classified as candidate peaks if they exceed this threshold. In order to identify the real R-peaks, a time threshold based on the refractory period of the heart (200 ms) is applied between consecutive candidate peaks and the final decision is made based on the maximum amplitude. In particular, if the R-R

interval of two consecutive peaks in $h(n)$ is less than 200 ms, then the peak with the maximum amplitude is considered to be the real peak, and the other is discarded. The results of our implementation of the D. S. Benitez et al. (2000); D. Benitez et al. (2001) detection algorithm on recording 100 from MIT-BIH is shown in Figure 4.3.

4.2 QRS Complex Detection based on Local Signal Energy and EMD

Over the past decade, most research in QRS complex detection has emphasised the use of Empirical Mode Decomposition (EMD) (Taouli & Bereksi-Reguig, 2011; Arafat & Hasan, 2009; Yang & Tang, 2008). The fact that the EMD method acts as an effective pre-processor which amplifies the QRS complex led Taouli and Bereksi-Reguig (2011), and Arafat and Hasan (2009) to decompose the ECG signal into its Intrinsic Mode Functions (IMFs) and then reconstruct it by adding the first three IMFs, to enhance the QRS complex. To summarise, the suggested algorithm reported in (Taouli & Bereksi-Reguig, 2011), and (Arafat & Hasan, 2009) is as follows:

1. The ECG signal is first de-noised using a moving average and a low-pass filter. The output of the filter is denoted as $x(t)$,
2. The EMD method is applied on $x(t)$ to extract the IMFs, $c_1(t), \dots, c_N(t)$, where N is the number of the extracted IMFs,
3. The ECG signal is reconstructed as follows,

$$x(t) = \sum_{i=1}^3 c_i(t), \quad (4.13)$$

4. The absolute value of the reconstructed signal is computed and denoted as $a(t)$,
5. The detection threshold is set to be $T = 0.5 \times \max(a(t))$,
6. The amplitudes in the absolute sequence are retained if they exceed the threshold T , while the rest are set to zero,
7. A search back mechanism is applied, where in a 200 ms segment, starting from the first non-zero value of $a(t)$, the maximum value is identified and is set to be the real R-peak.

Such approaches, however, have failed to address the problem of ectopic R-peaks. The serious weakness of these methods that are reported in Taouli and Bereksi-Reguig (2011), Arafat and Hasan (2009) and Yang and Tang (2008) is that the threshold is derived from the full length ECG signal. The latter affects the detection accuracy as the number of missed peaks is increased, due to ectopic R-peaks which make the threshold high. Thus, this results in failure to detect lower R-peaks. In addition, another drawback is that these methods cannot be implemented on-line, as they make use of the full length ECG signal. Furthermore, no research has been found that surveyed a solution to distinguish R-peaks from large Q-peaks in the absolute sequence. The latter affects the detection performance as large Q-peaks will be wrongly identified as R-peaks. All of these flaws will be addressed in our proposed QRS detector which will be discussed next.

4.3 Proposed QRS Complex Detector

This section discusses our novel QRS complex detector which is based on the local signal energy. The proposed algorithm overcomes the aforementioned problems in

the state of the art EMD-based methods through its integrating of the following features: (1) it uses an adaptive threshold which is based on the local energy of the reconstructed signal, (2) it makes use of the most recent history of the ECG signal, hence can be used as an on-line QRS detector for all patient types and (3) it combines a gradient-based and a refractory period checks in order to differentiate large Q-peaks and reject false R-peaks.

The suggested algorithm relies on the assumption that the QRS complex can be enhanced by reconstructing the signal from the first few IMFs. The validity of this assumption is verified on all of the tested recordings as will be shown in Section 4.4. During the pre-processing stage the signal is filtered in order to remove noise and improve computational speed, by decreasing the number of IMFs. The signal is then reconstructed from the first three IMFs after being analysed with EMD. During the decision stage, the reconstructed signal is divided into segments. For each segment the envelope of the maxima is computed. The threshold results from an averaging step which makes use of the local signal energy of each segment is then calculated.

Furthermore, during the decision stage a refractory period and gradient-based checks were combined in order to increase the accuracy of the detection, by eliminating the presence of false positives and negatives. The segment duration provides an adequate number of R-peaks for the threshold decision and depends on the sampling frequency of the signal. Moreover, for the averaging step the eight most recent segments were used. This is a pre-specified parameter which depends on the clinical condition of the patients and whether it is expected that their ECG signal is going to show a large heterogeneity. Nonetheless, the most recent history of the ECG signal is used, hence the eight most recent values are recommended. To summarise, the proposed QRS complex detector is as follows:

Pre-processing Stage

1. The raw ECG signal, $x(t)$, of length M is first filtered with a band-pass filter, whose coefficients were designed using a Kaiser-Bessel window (Proakis & Manolakis, 1996). The band-stop frequencies were set at 8 and 20 Hz (Elgendi Mohamed, 2005), in order to amplify the QRS complex, eliminate noise and reduce the number of IMFs. The output of the filter is denoted as $x_f(t)$ (Figure 4.4, Blocks 1 and 2),
2. The EMD method is applied on $x_f(t)$ to extract the IMFs, $c_1(t), \dots, c_N(t)$, where N is the total number of the extracted IMFs (Figure 4.4, Block 3),
3. The signal is reconstructed by summing the first three IMFs (Figure 4.4, Block 3),

$$x_r(t) = \sum_{i=1}^3 c_i(t), \quad (4.14)$$

4. Then, the absolute value of the reconstructed signal is computed, that is $a(t) = |x_r(t)|$. This makes all data points positive and implements a linear amplification of the reconstructed signal emphasising the higher frequencies (Figure 4.4, Block 4),

Decision Stage

5. In order to increase the algorithm efficiency, $a(t)$ is divided into k segments of 3 s duration, that is $k = M/(3 \times f_s)$. The starting point of the k -th segment should match the last R-peak located in the $k - 1$ segment in order to increase accuracy (Figure 4.4, Block 5),

6. Compute the envelope of the maxima, $\hat{a}_k(t)$ of $a_k(t)$ through a cubic spline interpolation of the local maxima (Figure 4.4, Blocks 6 and 7),
7. Compute the local signal energy as,

$$T_k = \sqrt{\frac{1}{K} \sum_{t=1}^K [\hat{a}_k(t)]^2}, \quad (4.15)$$

where K is the number of samples in the segment, that is $K = 3 \cdot f_s$ (Figure 4.4, Block 8),

8. The threshold of the k -th segment is set to be the mean of the eight most recent T_k values (Figure 4.4, Blocks 9, 10, 11 and 12),

$$DT_k = \frac{1}{8} \sum_{j=k-7}^k T_j, \quad (4.16)$$

9. The peaks, which exceed the threshold DT_k in the absolute sequence $a_k(t)$, are classified as candidate peaks (Figure 4.4, Block 13),
10. In order to segregate large Q-peaks from R-peaks, the first derivative of $x_f(t)$ is computed. Peaks with a negative derivative are further investigated at the refractory period check given next (Figure 4.4, Block 14),
11. Apply a refractory period check. When the R-R interval of two adjacent peaks is less than 200 ms, keep the peak with the maximum amplitude (Figure 4.4, Block 15),
12. In order to obtain the locations in the filtered ECG, $x_f(t)$, apply a search back mechanism of ± 10 samples (Figure 4.4, Blocks 16 and 17).

For the computation of the detection threshold, DT_k , a dynamic buffer of eight positions is required, which stores the T values. For the first seven segments, the detection threshold is set to be the last position of the buffer ($DT = \text{buff}(\text{end})$, Figure 4.4, Block 12). As soon as the 8-th segment is being processed, the detection threshold is set to be the mean of the buffer values ($DT = \text{mean}(\text{buff}(\text{end}-7:\text{end}))$). As soon as the T value of the 9-th segment is being ready, a left shift of one position is applied on the buffer, and the most recent T value is stored. To summarise, the buffer functions as a data queue (FIFO - First In First Out) and it is updated for each segment, thus the memory need is very low (Figure 4.5).

4.4 Statistical Analysis of the proposed QRS Complex Detector

The main assumption of our proposed QRS complex detector is that the first three IMFs correspond to the QRS complex based on their spectrum information. However, the number of IMFs can vary in real ECG data so it needs to be checked, for example using the Fourier transform. The suggested number of IMFs will be discussed later in this section. The QRS complex frequencies lie in the range 3-40 Hz, whereas P and T wave frequencies lie in the range 0.7-10 Hz (Malmivuo & Plonsey, 1995). Thus the idea is to attenuate low frequency ECG components and amplify the QRS complex by discarding the IMFs which correspond to P and T waves. Before proceeding to the performance evaluation of the proposed method, it is important to show the validity of the assumption discussed above.

In order to analyse the frequency spectrum of the IMFs, the EMD method was applied on a filtered ECG signal and a Fourier transform was applied on each IMF

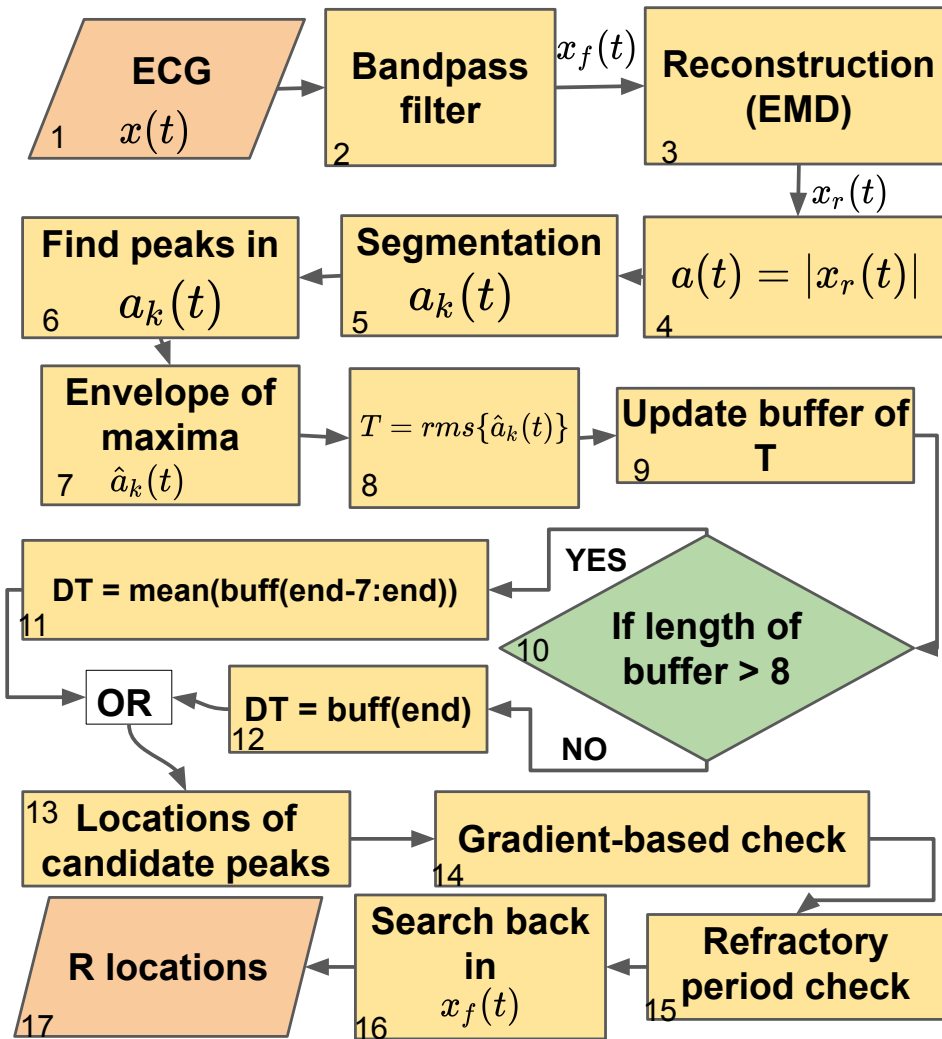


Figure 4.4: QRS Complex Detection Flow-Chart: The numbers are referring to the number of blocks. The pseudocode used in blocks 11 and 12 does not refer to a specific programming language. It is purely used to summarise the processes taking place at this stages.

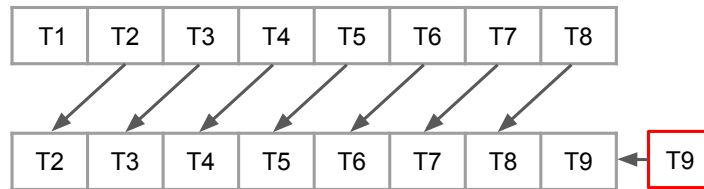


Figure 4.5: Schematic representation of the buffer's function for the computation of the detection threshold

to obtain their frequency bands. Figure 4.6 shows the filtered ECG signal, $x_f(t)$ and its first five IMFs. The figure also shows the frequency spectra of each IMF. It is apparent from this figure that the spectra of the first three IMFs coincide with the frequency band of the QRS complex. Moreover, it is observed that there is an overlap between the QRS and P, and T wave spectral ranges. However, the most dominant frequencies in Plots 7-9 are centred around 10-20 Hz (QRS complex spectral range). This indicates that the first three IMFs carry most of the QRS complex spectral information, whereas IMFs 10 and 11 carry information mostly related to P and T waves. Therefore, only the first three IMFs are used in the signal's reconstruction, and the rest are discarded. Figure 4.7 compares the filtered signal, $x_f(t)$, with the reconstructed signal, $x_r(t)$. It is also evident that the filtered signal can be sufficiently approximated by the reconstructed signal, since their difference (red dotted line) is small and the oscillatory nature of the QRS complex is retained. Therefore, it can be concluded that the first three IMFs are sufficient to characterise the QRS complex.

Our assumption was tested on all the recordings under study and the first three IMFs were found to be adequate for reconstructing the ECG signal, amplifying

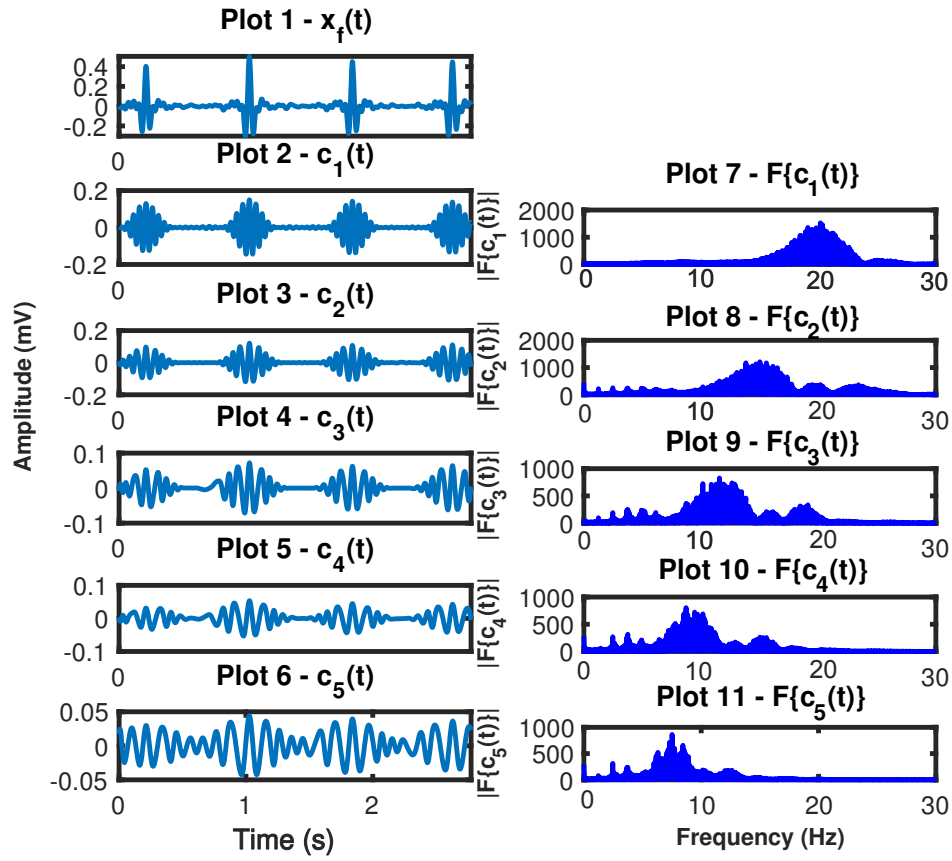


Figure 4.6: The extracted IMFs and their frequency spectra: Plot 1 corresponds to the filtered ECG, $x_f(t)$. Plot 2 to 6 show the first five IMFs, $c_1(t), \dots, c_5(t)$. Plots 7 to 11 correspond to the Fourier transform of each IMF.

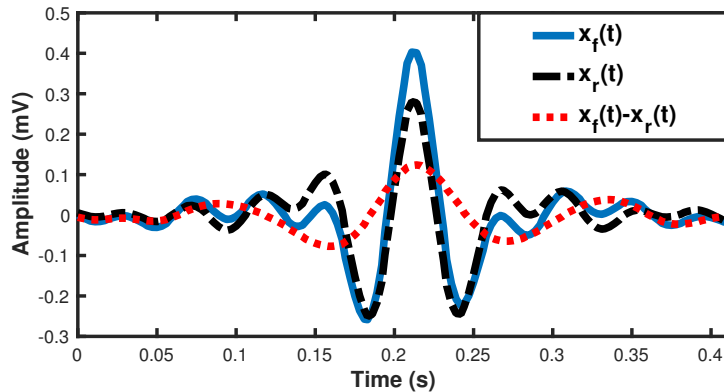


Figure 4.7: Reconstruction of the filtered signal, $x_f(t)$, by the summation of the first three IMFs, $x_r(t)$, and their difference, $x_f(t) - x_r(t)$.

the QRS complex frequencies and attenuating low frequency components. Following this validation step, the proposed QRS complex detector was evaluated using entire records from the MIT-BIH Arrhythmia database (Goldberger et al., 2000), which belongs to adults, and records from the Preterm Infant Cardio-Respiratory Signals (PICSDB) database (Gee, Barbieri, Paydarfar, & Indic, 2016; Goldberger et al., 2000). Furthermore, our algorithm was evaluated on real data from the Capnobase dataset (Karlen et al., 2013), which were collected during elective surgery or routine anaesthesia and belong to children of ages in the range 1-14 years old and adults of ages in the range 37-64 years old. It is important to point out that the aforementioned datasets provide recordings along with their annotated R-peaks. The sequential steps of our proposed QRS complex detector are shown in Figure 4.8 for recording 100 from MIT-BIH database. The identified R-peaks are marked by a red asterisk "*" in the filtered ECG signal, $x_f(t)$ (Plot 4).

The performance evaluation of the proposed QRS complex detector was based on the calculation of *Sensitivity* (Se), *Positive Predictivity* (+P) and *Detection Error Rate* (DER), which were computed as follows:

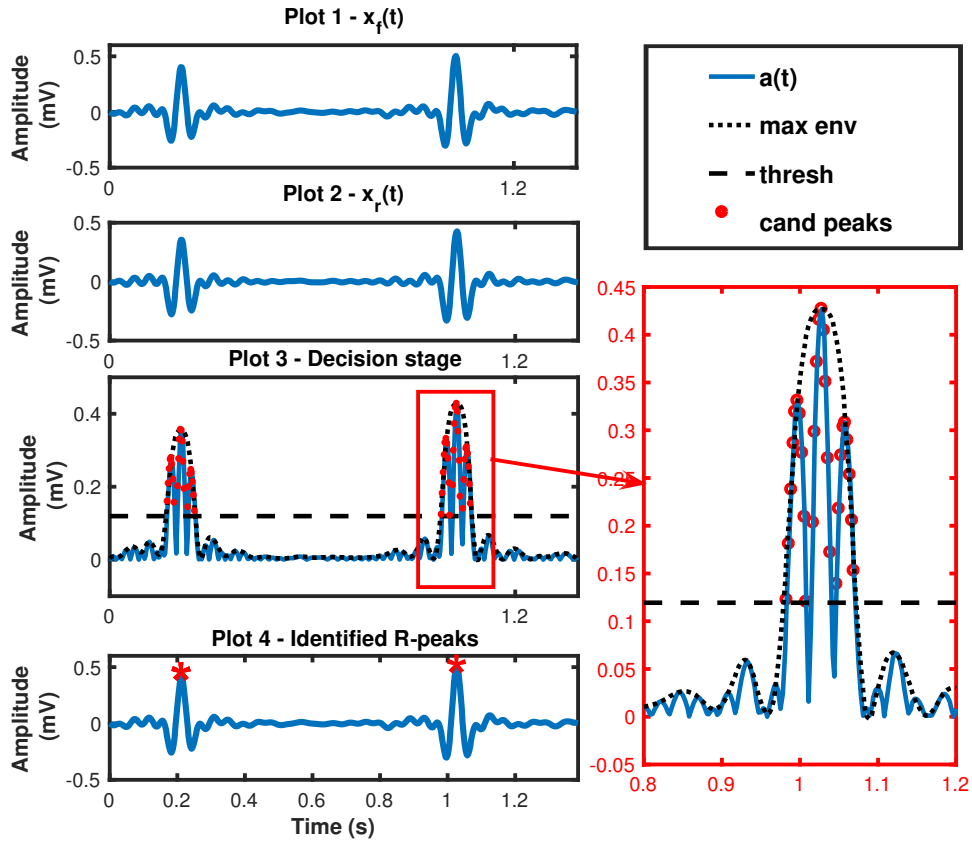


Figure 4.8: Steps of the proposed QRS complex detector: Plot 1 corresponds to the filtered ECG signal, $x_f(t)$. Plot 2 shows the reconstructed signal, $x_r(t)$. Plot 3 shows the absolute sequence, $a_k(t)$, (blue line) and its maximum envelope, $\hat{a}_k(t)$, (dotted black line) along with the estimated threshold (dashed black horizontal line) and candidate peaks marked with a red circle. Plot 4 shows the detected R-peaks on $x_f(t)$ as red asterisk "*".

$$Se(\%) = 100 \times \frac{TP}{TP + FN}, \quad (4.17)$$

$$+P(\%) = 100 \times \frac{TP}{TP + FP}, \quad (4.18)$$

$$DER(\%) = 100 \times \frac{FP + FN}{\text{total number of R-peaks}}. \quad (4.19)$$

A false negative (FN) occurs when the algorithm fails to detect an actual R-peak. A false positive (FP) represents a false peak detection and a true positive (TP) indicates a correctly identified R-peak by the algorithm. For the MIT-BIH database, we have also computed the *Average Time Error* (ATE) as follows:

$$ATE(ms) = \frac{\sum_{i=0}^{TP} |\text{located QRS} - \text{actual QRS}|}{TP}, \quad (4.20)$$

in order to track the time error of the proposed method, because the locations of R-peaks play a pivotal role in the BR estimation. Moreover, for each method we provide a confidence interval (CI) which is given as $\pm 2\sigma$, where σ is the standard deviation of the results for a specific metric.

For all the datasets under study the results obtained are shown in Tables 4.2, 4.3, 4.4 and 4.5. It is apparent from these tables that our method outperforms Pan and Tompkins (1985) and D. S. Benitez et al. (2000) across the entire records from MIT-BIH database, achieving higher *Se* of 99.92% (± 0.30) compared to 99.80% and 99.86% from Pan and Tompkins (1985) and D. Benitez et al. (2001) respectively, as well as lower DER of 0.42% (± 1.23) compared to 1.33% and 14.23% from Pan and Tompkins (1985) and D. Benitez et al. (2001) respectively. Moreover what is interesting about the proposed algorithm is that it shows better performance for infant and children recordings from PICSDB and Capnabase datasets, achieving the best *Se* of 99.95% (± 0.31) and 100% (± 0.00), respectively.

Furthermore, changes in threshold estimation were compared using the median of the eight most recent T_k values, instead of the mean. Figure 4.9 compares the DER

Record	Annotated peaks	DER (%)	<i>Se</i> (%)	<i>+P</i> (%)	ATE (ms)
100	2273	0.00	100	100	0.00
101	1865	0.48	99.95	99.57	0.22
103	2084	0.00	100	10	0.00
104	2229	1.57	100	98.45	2.90
105	2572	2.33	99.92	97.79	3.10
106	2027	0.98	99.41	99.60	1.34
107	2137	0.47	99.81	99.72	1.10
109	2532	0.28	99.72	100	0.96
111	2124	0.66	99.95	99.39	0.99
112	2539	0.20	100	99.80	0.34
113	1795	0.11	100	99.89	0.13
115	1953	0.00	100	100	0.14
117	1535	0.00	100	100	2.20
118	2278	0.04	100	99.96	0.28
119	1987	0.25	100	99.75	0.63
121	1863	0.16	99.95	99.90	0.44
122	2476	0.00	100	100	0.24
123	1518	0.06	100	99.93	0.20
124	1619	0.30	99.81	99.77	0.40
Average	35740	0.42	99.92	99.66	0.81
CI		± 1.23	± 0.3	± 1.17	± 1.89

Table 4.2: QRS detection performance using the MIT-BIH database

Record	Annotated peaks	DER (%)	<i>Se</i> (%)	<i>+P</i> (%)
infant1	4671	0.08	99.95	99.95
infant2	970	1.34	100	98.70
infant3	1757	0.91	100	99.10
infant4	2300	0.00	100	100
infant5	4434	0.04	100	99.95
infant6	3974	0.30	100	99.70
infant7	4451	0.13	100	99.87
infant8	4185	0.02	100	99.98
infant9	4426	0.59	99.50	99.91
infant10	4572	0.19	100	99.80
Average	15371	0.36	99.95	99.70
CI		± 0.90	± 0.31	± 0.88

Table 4.3: QRS detection performance using the PICSDDB

obtained from both the mean and median threshold estimators for all databases under study. The figure shows three plots, one for each database, where the y -axis represents the DER value and the x -axis represents the recording number from the corresponding database. From the figure, it can be seen that for some records the mean estimator gives the lower DER. Overall, both mean and median estimators show a similar performance for all databases under study.

Moreover, Table 4.6 shows a comparison of Se and $+P$ obtained for all datasets using the mean and median for the threshold estimation. What stands out from this table is that the overall $+P$ was decreased using the median estimator due to an increase of FPs. A possible explanation for this is that the median estimator gives lower threshold levels, allowing erroneous peaks to be identified as real R-peaks, and hence affecting the detection accuracy. Therefore, the proposed methods uses the mean estimator.

Record	Annotated peaks	DER (%)	Se (%)	+P (%)
capno9	815	0.00	100	100
capno15	960	0.00	100	100
capno16	1012	0.00	100	100
capno18	1131	0.00	100	100
capno23	818	0.00	100	100
capno32	685	0.00	100	100
capno35	900	0.18	100	99.89
capno38	956	0.00	100	100
capno103	826	0.00	100	100
capno104	912	0.00	100	100
capno105	530	0.37	100	99.62
capno121	579	0.00	100	100
capno122	588	0.00	100	100
capno125	627	0.00	100	100
capno127	615	0.00	100	100
capno128	541	0.18	100	99.82
capno134	578	1.53	100	98.50
capno142	739	0.00	100	100
capno147	538	3.58	100	97.52
capno148	624	0.00	100	100
capno311	555	0.17	100	99.82
capno312	432	0.00	100	100
capno313	588	0.00	100	100
capno322	589	0.16	100	99.83
capno325	584	0.00	100	100
Average	17716	0.25	100	99.80
CI		± 1.52	± 0.00	± 1.13

Table 4.4: QRS detection performance using the Capnobase dataset

DB	Method	DER (%)	Se (%)	$+P$ (%)
MIT-BIH	Pan and Tompkins (1985)	1.33	99.80	98.85
	D. S. Benitez et al. (2000)	14.23	99.86	99.71
	Our method	0.42	99.92	99.66
PICSDB	Pan and Tompkins (1985)	0.34	99.86	99.81
	D. S. Benitez et al. (2000)	0.14	99.92	99.84
	Our method	0.36	99.95	99.70
Capnobase	Pan and Tompkins (1985)	0.25	100	99.78
	D. S. Benitez et al. (2000)	0.31	100	99.70
	Our method	0.25	100	99.80

Table 4.5: Comparison of QRS detector performance with other methods for PICSDB and Capnobase

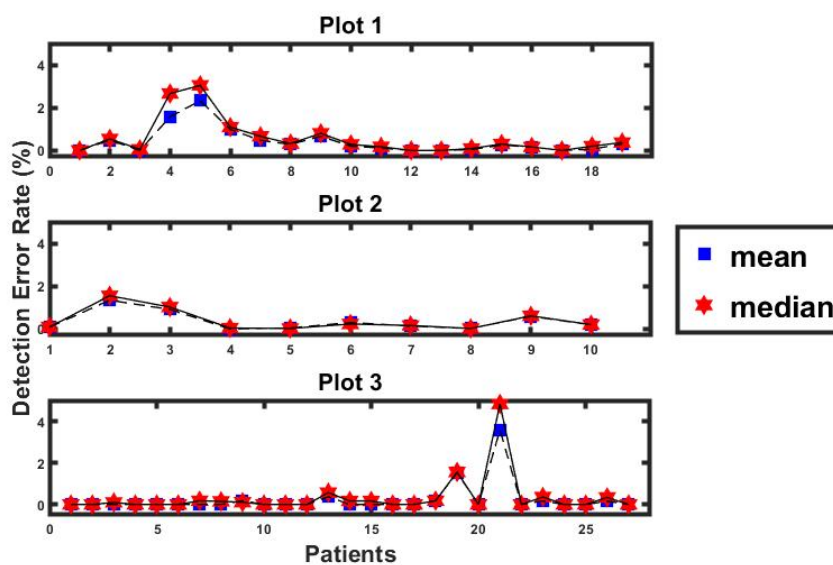


Figure 4.9: Comparison of Threshold Estimation: Plot 1 shows the DER for the mean and median estimators for MIT-BIH database. Plot 2 corresponds for PICSDB. Plot 3 corresponds for Capnobase dataset.

DB	Estimator	DER (%)	<i>Se</i> (%)	<i>+P</i> (%)
MIT-BIH	mean	0.42	99.92	99.66
	median	0.56	99.88	99.56
PICSDB	mean	0.36	99.95	99.70
	median	0.39	99.95	99.66
Capnobase	mean	0.25	100	99.80
	median	0.32	100	99.69

Table 4.6: Comparison of Threshold Estimators

Figure 4.10 shows the behaviour of the average DER as we increase the number of averaging segments from 1 to 10 for the MIT-BIH database. It is evident that as we increase the number of segments, the error decreases. At around 7 averaging segments we can observe that the error drops below 0.5 and then fluctuates between 0.3 and 0.4. As it has been previously stated in the result tables, the achieved DER for 7 averaging segments is 0.42% (± 1.23). Despite the fact that a higher number of segments would have slightly decreased the error, we chose to keep only the 7 most recent segments in order to keep the computational complexity low.

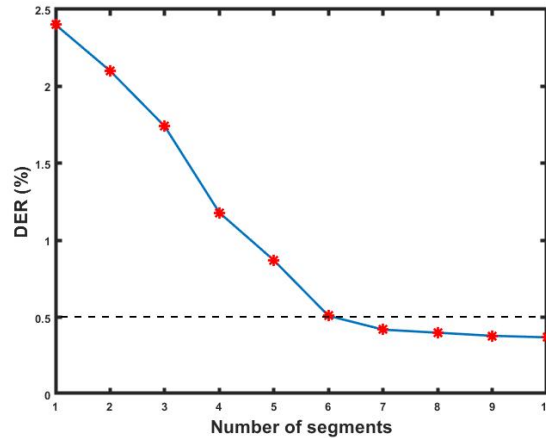


Figure 4.10: Comparison of averaging segments: DER performance as the number of averaging segments increases.

During the algorithm evaluation process the following observations were found, compared to existing QRS complex detectors based on the EMD method (Taouli & Bereksi-Reguig, 2011; Arafat & Hasan, 2009). It has been observed that some recordings which belong to MIT-BIH database and PICSDB include inverted R-peaks. The proposed QRS detector fails to identify those inverted R-peaks. Nonetheless a peak close to the inverted one is identified as a real R-peak because it is classified as candidate peak based on the proposed threshold scheme. However please note that the same issue occurs with existing QRS complex detectors (Taouli & Bereksi-Reguig, 2011; Arafat & Hasan, 2009; Yang & Tang, 2008; Pan & Tompkins, 1985), as it is normally hard to detect whether an R-peak is inverted.

Another interesting observation was found in some recordings from the MIT-BIH database, where the absolute amplitude of a Q-peak was higher than the absolute amplitude of an R-peak. Because the decision is made on the absolute of the reconstructed signal, this issue yields high error in the QRS detection since the faultlessly detected Q-peaks will be classified as FPs and the missed R-peaks as FNs.

Figure 4.11 shows part of record mitdb104 where the absolute value of a Q-peak exceeds the absolute value of an R-peak. To address this problem the first derivative of the ECG signal is computed and the decision stage was modified adding a step where the sign of the derivative is checked. The idea is based on the fact that the derivative after an R-peak is negative because the signal decreases in time, whereas the derivative after a Q-peak is positive as the signal increases in time. Hence peaks with positive derivatives were discarded, while peaks with negative derivatives were further investigated during the refractory period check. This modification of the decision stage contributes positively to the proposed QRS complex detectors as the proposed algorithm can efficiently distinguish Q- from R-peaks, whereas existing

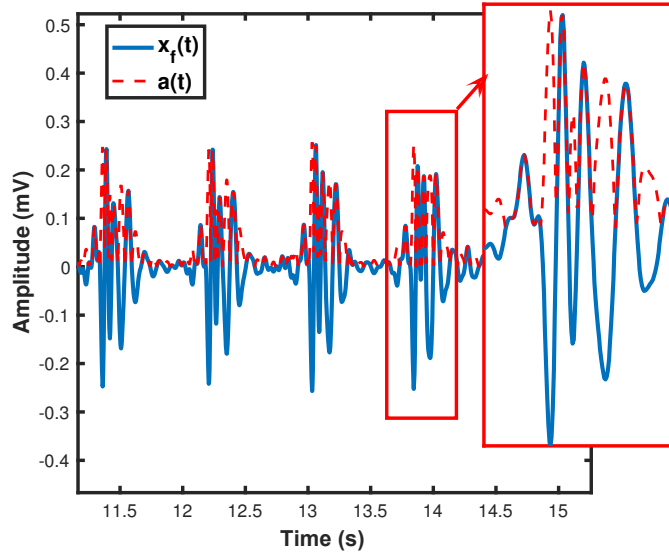


Figure 4.11: Part of the filtered ECG signal, $x_f(t)$, and its absolute value, $a(t)$, from recording mitdb104. Dashed red line shows that the amplitude of the Q-peak exceeds R-peak amplitude in the absolute sequence.

algorithms have not reported anything about this issue.

Another significant advantage of our proposed QRS detector is that the decision threshold is based on the most recent vital sign history of the patient as it is computed as the mean of the eight most recent T_k values and does not depend on the full length of the ECG signal. On the other hand, existing QRS complex detectors based on the EMD method use the average of all segments (Arafat & Hasan, 2009) and half of the maximum amplitude (Taouli & Bereksi-Reguig, 2011) in order to compute the threshold. During our experiments these thresholds were computed where the threshold of half of the maximum amplitude was found to be high, about 0.5161 (Figure 4.12, Plot 1), while the average of all segments was found to be very low, about 0.0847, hence increasing the number of FNs and FPs, respectively. The threshold computed based on the average of the RMS of the proposed segmented ECG was

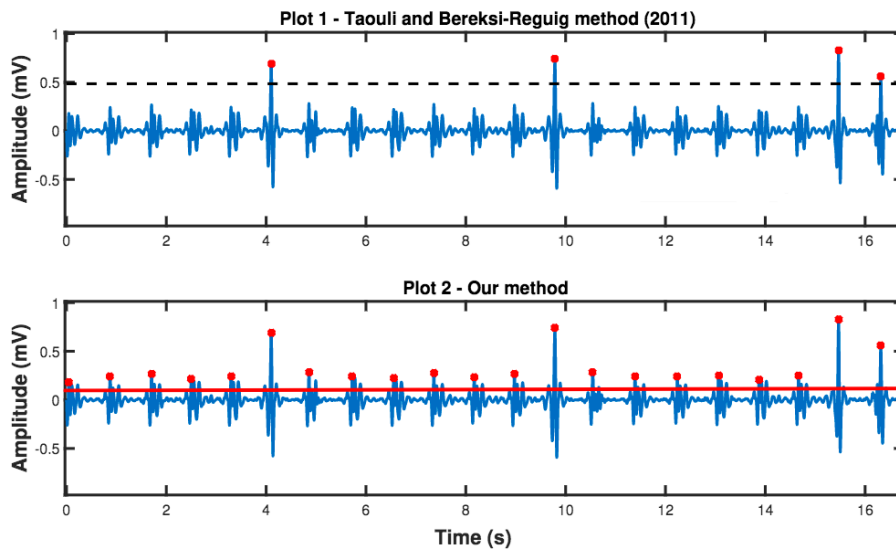


Figure 4.12: Threshold comparison: Plot 1 illustrates the threshold (black dashed line) obtained from Taouli and Bereksi-Reguig (2011). Plot 2 shows the threshold (red solid line) obtained from the proposed QRS detector.

found to be 0.1153, thus decreasing the number of FPs and FNs. It is evident from Figure 4.12 (Plot 2) that the proposed algorithm identifies all the peaks, whereas the 0.5 of the maximum amplitude threshold (Taouli & Bereksi-Reguig, 2011) misses too many peaks (Plot 1). Moreover the fact that the threshold is based on the most recent history of the ECG signal facilitates the R-peak identification for all patient types.

To conclude, in this section a novel QRS complex detector was discussed which is based on the EMD using an adaptive threshold which relies on the local signal energy. The proposed decision stage provides a solution for the detection of small R-peaks using a threshold derived from the average of the RMS over eight segments. An additional advantage of the proposed decision stage is the gradient-based check where the algorithm can effectively distinguish R-peaks from large Q-peaks in the absolute sequence. Furthermore, the proposed detector can be implemented

in real-time causing a detection delay equal to the segment duration. Real-time implementation requires a small modification in the decision stage. The segmentation step can be executed at the very beginning of the algorithm and the sequential steps can be applied to each segment. Thus the time between task request and response (identified R-peaks) requires to wait as long as one segment is processed.

4.5 Exploitation of the proposed QRS detector on ECG segmentation

This section focuses on the ECG segmentation, which here refers to the extraction of ECG features such as the Q-, S- and T-peaks (Figure 2.1 Chapter 2). The extraction of the ECG components requires first the identification of the R-peaks. Therefore, a high detection accuracy will also improve the accuracy in identifying other features from the ECG signal. The detection of these features is based on a study from Mukhopadhyay et al. (2011). The authors explored the relationship between the QRS complex and the rest of the ECG components. First, the R-peaks are identified using our proposed R-peak detection algorithm, presented in Sections 4.3 and 4.4. After successful extraction of the R-peak time locations, the ECG features identification is attempted.

Q-peak and QRS onset detection

Having as reference the most recent R-peak in the filtered ECG signal, a zero slope or slope reversal is searched for on the left side of the R-peak to identify a Q-peak. As soon as all the Q-peaks are detected, having as reference the most recent Q-peak, when the derivative of the signal becomes zero on the left of the Q-peak, it is counted

as the QRS onset.

S-peak and QRS offset detection

For the detection of the S-peak, having as reference the most recent R-peak in the filtered ECG signal, a zero slope or slope reversal is searched for now on the right side of the R-peak to identify an S-peak. After successful detection of the S-peaks, having as reference the most recent S-peak, when the derivative of the signal becomes zero on the right of the S-peak, it is counted as the QRS offset.

T-peak detection

The T-peak detection can be obtained based on the most recent QRS offset. Then, in the Hilbert transformed sequence find the maximum amplitude of the segment which starts at $QRS_{\text{offset}} + 30$ ms and ends at $QRS_{\text{offset}} + 300$ ms (Gupta et al., 2011). In this segment the amplitudes which are within 50% of the maximum amplitude are marked and where these marked samples undergo slope reversal, it is counted as a T-peak. Figure 4.13 and Figure 4.14 show the detection of Q-, S-, T-peaks and QRS onset/offset points for the recording mitdb100 from the MIT-BIH Arrhythmia database using the proposed QRS detector.

4.6 Conclusion

In this chapter, the aim was to demonstrate and analyse the proposed QRS complex detection algorithm to provide accurate results for all patient types. The developed R-peak detector prevails over the limitations encountered in the current state-of-the-art QRS complex detectors, because it uses an adaptive threshold which is based on the most recent history of the ECG signal. Moreover, the accuracy of R-peak

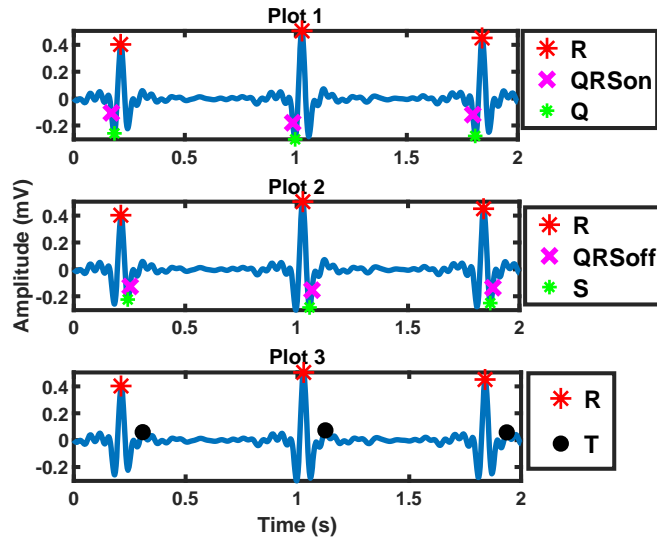


Figure 4.13: Q-, S-, T- peak and QRS onset/offset detection for recording mitdb100: Plot 1 shows the R peaks (red asterisk), the QRS onsets (purple cross) and the Q peaks (green asterisk). Plot 2 shows the QRS offsets (purple cross) and the S peak (green asterisk). Plot 3 shows the T peaks (black circle).

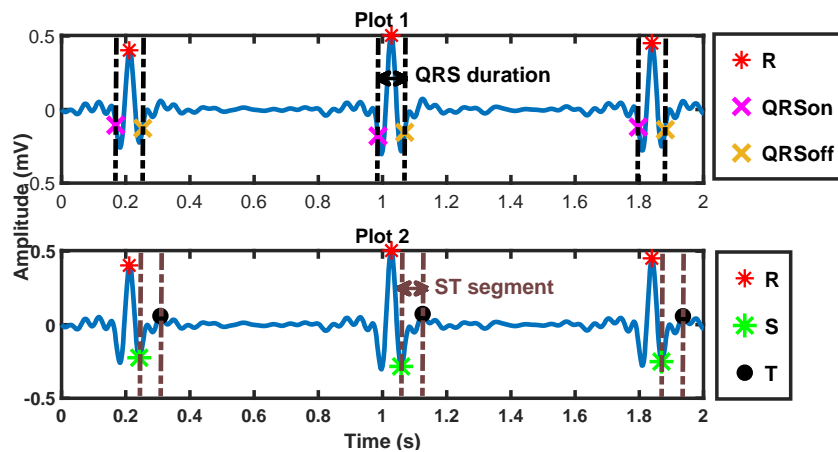


Figure 4.14: QRS duration and ST segment for recording mitdb100: Plot 1 shows the QRS complex duration which is the time interval between the QRS onset and offset. Plot 2 shows the ST segment duration.

identification is further increased due to the fact the R-peaks are amplified based on a frequency analysis of the oscillatory modes obtained after applying EMD. The proposed algorithm was tested on three different databases which belong to both adults and children and it achieved the best accuracy scores when compared with the most commonly used QRS complex detectors.

Chapter 5

Breathing Rate Estimation from Real Data

This chapter focuses on the BR estimation of real raw ECG and EMG data using the methods discussed in Chapter 3. Furthermore, additional contributions of this thesis to the BR estimation will be highlighted in this chapter which include: (1) the ECG signal extraction from EMG signals using the ICA method, (2) the use of peak-to-baseline amplitude for the EDR method which reduces computational cost, (3) the design of band-pass filters whose cut-off frequencies are based on the age and condition of the child, (4) the exploitation of the CSD for the first time on respiratory signals, (5) the use of a band-pass filter on PCA- and ICA-derived respiration signals to exclude non-respiratory frequencies in order to increase the BR estimation accuracy, (6) the development of an enhanced EMD-derived respiration method by introducing further signal processing filtering stages to the raw ECG signal, (7) the proposed data fusion technique and, (8) the use of the autocorrelation function for the AR model order selection.

Section 5.1 describes the databases used in this chapter. Section 5.2 focuses on the performance of single methods for BR estimation and how these methods were further enhanced in order to increase the estimation accuracy. Section 5.3 explores fusion techniques and investigates if the latter benefits the BR estimation performance.

5.1 Discussion of Investigated Real Databases

Before we discuss the proposed BR estimation methods, we first present the details of the databases under study. The methods were tested on three real datasets which belong to hospitalised children. In more details our developed methods will be tested on:

1. **Capnobase dataset:** This dataset consists of 25 recordings that were previously partly seen in Chapter 4. Capnobase contains real ECG data collected during elective surgery and routine anaesthesia and belongs to children in the age range of 1-14 years and adults of ages in the range of 37-64 years (Karlen et al., 2013). The duration of the ECG signals is 8 minutes and the sampling frequency was set at 300 Hz. A reference BR is provided for each minute where the BR varies from 7 to 39 bpm. For each recording, the code name is `capno` followed by the number of the patient. The reference BR was obtained via manual annotations of the capnography signals, which was performed by the authors of the study (Karlen et al., 2013).
2. **BCH ECG dataset:** This dataset contains children ECG recordings collected in the Birmingham's Children Hospital (BCH). The data were collected using wireless sensors, designed by Isansys Lifecare. The children ECG database contains 18 recordings which belong to children of ages in the range of 0-

5 years. The duration of the recordings varies from 1 to 2 minutes and the sampling frequency was set to 100 Hz. The reference BR was provided for each minute where BR varies from 35 to 91 bpm. The code name of the children ECG recordings is `ecgch`, followed by the patient number. The reference BR was estimated by skilled nurses, by counting how many times the chest rises within a minute, assuming that each rise corresponds to a breath.

3. **BCH EMG dataset:** This dataset contains newborn EMG signals provided by BCH. The EMG signals were sampled at 500 Hz and their duration varies from 1 minute to 7 hours and the reference BR are provided per hour. Moreover, the BR varies from 24 to 85 bpm. The code name of the EMG children recordings is `emgch`, followed by the patient number. The BCH EMG data were acquired by placing eight electrodes on the chest and diaphragm of the subject, thus obtaining eight channels which reflect the intercostal and diaphragmatic muscle activity. The latter points out that the EMG is a more convenient signal to extract the WOB, however it requires further signal processing in order to extract the BR. The reference BR was estimated by skilled nurses, by counting how many times the chest rises within a minute, assuming that each rise corresponds to a breath.

The EMG electrodes can also capture the heart activity, as they are placed around the heart, whose biopotential is quite dominant, around 1-5 mV (Thakor, 1999). Thus the heart signal can be seen as the unknown source and the eight EMG channels as the observations, hence this problem can be modelled as a BSS model and the ECG signal can be estimated using ICA, as described in Section 3.1.4. For this purpose, a data matrix, \mathbf{X} , which will undergo ICA, is constructed by stacking the eight EMG channels in the rows of the matrix. Hence \mathbf{X} is an $8 \times m$ matrix,

where m is the number of samples, which is the same for all the channels and 8 is the number of channels as mentioned earlier. The idea here is to find the non-noisy coefficients and filter out the noise from the data matrix and then re-apply ICA in order to get the ECG signal. Algorithm 4 summarises the proposed steps in order to extract an ECG signal using the provided EMG channels. Figure 5.1 shows the extracted components after applying the ICA on the data matrix for recording emgch4. It can be observed that components 7 and 8 are noisy thus the data will be filtered with the coefficients which correspond to the non-noisy components 1 to 6. The extracted ECG signal is presented in Figure 5.2 (component 6 - red curve). It can also be seen that the extracted ECG signal should be inverted in this case in order to further analyse it for BR estimation.

Algorithm 4: ECG extraction from EMG

- 1 Data matrix construction \mathbf{X} ;
 - 2 Apply ICA to get ICs: $\mathbf{S} \leftarrow \text{ICA}(\mathbf{X})$, \mathbf{S} contains 8 ICs;
 - 3 Locate non-noisy ICs, $\hat{\mathbf{S}}$, whose number is less than 8, and compute the non-noisy mixing coefficients, $\hat{\mathbf{A}}$, as follows: $\mathbf{X}\hat{\mathbf{S}}^T \leftarrow \hat{\mathbf{A}}\hat{\mathbf{S}}\hat{\mathbf{S}}^T$, where $\hat{\mathbf{S}}\hat{\mathbf{S}}^T \leftarrow \mathbf{I}$;
 - 4 Filter data matrix with non-noisy coefficients: $\mathbf{X}_f \leftarrow \hat{\mathbf{A}}\hat{\mathbf{S}}$;
 - 5 Apply ICA to get ECG: $\text{ECG} \leftarrow \text{ICA}(\mathbf{X}_f)$;
-

5.2 Single Methods

This section provides an account of the proposed BR estimation methods using the Capnobase, the children ECG and EMG data. Following our approach discussed earlier, the derived respiration signal is divided into one minute windows prior to estimating the BR using either the frequency or time domain analysis. In order to evaluate the performance of the methods described in the following sections, the

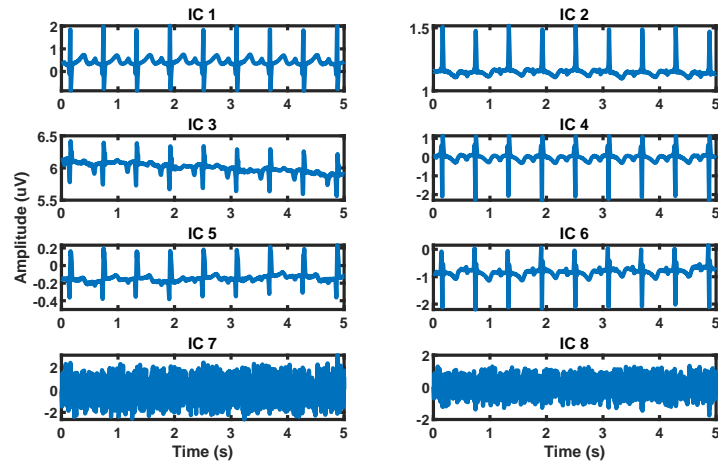


Figure 5.1: EMG ICA: A small part (5s) of the eight ICs found after applying ICA on the EMG data matrix for recording emgch4. Components 7 and 8 correspond to noise.

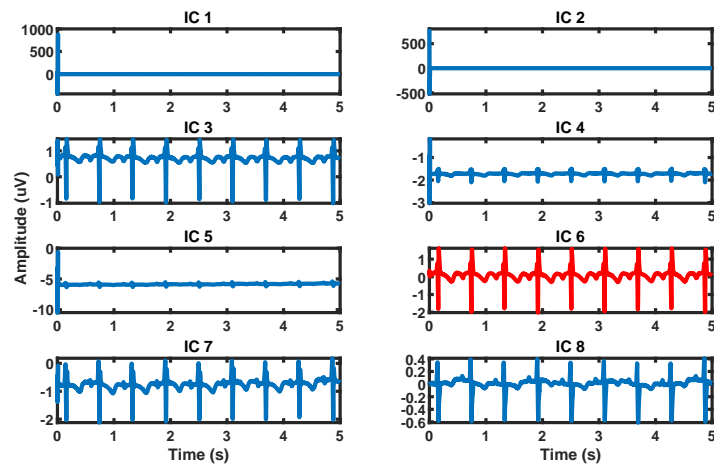


Figure 5.2: ECG extraction from EMG: A small part (5s) of the eight ICs found after applying ICA on the filtered data matrix for recording emgch4. Components 1 and 2 corresponds to noise. The (inverted) component 6 corresponds to the most dominant ECG (red curve).

Mean Absolute Error (MAE) in bpm was calculated as follows:

$$\text{MAE} = \frac{1}{N} \sum_{i=1}^N |\text{BR}_{\text{ref}_i} - \text{BR}_{\text{est}_i}|, \quad (5.1)$$

where BR_{ref} is the reference BR, BR_{est} is the estimated BR, and N is the total number of one minute windows. Moreover, for each method we provide a confidence interval (CI) which is given as $\pm 2\sigma$, where σ is the standard deviation of the MAEs for a specific method.

5.2.1 ECG-Derived Respiration (EDR)

This section discusses the results obtained using the proposed EDR estimation which is presented in Algorithm 5 on the recordings described above. The proposed method reduces the implementation time as the proposed algorithm uses the peak-to-baseline amplitude (Algorithm 5 line 3), whereas conventional EDR methods (E. Helfenbein et al., 2014; Babaeizadeh et al., 2011) use the peak-to-trough amplitude. This is because the computation of the peak-to-trough requires the identification of the S-peaks in addition to the R-peaks, thus increasing the computation cost and introducing delays to the BR estimation. However, we think this is unnecessary as one of the first processing steps of an ECG signal is the removal of the baseline wander thus peak-to-baseline, as proposed in this thesis, should provide accurate estimation of the BR as will be demonstrated later.

Furthermore, the majority of BR estimation methods filter the extracted respiration signal within reasonable respiration frequencies taking into account the BR limits of a healthy subject at rest. However, the proposed EDR method takes into account the patient age and the HR (Algorithm 5 line 4). The lower cut-off frequency is set to 0.4 Hz (24 bpm) for children with age in range 0-1 years old, and to 0.5 Hz

(30 bpm) for children with age in range 1-5 years old. The upper cut-off frequency is set to be the average of the maximum BR and the lower HR and it is always higher than 1.2 Hz (72 bpm) (Charlton et al., 2017).

Algorithm 5: Proposed EDR

- 1 **Locate R-peaks;**
 - 2 Discard outliers: $R \leftarrow \mu_R - 2\sigma_R < R < \mu_R + 2\sigma_R$ (where μ_R and σ_R are the mean and the variance of the R-peaks, respectively);
 - 3 **Interpolate R-peaks and then down-sample at 8 Hz;**
 - 4 **Filter within reasonable respiration frequencies depending on age and condition;**
-

Results

Tables 5.1, 5.2 and 5.3 show the results for Capnobase, BCH ECG and BCH EMG data, respectively. The results presented are structured as follows: first column corresponds to the patient code name, second column illustrates the results obtained after applying DFT to the respiration signal, third column the results from CSD and columns four and five show the results of the time domain analysis using the methods discussed in Section 3.1.

As can be seen from the tables, the EDR method gives the most promising results when applied on the Capnobase dataset. However, the results on the children data (BCH ECG and EMG) show a poor performance. This can be explained by the fact that these data were recorded in a hospital setting from under the age of 5 sick children with serious respiratory problems. In addition, the BR estimation of this hospital data is affected by the presence of noise such as sensors' imperfection, patient movements since children cannot stay still, misplaced sensors and imperfect sensor-patient contacts.

Figure 5.3 shows the ECG signal of patient ecgch1 in Plot 1. It is evident that the

Record	MAE_{DFT} (bpm)	MAE_{CSD} (bpm)	MAE_{3PT} (bpm)	MAE_{P2T} (bpm)
capno9	0.25	0.38	5.88	0.50
capno15	0.00	0.13	2.25	0.00
capno16	0.00	0.00	22.63	1.38
capno18	1.38	1.50	3.00	2.38
capno23	0.13	0.00	10.00	1.25
capno32	2.50	7.50	10.50	5.25
capno35	2.00	1.86	12.29	1.37
capno38	0.63	0.50	8.13	1.50
capno103	0.00	0.00	11.50	0.25
capno104	0.00	0.00	11.38	0.75
capno105	0.02	0.02	9.88	0.75
capno121	0.01	0.01	8.63	0.88
capno122	0.01	0.01	8.00	1.38
capno125	0.21	0.21	3.00	0.88
capno127	0.38	0.50	34.13	0.25
capno128	0.38	0.25	11.25	1.00
capno134	0.01	0.01	11.13	0.88
capno142	0.51	0.39	13.75	3.00
capno147	0.00	0.00	12.25	4.38
capno148	0.01	0.01	9.88	1.00
capno311	0.00	0.01	6.38	0.75
capno312	0.63	1.25	12.13	6.50
capno313	0.00	0.00	8.00	0.63
capno322	0.40	0.40	1.13	0.75
capno325	0.00	0.00	14.13	6.38
Average	0.38	0.60	10.45	1.76
CI	± 1.3	± 3.04	± 13.36	± 3.74

Table 5.1: Capnobase dataset: EDR performance

Record	MAE_{DFT} (bpm)	MAE_{CSD} (bpm)	MAE_{3PT} (bpm)	MAE_{P2T} (bpm)
ecgch1	7	7	9	5
ecgch2	31	34	14	22
ecgch3	9	9	10	4
ecgch4	4	4	7	2
ecgch5	2	22	5	6
ecgch6	25	25	0	9
ecgch7	27	24	2	12
ecgch8	10	6	11	6
ecgch9	55	52	40	49
ecgch10	20	20	8	14
ecgch11	11	10	12	4
ecgch12	2	2	7	3
ecgch13	2	17	14	4
ecgch14	17	16	13	13
ecgch15	26	16	5	12
ecgch16	7	3	5	3
ecgch17	16	24	0	6
ecgch18	3	1	7	2
Average	15.2	16.2	9.4	9.8
CI	± 27.6	± 26.0	± 17.6	± 22.2

Table 5.2: ECG children: EDR performance

Record	MAE_{DFT} (bpm)	MAE_{CSD} (bpm)	MAE_{3PT} (bpm)	MAE_{P2T} (bpm)
emgch1	23	26	16	21
emgch2	3	2.5	7	3.5
emgch3	6	5	3.8	2.8
emgch4	15.5	14.6	11.6	13.7
Average	11.8	12.0	9.6	10.3
CI	± 18.2	± 21.4	± 10.6	± 17.4

Table 5.3: EMG children: EDR performance

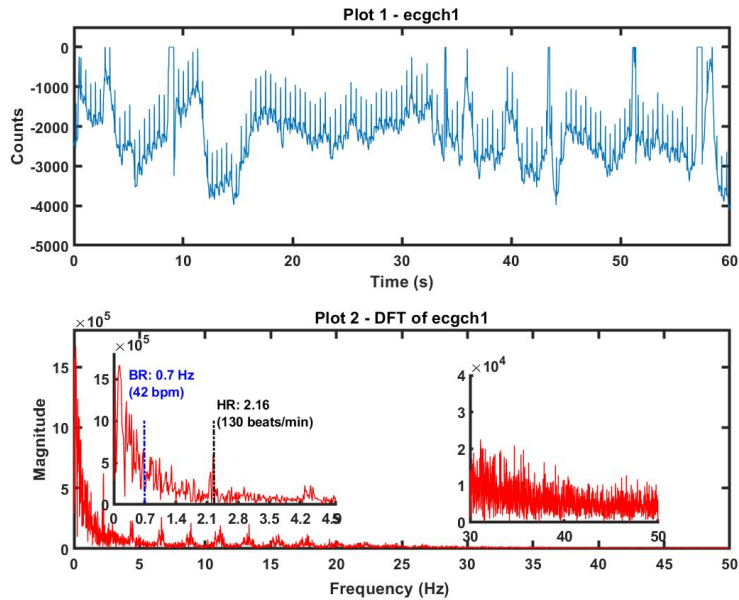


Figure 5.3: Noise in ecgch1: The baseline wander effect and muscular noise in ecgch1. Plot 1 shows the ECG signal. Plot 2 shows the DFT of the signal (DFT points = 6000). The blue and black dashed lines show the frequencies that correspond to BR and HR, respectively.

signal is governed by baseline wander, which results from excessive body movements. Plot 2 shows the DFT of this signal. Baseline wander is known as a low-frequency artefact, and it can be seen that the low frequencies are very dominant compared to the frequency corresponding to the BR. Moreover, a closer look at frequencies between 30-50 Hz reveals the presence of high frequency muscular noise.

Figure 5.4 shows the respiration signal obtained when the proposed EDR method was applied on recording capno9. Each plot corresponds to an one minute window. It has been already mentioned that the ECG signals' duration is 8 minutes, hence following our approach it is expected to see 8 respiration signals of one minute length. For each window the BR is estimated in the frequency domain by applying a DFT.

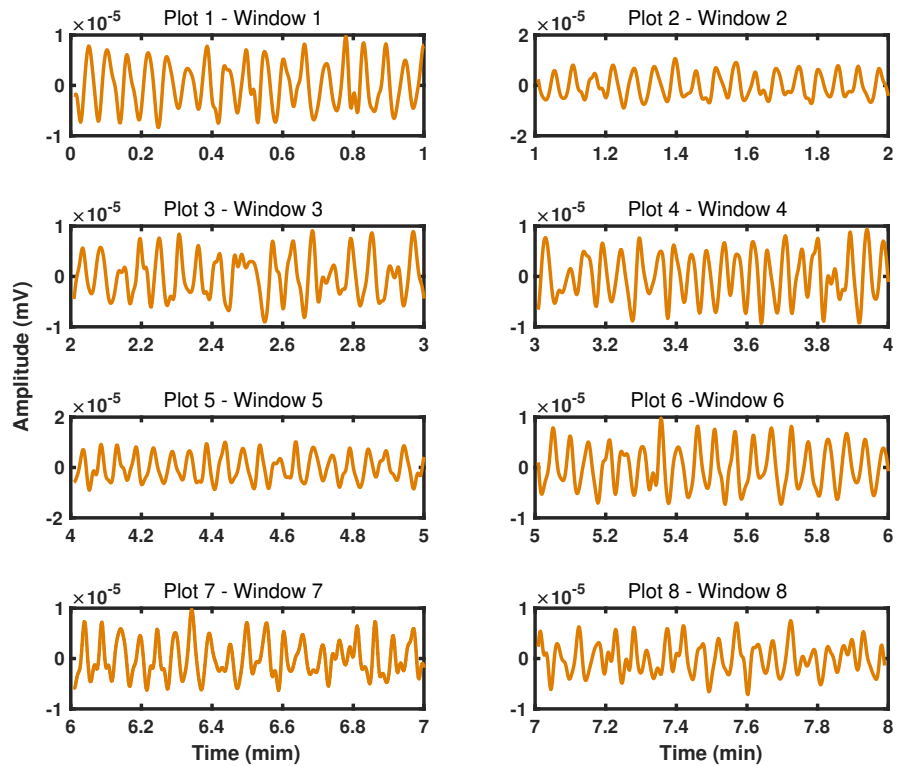


Figure 5.4: EDR method on capno9: The band-pass filtered respiration signal obtained from the proposed EDR method for recording capno9. Plots 1 to 8 correspond to the 8 one minute windows obtained from the proposed algorithm.

Figure 5.5 shows the frequency analysis of the band-pass filtered EDR signal obtained for capno9. Plots 1 to 8 of Figure 5.5 represent the DFT frequency domain analysis for the entire EDR signal, along with the reference BR. It can be seen that each window contains a dominant peak which corresponds to the estimated BR.

Figure 5.6 shows the frequency domain analysis of the band-pass filtered EDR respiratory signal obtained for recording ecgch1. The reference BR is only given for the second respiratory window and it is 42 bpm (0.7 Hz). From Plots 3 and 5 in the

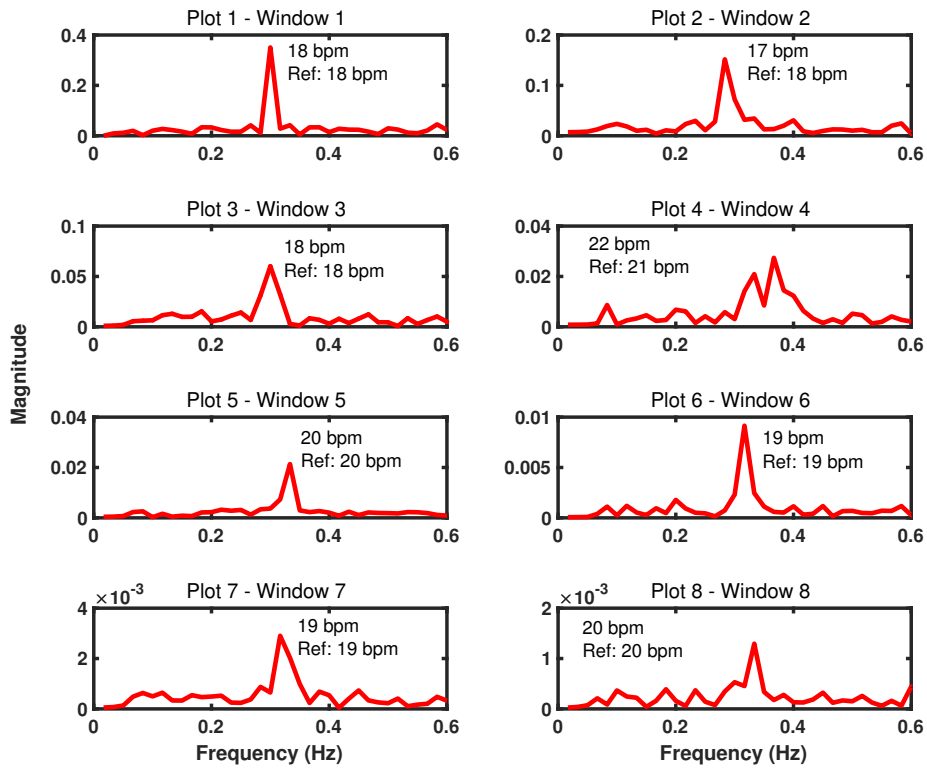


Figure 5.5: DFT analysis of the EDR signal on capno9: Frequency domain (FD) analysis of the band-pass filtered EDR signal using the DFT for recording capno9. Plots 1 to 8 show the frequency spectra of each one minute window, along with the reference BR.

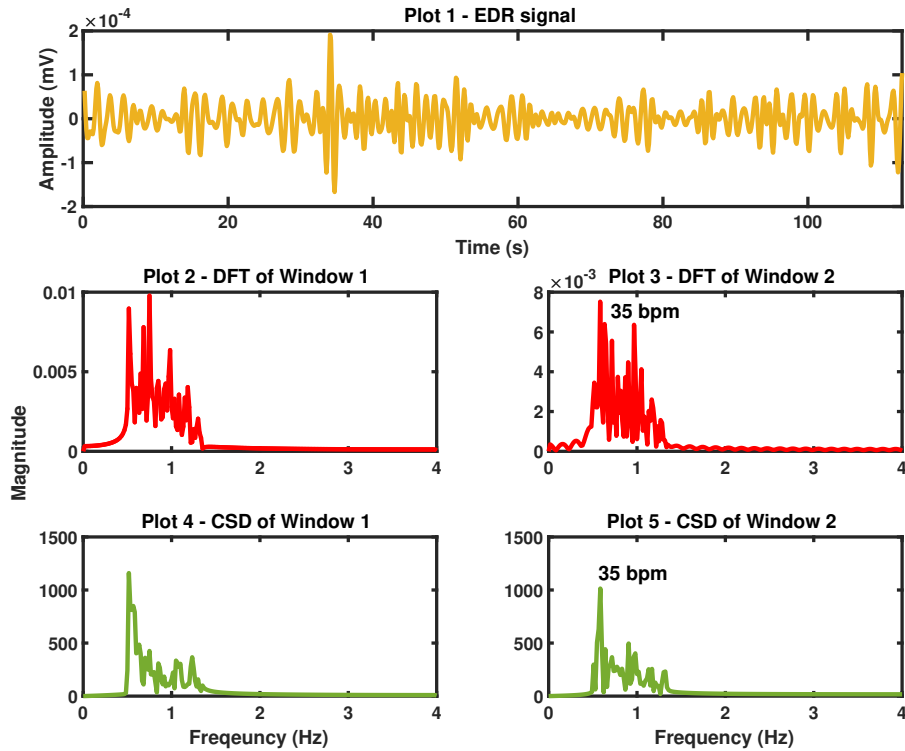


Figure 5.6: FD analysis of the EDR signal on ecgch1: Frequency domain analysis of the band-pass filtered EDR signal using the DFT and CSD for recording ecgch1. Plot 1 shows the obtained band-pass filtered EDR signal for the 2 min recording. Plots 2 and 3 represent the DFT analysis. Plots 4 and 5 show the CSD analysis.

figure, it is apparent that the most dominant DFT and CSD frequencies are at 35 bpm (0.58 Hz) for both methods. What is interesting about the frequency spectra in this figure is that both DFT and CSD spectra contain a peak at 0.7 Hz, which corresponds to the reference BR, proving that the respiration frequency is present in the data, however noise frequencies are more prominent.

Moreover, regarding the performance of the methods for recording ecgch9, the high MAE of recording ecgch9 can be explained from the fact that the BR cannot

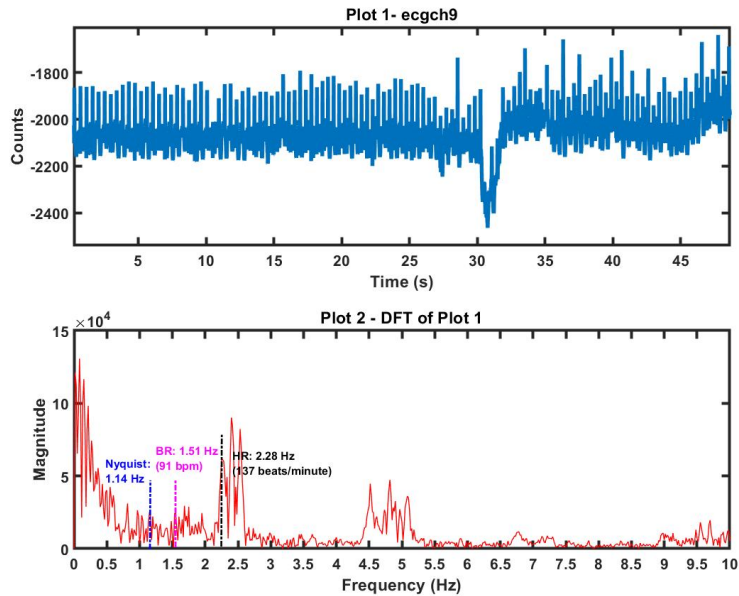


Figure 5.7: HR Nyquist limit on ecgch9: Plot 1 shows the ecgch9. Plot 2 shows the DFT of the signal (DFT points = 6000). The blue dashed line represents the Nyquist limit ($HR/2$). The pink and black dashed lines correspond to the BR and HR, respectively.

be estimated as it is 91 bpm and the corresponding HR is 137 bpm, meaning that the reference BR is much higher than half the HR causing aliasing. To elaborate in ECG-based BR extraction methods, the time series derived as respiration signal is sampled at the HR frequency because the respiration signal is based on the R-peaks which also define the HR. Hence frequencies above half of the HR frequency can not be retrieved due to the Nyquist limit. Figure 5.7 shows the DFT of ecgch9. It is evident that the BR frequency is higher than the Nyquist limit. Therefore the BR in this case cannot be retrieved from methods that depend on the R-peak extraction.

Figure 5.8 shows the frequency domain analysis of two one minute windows using the DFT and CSD techniques on the respiration signal obtained from the proposed

EDR method for emgch2. The reference BR for these windows is 28 bpm (0.4667 Hz). As shown in Plots 2 and 3 the most dominant peaks are close to the reference so the MAE is low. Furthermore, Plot 5 shows that the most dominant peak in the CSD spectrum is quite close to the reference frequency, hence the estimation accuracy is high.

Taken together, these results suggest that the developed EDR method provides accurate BR estimates for the Capnobase data. However, the MAE is higher for the BCH ECG and EMG data, suggesting that the EDR method is affected by the noise introduced to the ECG signals due to sensor's imperfections. The latter is also mirrored in the frequency domain analysis of the EDR signals of the children data, where it can be seen that the frequency spectrum is more spread and there is no clear dominant frequency. Moreover, the time domain methods show similar performances for the children data, suggesting that the advanced P2T method is somehow confused on which peak to chose as breaths, when it comes to patients who show difficulty in breathing, because it uses a set of conditions applied on the identified breaths which is based on normal breathing.

5.2.2 RSA-Derived Respiration (RSA)

The improved RSA estimation and the results obtained when applied to the databases discussed earlier in this chapter are described in this section. The novelty of the RSA method is that the extracted respiration signal is first filtered within reasonable respiration frequencies based on the age of the patient and their HR (Algorithm 6 line 4).

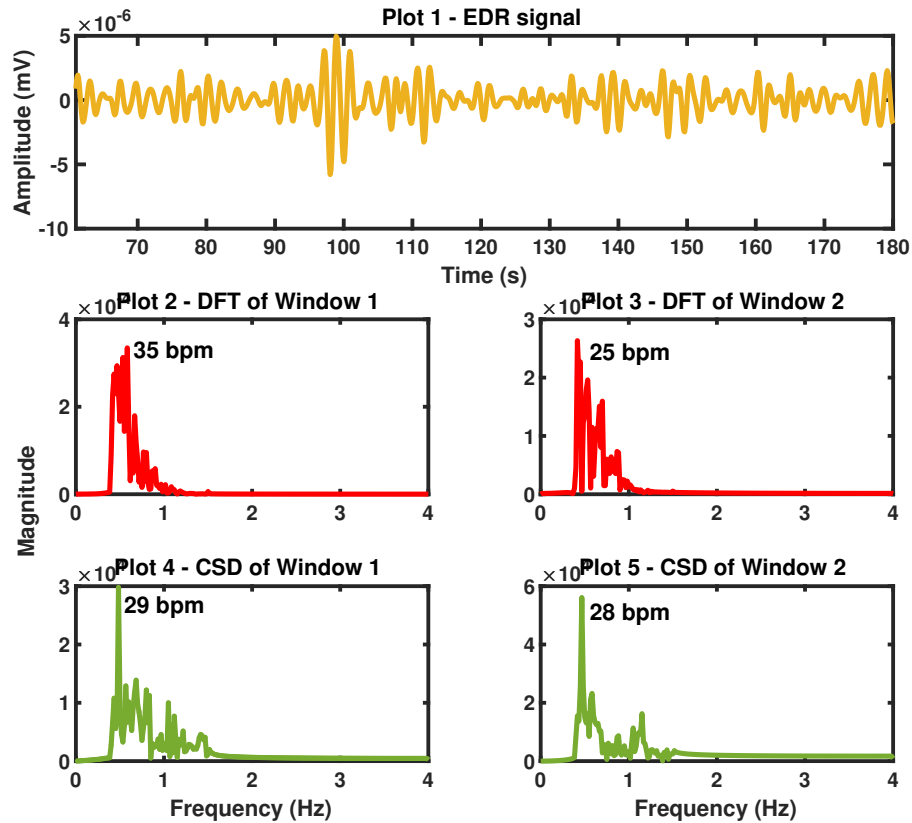


Figure 5.8: FD analysis of the EDR signal on emgch2: Frequency domain analysis of the band-pass filtered EDR signal using the DFT and CSD for recording emgch2. Plot 1 shows the obtained band-pass filtered EDR signal. Plots 2 and 3 represent the DFT analysis. Plots 4 and 5 show the CSD analysis.

Algorithm 6: Proposed RSA

- 1 Locate R-peaks;
 - 2 Compute the Instantaneous Heart Rate (IHR) values;
 - 3 Interpolate IHR values and then down-sample at 8 Hz;
 - 4 Filter within reasonable respiration frequencies depending on age and condition;
-

Results

The results from the frequency and time domain analysis for each dataset are summarised in Tables 5.4, 5.5 and 5.6. It is apparent from these tables that the frequency domain methods perform better when applied on the Capnobase dataset. Moreover, the overall performance appears not to be as good as when using EDR. A possible explanation for the high errors when analysing an RSA signal is that the ECG signal is not dominated by FM, meaning that the distances between the R-peaks are not affected by respiration and hence the RSA method cannot capture the respiratory behaviour of the signal. The latter can be related to the position of the ECG sensors. Nonetheless, it was previously shown that EDR can capture this behaviour, indicating that the Capnobase ECG signals are governed by AM.

Figure 5.9 shows the respiration signal obtained when the proposed RSA method was applied on recording capno16. Each plot illustrates a one minute window and for each window the frequency spectrum is computed using the DFT analysis, which is shown in Figure 5.10. The MAE of recording capno16 for the DFT method is high about 5.8781 bpm. It can be observed that the RSA signal is not very smooth and the respiratory oscillations are not distinct which will affect the frequency domain analysis as other frequencies are going to be present and deteriorate the accuracy of the BR estimation. This phenomenon can also be validated by having a closer inspection of the frequency spectra (Figure 5.10). The reference BR for capno16 is 10 bpm (0.1667 Hz). As can be seen only in Plots 2, 3 and 4 there is a dominant respiratory peak at 0.1667 Hz. However the most dominant frequency of the rest of the windows is around 0.06667 Hz, which is far from the reference.

It is also interesting to compare the RSA signal and its spectrum with the EDR signal. Figure 5.11 shows the EDR signal obtained for capno16. It is evident that

Record	MAE_{DFT} (bpm)	MAE_{CSD} (bpm)	MAE_{3PT} (bpm)	MAE_{P2T} (bpm)
capno9	2.13	0.38	6.13	0.88
capno15	0.00	0.00	3.50	0.00
capno16	5.88	2.63	38.38	16.75
capno18	2.00	5.76	18.50	3.75
capno23	0.25	0.10	6.75	0.50
capno32	1.62	1.63	11.25	0.75
capno35	15.83	19.97	33.57	4.86
capno38	2.88	3.13	6.50	1.25
capno103	0.00	0.00	21.88	6.38
capno104	0.00	0.00	35.63	11.88
capno105	1.25	2.27	9.88	2.00
capno121	3.76	5.01	13.50	2.63
capno122	0.51	0.01	10.50	1.75
capno125	0.21	0.21	3.38	1.00
capno127	6.02	8.75	3.13	3.14
capno128	7.00	7.13	17.13	2.25
capno134	8.26	10.88	37.00	6.63
capno142	0.00	3.00	14.63	2.75
capno147	11.63	8.25	32.13	3.50
capno148	3.38	3.26	14.50	2.63
capno311	7.10	7.72	10.63	2.60
capno312	0.00	0.00	11.25	3.00
capno313	2.00	4.50	18.38	9.00
capno322	2.00	2.53	5.25	1.25
capno325	5.88	7.24	28.75	4.00
Average	3.58	4.17	16.49	3.81
CI	± 8.1	± 9.3	± 22.82	± 7.7

Table 5.4: Capnobase dataset: RSA performance

Record	MAE_{DFT} (bpm)	MAE_{CSD} (bpm)	MAE_{3PT} (bpm)	MAE_{P2T} (bpm)
ecgch1	7	10	19	8
ecgch2	22	8	10	12
ecgch3	11	11	20	2
ecgch4	3	18	12	8
ecgch5	9	17	8	5
ecgch6	22	6	3	5
ecgch7	18	2	2	5
ecgch8	5	12	15	9
ecgch9	52	65	40	52
ecgch10	25	8	2	11
ecgch11	15	11	9	3
ecgch12	4	4	8	1
ecgch13	4	17	10	4
ecgch14	18	17	10	18
ecgch15	17	23	1	10
ecgch16	8	8	7	0
ecgch17	7	1	3	6
ecgch18	2	2	9	5
Average	13.8	13.3	10.4	9.1
CI	± 24.0	± 28.6	± 18.4	± 23.2

Table 5.5: ECG children: RSA performance

Record	MAE_{DFT} (bpm)	MAE_{CSD} (bpm)	MAE_{3PT} (bpm)	MAE_{P2T} (bpm)
emgch1	26	28	3	19
emgch2	2.5	2	5	2
emgch3	7.2	10.2	3.2	5.5
emgch4	22.3	21.9	13.7	11.0
Average	14.5	15.5	6.2	11.0
CI	± 22.8	± 23.3	± 10.1	± 17.0

Table 5.6: EMG children: RSA performance

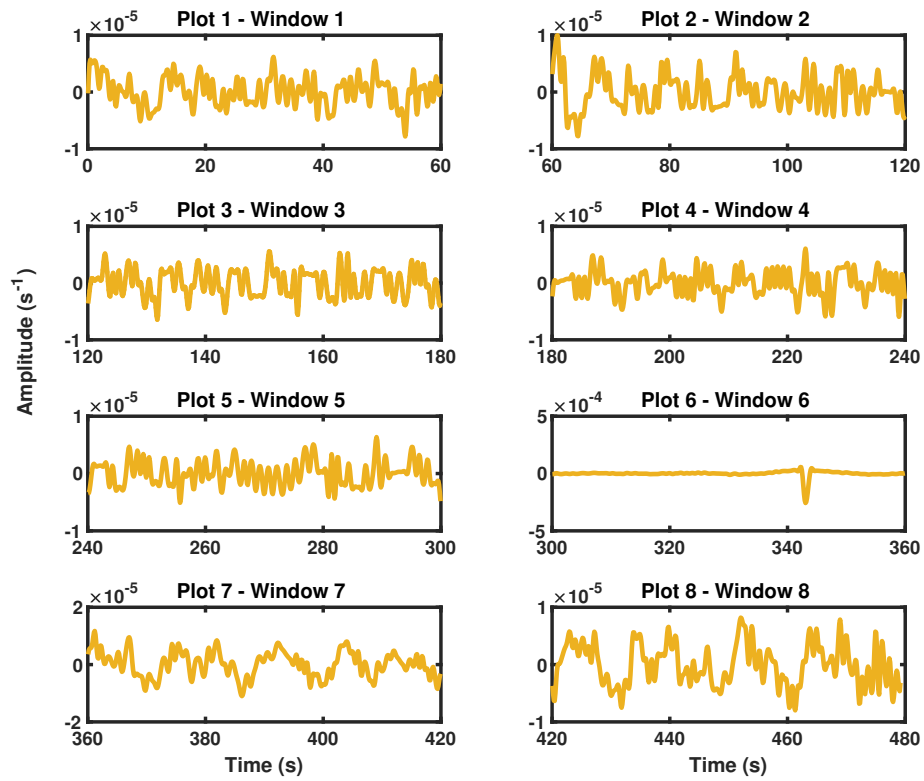


Figure 5.9: RSA method on capno16: The band-pass filtered respiration signal obtained from the proposed RSA method for recording capno16. Plots 1 to 8 correspond to the 8 one minute windows obtained from the proposed algorithm.

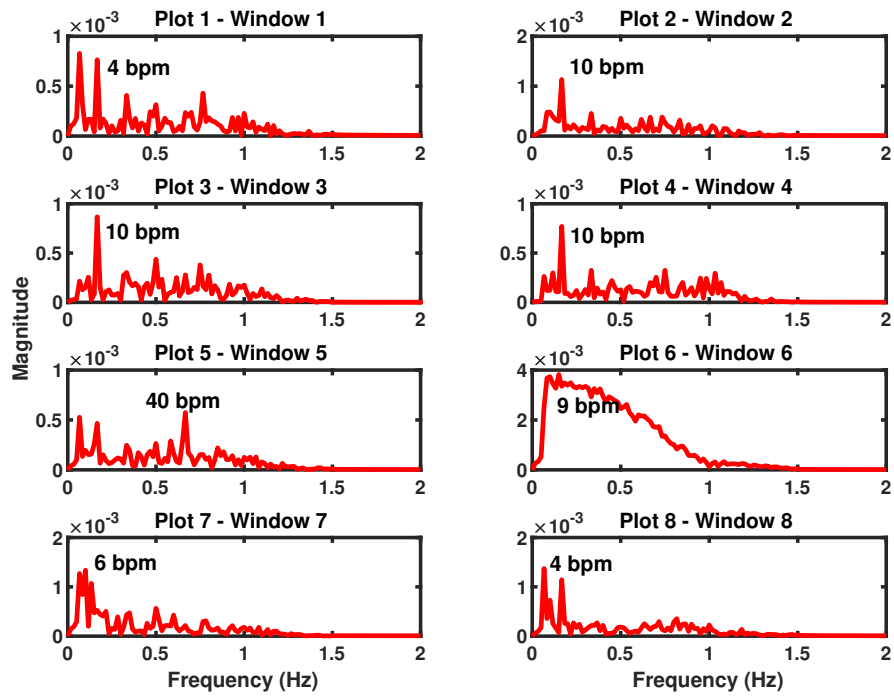


Figure 5.10: DFT analysis of the RSA signal on capno16: Frequency domain analysis of the band-pass filtered RSA signal using the DFT for recording capno16. Plots 1 to 8 shows the frequency spectra of each one minute window.

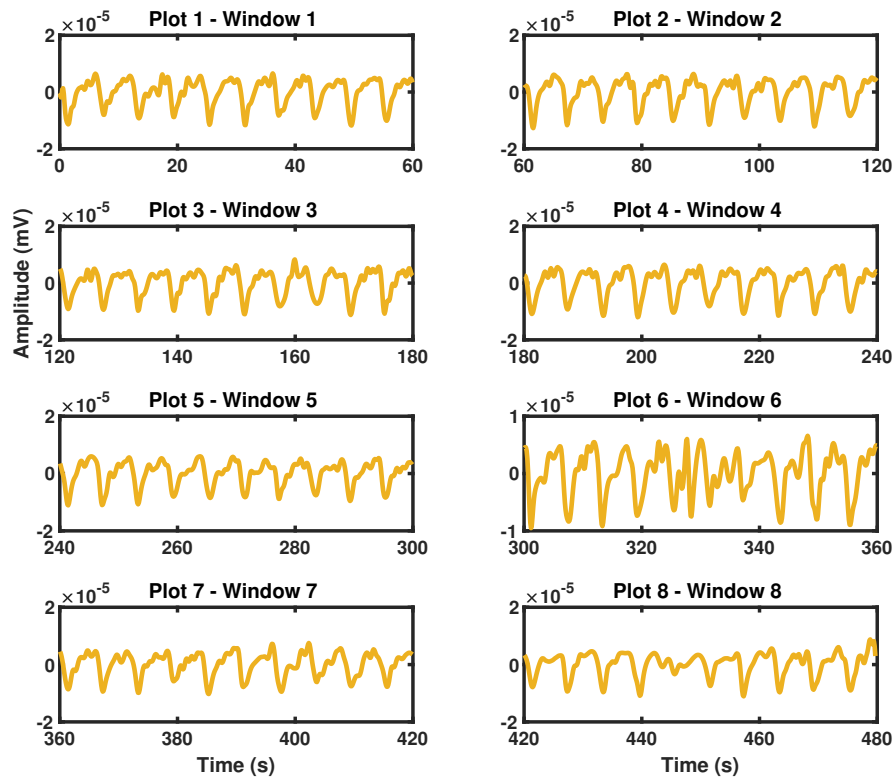


Figure 5.11: EDR method on capno16: The respiration signal obtained from the proposed EDR method for recording capno16. Plots 1 to 8 correspond to the 8 one minute windows obtained from the proposed algorithm.

the EDR signal is smoother, compared to the RSA signal, and also gives a clearer image of the respiratory oscillations. The latter conclusion can be further validated if the frequency spectrum of the signal is investigated. Figure 5.12 illustrates the DFT spectra of each window of the EDR signal for recording capno16. It can be observed that in all the windows there is a clear dominant spectral peak at 0.1667 Hz, which corresponds to the reference respiratory frequency.

Figure 5.13 illustrates the frequency and the time domain analysis of the RSA

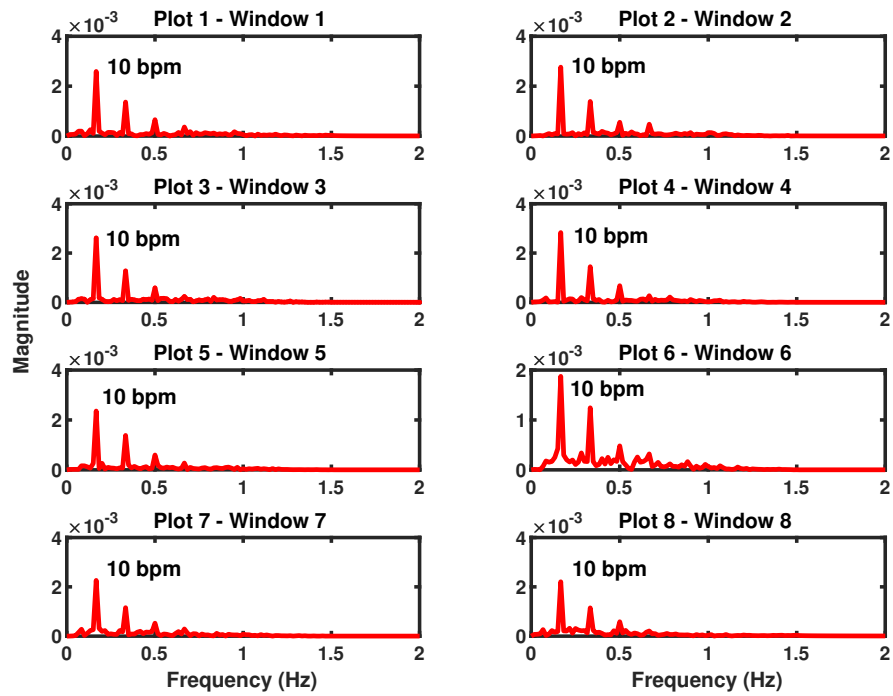


Figure 5.12: DFT analysis of the EDR signal on capno16: Frequency domain analysis of the EDR signal using the DFT for recording capno16. Plots 1 to 8 shows the frequency spectra of each one minute window.

signal extracted for recording ecgch1. As previously mentioned, the reference BR for recording ecgch1 is given only for the second window and it is at 42 bpm (0.7 Hz). From Plots 3 and 5 it is evident that the most dominant peak is far from the reference respiratory peak. However, there are peaks in both the DFT and CSD spectrum which are around 0.7 Hz, indicating the respiratory activity is present but it is overlapped and finally distorted by noise frequencies. Moreover, P2T method identifies 50 breaths, whereas the 3PT method identifies 61 breaths, when the reference is 42 bpm. This result suggests that P2T performs better than 3PT for the RSA signal which was also shown for the Capnobase dataset (Table 5.4). The latter conclusion can be explained by the fact that the prerequisites required by P2T method discard breath peaks which are present due to the specific jagged-shaped respiration signal obtained from the RSA method.

Figure 5.14 shows the BR estimation using the band-pass filtered RSA signal extracted for patient emgch3. The reference BR for the first hour of patient emgch3 is 37 bpm, which is 0.6167 Hz. It is evident from Plots 2, 3, 4 and 5 that the respiration frequency is present but it is not the most dominant. However, in both DFT and CSD spectra there are peaks which are at 0.6167 Hz whose amplitude is not so insignificant. This problem will be addressed later in a following section by using data fusion techniques. Moreover, 3PT identifies 36 and 37 breaths for each window, whereas the P2T 32 and 31 breaths, suggesting that the P2T method is discarding more breaths when it comes to patient who face difficulty in breathing.

Overall, these results suggest that RSA is a more sensitive method and in order to give sufficient BR estimates, the ECG signals should be distinctively governed by FM. Moreover, it has been shown again that the DFT and CSD analysis can both accurately estimate the BR of sick children. Finally, the RSA results demonstrate

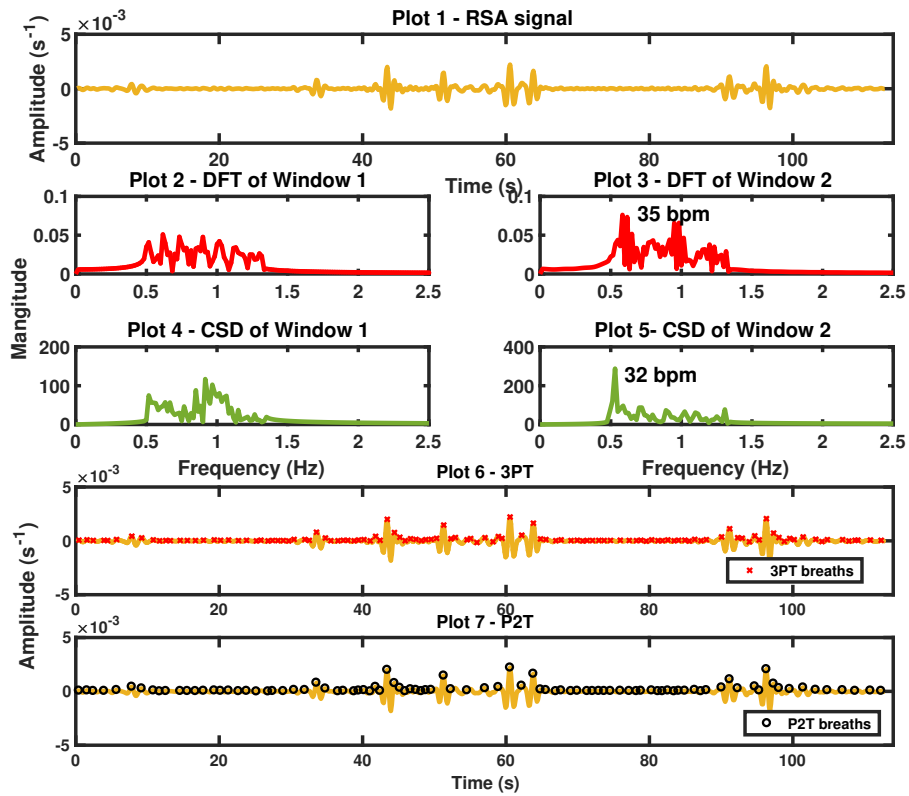


Figure 5.13: Frequency Domain (FD) and Time Domain (TD) analysis of the RSA signal on ecgch1: Frequency and time domain analysis of the band-pass filtered RSA signal using the DFT, CSD, 3PT and P2T for recording ecgch1. Plot 1 shows the obtained band-pass filtered RSA signal. Plots 2 and 3 represent the DFT analysis. Plots 4 and 5 show the CSD analysis. Plot 6 shows the breaths obtained from 3PT method as red crosses. Plot 7 shows the breaths obtained from the P2T method as black circles.

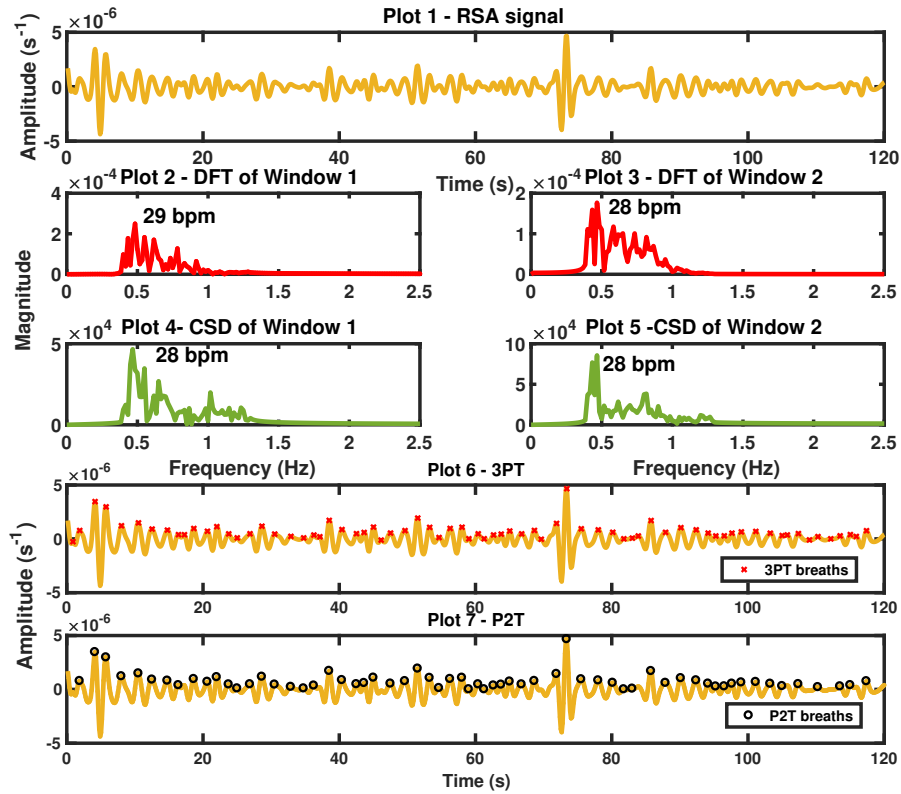


Figure 5.14: FD and TD analysis of the RSA signal on emgch3: Frequency and time domain analysis of the band-pass filtered RSA signal using the DFT, CSD, 3PT and P2T for recording emgch3. Plot 1 shows the obtained band-pass filtered RSA signal. Plots 2 and 3 represent the DFT analysis. Plots 4 and 5 show the CSD analysis. Plot 6 shows the breaths obtained from 3PT method as red crosses. Plot 7 shows the breaths obtained from the P2T method as black circles.

that the two time domain methods show comparable performances when processing signals which belong to patients with difficulty in breathing.

Having explored the two deterministic feature-based methods, the EDR and RSA, for the BR estimation, the next sections move on to discussing the statistical analysis methods, in order to investigate if the performance is improved.

5.2.3 PCA-Derived Respiration (PCADR)

The uncertainty of the patient's clinical condition, as well as the inter- or intra-patient variability can be factors which affect deterministic feature-based methods, such as the EDR and RSA. Moreover, the statistical properties of the unknown signal, i.e. respiration, could be known, hence statistical modelling might be more appropriate. In this section, the PCA-derived respiration will be investigated using Capnobase, BCH ECG, and EMG data. The enhanced proposed PCADR method filters the extracted respiration signal using a band-pass filter whose cut-off frequencies are based on the age and condition of the patient (Algorithm 7 line 5), prior to the estimation of the BR.

Algorithm 7: Proposed PCADR

- 1 Locate R-peaks;
 - 2 Create data matrix \mathbf{X} ;
 - 3 $\mathbf{R}_X \leftarrow \mathbf{U}\Sigma\mathbf{V}^T$;
 - 4 Filter the data matrix with the coefficients of the first PC and create $\hat{\mathbf{X}}$;
 - 5 Filter the first row of $\hat{\mathbf{X}}$ within reasonable respiration frequencies depending on age and condition of the patient;
-

Results

Tables 5.7, 5.8 and 5.9 outline the results obtained when estimating the BR using the PCADR method. These findings suggest that the use of the PCA method did not improve the BR estimation for real children ECG data. A possible explanation is that PCA is a basic statistical analysis method. Therefore, more advance techniques should be investigated.

Figures 5.15 and 5.16 show the frequency spectra obtained for each respiratory window of recording capno9 after applying the DFT and the CSD analysis, respectively, on the extracted PCADR signal. It can be observed that both methods perform identically. The reference BR is about 18 bpm (0.3 Hz). In all the respiratory windows, in the extracted spectra there is a dominant peak at or very close to 0.3 Hz, achieving a low MAE.

Figures 5.17 and 5.18 illustrate the time domain analysis for each respiratory window. It is evident that the 3PT method identifies more breaths, contributing to increasing the estimation error, compared to the P2T method, whose overall MAE is low at about 1.93 bpm. As previously mentioned this finding is expected as the 3PT method counts as breaths all the extrema of the respiration signal, whereas P2T applies additional conditions which discard the non-respiratory oscillations of the signal.

The frequency domain and time domain analysis of recording ecgch1, as well as the extracted band-pass filtered PCADR signal can be seen in Figure 5.19. To reemphasize, the reference BR of this recording is 42 bpm (0.7 Hz) and the reference is provided only for the second respiratory window. Plot 3 shows that the most dominant peak is at 0.6 Hz, which is not the reference frequency. What is interesting in this plot is that the second most dominant frequency is at 0.7 Hz which is the

Record	MAE_{DFT} (bpm)	MAE_{CSD} (bpm)	MAE_{3PT} (bpm)	MAE_{P2T} (bpm)
capno9	0.38	0.38	3.00	0.00
capno15	0.00	0.00	2.13	0.00
capno16	1.38	0.00	23.00	2.00
capno18	1.51	1.38	4.25	1.72
capno23	0.50	0.38	13.88	0.63
capno32	2.75	2.13	18.88	4.50
capno35	1.86	2.00	13.71	2.00
capno38	1.75	1.75	9.13	2.50
capno103	0.00	0.00	11.50	0.38
capno104	0.00	0.00	10.38	0.88
capno105	0.00	0.00	8.38	0.75
capno121	0.01	0.01	7.25	0.57
capno122	0.13	0.13	9.13	0.88
capno125	0.25	0.25	2.63	0.75
capno127	0.50	0.50	5.63	0.75
capno128	0.38	0.25	13.00	0.63
capno134	1.75	3.25	12.50	0.88
capno142	3.13	1.26	14.63	3.88
capno147	8.13	9.38	15.25	6.88
capno148	0.01	0.01	10.63	1.00
capno311	0.38	0.25	7.00	1.25
capno312	1.75	3.38	12.50	7.13
capno313	0.00	0.00	8.50	0.88
capno322	0.75	0.75	1.75	0.88
capno325	0.74	2.24	26.25	6.50
Average	1.12	1.19	10.60	1.93
CI	± 3.44	± 4.00	± 12.34	± 4.26

Table 5.7: Capnabase dataset: PCADR performance

Record	MAE_{DFT} (bpm)	MAE_{CSD} (bpm)	MAE_{3PT} (bpm)	MAE_{P2T} (bpm)
ecgch1	6	6	10	2
ecgch2	30	29	9	19
ecgch3	5	10	1	3
ecgch4	6	2	9	4
ecgch5	4	20	4	3
ecgch6	11	14	9	3
ecgch7	7	27	2	8
ecgch8	6	6	20	6
ecgch9	52	60	43	49
ecgch10	23	23	4	15
ecgch11	11	10	9	2
ecgch12	15	15	13	7
ecgch13	16	15	13	5
ecgch14	15	21	11	18
ecgch15	31	29	3	12
ecgch16	4	3	4	0
ecgch17	2	15	3	8
ecgch18	7	14	4	0
Average	13.9	17.7	9.5	9.1
CI	± 25.8	± 27.0	± 19.4	± 23.0

Table 5.8: ECG children: PCADR performance

Record	MAE_{DFT} (bpm)	MAE_{CSD} (bpm)	MAE_{3PT} (bpm)	MAE_{P2T} (bpm)
emgch1	18	35	10	20
emgch2	2	2	7.5	3.5
emgch3	6	6	3.8	4.2
emgch4	15.3	13.9	11.1	13.6
Average	10.3	14.2	8.1	10.3
CI	± 15.1	± 29.4	± 6.5	± 15.9

Table 5.9: EMG children: PCADR performance

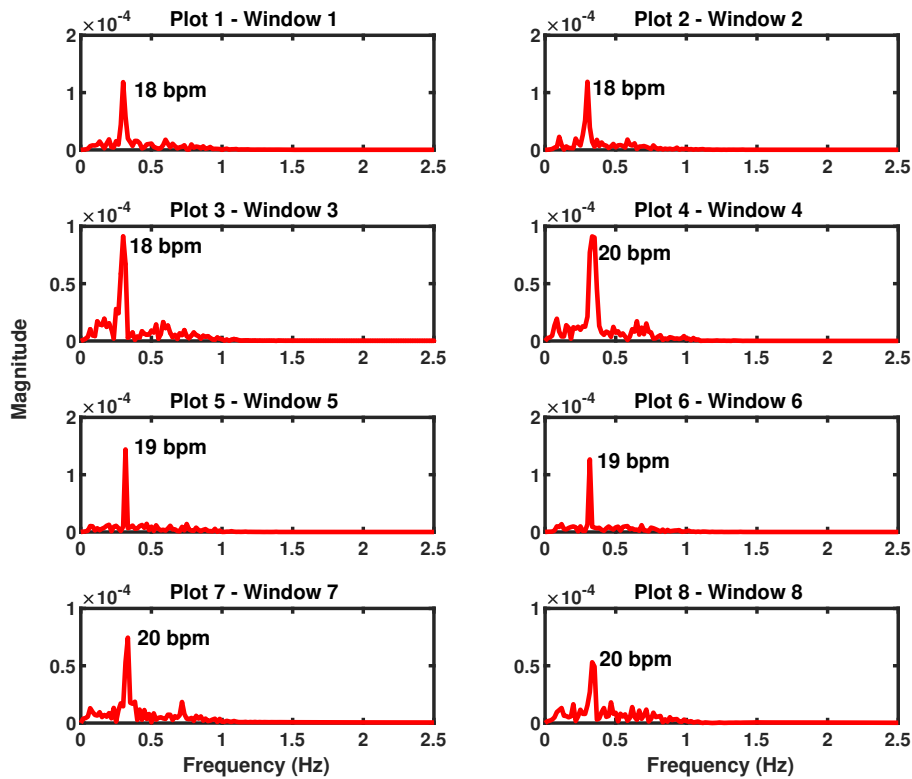


Figure 5.15: DFT analysis of the PCADR signal on capno9: Frequency domain analysis of the band-pass filtered PCADR signal using the DFT for recording capno9. Plots 1 to 8 show the frequency spectra of each one minute window.

reference, suggesting that sensor capturing noise while recording the ECG signals, affects the frequency spectrum of respiration. This problem will be addressed later in this chapter using data fusion techniques. Regarding the time domain estimation methods both of them achieved a promising MAE for real ECG data which belong to sick children. Closer inspection of Plot 6 shows that the 3PT method counted 52 breaths, whereas the P2T method (Plot 7) counted 44 breaths, which is closer to the reference, giving a MAE of 2 bpm.

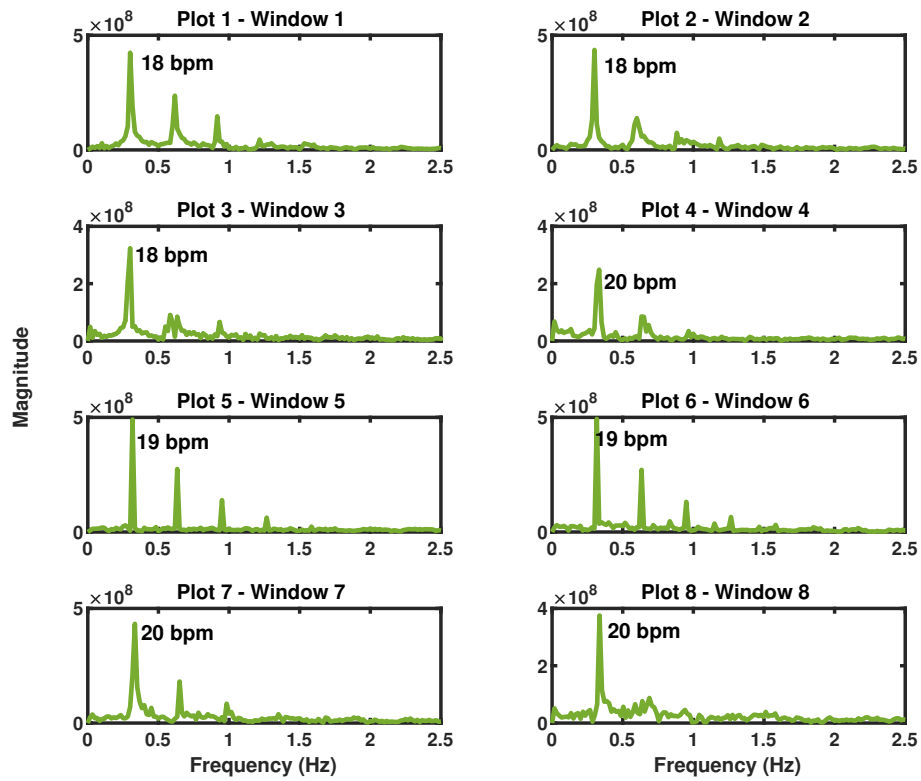


Figure 5.16: CSD analysis of the PCADR signal on capno9: Frequency domain analysis of the band-pass filtered PCADR signal using the CSD for recording capno9. Plots 1 to 8 show the frequency spectra of each one minute window.

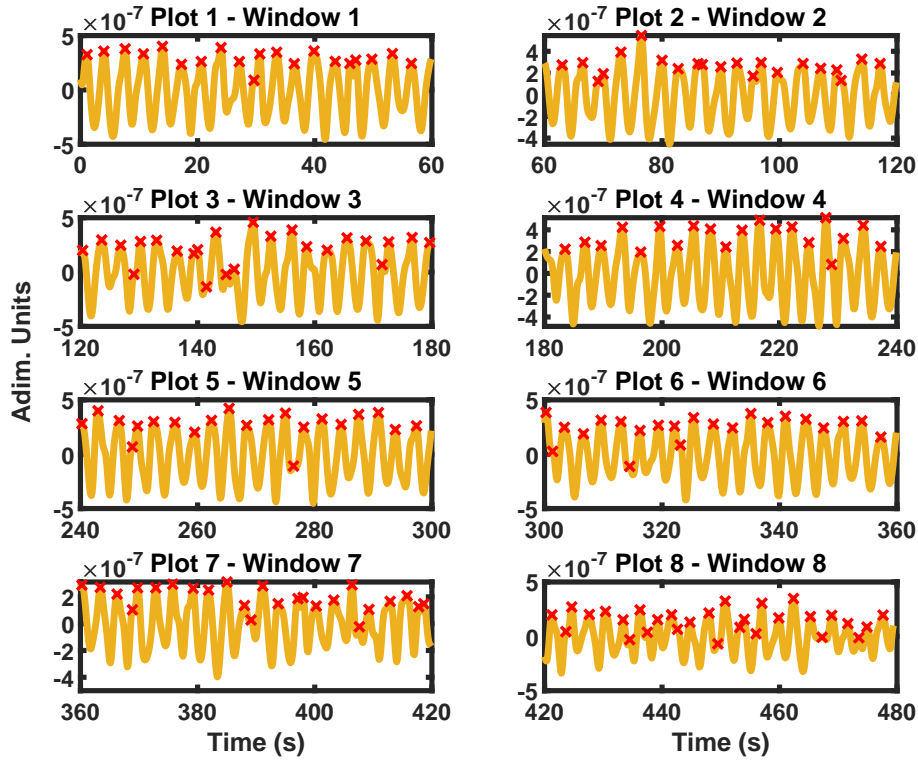


Figure 5.17: 3PT analysis of the PCADR signal on capno9: Time domain analysis of the band-pass filtered PCADR signal using the 3PT for recording capno9. Red crosses represent the identified breaths by the 3PT method.

Figure 5.20 shows the frequency and time domain analysis along with the PCADR signal extracted for patient emgch3. First it can be observed that the PCADR signal is smoother than the RSA signal (Figure 5.14), having more distinct respiratory-oscillations, whose behaviour can be retrieved from the frequency domain analysis. The depicted respiratory windows correspond to the first hour of the EMG channels and their reference BR is at 37 bpm, which is 0.6167 bpm. It is evident that the most dominant peaks in the DFT window are close to the reference BR. Nonetheless, the frequency domain estimation accuracy is affected due to the ECG sensors capturing

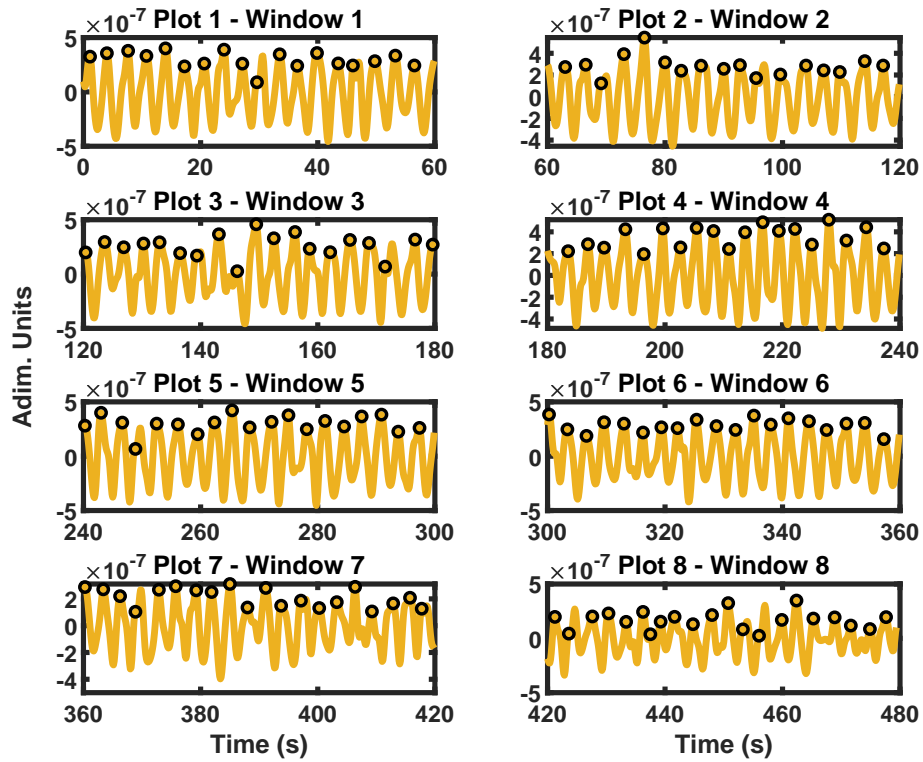


Figure 5.18: P2T analysis of the PCADR signal on capno9: Time domain analysis of the band-pass filtered PCADR signal using the P2T for recording capno9. Black circles represent the identified breaths by the P2T method.

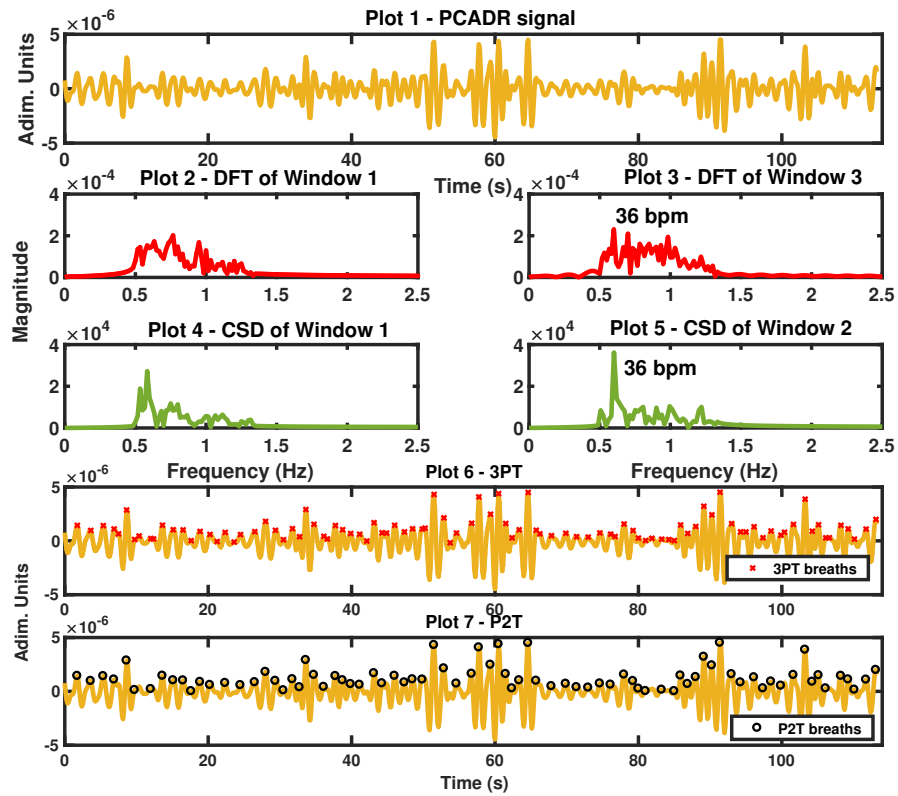


Figure 5.19: FD and TD analysis of the PCADR signal on ecgch1: Frequency and time domain analysis of the band-pass filtered PCADR signal using the DFT, CSD, 3PT and P2T for recording ecgch1. Plot 1 shows the obtained band-pass filtered PCADR signal. Plots 2 and 3 represent the DFT analysis. Plots 4 and 5 show the CSD analysis. Plot 6 shows the breaths obtained from 3PT method as red crosses. Plot 7 shows the breaths obtained from the P2T method as black circles.

noise.

In summary, these findings illustrate that the EDR and PCADR methods show similar performances for both ECG and EMG children data, while RSA is more sensitive. Furthermore, it is worth mentioning that the signals obtained for the Capnobase, children ECG, and EMG children data from the EDR (Figures 5.4, 5.6 and 5.8) and the PCADR methods have a smoother shape when compared to the RSA signal (Figures 5.13 and 5.14).

5.2.4 ICA-Derived Respiration (ICADR)

The main drawback of PCA analysis is that it assumes that the source signals, i.e. respiration, are mutually uncorrelated, whereas ICA assumes statistical independence. Therefore, it is interesting to investigate whether ICADR will improve the BR estimation. The innovativeness of the proposed ICADR method is the dimensionality reduction of the data matrix based on the cumulative sum of the eigenvalues of the latter (Algorithm 8 line 3), the selection of the corresponding to respiration IC (Algorithm 8 lines 5 and 6) and that the latter is filtered within reasonable respiration frequencies prior the BR estimation (Algorithm 8 line 7).

Algorithm 8: Proposed ICADR

- 1 **Locate R-peaks;**
 - 2 **Create data matrix \mathbf{X} ;**
 - 3 **Apply PCA to reduce dimensions of \mathbf{X} based on the cumulative sum of eigenvalues;**
 - 4 **$\mathbf{IC} \leftarrow \text{fastICA}(\mathbf{X})$;**
 - 5 **Analyse frequency content of IC;**
 - 6 **Choose respiratory IC;**
 - 7 **Filter within reasonable respiration frequencies depending on age and condition;**
-

The main assumption of the proposed ICADR method is that the size of the

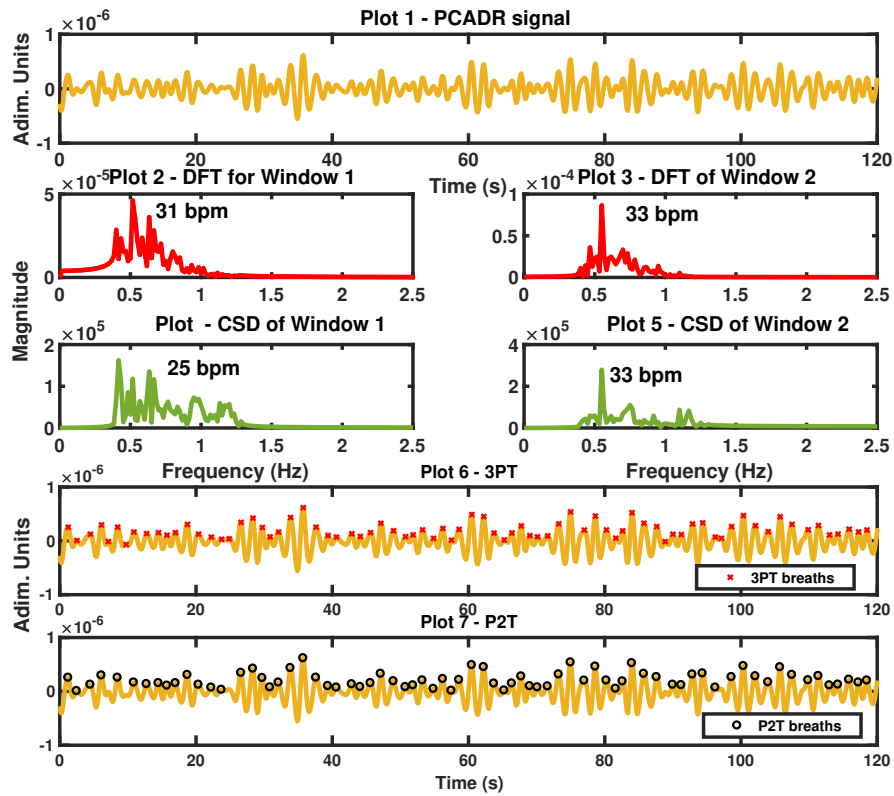


Figure 5.20: FD and TD analysis of the PCADR signal on emgch3: Frequency and time domain analysis of the band-pass filtered PCADR signal using the DFT, CSD, 3PT and P2T for recording emgch3. Plot 1 shows the obtained band-pass filtered PCADR signal. Plots 2 and 3 represent the DFT analysis. Plots 4 and 5 show the CSD analysis. Plot 6 shows the breaths obtained from 3PT method as red crosses. Plot 7 shows the breaths obtained from the P2T method as black circles.

data matrix can be reduced while keeping the same amount of information about the data. This can be achieved by applying the PCA analysis on the data matrix and investigating the eigenvalues. Therefore, the idea is to keep the PCs which correspond to the largest eigenvalues and thus represent a high enough percentage of the data and preserve the beat-to-beat variability which is essential in the respiration signal extraction. In order to achieve this, the cumulative sum of the eigenvalues is computed as follows:

$$cs = \sum_{j=1}^n \lambda_j, \quad (5.2)$$

where n is the total number of eigenvalues. Figure 5.21 shows the cumulative sum versus the eigenvalue number obtained after applying PCA on the data matrix of recording capno15. It is evident that by using the first 10 eigenvectors, over 95% of the dataset can be expressed. Close inspection of the red curve illustrates that the first 10 eigenvectors represent 96.87% of the data matrix for capno15. This assumption was tested on all Capnobase recordings, thus the first 10 PCs are kept for dimensionality reduction prior to applying the ICA analysis.

After applying the fastICA algorithm on the reduced data matrix it is expected to extract 10 ICs, one of which is likely to correspond to the respiration signal. Figure 5.22 shows the extracted ICs for recording capno15. In order to decide the respiratory IC, the frequency content of the ICs was investigated by applying the DFT method. Then the ICs whose frequency spectrum lies between reasonable respiration frequencies and contains a clear dominant peak is set to be the ICADR signal. Figure 5.23 shows the frequency spectra of the 10 extracted ICs. Plot 2 shows the respiration frequency close at 0.4795 Hz (29 bpm) which corresponds to the reference BR (29 bpm) of recording capno15.

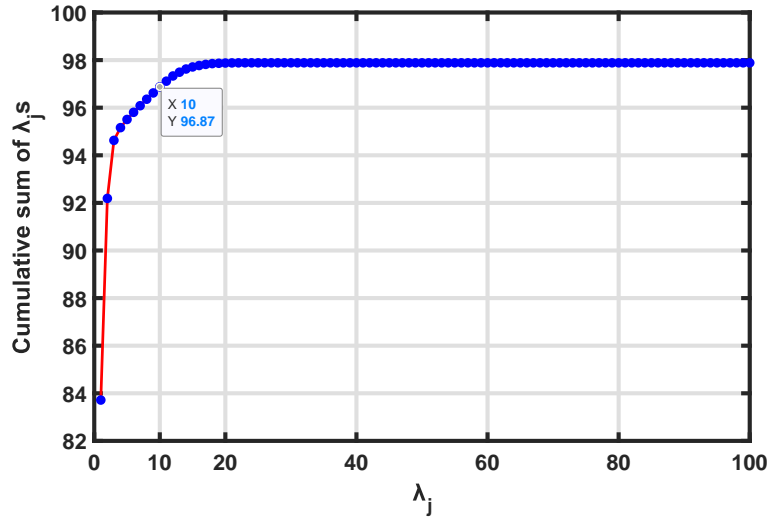


Figure 5.21: Cumulative sum of eigenvalues for recording capno15

Results

Table 5.10 illustrates our findings when applying the ICADR method on entire the recordings from Capnabase dataset and using both frequency (DFT and CSD) and time domain (3PT and P2T) estimation techniques. This table shows that the best performance is achieved by the DFT analysis. It is observed that the worst performance is achieved by the 3PT method. This can be explained by the fact that the extracted ICADR signal from the Capnabase dataset is smooth but the 3PT technique identifies extra breaths which are not meant to be counted as breaths. Nonetheless, the P2T method which imposes a number of conditions for the breath detection achieves a lower average MAE. Similar behaviour to the CSD analysis for PCADR and EDR when applied to the Capnabase recordings is also pointed out when using the proposed ICADR.

Figure 5.24 illustrates the frequency and time domain analysis of the ICADR

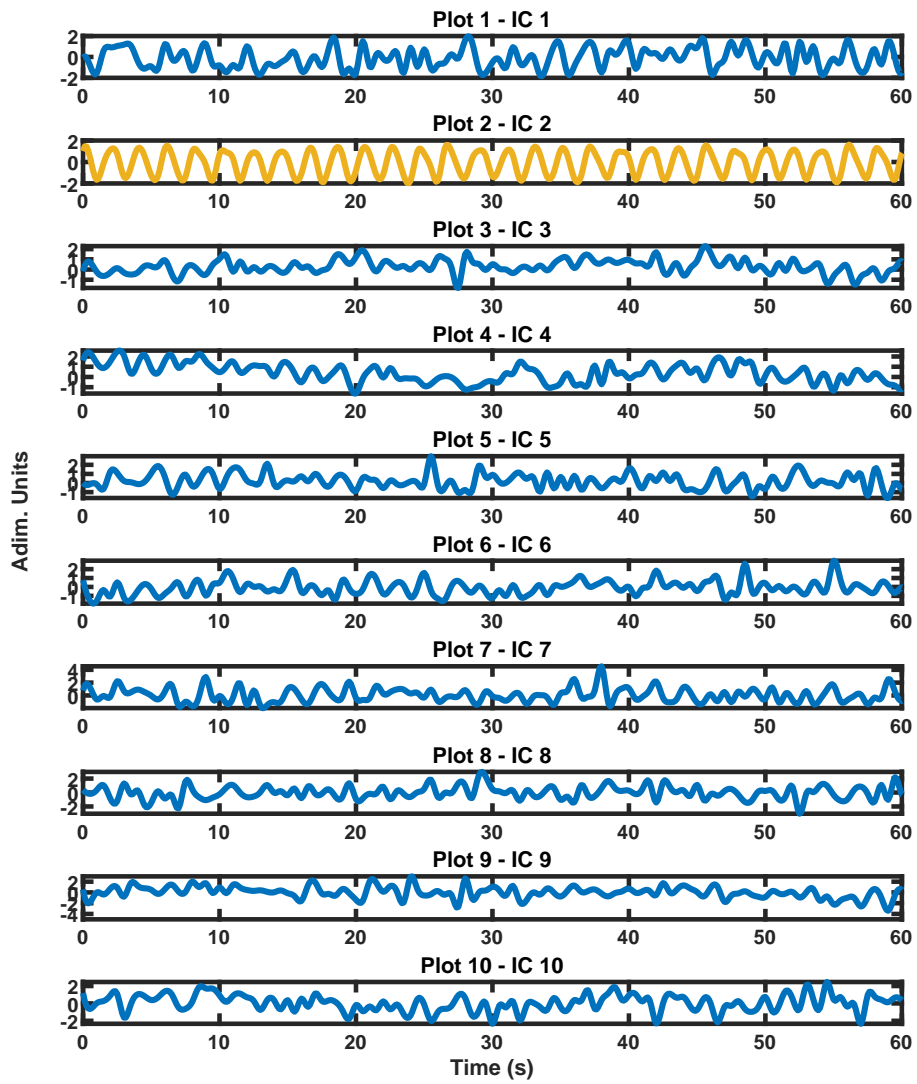


Figure 5.22: Extracted ICs for recording capno15: Plots 1 to 10 shows the 10 ICs extracted from the reduced data matrix of recording capno15. Plot 2 (yellow curve) illustrates the respiration signal.

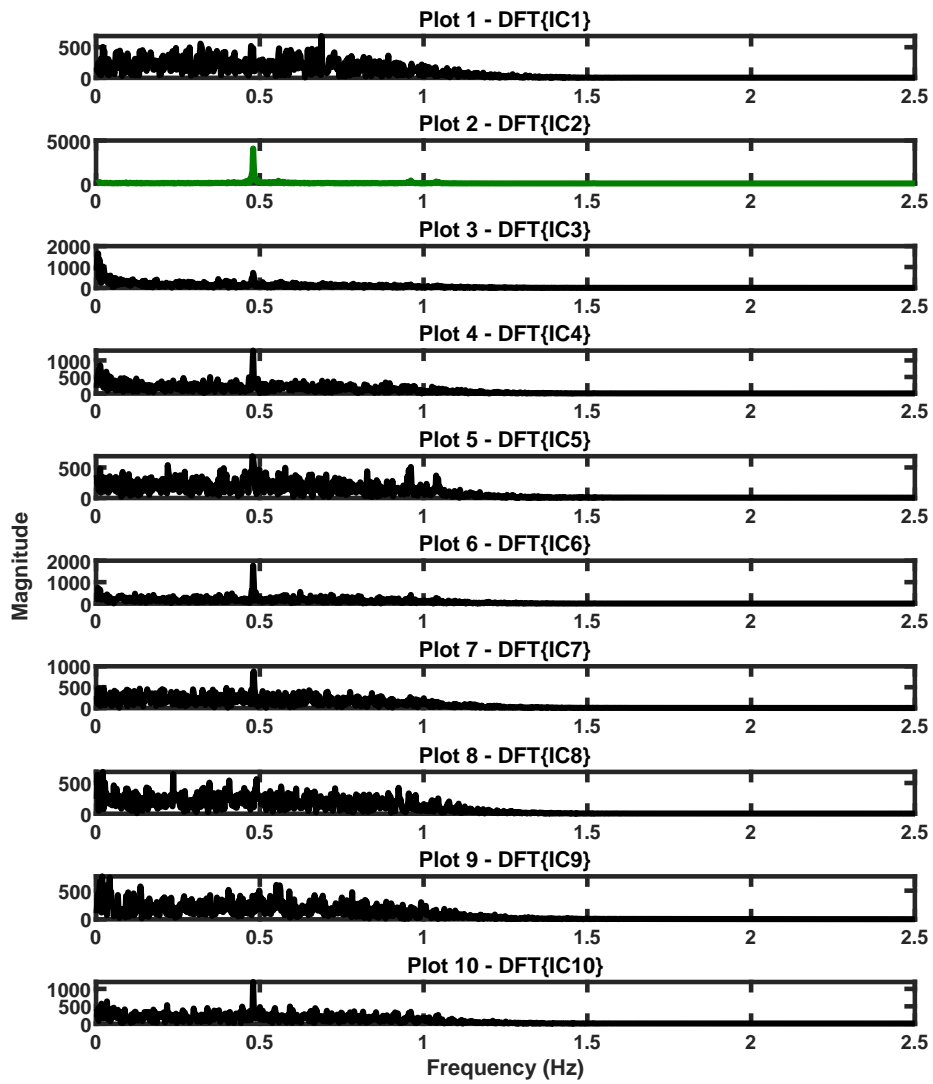


Figure 5.23: Frequency content of the extracted ICs for recording capno15: Plots 1 to 10 show the frequency spectra of the 10 ICs extracted from the reduced data matrix for recording capno15 (DFT points = 120). Plot 2 (green curve) illustrates the frequency spectrum of the respiration signal.

Record	MAE_{DFT} (bpm)	MAE_{CSD} (bpm)	MAE_{3PT} (bpm)	MAE_{P2T} (bpm)
capno9	0.38	0.38	3.50	0.75
capno15	0.00	0.00	0.25	0.00
capno16	0.00	0.00	25.50	5.38
capno18	1.38	5.13	8.63	1.88
capno23	0.50	0.38	5.75	1.13
capno32	1.00	3.50	13.63	4.38
capno35	1.86	2.00	13.00	1.57
capno38	1.75	1.75	9.50	1.88
capno103	0.00	0.00	10.12	0.63
capno104	0.00	0.00	15.13	0.88
capno105	0.02	0.02	8.38	1.88
capno121	0.01	0.01	9.25	2.25
capno122	0.00	0.13	16.63	8.50
capno125	0.25	3.63	12.38	6.00
capno127	0.50	0.50	6.13	0.75
capno128	0.38	0.25	11.88	4.88
capno134	0.50	0.50	11.13	4.25
capno142	0.14	0.01	16.38	4.00
capno147	5.38	8.25	17.88	8.75
capno148	0.01	1.13	17.38	8.50
capno311	0.88	1.63	11.13	3.63
capno312	0.00	0.00	10.00	4.38
capno313	0.00	0.00	7.88	0.75
capno322	0.63	0.75	3.25	1.13
capno325	0.13	0.00	14.75	5.50
Average	0.63	1.20	11.18	3.35
CI	± 2.26	± 4.00	± 10.92	± 5.32

Table 5.10: Capnabase dataset: ICADR performance

signal for recording capno15. The reference BR is 29 bpm (0.4795 Hz). It is spotted that the most dominant peak in both respiratory windows for DFT and CSD analysis is at 0.4795 Hz. Regarding the time domain estimation, for capno15 both the 3PT and P2T methods identified 29 breaths for the first two one minute windows, which is the same as the reference BR.

In summary, the proposed ICADR method shows comparable to EDR performance and it behaves better when a classic DFT analysis is applied on the respiratory one minute windows. After having investigated deterministic and statistical feature-based methods for the BR estimation, the next section will discuss the proposed filter-based EMD method which is based on the age and the condition of the patient.

5.2.5 EMD-Derived Respiration (EMDDR)

This section discusses a filter-based method which makes use of the EMD algorithm in order to extract the oscillatory modes of the ECG signal. The selection of the respiration signal is based on the spectral content of the IMFs extracted. The EMDDR method has been previously discussed in Section 3.1.5. To reemphasize, the EMD algorithm is applied on the ECG signal in order to extract its IMFs (oscillatory modes), and then the Fourier transform of each IMF is computed and the IMF whose frequencies lie between reasonable respiration frequencies is set to be the EMDDR signal. In order to improve the accuracy of this method, prior to estimating the BR, the EMDDR signal is processed by a band-pass filter whose cut-off frequencies depend on the age and condition of the patient.

However, because the EMD can extract a large number of IMFs depending on how many oscillatory modes the signal contains, the identification of the IMF that

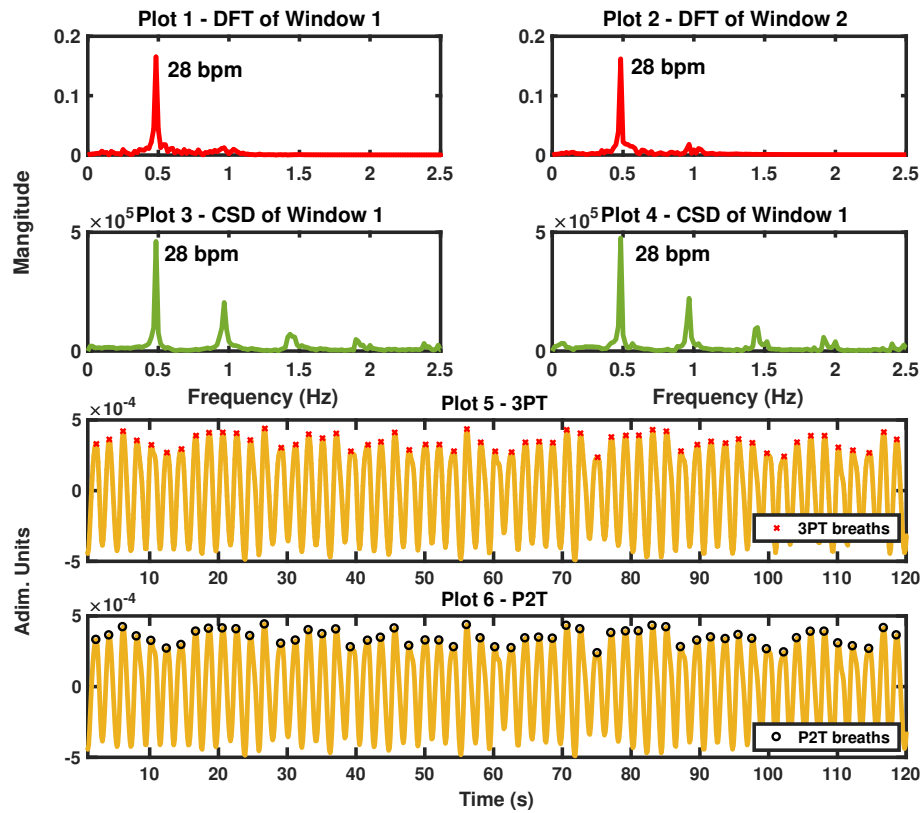


Figure 5.24: FD and TD analysis of the ICADR signal on capno15: Frequency and time domain analysis of the band-pass filtered ICADR signal using the DFT, CSD, 3PT and P2T for recording capno15. Plots 1 and 2 represent the DFT analysis. Plots 3 and 4 show the CSD analysis. Plot 5 shows the breaths obtained from 3PT method as red crosses. Plot 6 shows the breaths obtained from the P2T method as black circles.

corresponds to the respiration signal is hard. As such, we propose additional signal processing steps which will, as can be seen later, make the respiration signal the most dominant signal in the extracted IMFs. The proposed EMDDR method first processes the ECG signal using a band-pass filter, whose lower cut-off frequency is based on the BR range taking into account the age of the child and the higher cut-off frequency is based on the HR. This additional step will remove the modes related to the HR and thus shifting the respiration signal to a lower order IMF. The latter reduces the computational time because the EMD algorithm can be restricted to calculate a specific number of IMFs. Hence, it allows us not to wait to extract the full amount and then continue to the BR estimation.

Furthermore, after applying the EMD algorithm on the filtered ECG data, the respiration signal is expected to be the first IMF, which will be further processed taking into account the age and the HR of the patient. In more details the characteristics of the band-pass filter are: the lower cut-off frequency is set to 0.5 Hz (30 bpm) for children with age in range 0-1 years old, and to 0.4 Hz (24 bpm) for children with age in range 1-5 years old and the upper cut-off frequency is set at the HR. The proposed EMDDR method is summarised in Algorithm 9 and additional steps arose for this thesis are highlighted in red.

Algorithm 9: Proposed EMDDR

- 1 Locate R-peaks;
 - 2 Compute HR: $HR \leftarrow 60 \frac{1}{N-1} \sum_{i=1}^{N-1} \frac{1}{t_{R_{i+1}} - t_{R_i}}$, where N is the total number of R-peaks;
 - 3 Compute HR frequency: $HR \leftarrow \frac{HR}{60}$;
 - 4 Filter ECG within frequencies which depend on the age and HR of child;
 - 5 IMFs \leftarrow EMD(ECG);
 - 6 Filter the first IMF within frequencies which depend on the age and HR of child ;
-

Results

Tables 5.11 and 5.12 summarise the results of the proposed method. Compared to previously obtained EDR, RSA and ICADR results, EMDDR underperforms EDR and ICADR but outperforms RSA. Time domain analysis on the EMDDR signal extracted using this method, on the other hand, gives good results, suggesting that the shape of the EMDDR signal is smooth-shaped with distinct respiratory oscillations.

Figures 5.25 and 5.26 illustrate the EMD analysis of recording capno9. For simplicity only the IMFs from 7 to 11 are included because the respiratory signal is IMF 9, hence the difference between its adjacent IMFs is worth mentioning. It is observed that as the order of the IMFs decreases, the speed of the oscillations decreases. IMF 9 has a nice, smooth shape and its frequency spectrum (Figure 5.26 Plot 3) is spread around reasonable respiratory frequencies.

Figure 5.27 focuses on the frequency and time domain analysis of the EMDDR signal for capno9. Plots 2 and 3 depict the DFT spectra of the first and the second respiratory windows. The reference BR is 18 bpm and the most dominant peak of these windows is located at 0.3 Hz, which is 18 bpm. Moreover, Plots 4 and 5 show the time domain analysis, verifying similar performance of the two methods, which counted 21 and 20 breaths for each window, which is actually really close to the reference BR, but higher.

The most interesting aspect of the results obtained is that the error for recording ecgch9, whose reference BR is higher than half the HR, is drastically decreased when comparing to the other methods exploited in this chapter, suggesting that the EMDDR method could be a possible solution to overlapping frequencies. To reemphasize, Figure 5.7 shows the issue with this recording. Methods which depend

Record	MAE_{DFT} (bpm)	MAE_{3PT} (bpm)	MAE_{P2T} (bpm)
capno9	3.13	2.50	2.75
capno15	0.00	2.88	3.00
capno16	0.88	2.75	1.25
capno18	5.63	5.75	6.00
capno23	0.88	0.50	0.63
capno32	3.50	7.38	2.63
capno35	2.57	12.29	4.86
capno38	4.25	8.13	7.75
capno103	2.00	8.88	8.50
capno104	0.88	3.75	2.13
capno105	2.77	2.00	2.00
capno121	2.50	4.00	3.75
capno122	1.75	3.13	2.63
capno125	1.38	3.38	3.00
capno127	1.88	1.50	1.63
capno128	2.75	3.63	1.50
capno134	3.75	3.00	3.38
capno142	5.01	4.00	4.25
capno147	3.88	1.00	1.13
capno148	2.50	2.00	1.88
capno311	1.63	0.88	0.88
capno312	0.38	1.00	0.50
capno313	2.36	1.50	1.63
capno322	5.00	2.50	3.00
capno325	2.00	3.75	3.38
Average	2.53	3.68	2.96
CI	± 2.96	± 5.66	± 4.08

Table 5.11: Capnabase dataset: EMDDR performance

Record	MAE_{DFT} (bpm)	MAE_{3PT} (bpm)	MAE_{P2T} (bpm)
ecgch1	18	20	17
ecgch2	2	1	1
ecgch3	9	29	25
ecgch4	28	27	25
ecgch5	5	6	3
ecgch6	3	1	1
ecgch7	23	3	1
ecgch8	15	14	13
ecgch9	32	29	39
ecgch10	38	3	16
ecgch11	19	14	33
ecgch12	23	20	19
ecgch13	16	20	20
ecgch14	1	1	1
ecgch15	5	1	5
ecgch16	6	22	1
ecgch17	3	13	7
ecgch18	31	29	28
Average	15.4	14.1	14.2
CI	± 23.6	± 21.6	± 24.8

Table 5.12: ECG children: EMDDR performance

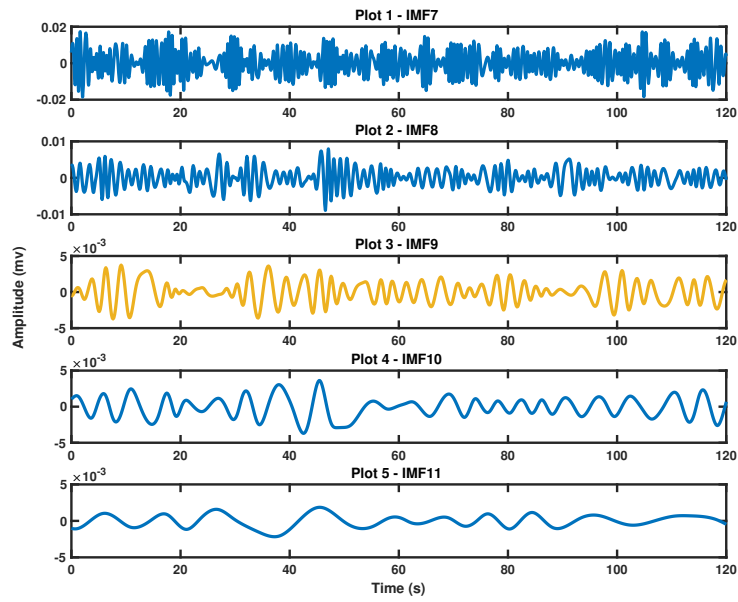


Figure 5.25: EMD analysis of recording capno9: Plots 1 to 5 show the IMFs 7 to 11 of recording capno9. Plot 3 (yellow curve) depicts the EMDDR signal.

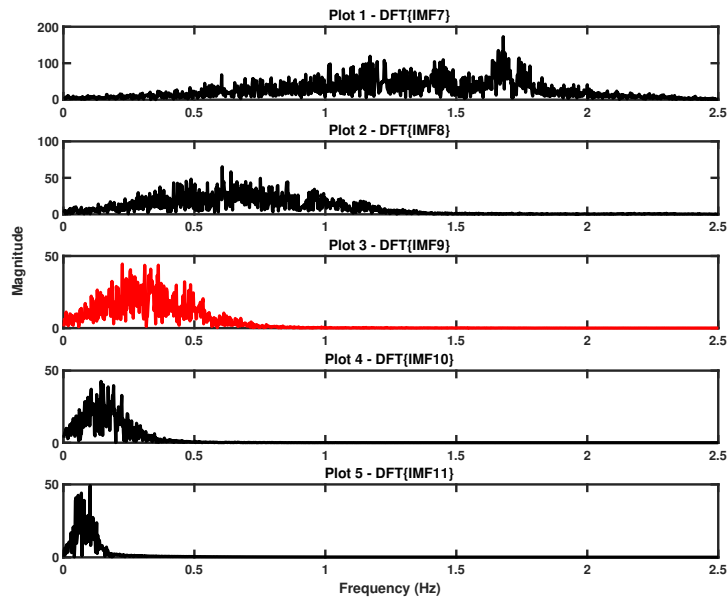


Figure 5.26: DFT analysis of IMFs of recording capno9: Plots 1 to 5 show the frequency spectra of IMFs 7 to 11 (DFT points = 12000). Plot 3 (red curve) depicts the respiratory spectrum.

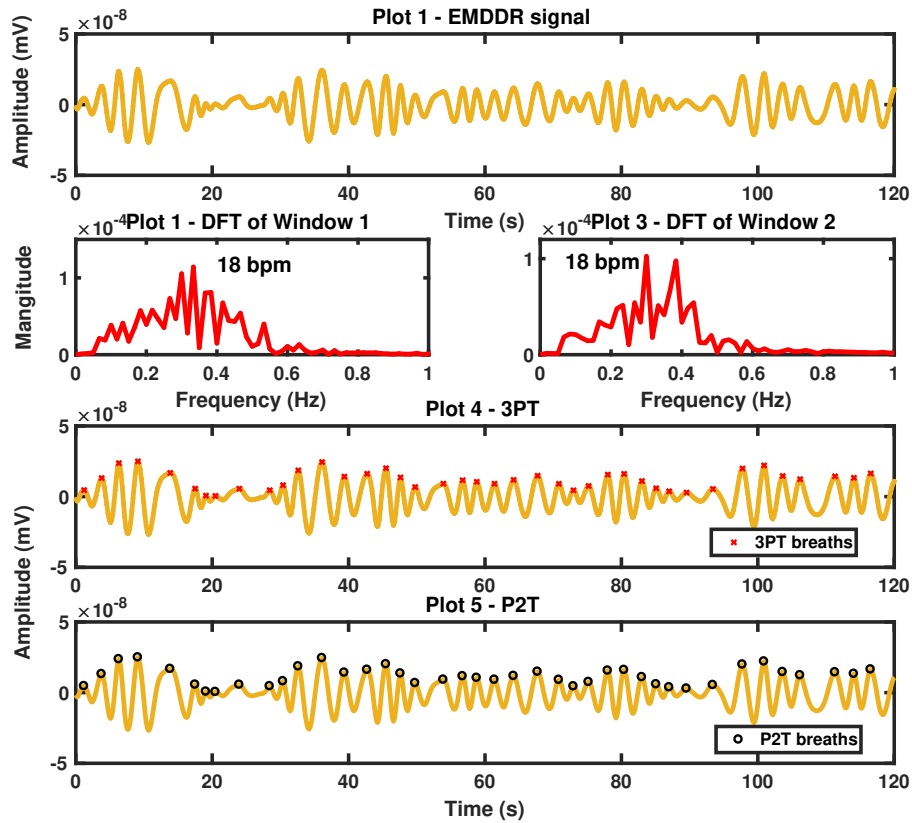


Figure 5.27: FD and TD analysis of the EMDDR signal on capno9: Frequency and time domain analysis of the EMDDR signal using the DFT (DFT points = 6000), 3PT and P2T for recording capno9. Plot 1 shows the EMDDR signal. Plots 2 and 3 represent the DFT analysis. Plot 4 shows the breaths obtained from 3PT method as red crosses. Plot 5 shows the breaths obtained from the P2T method as black circles.

on the timing of the R-peaks, such as the EDR, RSA, PCADR and ICADR, are limited by the HR frequency because the R-peaks are sampled at this rate. The EMD method extracts all the frequency bands involved in the spectrum, thus helps in identifying the IMFs which belong only to the BR. Therefore, it is a more reliable technique when the BR is higher than the Nyquist limit of the R-peaks.

Figure 5.28 shows an example of the proposed filter-based EMDDR method on recording ecgch9. The reference BR of this recording is high about 65 bpm. The EMD algorithm extracted 14 IMFs when it was applied on the raw ECG signal, whereas when applied to the band-pass filtered (BPF) ECG the number of the extracted IMFs is reduced to 8. The idea of filtering the ECG signal and then applying the EMD algorithm is to limit the range of frequencies and reduce the computational time. This can be clearly seen from Plot 1 and Plot 2 where Plot 1 shows frequencies between 5 and 30 Hz while Plot 2 shows a significantly lower frequency range between 0.5 and 0.25 Hz. A second BPF is applied on the extracted first IMF of the proposed EMDDR method in order to extract the final EMDDR signal (Plot 5). The most dominant frequencies of the EMDDR signal are around 1 Hz, corresponding to 60 bpm (Plot 6), which is very close to the reference BR of 65 bpm (Plot 6).

To conclude, the proposed filter-based EMDDR method shows promising results when applied to noisy real ECG children data and it might provide a solution to the issue of overlapping frequencies. However, further experimental investigations are needed in order to better understand the physical nature of the extracted IMFs and analyse the possible existence of novel biomedical indicators hidden in the IMFs. Moreover, the results emerged during the investigation of single feature- and filter-based methods for BR estimation on children data suggest that supplementary exploration can be done using fusion methods in order to research whether these can

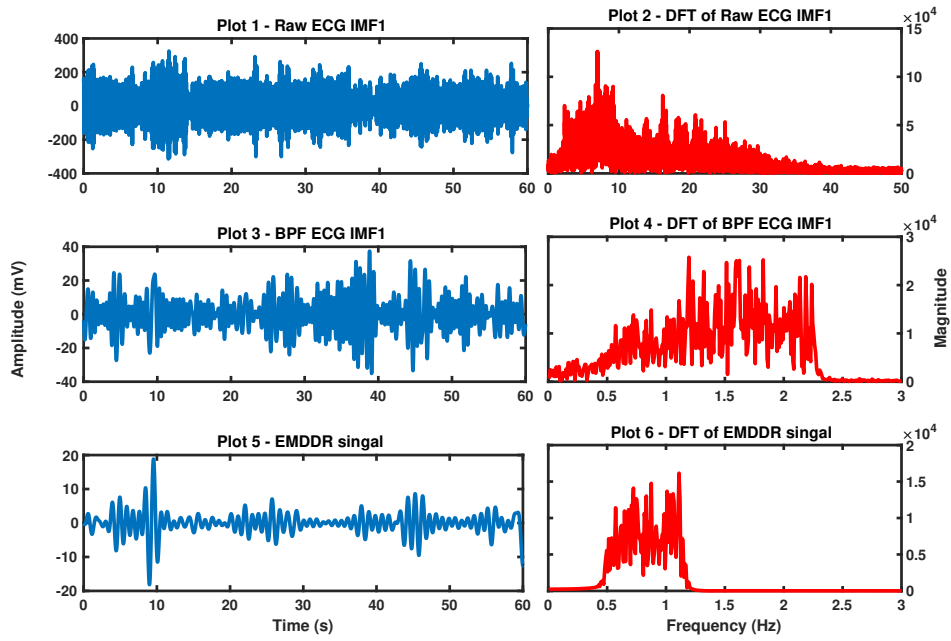


Figure 5.28: Proposed EMDDR method on ecgch2: Plot 1 shows the IMF1 of the raw ECG signal of ecgch2 and Plot 2 shows its frequency content (DFT points = 6000). Plot 3 represents the IMF1 of the BPF ECG and Plot 4 its frequency spectrum. Plot 5 shows the IMF1 of Plot 3, after applying a BPF and Plot 6 depicts its frequency spectrum.

improve the estimation accuracy. The next section, therefore, moves on to discuss data and method fusion techniques developed during this thesis.

5.3 Fusion Methods

One of the emerge directions of this research is to investigate fusion techniques and explore whether these techniques are capable of improving the BR estimation accuracy using ECG data which belong to sick children. Therefore, a data fusion technique is proposed here to improve the accuracy of the estimated BRs from single methods. In addition an enhanced method fusion technique based on (Orphanidou et al., 2013) is proposed as well. This method as discussed in Chapters 2 and 3 uses an AR model combined with a pole magnitude criterion in order to chose the final BR estimate (Algorithm 3). However, a major drawback of this technique is that the suggested model order is database-specific and there is a notable lack of empirical research where a model order estimation scheme is investigated. Our enhanced method exploits an algorithm for model order estimation which is based on the autocorrelation function of the respiration signal.

5.3.1 Data Fusion

Several studies in the literature dealing with the BR estimation have focused on method fusion techniques (Orphanidou, 2017; Orphanidou et al., 2013; Sobron et al., 2010; Nemati et al., 2010; S. G. Fleming & Tarassenko, 2007). The current literature on the other hand lacks the investigation of data fusion method to improve the accuracy of the required estimation of BR. However, data fusion has the potential of smoothing out the errors from the data, and therefore will be investigated for the first time in this work. The proposed data fusion technique first estimates the BRs

of respiratory windows whose duration is 10 sec, and then the final BR estimate is obtained by averaging over these 10 sec windows. Algorithm 10 summarises the steps of the proposed technique.

Algorithm 10: Proposed Data Fusion

- 1 Divide respiration signal into m 10 sec windows, where $m \leftarrow \frac{\text{length}(\text{respiration})}{10 \cdot f_s}$;
 - 2 For $(i:1:m)$ estimate br_i ;
 - 3 Estimate the final BR as: $\text{BR} \leftarrow \frac{1}{m} \sum_{i=1}^m \text{br}_i$;
-

Table 5.13 compares the summary statistics (average MAE) for the single methods and the proposed data fusion technique in both frequency and time domain for the ECG children data. What is interesting about these findings, is that in most cases the proposed data fusion technique improve the accuracy by reducing the error about 1.5 bpm on average. This conclusion suggests that data fusion techniques are more suitable for noisy, real data. Particularly the proposed data fusion method combined with the RSA signal processed by the P2T method achieved the best average MAE, 8.8 bpm, for the ECG children data.

The results in this section indicate that fusion techniques might be essential for the BR estimation from ECG signals which are contaminated by noise. The next section, therefore, moves on to discussing the improved AR model method fusion technique and how it affects the estimation.

5.3.2 Method Fusion

This section discusses an improvement of the pole magnitude and phase angle criterion for the method fusion technique suggested by Orphanidou et al. (2013). In Orphanidou et al. (2013) an all-pole AR model is designed for the spectral analysis of the respiration signals produced by different methods and the selection of the BR

	Single Method	Data fusion
EDR	MAE \pmCI	MAE \pmCI
FFT _(bpm)	15.2 (\pm 27.6)	11.2 (\pm 27.0)
3PT _(bpm)	9.4 (\pm 17.6)	9.8 (\pm 17.9)
P2T _(bpm)	9.8 (\pm 22.3)	9.9 (\pm 19.9)
RSA		
FFT _(bpm)	13.8 (\pm 24.0)	9.9 (\pm 23.0)
3PT _(bpm)	10.4 (\pm 18.4)	11.1 (\pm 18.5)
P2T _(bpm)	9.1 (\pm 23.1)	8.8 (\pm 22.0)
PCADR		
FFT _(bpm)	13.9 (\pm 25.7)	11.9 (\pm 24.2)
3PT _(bpm)	9.5 (\pm 19.4)	9.1 (\pm 19.2)
P2T _(bpm)	9.1 (\pm 23.0)	9.4 (\pm 22.8)
EMDDR		
FFT _(bpm)	15.4 (\pm 23.6)	13.9 (\pm 21.6)
3PT _(bpm)	14.1 (\pm 21.7)	14.2 (\pm 21.4)
PT2 _(bpm)	14.1 (\pm 24.7)	13.4 (\pm 24.1)

Table 5.13: ECG children: Single methods and Data Fusion performance comparison

poles is based on Algorithm 3 (Chapter 3). After testing models with orders ranging from 6 to 20, Orphanidou et al. (2013) selected the model order to be 8, as it gave the best results. Nonetheless, this method can be seen to be age and subject specific and hence the estimation accuracy can be affected when using a different dataset.

Therefore, a model order selection scheme is proposed in this work based on the partial autocorrelation function (PACF) of the respiration signals. The PACF gives an image of the relationship between a current value of the signal with its values at prior time steps and it is commonly used in AR model order selection (Burke, 2011). The idea is to select as model order the first lag where the PACF falls under 0.2, thus using an 80% confidence interval. Figure 5.29 shows the PACF obtained for the EDR signal of capno9. The number of lags are shown on the x -axis and the PACF values on the y -axis. The black dashed lines define the 80% confidence interval. It is

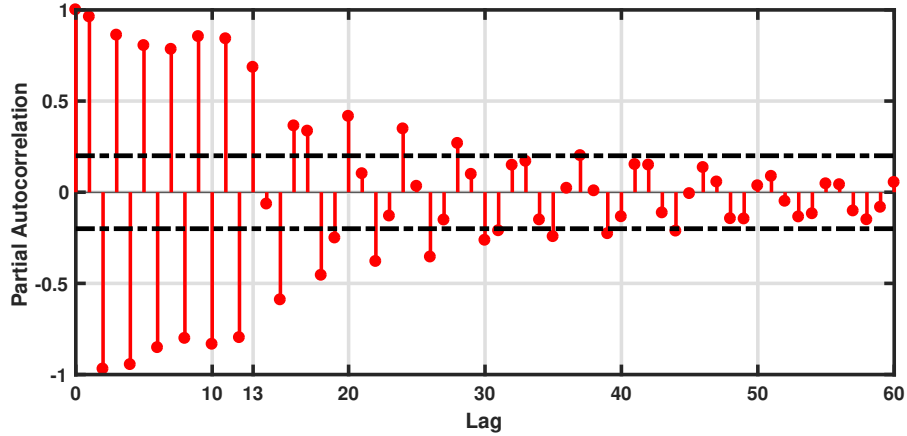


Figure 5.29: PACF of the EDR signal for capno9

observed that the model order is 13 because this is the first lag for which the PACF falls under 0.2. Algorithm 11 summarises the improved method fusion technique based on the poles magnitude and phase angle criterion of an AR model.

Algorithm 11: Improved Pole Magnitude and Phase Angle Criterion

- 1 Estimate model order p_1 : $p_1 \leftarrow \text{lag}, \{\text{lag} \mid -0.2 < \text{PACF}(\text{lag}) < 0.2\}$;
 - 2 Model respiratory signal: $\text{AR}(p_1)$;
 - 3 Calculate phase angles: θ ;
 - 4 Keep respiratory poles: $\text{poles} \leftarrow \text{poles}(0.1 \text{ Hz} < \theta < 0.6 \text{ Hz})$;
 - 5 Calculate pole magnitudes: $\text{mag} \leftarrow \sqrt{\text{Re}\{pole\}^2 + \text{Im}\{pole\}^2} s$;
 - 6 Find highest magnitude: $\text{mag}_{max} \leftarrow \max(\text{mag})$;
 - 7 Find candidate BR poles: $\text{poles}_{cand} \leftarrow \text{poles}(\text{mag} > 0.95 * \text{mag}_{max})$;
 - 8 Select BR pole: $\text{pole}_{BR} \leftarrow \text{poles}_{cand}(\min(\theta))$;
-

Results

For Capnobase dataset an AR model was designed for each respiratory signal extracted from the previously discussed methods, EDR, RSA, PCADR and ICADR. For each one minute window a pole from each signal was computed and finally only

one pole was kept as the estimated BR based on the pole magnitude and phase angle criterion. Table 5.14 shows the results obtained after applying the proposed method fusion technique on the Capnobase dataset. As can be seen, the average MAE is about 0.93 bpm which shows that the method fusion underperforms the single EDR and ICADR methods, however it overperforms the RSA and PCADR methods.

During the experiments the total number of respiratory windows produced for Capnobase was 224. The method chose 31% of the windows to get the EDR BR estimate, 6% to get the RSA, 35% to get the PCADR and 17% to get the ICADR estimate. The percentage of RSA windows was expected as it was previously discussed that the Capnobase ECG signals do not undergo FM, which is a requirement for the RSA method in order to extract the respiration signal.

Moving to the ECG children data, the EDR, RSA and PCADR signal were fused using the proposed method. Table 5.15 illustrates the results obtained after fusing the EDR, RSA and PCADR signal for the ECG children recordings. The average MAE achieved from the method fusion is 12.9 bpm, indicating a better performance compared to the frequency analysis of the corresponding single methods. Moreover, the total number of the produced respiratory window was 18. The method fusion chose 22% to be EDR windows, 6% to be RSA and 72% to be PCADR windows.

5.4 Conclusion

Returning to the main question of this chapter, the evidence from these findings suggest that the proposed enhanced BR estimation single methods, along with the fusion techniques, showed promising results for ECG children recordings provided by the Capnobase dataset. It has been observed that sensors used in the hospitalised ECG and EMG signal recordings induced noise which contaminated the frequency

Record	EDR (bpm)	RSA (bpm)	PCADR (bpm)	ICADR (bpm)	Fusion (bpm)
capno9	0.42	2.17	0.50	0.47	0.44
capno15	11.08	0.17	12.05	0.20	0.17
capno16	0.48	24.60	1.43	2.03	0.48
capno18	1.53	3.08	15.78	0.82	1.50
capno23	0.37	3.92	0.44	0.63	0.44
capno32	4.17	2.57	1.43	1.68	1.11
capno35	1.69	17.00	1.88	1.84	11.25
capno38	1.30	0.92	1.33	4.28	1.44
capno103	0.16	1.40	0.17	0.21	0.17
capno104	0.11	1.34	0.38	0.36	0.24
capno105	0.09	4.33	0.29	0.85	0.07
capno121	0.27	2.83	0.39	0.19	0.17
capno122	0.12	11.32	1.47	0.81	0.12
capno125	0.20	0.27	0.27	0.69	0.26
capno127	1.26	8.15	3.78	0.94	0.53
capno128	1.19	5.69	0.51	0.72	0.35
capno134	0.75	1.20	1.01	0.89	0.88
capno142	0.91	5.60	0.33	0.71	0.46
capno147	2.22	17.44	1.20	1.28	0.95
capno148	0.37	3.07	0.41	0.21	0.32
capno311	0.12	5.15	0.73	2.24	0.12
capno312	1.60	1.67	4.78	1.40	0.71
capno313	0.31	1.90	0.19	0.20	0.05
capno322	4.68	5.19	4.92	0.79	0.45
capno325	1.02	24.14	2.56	0.61	0.50
Average	1.46	6.20	2.33	1.00	0.93
CI	± 4.66	± 14.24	± 7.56	± 1.8	± 4.38

Table 5.14: Capnobase dataset: Method fusion

Record	EDR (bpm)	RSA (bpm)	PCADR (bpm)	Fusion (bpm)
ecgch1	5	2	8	8
ecgch2	21	10	30	21
ecgch3	27	23	9	9
ecgch4	4	3	7	4
ecgch5	9	1	20	20
ecgch6	12	10	28	28
ecgch7	25	18	2	2
ecgch8	5	6	2	6
ecgch9	45	49	65	45
ecgch10	27	25	15	15
ecgch11	0	9	8	8
ecgch12	13	13	16	16
ecgch13	18	7	15	15
ecgch14	14	10	13	13
ecgch15	13	16	6	6
ecgch16	0	8	7	0
ecgch17	13	9	9	9
ecgch18	0	7	7	7
Average	13.9	12.6	14.8	12.9
CI	± 23.6	± 22.4	± 29.6	± 21.6

Table 5.15: ECG children: Method fusion

content of the signals and thus affected the estimation accuracy.

Furthermore, during our experiments it was observed that the P2T time domain analysis technique is confused as to which peaks to count as breaths when the respiration signal belongs to a patient who has difficulty in breathing.

Moreover, it needs to be pointed out that the results presented in this section is the first attempt to further investigate CSD, when it has only been applied on PPG signals to differentiate HR and BR frequencies (Gavali & Upasani, 2015). Our findings indicate that the CSD analysis shows similar performance to the DFT, suggesting that this method can be applied also to respiration signals and accurately extract the BR.

Another major point of this work discussed in this chapter is the proposed EMDDR method, whose main advantage is that it overcomes the issue of the Nyquist limit, encountered in the feature-based methods, as the EMDDR signal is not sampled at the HR frequency, achieving a lower MAE when the reference BR is higher than half the HR.

Chapter 6

Breathing Rate Estimation from Seismocardiograms

As previously discussed in Chapters 1 and 2, this thesis sets out also to investigate the usefulness of Seismocardiogram (SCG) recordings in BR estimation. Focus is given on the SCG as it is a non-invasive, inexpensive and high-quality method for recording and analysing heart vibrations, which can be acquired using accelerometers placed on the chest of the patient (Inan et al., 2014; Zanetti & Salerno, 1991). However, there is a relatively small body of literature that is concerned with BR estimation from SCG signals (Zakeri et al., 2016; Haescher et al., 2015; Pandia et al., 2013, 2012; Reinvoio et al., 2006).

A significant advantage of using SCG is that the accelerometer can be integrated in the sensor/device that measures the ECG, enabling the simultaneous extraction of both ECG and SCG signals. This can also lead to the estimation of two respiration signals which can be later fused as a more robust BR estimation approach. Furthermore, it was discussed in Chapter 5 that the BR estimation on sick children is

quite complicated due to sensor imperfections, thus having an extra signal to extract respiration can be very advantageous in a clinical ward.

This chapter will first review standard methods for extracting the BR from an SCG signal, which were found in the literature, by evaluating them using an SCG database which belongs to healthy adults. The remaining part of the chapter will discuss a novel method developed in this thesis for the SCG BR estimation, which is based on the amplitude variations of the SCG signal due to respiration. Moreover, a filter-based method which decomposes the SCG signal using the EMD analysis and identifies the respiration component based on spectral analysis was developed during this thesis and it will be exploited on the SCG signal.

6.1 Current State of the Art Methods

This section investigates the current state of the art methods which attempt BR estimation from SCG recordings. In more details, the methods will be tested on 20 recordings from the Combined measurement of ECG, Breathing and Seismocardiograms database (CEBSDB) (García-González, Argelagós-Palau, Fernández-Chimeno, & Ramos-Castro, 2013). The SCG signals belong to healthy male and female adult volunteers, who were asked to be very still in supine position and their ages range from 19 to 30 years old. The duration of the SCG signals is 5 minutes and the sampling frequency was set at 5 kHz. A reference BR is also provided for each minute which varies from 10 to 26 bpm. The code name of the SCG adult recordings is `b00`, followed by the volunteer number. The performance of the current state of the art methods is evaluated using the MAE in bpm.

A study conducted in 2012 (Pandia et al., 2012) lists three respiration-dependent SCG features which arise from the variations in timings and intensity of the primary

heart sounds, S1 and S2 of the SCG signal. It was also made clear that R-peak identification plays a major role in SCG analysis, as the R-peak is used as a fiducial point in order to identify critical points in the SCG signal.

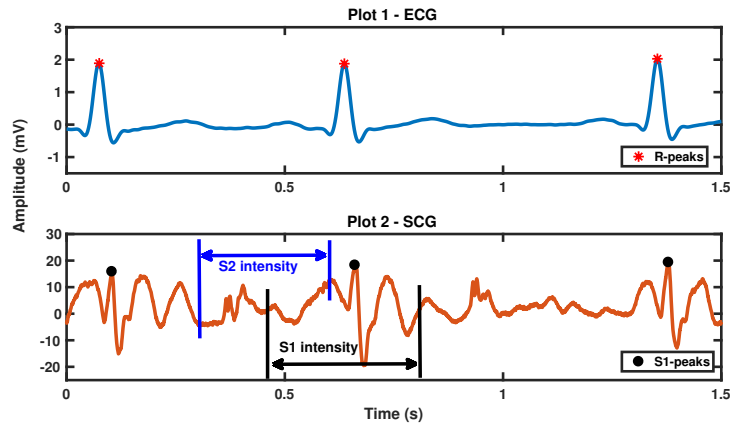


Figure 6.1: S1-peak identification on SCG: Plot 1 shows the ECG signal of subject b001, along with the detected R-peaks (red asterisks). Plot 2 shows the corresponding SCG signal, along with the identified S1-peaks (black circles). Also the time intervals for the S1- and S2-intensity are defined.

S1-S1 Interval

The first respiratory-dependent SCG feature is the S1-S1 interval, which is defined as the time interval between two consecutive S1-peaks in the SCG signal. The S1-peak is set to be the maximum amplitude of the SCG signal in a 0.1 sec time interval following the R-peak. Figure 6.1 shows a small part of the ECG signal which belongs to subject b001. For each R-peak (red asterisks in Plot 1), an S1-peak is identified in the SCG signal and it is represented by black circles in Plot 2.

The S1-S1 interval method explores the frequency modulation in the S1-peaks induced by respiration. This feature creates a discrete non-uniform time series which is sampled at the HR frequency. In order to get a uniformly sampled signal, the S1-

S1 interval time series is down-sampled at 8 Hz using cubic spline interpolation. In our implementations, the accuracy of the BR estimation is increased by processing the uniformly sampled signal by a band-pass filter, whose cut-off frequencies are at 0.0666 Hz and 0.5 Hz, reflecting the reasonable respiration frequencies for a healthy person.

After successful extraction of the filtered S1-S1 respiration signal, the latter was further processed either in the frequency (DFT) or time domain (3PT and P2T) in order to obtain the BR estimates. Table 6.1 summarises the results obtained for the CEBSDB recordings for the S1-S1 interval method. It is observed that the results obtained are quite promising especially from the time domain analysis. The best performance is achieved by the 3PT time domain analysis, giving an average MAE of 3.2 bpm.

Figure 6.2 shows the frequency and time domain analysis of the S1-S1 interval signal obtained for subject b001. The reference BR of the first two respiratory one minute windows is 24 bpm (0.4 Hz). It can be seen in Plots 2 and 3 that the most dominant frequencies are far from the reference. This can be explained by the shape of the derived respiration signal (Plot 1). It is evident that the most dominant in amplitude oscillations in the first one minute window is 8, which is equal to the most dominant frequency (0.125 Hz) in Plot 2. Similar behaviour is observed for the second window, where the number of the most dominant in amplitude oscillations is 5, which is the same as the most dominant frequency of 0.08 Hz in Plot 3. What is interesting about the frequency domain analysis is that the BR frequency (0.4 Hz) is still present. This combination of findings provides some support for the conceptual premise that S1-S1 interval method does not capture the power of the respiratory-induced modulations of the SCG signal, consequently the latter cannot be adequately

Record	MAE_{DFT} (bpm)	MAE_{3PT} (bpm)	MAE_{P2T} (bpm)
b001	16.8	3	10.2
b002	6.2	0.6	2.2
b003	0.0	1.0	0.0
b004	7.8	5.4	4.4
b005	0.0	2.4	0.6
b006	3.0	1.8	1.4
b007	1.4	10.2	5.6
b008	16.8	3	10.2
b009	1.2	6.8	1.4
b010	1.4	0.8	0.4
b011	0.8	0.6	1.4
b012	17	1.2	10.4
b013	14.6	2.2	8.8
b014	7.2	0.8	1.4
b015	11.0	2.2	6.4
b016	5.2	2.0	3.0
b017	2.4	0.4	1.8
b018	2.0	9.4	4.0
b019	2.6	0.6	1.4
b020	1.4	10.4	2.2
Average	5.9	3.2	3.9
CI	± 12.1	± 6.7	± 7.0

Table 6.1: SCG data: S1-S1 interval performance

reflected in the frequency spectrum of the respiration signal.

Regarding the time domain analysis, both methods responded better compared to DFT, however the shape of the respiration signal does not allow to clearly investigate their performance, as the most dominant in amplitude oscillations in the signal affect also the P2T method, giving a high MAE of 10.2 bpm for subject b001.

S1 Intensity, S2 Intensity

As previously mentioned in Section 6.1, additional respiration-dependent features were explored in the study conducted by Pandia et al. (2012), which are based on

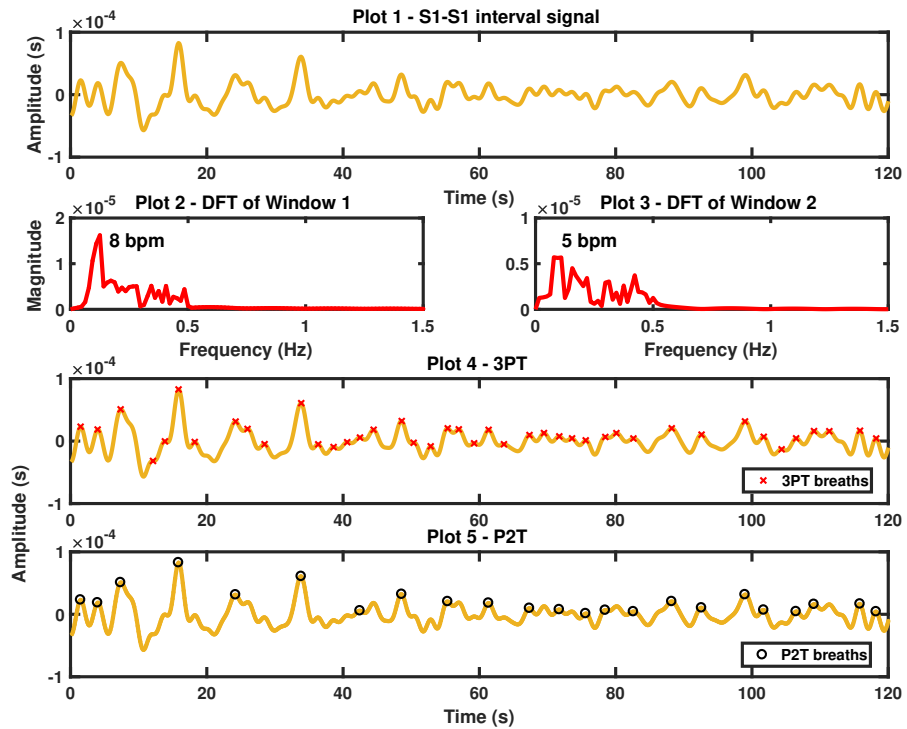


Figure 6.2: DFT and TD analysis of the S1-S1 interval signal on b001: Plot 1 shows the S1-S1 interval signal for subject b001. Plots 2 and 3 represent the DFT analysis. Plot 4 shows the breaths obtained from 3PT method as red crosses. Plot 5 shows the breaths obtained from P2T method as black circles.

the intensity of the S1 and S2 primary sounds of the SCG signal. The S1 intensity is defined as the RMS of the SCG windowed at 0.2 sec before and 0.15 sec after the S1-peak. Figure 6.1 Plot 2 defines the S1 interval used in the S1 intensity method. Similarly, S2 intensity is calculated as the RMS of the SCG windowed at 0.22 sec to 0.5 sec following the S1-peak. The S2-interval used in the S2 intensity method is also depicted in Figure 6.1 Plot 2. Moreover, the S1/S2 intensity ratio was calculated as a respiratory-measure which can extract respiration from the SCG signal.

The aforementioned features extract a discrete non-uniform time series which is sampled at the HR frequency. Therefore, these time series are interpolated and down-sampled at 8 Hz, in order to get uniformly sampled respiration signals. Furthermore, in order to increase the accuracy of the BR estimation the uniformly sampled signal is further processed by a band-pass filter, whose cut-off frequencies are at 0.0666 Hz and 0.5 Hz.

Tables 6.2, 6.3 and 6.4 illustrate the results obtained from the S1, S2 intensity, along with their ratio (S1/S2 intensity). The intensity methods were further processed in the frequency (DFT) and the time domain (3PT and P2T) for the final estimation of the BRs. As can be seen from these tables the intensity methods outperform the S1-S1 interval method. In accordance with the present results, the study of Pandia et al. (2012) demonstrated the superiority of the intensity methods. The best performance is achieved by the frequency domain analysis of the S2 intensity respiration signal, giving an average MAE of 1.6 bpm.

Figure 6.3 demonstrates in Plots 1 to 3 the S1, S2 and S1/S2 intensity signals obtained for subject b001, respectively. It is apparent that these signals capture more adequately the respiratory oscillations, compared to the S1 interval signal (Figure 6.2 Plot 1), meaning that the amplitude of the non-respiratory oscillations does not

Record	MAE_{DFT} (bpm)	MAE_{3PT} (bpm)	MAE_{P2T} (bpm)
b001	10.0	1.8	3.4
b002	0.6	2.4	1.0
b003	0.0	0.6	0.2
b004	2.2	7.0	2.2
b005	0.0	2.8	0.8
b006	3.0	6.2	1.8
b007	1.6	6.6	3.2
b008	10	1.8	3.4
b009	1.2	12.0	2.4
b010	1.8	6.0	1.2
b011	0.2	4.4	1.0
b012	15.6	1.2	4.8
b013	2.6	0.6	0.6
b014	0.4	2.4	1.2
b015	1.0	0.4	0.8
b016	5.8	5.4	2.0
b017	0.3	0.4	0.8
b018	4.4	12.8	4.2
b019	1.0	1.0	0.6
b020	0.6	9.0	1.4
Average	3.1	4.2	1.9
CI	± 8.4	± 7.6	± 2.6

Table 6.2: SCG data: S1 Intensity performance

Record	MAE_{DFT} (bpm)	MAE_{3PT} (bpm)	MAE_{P2T} (bpm)
b001	3.2	1.4	2.2
b002	0.4	2.0	0.6
b003	1.6	4.2	1.8
b004	0.2	6.0	2.0
b005	0.0	1.0	0.6
b006	1.4	6.6	2.4
b007	1.4	6.0	2.4
b008	3.2	1.2	2.2
b009	6.0	15.6	7.2
b010	1.0	4.6	1.0
b011	0.0	1.8	0.6
b012	2.2	0.6	3.0
b013	0.6	0.8	0.8
b014	1.2	3.4	1.4
b015	1.0	0.6	0.6
b016	3.4	4.8	3.4
b017	0.2	0.4	0.6
b018	3.4	10.0	3.0
b019	1.6	0.8	0.6
b020	0.8	8.0	4.4
Average	1.6	4.0	2.0
CI	± 3.1	± 7.8	± 3.3

Table 6.3: SCG data: S2 Intensity performance

Record	MAE_{DFT} (bpm)	MAE_{3PT} (bpm)	MAE_{P2T} (bpm)
b001	1.6	1.8	2.6
b002	1.2	2.8	0.8
b003	0.2	3.6	1.2
b004	3.0	6.8	1.4
b005	0.0	2.8	1.0
b006	2.4	5.4	1.8
b007	0.4	6.0	2.0
b008	1.6	1.8	2.4
b009	1.6	13.4	4.6
b010	1.6	3.4	1.8
b011	0.4	3.6	1.0
b012	6.6	1.0	4.8
b013	2.6	0.6	0.6
b014	3.6	4.0	1.8
b015	0.8	1.0	0.8
b016	4.8	6.0	2.6
b017	0.2	0.6	0.4
b018	1.6	11.6	5.8
b019	1.8	1.6	1.0
b020	0.2	10.2	3.0
Average	1.8	4.4	2.1
CI	± 3.4	± 7.4	± 3.0

Table 6.4: SCG data: S1/S2 Intensity performance

overlap the power of the respiratory ones. This is also reflected in the frequency spectrum of the three respiration signals, which is shown in Figure 6.3 Plots 4 and 5. The reference BR of the first two respiratory windows is 24 bpm (0.4 Hz). As can be seen the most dominant frequencies of the S2 intensity spectrum are at 0.4 Hz. The same applies for the S1/S2 intensity spectrum, a finding which is expected as this signal is affected by the S2 intensity, thus its performance is expected to be similar.

Regarding the time domain methods, it is observed that for the intensity signals the P2T analysis provides the best results, compared to the 3PT analysis. However, the best performance is still achieved by the DFT analysis of the S2 intensity signal. The observed increased MAE of the 3PT analysis can be attributed to the fact that the latter identifies as breaths all maxima present in the respiration signal, returning a higher BR.

6.2 Advanced Methods

Thus far, previous studies have focused on feature-based techniques in order to extract the BR from an SCG signal, by analysing the frequency (S1-S1 interval) and intensity (S1, S2, S1/S2 intensity) modulations in the SCG induced by respiration. What it is not investigated in the current literature is the impact of respiration on the amplitude of the S1-peaks. Therefore, an obvious effect will be investigated for the first time in this thesis.

Furthermore, an obvious disadvantage of feature-based BR estimation methods is that they require the identification of both the R- and S1-peaks, which can introduce delays in the estimation and increase the computational cost. Thus, the need for a filter-based technique which does not demand the detection of the S1-peaks is evident. Consequently, the exploitation of the EMD method for the extraction of

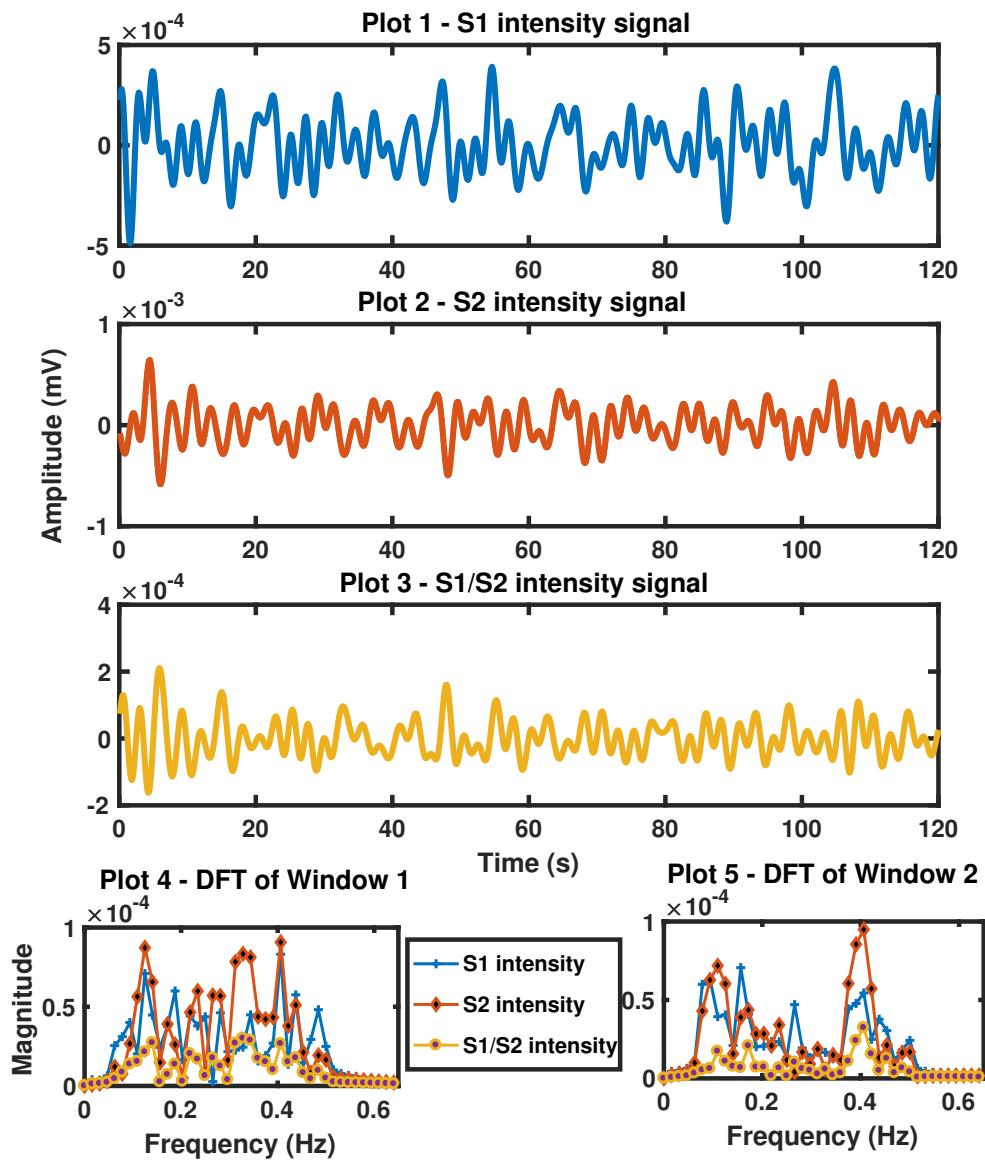


Figure 6.3: DFT analysis of the intensity methods on b001: Plots 1 and 2 show the S1 and S2 intensity signals, respectively. Plot 3 depicts the S1/S2 intensity signal. Plot 4 shows the DFT analysis of the three methods for the first respiratory window, where Plot 5 gives the corresponding information for the second respiratory window.

respiration signals from SCG recordings will be explored for the first time in this thesis.

AM in SCG

This method takes advantage of the Amplitude Modulation (AM) of the S1-peaks over time, assuming that these modulations are induced by respiration. The S1-peaks are detected with respect to the locations of the R-peaks, as described previously in Section 6.1. Then the amplitude of the S1-peaks is computed and kept for further processing. The AM feature produces a discrete non-uniform time series which is sampled at the HR frequency. Therefore, the time series are interpolated and then down-sampled at 8 Hz, in order to get a uniformly sampled respiration signal. Finally, the respiration signal is filtered within reasonable respiration frequencies (0.0666 - 0.5 Hz).

The AM S1 signal is further investigated in both frequency and time domains in order to extract the BR. Table 6.5 summarises the results obtained for the CEBSDB data using the proposed method. It is observed that the best performance is achieved by the DFT analysis of the AM S1 respiration signal, giving an average MAE of 3.2 bpm. It is interesting to note that these results are very close to the ones obtained from the S1 intensity signal. A possible explanation for this might be that both methods are taking advantage of the amplitude information of either the S1-peak or its RMS values over a prespecified interval. However, the proposed method is computationally less intensive as it does not require further processing to calculate RMS values and at the same time achieves similar accuracy.

Figure 6.4 shows the DFT analysis of the first two respiratory windows of the AM S1 signal for subject b001. The reference BR of these windows is at 24 bpm (0.4 Hz).

Record	MAE_{DFT} (bpm)	MAE_{3PT} (bpm)	MAE_{P2T} (bpm)
b001	4.4	1.4	4.8
b002	1.2	5.0	1.8
b003	0.0	0.2	0.2
b004	6.8	8.4	2.2
b005	8.6	6.6	2.8
b006	5.4	7.6	2.8
b007	1.6	7.8	3.2
b008	4.4	1.4	4.6
b009	4.2	13.8	5.6
b010	1.6	7.2	2.6
b011	0.4	3.0	3.2
b012	3.6	1.6	3.2
b013	8.4	1.0	3.8
b014	1.4	2.0	0.8
b015	1.0	2.6	1.0
b016	1.6	5.2	3.8
b017	0.2	0.6	0.8
b018	2.4	10.6	5.4
b019	6.0	1.0	2.8
b020	1.4	9.2	4.2
Average	3.2	4.8	3.9
CI	± 5.4	± 7.8	± 3.1

Table 6.5: SCG data: S1 AM performance

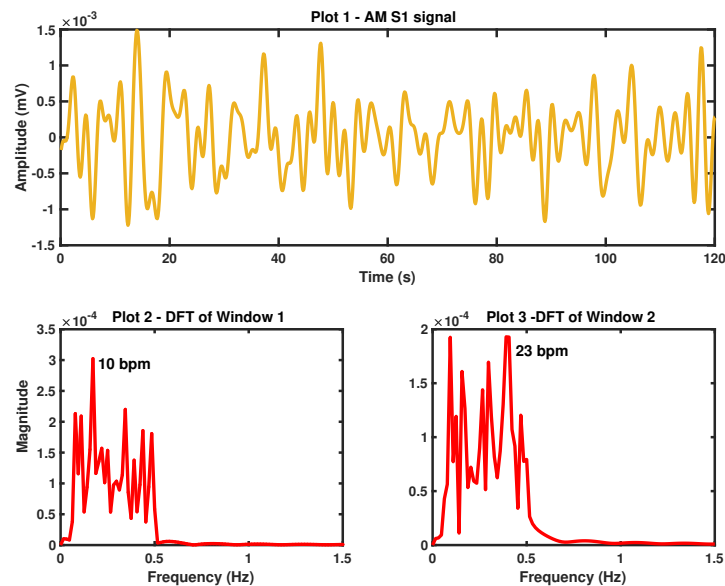


Figure 6.4: DFT analysis of the AM S1 signal on b001: Plot 1 shows the obtained AM S1 signal. Plots 2 and 3 depict the DFT analysis of the first two respiratory windows.

It can be seen from Plot 2 that the most dominant peak is at 0.1667 Hz (10 bpm), which is quite far from the reference. This can be possibly justified by the shape of the obtained respiration signal in the first 60 sec, where the slower oscillations seem to be more prominent in amplitude, compared to the fast ones which are related to respiration.

EMDDR

It has been previously discussed that the EMD method can possibly extract signals which are hidden in an observed signal, such as the ECG. Therefore, it has been suggested as a method for the extraction of the respiration signal in Section 5.2.5. The accelerometers, used in the SCG signal acquisition, are usually located on the

subject's chest, thus the respiration signal is expected to be embedded in an SCG signal. Therefore, the EMD method is proposed here as a potential approach to extract the respiration signal from the SCG signal. Firstly, the IMFs of the SCG signal are obtained after applying the EMD method. The selection of the respiratory IMF is then based on a spectral analysis. The IMF whose frequencies lie between reasonable respiration frequencies is set to be the EMDDR signal. The frequency spectrum of the respiratory IMF (IMF 17) of subject b001 is shown in Figure 6.5 Plot 3. It is also shown that the spectrum has a dominant frequency which lies between 0.0666 Hz and 0.5 Hz (Plot 4), which are the normal respiration frequencies for a healthy person. Moreover, it can be observed that the dominant frequency of IMF 17 is more distinct, compared to the frequency peaks of IMFs 16 and 18 (Plots 2 and 6).

The EMDDR signal extracted for the CEBSDB data were further processed by the DFT analysis and the time domain methods (3PT and P2T). The results are summarised in Table 6.6. The overall response of the EMDDR method on the SCG is very promising, as it outperforms all the state of the art and the proposed in this work AM S1 method, achieving a low average MAE of 1.5 bpm for the DFT analysis. This is an interesting finding which can be explained by the fact that this method does not depend on the S1-peaks, whose identification is not well defined, as there is a lack of studies which clarify their detection.

Figure 6.6 illustrates the DFT and time domain analysis of the EMDDR signal obtained for subject b001. The reference BR of the first two respiratory windows is 24 bpm (0.4 Hz). It is evident from Plots 1 and 2 that the most dominant spectral peak is located at 0.4 Hz (24 bpm), achieving a low error for these windows.

Overall, the present results on the EMDDR method using SCG data are encour-

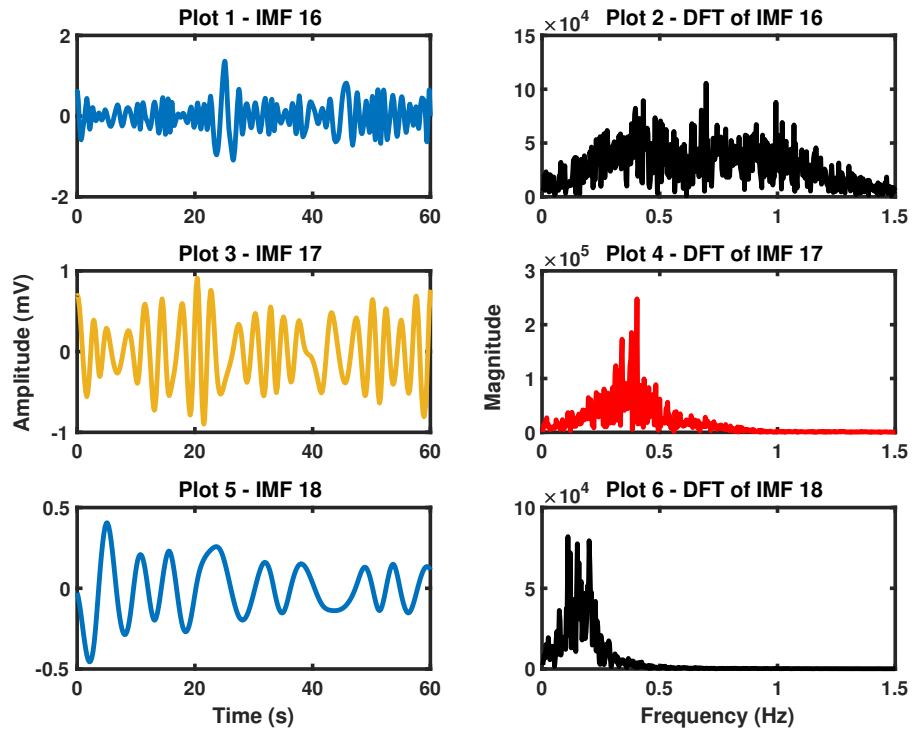


Figure 6.5: DFT analysis of the IMFs of b001. Plots 1, 3 and 5 depict the IMFs 16, 17 and 18, respectively. Plots 2, 4 and 6 show the corresponding spectra (DFT points = 300000). Plot 3 is the EMDDR signal (yellow curve) whose frequency spectrum is shown in Plot 4 (red curve).

Record	MAE_{DFT} (bpm)	MAE_{3PT} (bpm)	MAE_{P2T} (bpm)
b001	0.6	2.6	2.6
b002	1.2	1.6	1.6
b003	0.2	7.6	6.2
b004	1.6	2.6	2.4
b005	0.6	2.0	2.0
b006	2.2	21.4	21.4
b007	2.4	9.0	9.0
b008	0.6	2.6	2.6
b009	0.8	1.0	0.8
b010	1.6	1.8	1.4
b011	2.6	3.0	3.0
b012	3.4	3.4	3.4
b013	1.4	3.8	3.8
b014	0.2	2.8	2.8
b015	1.6	2.0	2.0
b016	4.4	4.0	3.8
b017	0.0	1.0	1.0
b018	3.6	4.0	4.0
b019	0.2	4.2	4.2
b020	0.8	5.0	4.6
Average	1.5	4.3	4.1
CI	± 2.5	± 9.0	± 9.0

Table 6.6: SCG data: EMDDR performance

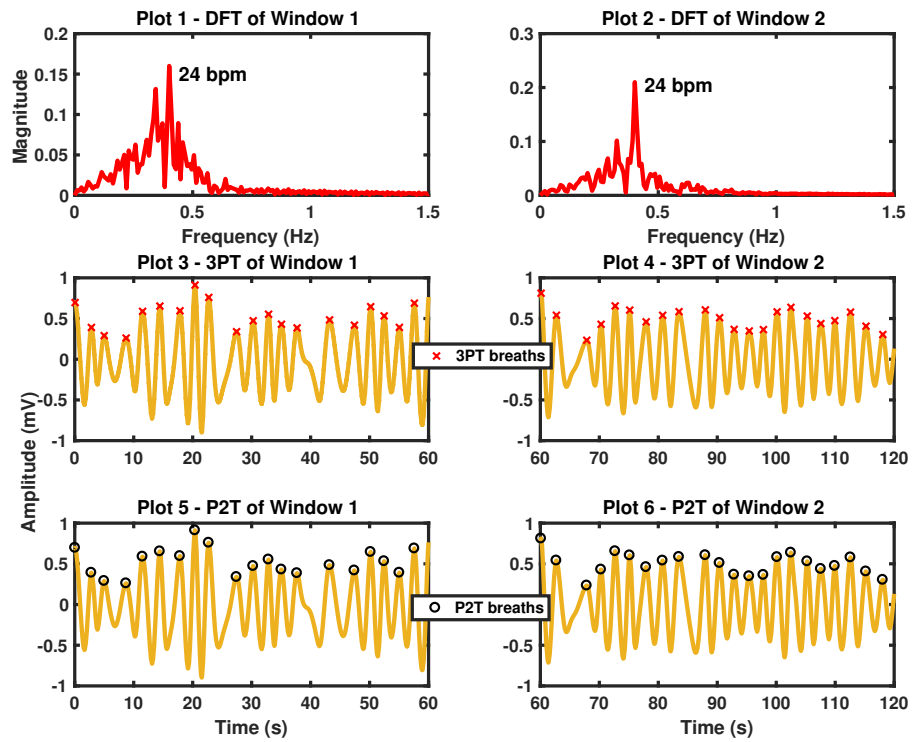


Figure 6.6: DFT and TD analysis of the EMDDR signal of b001: Plots 1 and 2 depict the DFT analysis of the first two respiratory windows (DFT points = 300000). Plots 3 and 4 show the identified breaths (red crosses) by the 3PT analysis. Plots 5 and 6 represent the identified breaths (black circles) by the P2T analysis.

aging and significant in at least two major respects: (1) the proposed method does not involve the detection of the S1-peaks, consequently the identification of the R-peaks is not needed, making the BR estimation less computationally expensive and less exposed to R-peak detection artefacts and, (2) the EMDDR method does not require the re-sampling of the respiration signal as the latter is uniformly sampled at the SCG sampling frequency. Moreover, the results of this section indicate that further investigations can be done in order to improve the BR estimation from the SCG data. The next section, therefore, moves on to discussing the application of fusion techniques on the SCG signals.

6.3 Method Fusion in SCG

This section focuses on the fusion of the S1-S1 interval, S1, S2 and S1/S2 intensity and the AM S1 methods, which were reviewed in Sections 6.1 and 6.2. These methods will be fused using the proposed fusion technique presented in Section 5.3.2 Algorithm 11. For each respiration signal an AR model is designed, whose order is based on the PACF of the respiration signal. For each respiratory one minute window a pole from each signal is computed and finally only one pole is kept as the estimated BR based on the pole magnitude and phase angle criterion.

The results obtained from the AR-based method fusion are illustrated in Table 6.7. The statistical analysis reveals that the method fusion achieved a low MAE of 1.5 bpm, which outperforms the single intensity and AM S1 methods. Furthermore, during the experiments it was observed that the total number of respiratory windows produced for the CEBSDB data is 100. The method chose 40% of the windows to get the S2 intensity estimate, 25% to get the S1 intensity, 16% to get the S1/S2 intensity, 11% to get the AM S1 estimate and 8% to get the S1-S1 interval estimate.

Record	MAE_{method fusion} (bpm)
b001	2.4
b002	1.6
b003	0.2
b004	1.2
b005	0.4
b006	2.4
b007	1.2
b008	2.4
b009	1.4
b010	0.8
b011	0.6
b012	1.4
b013	2.4
b014	1.8
b015	1.0
b016	3.4
b017	0.6
b018	2.8
b019	1.2
b020	0.6
Average	1.5
CI	± 1.8

Table 6.7: SCG data: Method Fusion performance

This observation is also illustrated in Figure 6.7. This also accords with our earlier observations for the intensity and S1-S1 interval methods, which showed that intensity methods outperform the S1-peak time variation method, which is consistent to the study of Pandia et al. (2012). Therefore, the method fusion correctly selects more BR estimates extracted by the intensity methods.

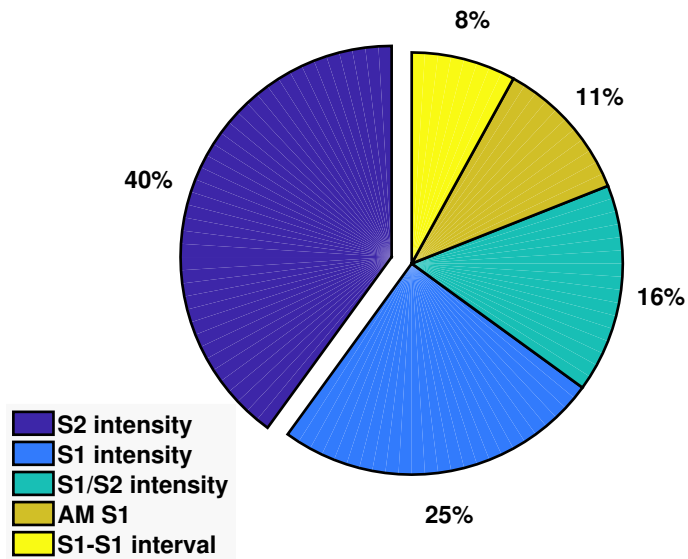


Figure 6.7: Distribution of respiratory windows based on method fusion

6.4 Conclusion

To summarise, one of the main aims of this thesis is to develop novel methods for extracting the BR from SCG signals. This chapter has provided a deeper insight into SCG BR estimation, suggesting that the proposed EMDDR method showed the most encouraging results, giving an average MAE of 1.5 bpm. It is also important to point out that no attempt has been made to investigate the application of the EMD method on SCG data. The latter can be a good starting point for identifying new biomarkers related to cardiopulmonary system by analysing the extracted IMFs of the SCG signal. Furthermore, this is the first study which exploits the AR-based method fusion on raw SCG data, suggesting that fusion of the intensity methods can provide accurate BR estimates from the SCG signal.

Chapter 7

Respiratory Distress Estimation from the ECG

This chapter focuses on one of the primary aims of this thesis which is the investigation of the potential correlation of the ECG signal with respiratory distress. The WOB, which has been used in respiratory distress estimation, is a significant indicator of a patient's respiratory status (Addison, 2016b; Cohen & Schwartz, 2013). The key finding of this chapter, which also highlights this thesis contribution to the respiratory distress estimation, is the correlation between the changes in R-to-S (RS) amplitude and the WOB over a respiratory cycle. This idea stems from the amplitude modulation in the ECG signal induced by respiration and it will be later elaborated in this chapter. The aforementioned association helped us develop an ECG-based measure for assessing the WOB in real-time.

The first section focuses on the clinical interpretation of the WOB and its importance in patients monitoring. The second section discusses the reference WOB data which will be used for the performance evaluation of the proposed measure. The

third section illustrates some preliminary results obtained when using as a WOB measure the R-peak amplitude variability over respiratory cycles. The developed WOB measure based on the RS amplitude will be discussed in the fourth section of this chapter.

7.1 Work-of-Breathing (WOB)

WOB is a key parameter in a hospital environment, especially on paediatric and neonatal wards, which is used by skilled nurses in order to assess the effort expended by a patient during breathing (Ahrens, 1993; Cohen & Schwartz, 2013). As previously discussed in Chapter 2, the assessment of the WOB can be beneficial for optimising the mechanical ventilation process in a hospital ward, regulating the amount of ventilation needed, indicating weaning from ventilation and to which extent, and also defining a suitable ventilation support.

Generation of airflow into the lungs during normal breathing is produced by contraction of respiratory muscles, such as the diaphragm and intercostal muscles. Moreover, the power produced by these muscles is proportional to the negative pressure (product of contraction of the respiratory muscles during inspiration) in the pleural space, which is the space between the inner walls of the thoracic cavity and the lungs. It has been observed that a more negative pressure within the pleural space, an increased load for the respiratory muscles, can be associated with a number of diseases. The resulting respiratory distress (increased WOB) can be related to a number of respiratory diseases such as asthma or lung oedema (Cohen & Schwartz, 2013; Ketai & Godwin, 1998). The identification of an evolving WOB allows clinicians to escalate patient care and introduce interventions, such as positive pressure ventilation.

In children where the chest bones, soft tissues and cartilages are softer, compared to adults, when respiratory distress develops, subcostal and intercostal retractions are observed (Baram & Richman, 2010). Hence the clinical estimation of WOB is subjective and can lead to false diagnostic conclusions. The latter is really critical as the level of increased WOB is one of the three most important clinical parameters to evaluate the respiratory system in a paediatric clinical, with other two being the BR and the oxygen saturation of the blood (Duncan, Hutchison, & Parshuram, 2006).

7.2 BCH data and reference WOB

The assessment of increased WOB will be explored on the previously used BCH ECG children recordings discussed in Chapter 5, which were collected in 2015-2017 at the Birmingham Children's Hospital using the Lifetouch Device (Isansys Lifecare Ltd, Oxford). Moreover, the developed measures will be also evaluated on the BCH EMG data. Nurses evaluated the level of WOB according to the BCH policies and as described in the Paediatric Early Warning Score (PEWS) system (Duncan et al., 2006). This is based on the presence and severity of clinical signs of respiratory distress such as subcostal-, intercostal-recessions and tracheal tug, which are defined as inward movements of the lower sternum, the soft tissues between the ribs and the soft tissues between the trachea and the upper edge of the sternum, respectively. Depending on deviation of the respiratory distress from normal, points ranging from 0 to 4 are allocated to each patient, as shown in Table 7.1. Additional information are also provided in Appendix F.

Respiratory Distress Deviation	PEWS Score
Normal	0
Mild	1
Moderate	2
Severe	3
Extremely Severe	4

Table 7.1: WOB reference score

7.3 R-peak Variance

As an initial investigation the variance of the R-peaks in one respiratory cycle is studied as a potential measure for the WOB. The exploration of the variance of the R-peaks first requires the identifications of the R-peaks and the estimation of the BR over one minute windows. The respiratory cycles are then computed based on the BR. In each respiratory cycle the variance of the R-peaks is evaluated and the final variance is set to be the average over one minute windows. The steps of the R-peak variance measure are presented in more detail in Algorithm 12. The results obtained using the R-peak variance measure for the ECG and EMG children data are illustrated in Tables 7.2 and 7.3, respectively. It can be observed from these tables that there is a relation between the variance of the R-peaks and the increase in the respiratory distress.

Table 7.2 consists of three columns. The first column contains the ECG children record number, the second represents the reference WOB identified by skilled nurses in the BCH wards and the last column shows the results obtained from the proposed R-peak variance measure applied on the children ECG signals. The table is ordered with respect to the reference WOB level. The children EMG data (Table 7.3) vary in duration from 3 min to 7 hours. For example, the R-peak variance was averaged over 3 min for patient emgch1 as the provided WOB corresponds to 3 min, whereas for

Algorithm 12: R-peak variance

- 1 Locate R-peaks;
- 2 Estimate BR for N one minute windows, ($N = \frac{\#samples}{60}$);
- 3 For each estimated BR_i ($i = 1, \dots, N$), define the length of the respiratory cycle: $\frac{60}{BR_i}$;
- 4 Divide each one minute window i of ECG signal into $M_i = BR_i$ segments of duration $\frac{60}{BR_i}$ (respiratory cycle);
- 5 In each respiratory cycle j , where $j = 1, \dots, M_i$, calculate the R-peak variance:

$$V_j \leftarrow \frac{1}{K_j - 1} \sum_{k=1}^{K_j} |R_k - \hat{\mu}_j|^2, \quad (7.1)$$

where K_j is the number of R-peaks in the j -th respiratory cycle and $\hat{\mu}_j$ is the average of R-peaks: $\hat{\mu}_j \leftarrow \frac{1}{K_j} \sum_{k=1}^{K_j} R_k$. Then, average V_j over one minute window:

$$\bar{V}_i \leftarrow \frac{1}{M_i} \sum_{j=1}^{M_i} V_j \quad (7.2)$$

patient emgch4 the average R-peak variance is given over one hour as the reference data are provided each hour. What stands out in the table is that there is a positive monotonic relationship between the R-peak variance amplitude changes in the ECG signal and the increased respiratory distress (WOB), but it appears to be not really strong, indicating that further investigation should be conducted.

To evaluate the R-peak variance measure, the accuracy of classification was computed as follows:

$$\text{Accuracy}(\%) = \frac{\text{Number of correctly classified patients}}{\text{Total number of patients}} \cdot 100. \quad (7.3)$$

In order to decide the number of correctly classified patients, two different methods were used. In the first method, the estimated WOBs were plotted against the number of patients and by visual inspection the thresholds of each WOB band were

Record	Reference WOB	V
ecgch4	0	0.0154
ecgch12	0	0.0091
ecgch13	0	0.0011
ecgch1	1	0.0088
ecgch5	1	0.0149
ecgch6	1	0.0125
ecgch7	1	0.0097
ecgch8	1	0.0057
ecgch10	1	0.0211
ecgch11	1	0.0040
ecgch14	1	0.0148
ecgch15	1	0.0125
ecgch16	1	0.0076
ecgch18	1	0.0233
ecgch2	2	0.0075
ecgch3	2	0.0107
ecgch17	2	0.0216
ecgch9	3	0.0207

Table 7.2: ECG children: R-peak variance measure

emgch1	3m						
Ref. WOB	1						
V	0.0050						
emgch2	1h	2h					
Ref. WOB	0	0					
V	0.0023	0.0019					
emgch3	1h	2h	3h	4h	5h	6h	
Ref. WOB	1	1	1	1	1	1	
V	0.0024	0.0029	0.0024	0.0044	0.0012	0.0015	
emgch4	1h	2h	3h	4h	5h	6h	7h
Ref. WOB	1	1	1	1	1	1	1
V	0.0006	0.0021	0.0020	0.0017	0.0019	0.0016	0.0023

Table 7.3: EMG children: R-peak variance measure

decided. In the second method, the k -means algorithm was used, which is a standard unsupervised clustering method. This clustering algorithm aims to separate the data into objects which belong to different clusters, in which each object belongs to the cluster with the nearest mean (centroid). The thresholds were decided based on the centroid and the standard deviation of each cluster. Additional information on the theoretical basis of the k -means method are also provided in Appendix F. The k -means algorithm partitions the 34 calculated WOB values shown in Tables 7.2 and 7.3 from which we then obtain the limits of the four clusters and identify the WOB levels. In this k -means implementation the squared Euclidean distance metric is used.

Figure 7.1 shows the WOB bands obtained by the visual inspection of the R-peak variance measure values (y -axis) against the number of patients for both ECG and EMG data (x -axis). Red colour represents the ECG data and the blue colour the EMG data. The reference WOB 0 is represented by crosses, the reference WOB 1 is represented by triangles, and the reference WOB 2 and 3 are depicted by asterisks and circles, respectively. The colour bands define the limits of the clusters for each WOB level. The identified thresholds for each level of WOB by visual inspection along with the reference WOB are summarised in Table 7.4. This measure correctly identifies 15 patients out of 34, thus giving an accuracy of 44%, based on Equation 7.3.

To further clarify the correlation between the increased WOB and the R-peak variance using the results of the visual inspection, the classified WOB values were plotted against the reference in Figure 7.2. The numbers shown at data points represent the number of patients that were classified at the corresponding points in the figure. For example, five patients were labelled to have a reference WOB equal

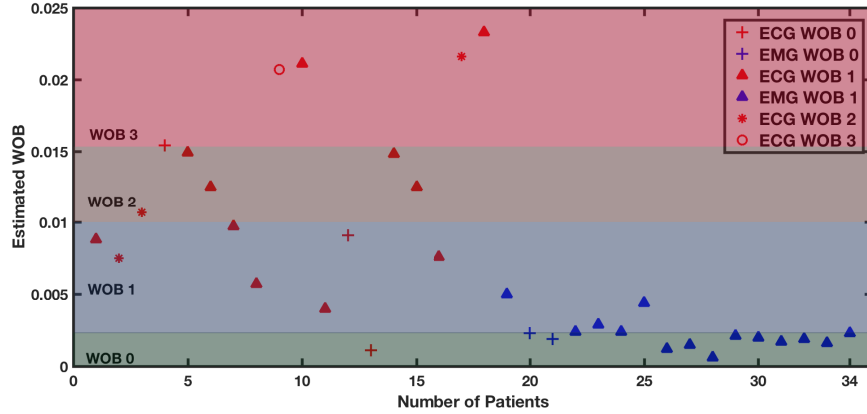


Figure 7.1: Visual inspection of V values for BCH ECG and EMG data

	V
WOB 0 (+)	< 0.0023
WOB 1 (\triangle)	$0.0023 - 0.01$
WOB 2 (*)	$0.01 - 0.0155$
WOB 3 (\circ)	> 0.0155

Table 7.4: Distinct bands of each level of WOB (R-peak variance) by visual inspection

to zero. Three of these patients were classified correctly, one was classified to have WOB one and one was classified to have WOB two. Moreover, the Pearson's linear correlation coefficient (detailed in Appendix F) was calculated for this classification and it was found that there is a positive correlation between the R-peak variance measure and the reference WOB ($r = 0.4463$, $p < 0.05$) when using visual inspection.

Figure 7.3 shows the clusters obtained for the R-peak variance measure. The identified cluster 1 from the k -means algorithm corresponds to WOB 0, cluster 2 to WOB 1, cluster 3 to WOB 2 and cluster 4 to WOB 3. Each cluster is surrounded by a dotted line rectangle. It is evident from this figure that most of the WOB 1 data are misclassified, thus the accuracy is expected to be lower. The thresholds

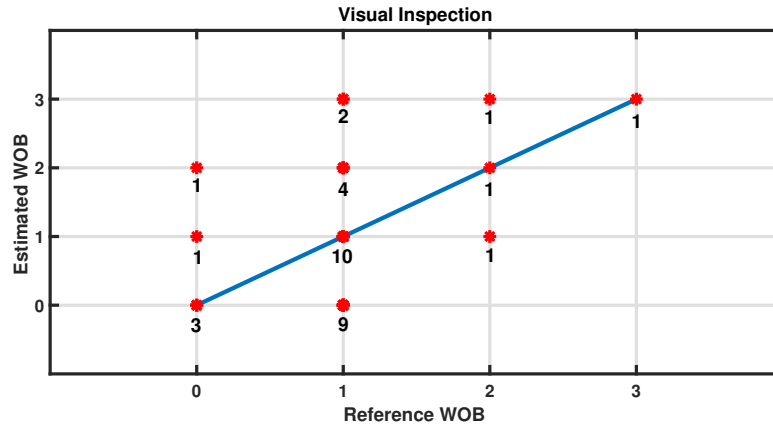


Figure 7.2: Correlation between reference and estimated WOB using the R-peak variance measure with visual inspection for BCH ECG and EMG data

are based on the centroid of each cluster and the standard deviation of the data which belong to the corresponding cluster. They are summarised in Table 7.5, which also illustrates the centroids for each cluster. The k -means correctly classified only 12 patients, giving a low accuracy of 35%. The number of the correctly classified patients can also be clarified by the diagonal of the k -means confusion matrix given in Table 7.6.

Furthermore to have a better understanding of the correlation between the reference and estimated WOB, the classified WOB values were plotted against the reference in Figure 7.4. The calculated Pearson's linear coefficient shows a positive correlation between the R-peak variance measure and the reference WOB ($r = 0.4273$, $p < 0.05$) when using k -means. The lower correlation when using the k -means algorithm was expected as the accuracy achieved is lower than the accuracy of the visual inspection.

The findings from both classification methods suggest that in order to develop a full picture of the correlation between the R-peak variability and increased respira-

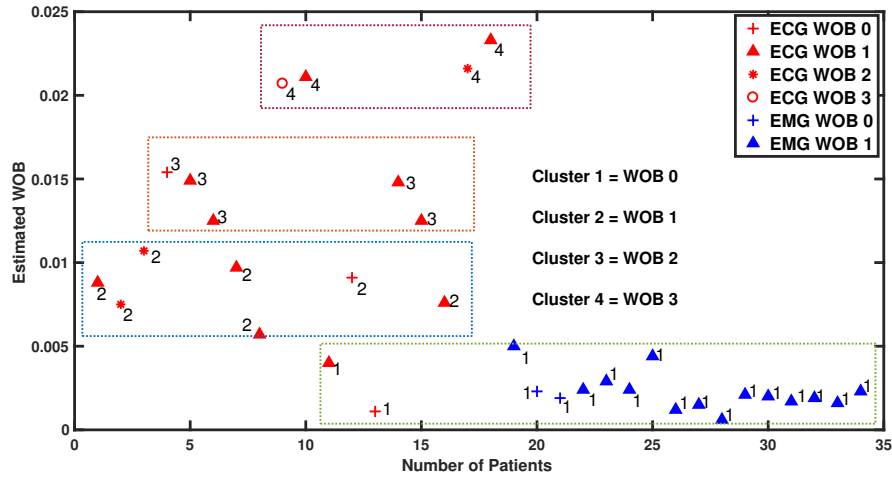


Figure 7.3: k -means classification of V values for BCH ECG and EMG data

	Centroid	V
WOB 0 (+)	0.0023	< 0.0034
WOB 1 (▲)	0.0084	$0.0034 - 0.0101$
WOB 2 (*)	0.0140	$0.0101 - 0.0154$
WOB 3 (○)	0.0217	> 0.0154

Table 7.5: Distinct bands of each level of WOB (R-peak variance) by k -means classification

tory distress, additional work will be needed. Hence, next section will discuss a more advanced measure for the WOB which is based on the variability of the R-peaks over respiratory cycles.

7.4 RS Variability

This section focuses on a more advanced measure for the increased respiratory distress which is based on R-to-S variability over a respiratory cycle. The developed measure will be evaluated using 34 recordings from the BCH ECG and EMG chil-

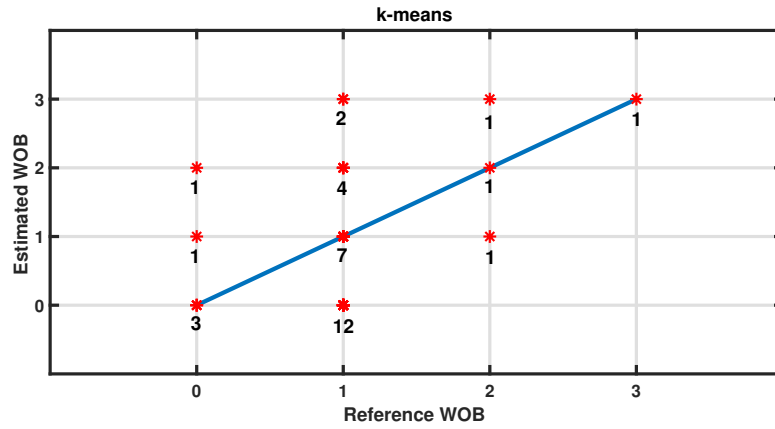


Figure 7.4: Correlation between reference and estimated WOB using the R-peak variance measure with k -means for BCH ECG and EMG data

		Actual Class			
		WOB	0	1	2
Predicted Class	0	3	1	1	0
	1	12	7	4	2
	2	0	1	1	1
	3	0	0	0	1

Table 7.6: Confusion matrix for R-peak variance measure

dren data.

7.4.1 Δ RS Measure

The aim of this section is to investigate whether the RS amplitude changes over a respiratory cycle show any relevance to the WOB. The idea stems from the amplitude modulations in the ECG signal induced by respiration, which have been previously used in the BR estimation (Moody et al., 1985) and discussed in Sections 3.1 and 5.2.1. As discussed in these sections the amplitude modulations in the ECG signal are due to the heart-to-electrode distance changes during the thoracic expansion (E. Helfenbein et al., 2014). A preliminary study (Addison, 2016b, 2016a) proved that there is a positive monotonic relationship between the amplitude changes in the PPG signal over a respiratory cycle and the WOB. This is achieved by using the PPG fluid responsiveness parameter, Δ POP, as defined in Equation 2.1 Chapter 2. This finding raises an intriguing question regarding the relationship between the changes in the PPG amplitude with the changes in the ECG amplitude, which is discussed in detail in the following section.

The Δ QRS measure as an Δ POP analogue

A recently published article by Giraud et al. (2013) conducted a series of experiments using data from 17 domestic pigs, in order to investigate the correlation between the changes in the PPG amplitude (Δ POP) and the changes in ECG amplitude (Δ QRS) as a way to estimate the intravascular volume status. It has been claimed that intravascular volume loss increased the amplitude changes in both PPG and ECG signals significantly, suggesting that those changes are highly correlated and consequently ECG can be used in the estimation of the intravascular volume status.

Returning to the WOB assessment, this thesis attempts to find a positive monotonic relationship between changes in the WOB and changes in the RS amplitude in an ECG signal, taking into account that the ΔPOP is a measure of respiratory distress and also is significantly correlated with the ΔQRS . Furthermore, when respiratory distress is associated with increased tidal volume (lung volume), the diaphragmatic contractions can increase, thus affecting the heart axis over respiratory cycles, and causing morphological changes in the shape of the QRS complex. The aforementioned suggests one potential way of how increased respiratory distress can cause significant variation in the RS amplitude, thus enabling the WOB evaluation using ECG signals.

ΔRS Measure for Estimation of WOB

To exploit the assumed correlation between the RS amplitude modulation and the WOB, the ECG signals are first processed in order to identify the locations of the R- and S-peaks. Then the respiration signal is extracted and the BR is estimated over one minute respiratory windows. The duration of the respiratory cycle is then computed based on the BR. For each respiration cycle the maximum and minimum RS amplitudes in the filtered ECG signal are evaluated and their difference is computed. Finally, the WOB is set to be the average of the differences over one minute windows. The steps of the ΔRS measure are presented in more details in Algorithm 13.

Figure 7.5 explains visually the ΔRS measure for WOB. The ECG signal is filtered and processed in order to identify the locations of the R- and S-peaks. The BR for this specific ECG signal, whose length is one minute and 55 seconds and was sampled at 100 Hz, was 42 bpm which gives 81 respiratory cycle segments of

Algorithm 13: Δ RS measure

- 1 Locate R- and S-peaks;
- 2 Estimate BR for N one minute windows, ($N = \frac{\#samples}{60}$);
- 3 For each estimated BR_i ($i = 1, \dots, N$), define the length of the respiratory cycle: $\frac{60}{BR_i}$;
- 4 Divide each one minute window i of ECG signal into $M_i = BR_i$ segments of duration $\frac{60}{BR_i}$ (respiratory cycle);
- 5 In each respiratory cycle j , where $j = 1, \dots, M_i$, identify the maximum and minimum RS amplitude, defined as $\max RS_j$ and $\min RS_j$, and evaluate their difference:

$$\Delta RS_j \leftarrow \frac{\max RS_j - \min RS_j}{(\max RS_j + \min RS_j)/2} \quad (7.4)$$

Average ΔRS_j over one minute window:

$$\overline{\Delta RS}_i \leftarrow \frac{1}{M_i} \sum_{j=1}^{M_i} \Delta RS_j \quad (7.5)$$

1.42 seconds duration. In each respiratory cycle the maximum and minimum RS amplitudes are computed and the Δ RS value is evaluated based on Equation 7.4.

As previously discussed in this chapter, the proposed measure will be evaluated using the 18 signals of the BCH ECG database and the 16 hours of the BCH EMG data. The obtained results for the ECG and EMG children data are summarised in the Tables 7.7 and 7.8, respectively. What stands out in the tables is that there is a positive monotonic relationship between the RS amplitude changes in the ECG signal and the increased respiratory distress (WOB). For example, for level 0 of WOB, most of the calculated Δ RS values are below 0.15 and for level 1, values between 0.15 and 0.25 are observed. Interestingly, the average Δ RS is rising above 0.3 when the level of WOB is high about 3. The latter indicates that the proposed measure might be able to detect automatically patients with increased respiratory distress, which if combined with continuous BR and HR monitoring will assist clinicians to decide the

level of patient’s criticality.

To further evaluate the ΔRS measure, the accuracy of classification was computed based on Equation 7.3. Moreover, in order to decide the number of correctly classified patients the visual inspection method and the k -mean classification were used.

Figure 7.6 illustrates the WOB bands obtained after visually inspecting the estimated WOB (y -axis) against the number of patients for both databases (x -axis). It can be observed that 22 patients were correctly classified, thus giving a higher accuracy of 64%. The identified thresholds for each level of WOB by visual inspection of the ΔRS measure are summarised in Table 7.9. Figure 7.7 depicts the classified patients against the reference data using visual inspection. To re-emphasize, the number at each data point represents the number of classified patients. Moreover the Pearson’s linear correlation coefficient was computed and it shows that there is a positive correlation between the ΔRS measurements and the reference WOB

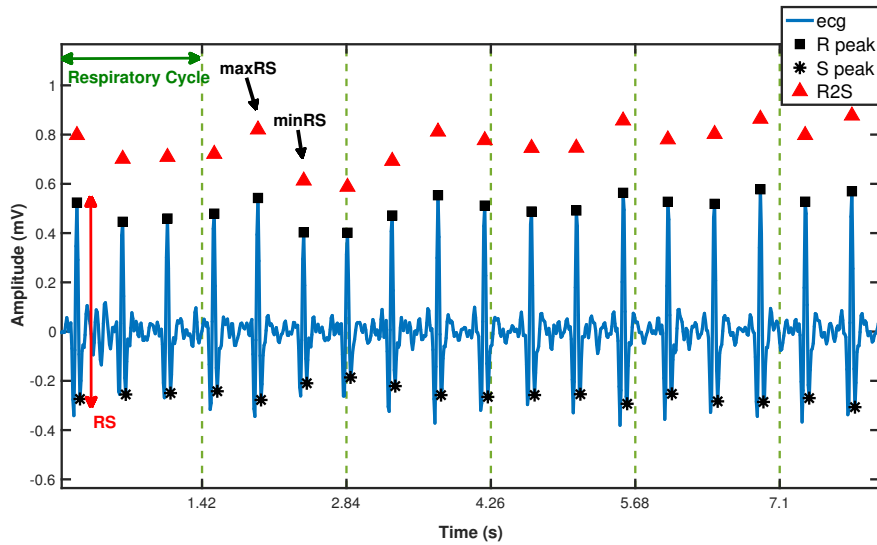


Figure 7.5: ΔRS measure for WOB: The R- (black squares) and S-peaks (black asterisks) are identified in the filtered ECG signal (blue solid line). In each respiratory cycle (green dashed line) the RS amplitudes (red triangles) are identified.

Record	Reference WOB	Δ RS
ecgch4	0	0.2658
ecgch12	0	0.1235
ecgch13	0	0.1054
ecgch1	1	0.1933
ecgch5	1	0.2493
ecgch6	1	0.2255
ecgch7	1	0.2112
ecgch8	1	0.1462
ecgch10	1	0.3032
ecgch11	1	0.0895
ecgch14	1	0.1658
ecgch15	1	0.3780
ecgch16	1	0.1346
ecgch18	1	0.3601
ecgch2	2	0.3347
ecgch3	2	0.6727
ecgch17	2	0.2889
ecgch9	3	0.3824

Table 7.7: ECG children: Δ RS measure

emgch1	3m						
Ref. WOB	1						
Δ RS	0.0681						
emgch2	1h	2h					
Ref. WOB	0	0					
Δ RS	0.0678	0.0800					
emgch3	1h	2h	3h	4h	5h	6h	
Ref. WOB	1	1	1	1	1	1	
Δ RS	0.1501	0.1957	0.1386	0.1961	0.2986	0.0700	
emgch4	1h	2h	3h	4h	5h	6h	7h
Ref. WOB	1	1	1	1	1	1	1
Δ RS	0.0759	0.1370	0.1173	0.1671	0.1433	0.2228	0.2279

Table 7.8: EMG children: Δ RS measure

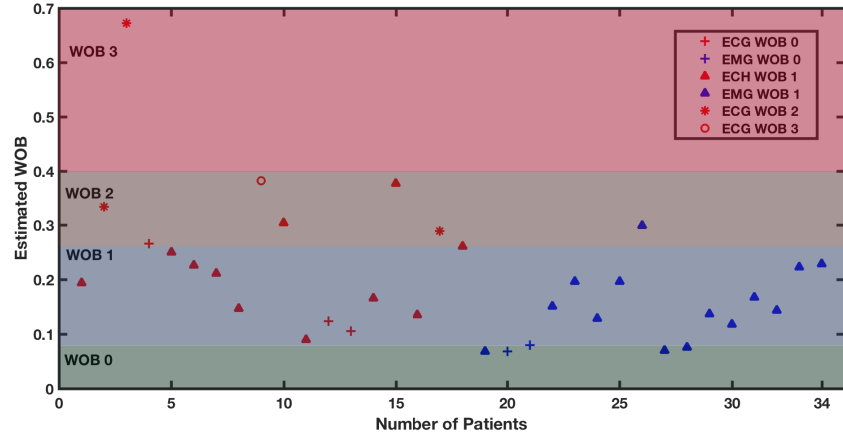


Figure 7.6: Visual inspection of ΔRS values for BCH ECG and EMG data

	ΔRS
WOB 0 (+)	< 0.08
WOB 1 (Δ)	$0.08 - 0.2658$
WOB 2 (*)	$0.2658 - 0.4$
WOB 3 (o)	> 0.4

Table 7.9: Distinct bands of each level of WOB (ΔRS measure) by visual inspection

($r = 0.5733$, $p < 0.05$), which is considerably higher compared to the R-peak variance measure ($r = 0.4463$) when using visual inspection.

Figure 7.8 shows the clusters obtained for the ΔRS measure using the k -mean classification. Each estimated WOB value is labelled by a number which represents the cluster that it belongs to. Closer inspection of the figure reveals that the measure correctly identifies 19 patients, which gives an accuracy of 56%. The number of the correctly classified patients can also be clarified by the diagonal of the k -means confusion matrix given in Table 7.11. The thresholds are based on the centroid of each cluster and the standard deviation of the data which belong to the corresponding cluster and they are summarised in Table 7.10, which also illustrates the centroids

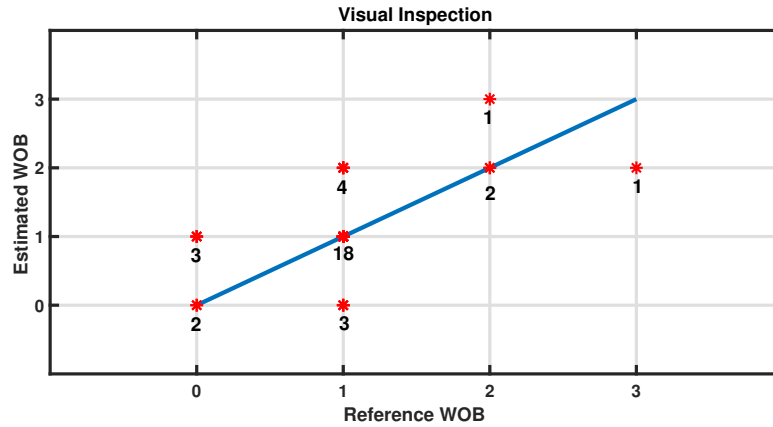


Figure 7.7: Correlation between reference and estimated WOB from Δ RS with visual inspection for BCH ECG and EMG data

	Centroid	Δ RS
WOB 0 (+)	0.1092	< 0.1404
WOB 1 (Δ)	0.2055	0.1404 - 0.2324
WOB 2 (*)	0.3140	0.2324 - 0.3609
WOB 3 (\circ)	0.6727	> 0.3609

Table 7.10: Distinct bands of each level of WOB (Δ RS measure) by k -means classification

for each cluster.

Figure 7.9 shows the the number of classified patients versus the reference data for both BCH ECG and EMG recordings. The Pearson’s correlation coefficient of this measure when using the k -means algorithm shows that there is a positive relationship between the Δ RS values and the reference WOB ($r = 0.5753$, $p < 0.05$), which is higher compared to the R-peak variance values ($r = 0.4273$), when using the k -means algorithm.

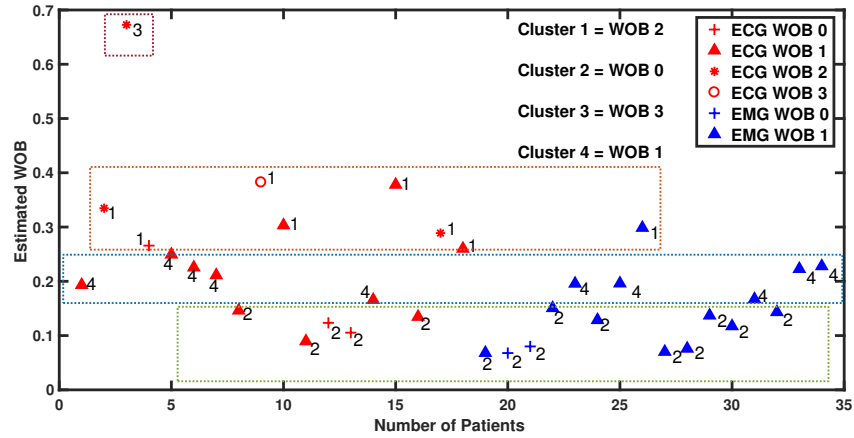


Figure 7.8: k -means clustering of ΔRS values for BCH ECG and EMG data

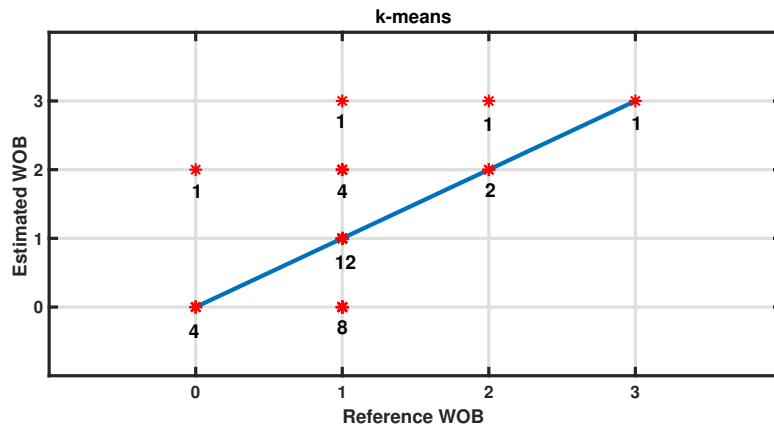


Figure 7.9: Correlation between reference and estimated WOB from ΔRS with k -means for BCH ECG and EMG data

		Actual Class			
		WOB	0	1	2
Predicted Class	0	4	0	1	0
	1	8	12	4	1
	2	0	0	2	1
	3	0	0	0	1

Table 7.11: Confusion matrix for ΔRS measure

7.5 Conclusion

In this investigation, the aim was to exploit the potential correlation of the ECG signal with the respiratory distress. This study has found for the first time that there is a positive monotonic relationship between the RS amplitude variability and increased WOB over respiratory cycles. This finding sheds new light on the automatic evaluation of the WOB from ECG signals. The key advantage of the proposed measure is that it can be incorporated into sensors/devices which measure the ECG signal, because its simplicity encourages a straight forward implementation as it does not require complicated circuits. Therefore, it can be part of a diagnostic screening tool in a hospital ward, which combines the evaluation of BR, HR and WOB in order to decide the level of patient deterioration.

The exploitation of WOB evaluation was limited by the lack of an adequate number of data, which also affects the clustering performance. It is crucial to evaluate this measure using more patients and also have samples which contain all levels of WOB. For example, the EMG database contains only children with reference WOB at levels 0 and 1. Considerably more work will need to be done to determine accurate bands for each WOB level by using more advanced clustering methods, since non-linear clustering methods are expected to perform better on the current results.

Chapter 8

Conclusions and Directions for Future Work

This chapter presents the conclusion of the thesis by presenting a synopsis of its contributions in Section 8.1. The directions and recommendations for future research will be discussed in Section 8.2.

8.1 Research Question Reflection

The aim of this thesis was to develop and assess a breathing rate (BR) monitoring and fusion systems to be used in hospital wards using children Electrocardiogram (ECG), Electromyogram (EMG) and Seismocardiogram (SCG) signals in order to benefit continuous patient monitoring and triage. Moreover, the thesis provided for the first time new insights into R-peak variability as a measure of increased respiratory distress or Work-of-Breathing (WOB).

In support of the thesis aims, Chapter 4 presented a novel QRS complex detector, based on the Empirical Mode Decomposition (EMD), which can be applied to all

patient types. The R-peak identification is of significant importance for the accurate estimation of the BR and WOB estimations. Therefore, the developed R-peak identification method in this PhD research is essential for these methods. The proposed detector overcomes many of the limitations of the EMD-based R-peak detectors as it is based on the local signal energy and uses an adaptive threshold which is updated at regular times. Another advantage of the proposed method is that it can be implemented on-line because the R-peak identification is based on the most recent history of the patient.

Chapter 5 presented a systematic review of feature-based BR estimation methods by using ECG and EMG data which belong to hospitalised children. The obtained respiration signals from these methods were later processed in the frequency and time domains for the BR estimation. The latter's performance gained from the design of a band-pass filter whose cut-off frequencies are based on the age and condition of the patient and it is applied on the respiration signal in order to exclude non-respiratory frequencies. The designed band-pass filter was applied for the first time on the PCA- and ICA-derived respiration signals. Moreover, a more advanced frequency domain technique which was based on the correntropy transformation was used for the first time in the BR estimation from respiration signals. Furthermore, Chapter 5 presented a novel filter-based EMD algorithm for continuous BR monitoring which does not require the R-peak identification.

The findings in Chapter 5 suggested that the sensors being used in ECG and EMG signals acquisition are capturing noise which contaminates the frequency spectrum of the respiration signal and thus affects the accuracy. However, the respiration frequency is still present but it is not the most prominent. This issue was attempted to be addressed by using the proposed fusion method in order to improve the estimation

accuracy by selecting the best estimates according to some criteria. Regarding the time domain methods, it was observed that when a smooth signal is being processed, the Peak-to-Trough (P2T) technique will smooth the identified peaks and will give a more accurate result. Nonetheless, when the respiration signal belongs to a patient who has difficulty breathing, this method will be confused as to which peaks should be counted as breaths and the Three-Point (3PT) technique will give better results, as it counts as breaths all the extrema in the respiration signal.

Chapter 6 explored the use of the SCG signals in BR estimation, because their acquisition does not require invasive methods, are inexpensive and provide high-quality data. Current state of the art methods for respiration signal extraction from SCG recordings were reviewed and further analysed in both frequency and time domain. The conclusions made from the obtained results are very similar to the ones of Chapter 5 regarding the BR estimation in frequency and time domain. Furthermore, the EMD-derived respiration method discussed in Chapter 5 was applied on the SCG signal database and it was observed that it outperforms the current standard methods. The main advantage of these results is that the EMD-derived respiration signal method does not require the identification of the R- and S1-peaks. Moreover, from an implementation point of view, EMD is straight-forward. The latter paves the way to design sensor/devices which measure both ECG and SCG in order to obtain two respiration signals using the EMD-derived respiration method, which can be latter fused and provide a more robust BR estimation approach.

Chapter 7 focused on assessing the potential utility of the ECG signals in order to evaluate the increased respiratory distress. A measure based on the R-to-S (RS) amplitude variability due to respiration in the ECG signal was developed in this thesis and it was found for the first time that there is a positive monotonic relationship

between the RS variability and increased WOB over respiratory cycles. The latter finding suggests that ECG sensors/devices can be used as a diagnostic screening tool which incorporates the evaluation of the BR, HR and WOB, which allows clinicians to escalate patient care and introduce interventions in hospital wards. Although the current study is based on a small sample of patients, the proposed measure is the only empirical investigation into the impact of increased respiratory distress on the ECG signal.

8.2 Direction for Future Research

Future investigations on the WOB evaluation using more comprehensive real data are required in order to establish the most suitable techniques and hence future work should be designed as follows:

Further assessment and design of WOB evaluation algorithm

The conclusion of Chapter 7 was that the automatic evaluation of the WOB from the ECG signals would be a fruitful area of future work. It would be really beneficial to evaluate WOB measures using more patients and also have samples which contain all levels of WOB. The latter also facilitates the use of advanced clustering methods which can be used in the selection of accurate bands for each WOB level. Moreover, SCG signals are acquired by accelerometer sensors placed on the chest of the patient, thus it may be convenient to evaluate the WOB from SCG signals either as a stand-alone measure, or to combine them with estimates from the ECG signal in order to improve performance.

On this direction the proposed WOB measure needs to be further evaluated. Thus more research using controlled clinical trials involving a large number of healthy sub-

jects is required. The study volunteers should experience a controlled difficulty in breathing, hence the use of a facemask with interchangeable flow resistors or drug injection need to be considered for these trials. Furthermore, the aforementioned trials should be combined with extensive empirical studies in both adult and paediatric wards where ECG and SCG measures for WOB are compared with the nurse assessments.

References

- Addison, P. S. (2016a). Photoplethysmogram Baseline Modulation as a Measure of Respiratory Effort: A Free Breathing Protocol with Progressive Flow Restrictions at the Mouth. In *ANESTHESIA AND ANALGESIA* (Vol. 122).
- Addison, P. S. (2016b). Respiratory modulations in the photoplethysmogram (DPOP) as a measure of respiratory effort. *Journal of Clinical Monitoring and Computing*, 30(5), 595–602.
- Addison, P. S. (2017). Respiratory effort from the photoplethysmogram. *Medical Engineering & Physics*, 41, 9–18.
- Ahlstrom, M. L., & Tompkins, W. J. (1983). Automated high-speed analysis of Holter tapes with microcomputers. *IEEE Transactions on Biomedical Engineering*(10), 651–657.
- Ahrens, T. (1993). Respiratory monitoring in critical care. *AACN Advanced Critical Care*, 4(1), 56–65.
- Álvarez, R. A., Penín, A. J. M., & Sobrino, X. A. V. (2013). A comparison of three QRS detection algorithms over a public database. *Procedia Technology*, 9, 1159–1165.
- Arafat, M. A., & Hasan, M. K. (2009). Automatic detection of ECG wave boundaries using Empirical Mode Decomposition. In *Acoustics, Speech and Signal Processing, 2009. ICASSP 2009. IEEE International Conference on* (pp. 461–464).
- Arzeno, N. M., Deng, Z.-D., & Poon, C.-S. (2008). Analysis of first-derivative based QRS detection algorithms. *IEEE Transactions on Biomedical Engineering*, 55(2), 478–484.
- Babaeizadeh, S., Zhou, S. H., Pittman, S. D., & White, D. P. (2011). Electrocardiogram-derived respiration in screening of sleep-disordered breathing. *Journal of Electrocardiology*, 44(6), 700–706.
- Bailón, R., Sörnmo, L., & Laguna, P. (2006). ECG-derived respiratory frequency estimation. *Advanced methods and tools for ECG data analysis*, 1.
- Baram, D., & Richman, P. (2010). CHAPTER 50 - Mechanical Ventilation in the Cardiac Care Unit". In Allen Jeremias and David L. Brown (Ed.), *Cardiac Intensive Care (Second Edition)* (Second Edition

- ed., p. 632 - 643). Philadelphia: W.B. Saunders. Retrieved from <http://www.sciencedirect.com/science/article/pii/B9781416037736100503> doi: <https://doi.org/10.1016/B978-1-4160-3773-6.10050-3>
- Baumert, M., Smith, J., Catcheside, P., McEvoy, R. D., Abbott, D., Sanders, P., & Nalivaiko, E. (2008). Variability of QT interval duration in obstructive sleep apnea: an indicator of disease severity. *Sleep*, *31*(7), 959–966.
- Bellani, G., & Pesenti, A. (2014). Assessing effort and work of breathing. *Current Opinion in Critical Care*, *20*(3), 352–358.
- Benitez, D., Gaydecki, P., Zaidi, A., & Fitzpatrick, A. (2001). The use of the Hilbert transform in ECG signal analysis. *Computers in Biology and Medicine*, *31*(5), 399–406.
- Benitez, D. S., Gaydecki, P., Zaidi, A., & Fitzpatrick, A. (2000). A new QRS detection algorithm based on the Hilbert transform. In *Computers in Cardiology 2000* (pp. 379–382).
- Berntson, G. G., Cacioppo, J. T., & Quigley, K. S. (1993). Respiratory sinus arrhythmia: autonomic origins, physiological mechanisms, and psychophysiological implications. *Psychophysiology*, *30*(2), 183–196.
- Berntson, G. G., Thomas Bigger Jr, J., Eckberg, D. L., Grossman, P., Kaufmann, P. G., Malik, M., . . . Van Der Molen, M. W. (1997). Heart rate variability: origins, methods, and interpretive caveats. *Psychophysiology*, *34*(6), 623–648.
- Birrenkott, D. A., Pimentel, M. A., Watkinson, P. J., & Clifton, D. A. (2016). Robust estimation of respiratory rate via ECG-and PPG-derived respiratory quality indices. In *2016 38th Annual International Conference of the IEEE Engineering in Medicine and Biology Society (EMBC)* (pp. 676–679).
- Birrenkott, D. A., Pimentel, M. A., Watkinson, P. J., & Clifton, D. A. (2018). A robust fusion model for estimating respiratory rate from photoplethysmography and electrocardiography. *IEEE Transactions on Biomedical Engineering*, *65*(9), 2033–2041.
- Bishop, C. M. (1995). *Neural Networks for Pattern Recognition*. Oxford University press.
- Brenyo, A., & Zaręba, W. (2011). Prognostic significance of QRS duration and morphology. *Cardiology journal*, *18*(1), 8–17.
- Burke, O. (2011). Statistical Methods. Autocorrelation, Decomposition and Smoothing. *Michaelmas Term. Department of Statistics, Oxford*.
- Burt, R., Cinar, G. T., & Principe, J. C. (2014). Pitch estimation using non-negative matrix factorization. In *2014 International Joint Conference on Neural Networks (IJCNN)* (pp. 2058–2062).
- Campolo, M., Labate, D., La Foresta, F., Morabito, F., Lay-Ekuakille, A., & Vergallo, P. (2011). ECG-derived respiratory signal using Empirical Mode Decomposition. In *Medical Measurements and Applications Proceedings (MeMeA), 2011 IEEE International Workshop on* (pp. 399–403).

- Cardose, J. (1998). Blind Source Separation: Statistical Principles. In *IEEE Proceedings* (Vol. 9035, pp. 2009–2026).
- Castiglioni, P., Faini, A., Parati, G., & Di Rienzo, M. (2007). Wearable seismocardiography. In *2007 29th Annual International Conference of the IEEE Engineering in Medicine and Biology Society* (pp. 3954–3957).
- Chan, A. M., Ferdosi, N., & Narasimhan, R. (2013). Ambulatory respiratory rate detection using ECG and a triaxial accelerometer. In *2013 35th Annual International Conference of the IEEE Engineering in Medicine and Biology Society (EMBC)* (pp. 4058–4061).
- Charlton. (2016). *Peter Charlton: Respiratory Rate Estimation Algorithms*. Retrieved from <https://github.com/peterhcharlton/RRest>
- Charlton, P. H. (2017). *Continuous Respiratory Rate Monitoring to Detect Clinical Deteriorations using Wearable Sensors* (Unpublished doctoral dissertation). King’s College London.
- Charlton, P. H., Bonnici, T., Tarassenko, L., Alastruey, J., Clifton, D. A., Beale, R., & Watkinson, P. J. (2017). Extraction of respiratory signals from the electrocardiogram and photoplethysmogram: technical and physiological determinants. *Physiological measurement*, *38*(5), 669.
- Charlton, P. H., Bonnici, T., Tarassenko, L., Clifton, D. A., Beale, R., & Watkinson, P. J. (2016). An assessment of algorithms to estimate respiratory rate from the Electrocardiogram and Photoplethysmogram. *Physiological Measurement*, *37*(4), 610.
- Cherix, E., Brugada, P., & Wellens, H. J. (1986). Pseudo-atrial dissociation: a respiratory artifact. *European heart journal*, *7*(4), 357–359.
- Cohen, N. H., & Schwartz, D. E. (2013). Monitoring the Airway and Pulmonary Function. In *Benumof and Hagberg’s Airway Management* (pp. 998–1017). Elsevier.
- Comon, P. (1994). Independent Component Analysis, a new concept? *Signal Processing*, *36*(3), 287–314.
- Contal, O., Carnevale, C., Borel, J.-C., Sabil, A., Tamisier, R., Lévy, P., . . . Pépin, J.-L. (2013). Pulse transit time as a measure of respiratory effort under non-invasive ventilation. *European Respiratory Journal*, *41*(2), 346–353.
- Cretikos, M. A., Bellomo, R., Hillman, K., Chen, J., Finfer, S., & Flabouris, A. (2008). Respiratory rate: the neglected vital sign. *Medical Journal of Australia*, *188*(11), 657–659.
- Cysarz, D., Zerm, R., Bettermann, H., Frühwirth, M., Moser, M., & Kröz, M. (2008). Comparison of respiratory rates derived from heart rate variability, ECG amplitude, and nasal/oral airflow. *Annals of Biomedical Engineering*, *36*(12), 2085–2094.
- Department of Education. (2017). *Child death reviews: year ending 31 March 2017*. Retrieved 2017-07-13, from

<https://www.gov.uk/search/research-and-statistics>

- Dodd, K. W., Elm, K. D., & Smith, S. W. (2016). Comparison of the QRS complex, ST-segment, and T-wave among patients with left bundle branch block with and without acute myocardial infarction. *The Journal of Emergency Medicine*, *51*(1), 1–8.
- Duncan, H., Hutchison, J., & Parshuram, C. S. (2006). The Pediatric Early Warning System score: a severity of illness score to predict urgent medical need in hospitalized children. *Journal of Critical Care*, *21*(3), 271–278.
- Ehman, R. L., McNamara, M., Pallack, M., Hricak, H., & Higgins, C. (1984). Magnetic resonance imaging with respiratory gating: techniques and advantages. *American journal of Roentgenology*, *143*(6), 1175–1182.
- Elgendi Mohamed, D. F., Jonkman Mirjam. (2005). Frequency bands effects on QRS detection. *International Joint Conference on Biomedical Engineering Systems and Technologies, BIOSIGNALS 2010, Valencia, Spain*, *5*, 428–431.
- Elhendy, A., Hammill, S. C., Mahoney, D. W., & Pellikka, P. A. (2005). Relation of QRS duration on the surface 12-lead electrocardiogram with mortality in patients with known or suspected coronary artery disease. *The American journal of Cardiology*, *96*(8), 1082–1088.
- Elliott, M. (2016). Why is Respiratory Rate the Neglected Vital Sign? A Narrative Review. *Int Arch Nurs Health Care*, *2*, 050.
- Fieselmann, J. F., Hendryx, M. S., Helms, C. M., & Wakefield, D. S. (1993). Respiratory rate predicts cardiopulmonary arrest for internal medicine inpatients. *Journal of General Internal Medicine*, *8*(7), 354–360.
- Fleming, S. (2010). *Measurement and Fusion of Non-Invasive Vital Signs for Routine Triage of Acute Paediatric Illness* (Unpublished doctoral dissertation). Oxford University, UK.
- Fleming, S., Tarassenko, L., Thompson, M., & Mant, D. (2008). Non-invasive measurement of respiratory rate in children using the photoplethysmogram. In *2008 30th Annual International Conference of the IEEE Engineering in Medicine and Biology Society* (pp. 1886–1889).
- Fleming, S. G., & Tarassenko, L. (2007). A comparison of signal processing techniques for the extraction of breathing rate from the photoplethysmogram. *Int. J. Biol. Med. Sci.*, *2*(4), 232–236.
- Forbes, A. D., & Helfenbein, E. D. (2000). *Intramyocardial anomalous activity detection by subtracting modeled respiratory effect*. Google Patents. (US Patent 6,132,381)
- Friesen, G. M., Jannett, T. C., Jadallah, M. A., Yates, S. L., Quint, S. R., & Nagle, H. T. (1990). A comparison of the noise sensitivity of nine QRS detection algorithms. *IEEE Transactions on Biomedical Engineering*, *37*(1), 85–98.
- Gallego, A., Weir, R., & Errey, K. (2019). *Health monitoring*. Google Patents. (US Patent App. 10/327,660)

- García-González, M. A., Argelagós-Palau, A., Fernández-Chimeno, M., & Ramos-Castro, J. (2013). A comparison of heartbeat detectors for the seismocardiogram. In *Computing in Cardiology 2013* (pp. 461–464).
- Garde, A., Karlen, W., Ansermino, J. M., & Dumont, G. A. (2014). Estimating respiratory and heart rates from the correntropy spectral density of the photoplethysmogram. *PloS one*, *9*(1), e86427.
- Garde, A., Karlen, W., Dehkordi, P., Ansermino, J. M., & Dumont, G. A. (2013). Empirical mode decomposition for respiratory and heart rate estimation from the photoplethysmogram. In *Computing in Cardiology 2013* (pp. 799–802).
- Gavali, M. M., & Upasani, D. (2015). Extraction of Respiratory Signal from ECG using Empirical Mode Decomposition. *Extraction*, *3*(7).
- Gee, A. H., Barbieri, R., Paydarfar, D., & Indic, P. (2016). Predicting Bradycardia in Preterm Infants Using Point Process Analysis of Heart Rate. *IEEE Transactions on Biomedical Engineering*.
- Giraud, R., Siegenthaler, N., Morel, D. R., Romand, J.-A., Brochard, L., & Bendjelid, K. (2013). Respiratory change in ECG-wave amplitude is a reliable parameter to estimate intravascular volume status. *Journal of Clinical Monitoring and Computing*, *27*(2), 107–111.
- Goldberger, A. L., Amaral, L. A., Glass, L., Hausdorff, J. M., Ivanov, P. C., Mark, R. G., . . . Stanley, H. E. (2000). PhysioBank, PhysioToolkit, and PhysioNet: components of a new research resource for complex physiologic signals. *Circulation*, *101*(23), 1–9.
- Goldhill, D., McNarry, A., Mandersloot, G., & McGinley, A. (2005). A physiologically-based early warning score for ward patients: the association between score and outcome. *Anaesthesia*, *60*(6), 547–553.
- Gupta, R., Mitra, M., Mondal, K., & Bhowmick, S. (2011). A derivative-based approach for QT-segment feature extraction in digitized ECG record. In *Emerging Applications of Information Technology (EAIT), 2011 Second International Conference on* (pp. 63–66).
- Haescher, M., Matthies, D. J., Trimpop, J., & Urban, B. (2015). A study on measuring heart-and respiration-rate via wrist-worn accelerometer-based seismocardiography (SCG) in comparison to commonly applied technologies. In *Proceedings of the 2nd international Workshop on Sensor-based Activity Recognition and Interaction* (p. 2).
- Hamilton, P. S., & Tompkins, W. J. (1986). Quantitative investigation of QRS detection rules using the MIT/BIH arrhythmia database. *IEEE transactions on Biomedical Engineering*(12), 1157–1165.
- Helpenbein, E., Firoozabadi, R., Chien, S., Carlson, E., & Babaeizadeh, S. (2014). Development of three methods for extracting respiration from the surface ECG: a review. *Journal of Electrocardiology*, *47*(6), 819–825.
- Helpenbein, E. D., & Forbes, A. D. (2007). *Respiration-gated cardiography*. Google

- Patents. (US Patent App. 12/293,552)
- Herault, J., & Jutten, C. (1986). Space or time adaptive signal processing by neural network models. In *AIP conference proceedings* (Vol. 151, pp. 206–211).
- Higgins, T. G., Phillips Jr, J. H., & Sumner, R. G. (1966). Atrial dissociation: an electrocardiographic artifact produced by the accessory muscles of respiration. *The American Journal of Cardiology*, *18*(1), 132–139.
- Huang, N. E., Shen, Z., Long, S. R., Wu, M. C., Shih, H. H., Zheng, Q., . . . Liu, H. H. (1998). The Empirical Mode Decomposition and the Hilbert spectrum for nonlinear and non-stationary time series analysis. In *Proceedings of the Royal Society of London A: Mathematical, Physical and Engineering Sciences* (Vol. 454, pp. 903–995).
- Hyvarinen, A. (1999). Fast ica for noisy data using gaussian moments. In *Iscas'99. proceedings of the 1999 ieee international symposium on circuits and systems vlsi (cat. no. 99ch36349)* (Vol. 5, pp. 57–61).
- Hyvärinen, A., & Oja, E. (2000). Independent Component Analysis: algorithms and applications. *Neural Networks*, *13*(4-5), 411–430.
- Inan, O. T., Baran Pouyan, M., Javaid, A. Q., Dowling, S., Etemadi, M., Dorier, A., . . . Klein, L. (2018). Novel wearable seismocardiography and machine learning algorithms can assess clinical status of heart failure patients. *Circulation: Heart Failure*, *11*(1), e004313.
- Inan, O. T., Migeotte, P.-F., Park, K.-S., Etemadi, M., Tavakolian, K., Casanella, R., . . . Di Rienzo, M. (2014). Ballistocardiography and seismocardiography: A review of recent advances. *IEEE Journal of Biomedical and Health Informatics*, *19*(4), 1414–1427.
- Jarchi, D., Salvi, D., Tarassenko, L., & Clifton, D. (2018). Validation of Instantaneous Respiratory Rate Using Reflectance PPG from Different Body Positions. *Sensors*, *18*(11), 3705.
- Jolliffe, I. T. (1986). Principal Component Analysis and Factor Analysis. In *Principal Component Analysis* (pp. 115–128). Springer.
- Jutten, C., & Herault, J. (1991). Blind Separation of Sources, part I: An adaptive algorithm based on neuromimetic architecture. *Signal Processing*, *24*(1), 1–10.
- Karagiannis, A., & Constantinou, P. (2009). Noise components identification in biomedical signals based on empirical mode decomposition. In *Information technology and applications in biomedicine, 2009. itab 2009. 9th international conference on* (pp. 1–4).
- Karlen, W., Raman, S., Ansermino, J. M., & Dumont, G. A. (2013). Multiparameter respiratory rate estimation from the Photoplethysmogram. *IEEE Transactions on Biomedical Engineering*, *60*(7), 1946–1953.
- Kelly, C. (2018). Respiratory rate 1: why measurement and recording are crucial. *Nursing Times*, *114*(4), 23–24.

- Ketai, L. H., & Godwin, J. D. (1998). A new view of pulmonary edema and acute respiratory distress syndrome. *Journal of thoracic imaging*, *13*(3), 147–171.
- Kim, H., Kim, H., Chun, S., Kang, J.-H., Oakley, I., Lee, Y., . . . Kim, S.-P. (2018). A wearable wrist band-type system for multimodal biometrics integrated with multispectral skin photomatrix and electrocardiogram sensors. *Sensors*, *18*(8), 2738.
- Kohler, B.-U., Hennig, C., & Orglmeister, R. (2002). The principles of software QRS detection. *IEEE Engineering in Medicine and Biology Magazine*, *21*(1), 42–57.
- Kozia, C., Herzallah, R., & Lowe, D. (2018a). Adaptive R-peak Detection Using Empirical Mode Decomposition.
- Kozia, C., Herzallah, R., & Lowe, D. (2018b). ECG-Derived Respiration Using a Real-Time QRS Detector Based on Empirical Mode Decomposition. In *2018 12th International Conference on Signal Processing and Communication Systems (ICSPCS)* (pp. 1–8).
- Kozia, C., Herzallah, R., & Lowe, D. (2018c). ICA-Derived Respiration Using an Adaptive R-Peak Detector. In *International Conference on Time Series and Forecasting* (pp. 363–377).
- Labate, D., La Foresta, F., Occhiuto, G., Morabito, F. C., Lay-Ekuakille, A., & Vergallo, P. (2013). Empirical mode decomposition vs. wavelet decomposition for the extraction of respiratory signal from single-channel ECG: A comparison. *IEEE Sensors Journal*, *13*(7), 2666–2674.
- Langley, P., Bowers, E. J., & Murray, A. (2010). Principal component analysis as a tool for analysing beat-to-beat changes in electrocardiogram features: application to electrocardiogram derived respiration. *IEEE Trans. Biomed. Eng.*, *57*(4), 821–829.
- Lázaro, J., Gil, E., Bailón, R., & Laguna, P. (2011). Deriving respiration from the pulse photoplethysmographic signal. In *2011 Computing in Cardiology* (pp. 713–716).
- Lázaro, J., Gil, E., Bailón, R., Mincholé, A., & Laguna, P. (2013). Deriving respiration from photoplethysmographic pulse width. *Medical & biological engineering & computing*, *51*(1-2), 233–242.
- Li, H., Wang, X., Chen, L., & Li, E. (2014). Denoising and R-peak detection of electrocardiogram signal based on EMD and improved approximate envelope. *Circuits, Systems, and Signal Processing*, *33*(4), 1261–1276.
- Li, J., Jin, J., Chen, X., Sun, W., & Guo, P. (2010). Comparison of respiratory-induced variations in photoplethysmographic signals. *Physiological measurement*, *31*(3), 415.
- Li, Y., Yan, H., Zhang, L., & Yang, Y. (2014). Respiratory modulation on the time span and amplitude indices of Electrocardiogram and Photoplethysmogram. In *2014 IEEE International Conference on Mechatronics and Automation* (pp.

1643–1648).

- Littmann, L. (2015). *Respiratory artifact: A second vital sign on the electrocardiogram*. CLEVELAND CLINIC 9500 EUCLID AVE, CLEVELAND, OH 44106 USA.
- Littmann, L., Rennyson, S. L., Wall, B. P., & Parker, J. M. (2008). Significance of respiratory artifact in the electrocardiogram. *The American Journal of Cardiology*, *102*(8), 1090–1096.
- Lu, Y., Yan, J., & Yam, Y. (2009). Model-based ECG denoising using empirical mode decomposition. In *2009 IEEE International Conference on Bioinformatics and Biomedicine* (pp. 191–196).
- Maglaveras, N., Stamkopoulos, T., Diamantaras, K., Pappas, C., & Strintzis, M. (1998). ECG pattern recognition and classification using non-linear transformations and neural networks: a review. *International journal of Medical Informatics*, *52*(1), 191–208.
- Malik, M., Bigger, J. T., Camm, A. J., Kleiger, R. E., Malliani, A., Moss, A. J., & Schwartz, P. J. (1996). Heart Rate Variability: Standards of Measurement, Physiological Interpretation, and Clinical Use. *European heart journal*, *17*(3), 354–381.
- Malmivuo, J., & Plonsey, R. (1995). *Bioelectromagnetism: principles and applications of bioelectric and biomagnetic fields*. Oxford University Press, USA.
- Margolis, P., & Gadomski, A. (1998). Does this infant have pneumonia? *Jama*, *279*(4), 308–313.
- Milic-Emili, J., Rocca, E., & D Angelo, E. (1999). Work of breathing. In *Basics of respiratory mechanics and artificial ventilation* (pp. 165–175). Springer.
- Mlgaard, R. R., Larsen, P., & Håkonsen, S. J. (2016). Effectiveness of respiratory rates in determining clinical deterioration: a systematic review protocol. *JBIC Database of Systematic Reviews and Implementation Reports*, *14*(7), 19–27.
- Moody, G. B., Mark, R. G., Zoccola, A., & Mantero, S. (1985). Derivation of respiratory signals from multi-lead ECGs. *Computers in Cardiology*, *12*(1985), 113–116.
- Mukhopadhyay, S., Mitra, M., & Mitra, S. (2011). Time plane ECG feature extraction using Hilbert transform, variable threshold and slope reversal approach. In *Communication and Industrial Application (ICCIA), 2011 International Conference on* (pp. 1–4).
- National Collaborating Centre for Women’s and Children’s Health (UK). (2013). Feverish illness in children: assessment and initial management in children younger than 5 years.
- National Institute for Health and Care Excellence (NICE). (2007). *Acutely ill adults in hospital: recognising and responding to deterioration*. Retrieved 2007-07-25, from <https://www.nice.org.uk/guidance/cg50>
- Nayan, A., Risman, N., & Jaafar, R. (2015). Breathing rate estimation from a single-

- lead electrocardiogram acquisition system. *International Journal of Applied Engineering Research*, 10(17), 38154–38158.
- Nemati, S., Malhotra, A., & Clifford, G. D. (2010). Data fusion for improved respiration rate estimation. *EURASIP Journal on Advances in Signal Processing*, 2010, 10.
- Nimunkar, Amit J, & Tompkins, W. J. (2007). R-peak detection and signal averaging for simulated stress ECG using EMD. In *2007 29th Annual International Conference of the IEEE Engineering in Medicine and Biology Society* (pp. 1261–1264).
- Orphanidou, C. (2017). Derivation of respiration rate from ambulatory ECG and PPG using Ensemble Empirical Mode Decomposition: Comparison and Fusion. *Computers in Biology and Medicine*, 81, 45–54.
- Orphanidou, C., Bonnici, T., Charlton, P., Clifton, D., Vallance, D., & Tarassenko, L. (2014). Signal-quality indices for the electrocardiogram and photoplethysmogram: Derivation and applications to wireless monitoring. *IEEE Journal of Biomedical and Health Informatics*, 19(3), 832–838.
- Orphanidou, C., Bonnici, T., Vallance, D., Darrell, A., Charlton, P., & Tarassenko, L. (2012). A method for assessing the reliability of heart rates obtained from ambulatory ECG. In *2012 IEEE 12th International Conference on Bioinformatics & Bioengineering (BIBE)* (pp. 193–196).
- Orphanidou, C., Brain, O., Feldmar, J., Khan, S., Price, J., & Tarassenko, L. (2009). Spectral fusion for estimating respiratory rate from the ECG. In *2009 9th International Conference on Information Technology and Applications in Biomedicine* (pp. 1–4).
- Orphanidou, C., Fleming, S., Shah, S. A., & Tarassenko, L. (2013). Data fusion for estimating respiratory rate from a single-lead ECG. *Biomedical Signal Processing and Control*, 8(1), 98–105.
- Pahlm, O., & Sörnmo, L. (1984). Software QRS detection in ambulatory monitoring - A review. *Medical and Biological Engineering and Computing*, 22(4), 289–297.
- Pan, J., & Tompkins, W. J. (1985). A real-time QRS detection algorithm. *IEEE transactions on Biomedical Engineering*(3), 230–236.
- Pandia, K., Inan, O. T., & Kovacs, G. T. (2013). A frequency domain analysis of respiratory variations in the seismocardiogram signal. In *2013 35th Annual International Conference of the IEEE Engineering in Medicine and Biology Society (EMBC)* (pp. 6881–6884).
- Pandia, K., Inan, O. T., Kovacs, G. T., & Giovangrandi, L. (2012). Extracting respiratory information from seismocardiogram signals acquired on the chest using a miniature accelerometer. *Physiological Measurement*, 33(10), 1643.
- Pandit, P. B., Courtney, S. E., Pyon, K. H., Saslow, J. G., & Habib, R. H. (2001). Work of breathing during constant-and variable-flow nasal continuous positive airway pressure in preterm neonates. *Pediatrics*, 108(3), 682–685.

- Pearson, G. A. (2008). *Why children die: A pilot study 2006: May 2008 england (south west, north east and west midlands), wales and northern ireland*. CEMACH.
- Prasad, S. T., & Varadarajan, S. (2013). Heart rate detection using Hilbert transform. *International Journal of Research in Engineering and Technology*, 2, 508–513.
- Proakis, J. G., & Manolakis, D. G. (1996). *Digital Signal Processing (3rd Ed.): Principles, Algorithms, and Applications*. Upper Saddle River, NJ, USA: Prentice-Hall, Inc.
- Rajagopalan, P., & Ramachandran, S. (2017). ECG derived respiratory rate estimation for wearable devices. In *2017 International Conference on Computational Intelligence in Data Science (ICCIDS)* (pp. 1–5).
- Reinvuo, T., Hannula, M., Sorvoja, H., Alasaarela, E., & Myllyla, R. (2006). Measurement of respiratory rate with high-resolution accelerometer and EMFit pressure sensor. In *Proceedings of the 2006 IEEE Sensors Applications Symposium, 2006*. (pp. 192–195).
- Rezuş, C., Moga, V. D., Ouatu, A., & Floria, M. (2015). QT interval variations and mortality risk: Is there any relationship? *Anatolian Journal of Cardiology*, 15(3), 255.
- Royal College of Paediatrics and Child Death (RCPCH). (2014). *Why children die: death in infants, children and young people int the UK, Part A*. Retrieved 2014-05-31, from <https://www.rcpch.ac.uk/resources/why-children-die-research-recommendations>
- Royal College of Physicians. (2017). *National Early Warning Score (NEWS) 2*. Retrieved from <https://www.rcplondon.ac.uk/projects/outputs/national-early-warning-score-news-2>
- Ruangsuwana, R., Velikic, G., & Bocko, M. (2010). Methods to extract respiration information from ECG signals. In *2010 IEEE International Conference on Acoustics, Speech and Signal Processing* (pp. 570–573).
- Sadr, N., & de Chazal, P. (2016). Comparing ECG derived respiratory signals and chest respiratory signal for the detection of obstructive sleep apnoea. In *2016 Computing in Cardiology Conference (CinC)* (pp. 1029–1032).
- Santamaria, I., Pokharel, P. P., & Principe, J. C. (2006). Generalized correlation function: definition, properties, and application to blind equalization. *IEEE Transactions on Signal Processing*, 54(6), 2187–2197.
- Schinkel, A. F., Elhendy, A., van Domburg, R. T., Biagini, E., Rizzello, V., Veltman, C. E., . . . Poldermans, D. (2009). Prognostic significance of QRS duration in patients with suspected coronary artery disease referred for noninvasive evaluation of myocardial ischemia. *The American Journal of Cardiology*, 104(11), 1490–1493.

- Shah, S. A. (2012). *Vital sign monitoring and data fusion for paediatric triage* (Unpublished doctoral dissertation). Oxford University, UK.
- Shah, S. A., Fleming, S., Thompson, M., & Tarassenko, L. (2015). Respiratory rate estimation during triage of children in hospitals. *Journal of Medical Engineering & Technology*, *39*(8), 514–524.
- Sharma, H., Sharma, K., & Bhagat, O. L. (2015). Respiratory rate extraction from single-lead ECG using homomorphic filtering. *Computers in Biology and Medicine*, *59*, 80–86.
- Sierra-Alonso, E. F., Sepúlveda-Cano, L. M., Bailón-Luesma, R., Laguna, P., & Castellanos-Dominguez, G. (2013). Estimating respiratory frequency from HRV during treadmill exercise testing. In *Computing in Cardiology 2013* (pp. 121–124).
- Sievi, N. A., Clarenbach, C. F., Camen, G., Rossi, V. A., van Gestel, A. J., & Kohler, M. (2014). High prevalence of altered cardiac repolarization in patients with COPD. *BMC Pulmonary Medicine*, *14*(1), 55.
- Sobron, A., Romero, I., & Lopetegi, T. (2010). Evaluation of methods for estimation of respiratory frequency from the ECG. In *2010 Computing in Cardiology* (pp. 513–516).
- Stewart, M., Werneke, U., MacFaul, R., Taylor-Meek, J., Smith, H., & Smith, I. (1998). Medical and social factors associated with the admission and discharge of acutely ill children. *Archives of Disease in Childhood*, *79*(3), 219–224.
- Stoller, J. K., & Hill, N. S. (2012). 103 - respiratory monitoring in critical care. In L. Goldman & A. I. Schafer (Eds.), *Goldman's cecil medicine (twenty fourth edition)* (Twenty Fourth Edition ed., p. 626 - 629). Philadelphia: W.B. Saunders. doi: <https://doi.org/10.1016/B978-1-4377-1604-7.00103-2>
- Stuart, A., Kendall, M. G., et al. (1963). *The advanced theory of statistics*. Griffin.
- Tadi, M. J., Koivisto, T., Pänkäälä, M., & Paasio, A. (2014). Accelerometer-based method for extracting respiratory and cardiac gating information for dual gating during nuclear medicine imaging. *Journal of Biomedical Imaging*, *2014*, 6.
- Tanskanen, J. M., & Viik, J. J. (2012). Independent Component Analysis in ECG Signal Processing. In *Advances in Electrocardiograms-Methods and Analysis*. InTech.
- Taouli, S., & Bereksi-Reguig, F. (2011). Detection of QRS complexes in ECG signals based on Empirical Mode Decomposition. *Global Journal of Computer Science and Technology*, *11*(20).
- Tayel, M. B., & AlSaba, E. I. (2015). Poincaré plot for Heart Rate Variability. *World Academy of Science, Engineering and Technology, International Journal of Medical, Health, Biomedical, Bioengineering and Pharmaceutical Engineering*, *9*(9), 708–711.

- Thakor, N. V. (1999). Biopotentials and electrophysiology measurement. *The Measurement, Instrumentation, and Sensors Handbook*, 74.
- Thompson, M., Mayon-White, R., Harnden, A., Perera, R., McLeod, D., & Mant, D. (2008). Using vital signs to assess children with acute infections: a survey of current practice. *Br J Gen Pract*, 58(549), 236–241.
- Tiinanen, S., Noponen, K., Tulppo, M., Kiviniemi, A., & Seppänen, T. (2015). ECG-derived respiration methods: Adapted ICA and PCA. *Medical Engineering & Physics*, 37(5), 512–517.
- Todoran, G., Holonec, R., & Iakab, C. (2008). Discrete Hilbert transform. Numeric algorithms. *Acta Electrotehnica*, 49(4), 485–490.
- Varon, C., & Van Huffel, S. (2015). ECG-derived respiration for ambulatory monitoring. In *2015 Computing in Cardiology Conference (CinC)* (pp. 169–172).
- Vogel, B., Claessen, B. E., Arnold, S. V., Chan, D., Cohen, D. J., Giannitsis, E., ... Mehran, R. (2019). ST-segment elevation myocardial infarction. *Nature Reviews Disease Primers*, 5(1), 39.
- Xiang, Y., Lin, Z., & Meng, J. (2018). Automatic QRS complex detection using two-level convolutional neural network. *Biomedical Engineering Online*, 17(1), 13.
- Yang, X.-L., & Tang, J.-T. (2008). Hilbert-Huang transform and Wavelet transform for ECG detection. In *Wireless Communications, Networking and Mobile Computing, 2008. WiCOM'08. 4th International Conference on* (pp. 1–4).
- Zakeri, V., Akhbardeh, A., Alamdari, N., Fazel-Rezai, R., Paukkunen, M., & Tavakolian, K. (2016). Analyzing seismocardiogram cycles to identify the respiratory phases. *IEEE Transactions on Biomedical Engineering*, 64(8), 1786–1792.
- Zanetti, J. M., & Salerno, D. M. (1991). Seismocardiography: a technique for recording precordial acceleration. In *[1991] Computer-Based Medical Systems@ m_Proceedings of the Fourth Annual IEEE Symposium* (pp. 4–9).
- Zanetti, J. M., & Tavakolian, K. (2013). Seismocardiography: Past, present and future. In *2013 35th annual international conference of the IEEE engineering in medicine and biology society (EMBC)* (pp. 7004–7007).
- Zhu, W., Zhao, H., & Chen, X. (2010). A new QRS detector based on empirical mode decomposition. In *Signal Processing (ICSP), 2010 IEEE 10th International Conference on* (pp. 1–4).

Appendix A

Results related to Capnabase dataset

The results on BR estimation for Capnabase dataset in Chapter 5 were summarised for easy reading, rather than being given in full. Additional result tables are now provided for completeness. The following tables illustrate the estimated BR for each one minute window of the 8 minutes long ECG recordings from Capnabase dataset from the EDR, RSA, PCADR, ICADR and EMDDR methods. Moreover, the results from frequency and time domain analysis are also provided, along with the reference BR of each one minute window.

EDR method	1 min	2 min	3 min	4 min	5 min	6 min	7 min	8 min
capno9 (ref)	18	18	18	21	20	19	19	20
DFT	18	17	18	22	20	19	19	20
CSD	18	17	18	20	20	19	19	19
3PT	20	24	27	24	25	21	32	28
P2T	18	17	18	21	20	19	20	22
capno15 (ref)	29	29	29	29	29	29	29	29
DFT	29	29	29	29	29	29	29	29
CSD	29	29	29	29	29	29	29	28
3PT	30	32	33	31	30	32	32	30
P2T	29	29	29	29	29	29	29	29
capno16 (ref)	10	10	10	10	10	10	10	10
DFT	10	10	10	10	10	10	10	10
CSD	10	10	10	10	10	10	10	10
3PT	35	35	37	29	36	30	35	25
P2T	13	10	10	10	12	15	10	11

capno18 (ref)	39	38	37	37	36	35	35	33
DFT	39	37	36	35	35	34	32	31
CSD	39	37	36	35	35	34	32	30
3PT	43	40	38	39	40	39	34	36
P2T	38	37	35	33	34	31	30	30
capno23 (ref)	23	23	22	22	21	21	21	21
DFT	23	24	22	22	21	21	21	22
CSD	23	23	22	22	21	21	21	21
3PT	32	36	37	33	32	30	29	27
P2T	24	24	23	20	22	23	21	18
capno32 (ref)	11	12	12	15	11	10	14	14
DFT	22	12	12	15	13	14	11	14
CSD	2	12	12	1	1	1	19	1
3PT	31	31	28	28	30	28	25	27
P2T	17	18	17	15	19	18	17	20
capno35 (ref)	24	23	24	23	25	25	32	
DFT	25	22	23	23	23	23	25	
CSD	25	24	23	23	23	23	26	
3PT	38	39	35	38	39	39	35	
P2T	25	23	24	23	24	24	25	
capno38 (ref)	18	18	19	18	18	22	23	22
DFT	18	18	19	19	18	18	23	22
CSD	18	18	19	19	18	19	23	22
3PT	30	30	30	28	24	24	28	27
P2T	19	20	22	19	20	20	23	22
capno103 (ref)	18	18	18	18	18	18	18	18
DFT	18	18	18	18	18	18	18	18
CSD	18	18	18	18	18	18	18	18
3PT	34	30	27	31	28	31	29	26
P2T	18	18	18	19	18	19	18	18
capno104 (ref)	11	11	11	11	11	11	11	11
DFT	11	11	11	11	11	11	11	11
CSD	11	11	11	11	11	11	11	11
3PT	20	23	26	21	22	22	21	24
P2T	12	11	12	12	11	12	12	12
capno105 (ref)	10	10	10	10	10	10	10	10
DFT	10	10	10	10	10	10	10	10
CSD	10	10	10	10	10	10	10	10
3PT	22	16	18	21	19	23	22	18

P2T	11	11	12	10	12	10	10	10
capno121 (ref)	9	9	9	9	9	9	9	9
DFT	9	9	9	9	9	9	9	9
CSD	9	9	9	9	9	9	9	9
3PT	17	15	17	18	16	22	16	20
P2T	9	11	11	9	10	10	10	9
capno122 (ref)	9	9	9	9	9	9	9	9
DFT	9	9	9	9	9	9	9	9
CSD	9	9	9	9	9	9	9	9
3PT	19	17	17	16	16	16	15	18
P2T	12	11	10	10	10	10	10	10
capno125 (ref)	15	14	14	14	14	15	14	14
DFT	15	14	14	14	14	15	14	14
CSD	15	14	14	14	14	15	14	14
3PT	16	17	15	16	17	18	19	20
P2T	16	15	15	15	15	15	15	15
capno127 (ref)	18	18	18	19	18	18	17	18
DFT	19	18	18	19	18	18	18	17
CSD	19	18	18	19	18	18	18	16
3PT	24	22	22	21	23	23	22	20
P2T	19	18	18	19	18	18	18	18
capno128 (ref)	12	13	12	11	12	12	13	13
DFT	12	13	12	12	11	13	13	13
CSD	12	13	12	12	12	13	13	13
3PT	23	26	26	23	21	23	23	23
P2T	13	14	13	13	13	13	13	14
capno134 (ref)	14	14	14	14	14	14	14	14
DFT	14	14	14	14	14	14	14	14
CSD	14	14	14	14	14	14	14	14
3PT	30	26	22	24	24	25	23	27
P2T	15	15	15	15	15	15	14	15
capno142 (ref)	15	15	15	15	15	15	15	15
DFT	15	15	15	15	15	15	15	15
CSD	15	15	15	15	15	15	15	15
3PT	24	29	31	32	30	27	27	30
P2T	17	17	22	20	17	17	17	17
capno147 (ref)	11	11	11	11	11	11	11	11
DFT	11	11	11	11	11	11	11	11
CSD	11	11	11	11	11	11	11	11
3PT	21	24	26	21	23	25	24	22

P2T	12	17	18	12	17	15	18	14
capno148 (ref)	10	10	10	10	10	10	10	10
DFT	10	10	10	10	10	10	10	10
CSD	10	10	10	10	10	10	10	10
3PT	18	21	23	19	19	20	22	17
P2T	10	11	11	11	12	10	12	11
capno311 (ref)	12	12	12	12	12	12	12	12
DFT	12	12	12	12	12	12	12	12
CSD	12	12	12	12	12	12	12	12
3PT	19	21	15	18	20	17	19	18
P2T	12	12	12	12	14	12	14	14
capno312 (ref)	7	7	7	7	7	7	7	7
DFT	7	7	7	7	7	11	8	7
CSD	7	7	7	7	7	15	9	7
3PT	24	21	18	16	14	19	20	21
P2T	8	6	6	7	6	10	13	12
capno313 (ref)	10	10	10	10	10	10	10	10
DFT	10	10	10	10	10	10	10	10
CSD	10	10	10	10	10	10	10	10
3PT	21	18	20	15	17	17	19	17
P2T	13	10	11	10	10	10	11	10
capno322 (ref)	17	18	18	18	18	18	19	20
DT	17	17	18	18	18	18	18	18
CSD	17	17	18	18	18	18	18	18
3PT	18	18	20	18	19	21	20	19
P2T	18	18	19	18	19	20	19	19
capno325 (ref)	10	10	10	10	10	10	10	10
DFT	10	10	10	10	10	10	10	10
CSD	10	10	10	10	10	10	10	10
3PT	24	21	26	23	27	23	25	24
P2T	16	15	16	15	19	14	20	16

Table A.1: EDR method for Capnabase

RSA method	1 min	2 min	3 min	4 min	5 min	6 min	7 min	8 min
capno5 (ref)	18	18	18	21	20	19	19	20
DFT	18	17	18	5	20	19	19	20
CSD	18	17	18	22	20	19	20	20

3PT	22	21	21	32	28	24	25	28
P2T	18	17	18	18	20	20	17	20
capno15 (ref)	29	29	29	29	29	29	29	29
DFT	29	29	29	29	29	29	29	29
CSD	29	29	29	29	29	29	29	29
3PT	32	31	32	35	32	33	32	33
P2T	29	29	29	29	29	29	29	29
capno16 (ref)	10	10	10	10	10	10	10	10
DFT	4	10	10	10	40	9	6	4
CSD	4	4	4	4	8	1	6	4
3PT	52	50	50	53	49	44	42	47
P2T	31	30	30	35	34	17	20	17
capno18 (ref)	39	38	37	37	36	35	35	33
DFT	39	37	42	35	35	34	32	30
CSD	39	37	1	35	35	34	32	30
3PT	54	54	60	53	52	56	54	54
P2T	39	40	39	41	41	36	46	36
capno23 (ref)	23	24	22	22	21	21	21	21
DFT	23	24	22	22	21	21	20	22
CSD	23	24	22	22	21	21	21	21
3PT	32	31	31	27	27	27	27	28
P2T	23	24	23	22	21	21	22	24
capno32 (ref)	11	12	12	15	11	10	14	14
DFT	6	12	12	15	9	7	12	14
CSD	5	12	12	15	14	7	13	14
3PT	23	19	24	19	27	20	27	30
P2T	9	11	13	16	11	11	14	16
capno35 (ref)	24	23	24	23	25	25	32	
DFT	7	5	23	7	8	7	9	
CSD	5	5	1	7	4	1	14	
3PT	46	39	43	41	40	46	46	
P2T	24	24	31	25	19	30	19	
capno38 (ref)	18	18	19	18	18	22	23	22
DFT	18	18	19	19	18	18	23	4
CSD	18	18	19	19	18	19	23	1
3PT	24	21	23	19	19	27	35	41
P2T	17	18	19	19	18	20	25	17
capno103 (ref)	18	18	18	18	18	18	18	18
DFT	18	18	18	18	18	18	18	18
CSD	18	18	18	18	18	18	18	18

3PT	40	39	41	37	39	40	40	43
P2T	22	25	24	22	27	21	26	28
capno104 (ref)	11	11	11	11	11	11	11	11
DFT	11	11	11	11	11	11	11	11
CSD	11	11	11	11	11	11	11	11
3PT	52	49	42	49	45	47	46	43
P2T	31	23	30	23	20	18	20	18
capno105 (ref)	10	10	10	10	10	10	10	10
DFT	10	10	10	10	10	20	10	10
CSD	10	10	1	10	10	1	10	10
3PT	17	21	20	20	21	22	20	18
P2T	11	11	8	12	13	8	12	13
capno121 (ref)	9	9	9	9	9	9	9	9
DFT	4	5	4	5	6	9	5	4
CSD	4	1	9	5	4	5	1	3
3PT	22	21	23	23	21	23	21	26
P2T	13	9	10	10	11	16	9	15
capno122 (ref)	9	9	9	9	9	9	9	9
DFT	9	9	9	9	9	9	9	5
CSD	9	9	9	9	9	9	9	9
3PT	24	17	19	15	20	17	17	27
P2T	9	12	12	11	12	10	10	10
capno125 (ref)	15	14	14	14	14	15	14	14
DFT	15	14	14	14	14	15	14	14
CSD	15	14	14	14	14	15	14	14
3PT	18	16	18	16	17	17	21	18
P2T	16	15	15	15	15	15	15	16
capno127 (ref)	18	18	18	19	18	18	17	18
DFT	11	12	17	11	12	10	5	17
CSD	12	1	1	13	1	13	18	17
3PT	23	21	19	20	21	23	24	18
P2T	16	14	14	16	13	14	16	15
capno128 (ref)	12	13	12	11	12	12	13	13
DFT	6	4	4	30	6	13	13	6
CSD	6	4	4	5	1	13	17	1
3PT	32	21	33	46	36	23	24	20
P2T	10	8	8	11	8	14	13	12
capno134 (ref)	14	14	14	14	14	14	14	14
DFT	4	4	4	4	4	11	5	10
CSD	4	4	4	4	4	1	1	3

3PT	78	60	43	49	46	28	64	40
P2T	7	8	11	5	6	7	7	8
capno142 (ref)	15	15	15	15	15	15	15	15
DFT	15	15	15	15	15	15	15	15
CSD	25	15	15	1	15	15	15	15
3PT	34	28	28	29	29	27	29	33
P2T	21	17	17	18	18	18	17	16
capno147 (ref)	11	11	11	11	11	11	11	11
DFT	25	8	26	16	32	31	5	20
CSD	2	2	2	6	3	4	2	1
3PT	61	46	41	39	43	36	47	32
P2T	8	13	17	10	16	11	20	9
capno148 (ref)	10	10	10	10	10	10	10	10
DFT	10	5	5	5	5	7	6	10
CSD	10	4	5	5	7	7	6	10
3PT	26	24	26	23	26	22	24	25
P2T	15	11	12	13	14	10	13	13
capno311 (ref)	12	12	12	12	12	12	12	12
DFT	5	7	4	4	5	4	4	6
CSD	5	7	8	6	1	4	2	1
3PT	33	21	24	16	19	20	19	29
P2T	9	11	10	9	6	12	9	9
capno312 (ref)	7	7	7	7	7	7	7	7
DFT	7	7	7	7	7	7	7	7
CSD	7	7	7	7	7	7	7	7
3PT	26	15	16	16	16	15	18	24
P2T	10	10	10	9	11	7	11	12
capno313 (ref)	10	10	10	10	10	10	10	10
DFT	10	20	10	10	10	10	4	10
CSD	10	29	10	6	10	1	6	10
3PT	29	27	29	27	28	28	27	32
P2T	19	21	20	16	22	23	14	17
capno322 (ref)	17	18	18	18	18	18	19	20
DFT	17	17	18	18	18	18	18	34
CSD	17	17	18	18	18	18	18	1
3PT	20	20	19	23	22	22	24	38
P2T	18	20	18	19	18	18	18	15
capno325 (ref)	10	10	10	10	10	10	10	10
DFT	4	20	4	5	4	7	5	4
CSD	4	1	1	1	6	6	1	2

3PT	67	28	27	28	26	28	38	68
P2T	16	15	12	13	10	16	15	15

Table A.2: RSA method for Capnabase

PCADR method	1 min	2 min	3 min	4 min	5 min	6 min	7 min	8 min
capno9 (ref)	18	18	18	21	20	19	19	20
DFT	18	18	18	20	19	19	20	20
CSD	18	18	18	20	19	19	20	20
3PT	21	22	23	21	21	22	25	30
P2T	18	18	18	29	19	19	20	21
capno15	29	29	29	29	29	29	29	29
DFT	29	29	29	29	29	29	29	29
CSD	29	29	29	29	29	29	29	29
3PT	31	31	32	29	31	32	32	30
P2T	29	29	29	29	29	29	29	29
capno16 (ref)	10	10	10	10	10	10	10	10
DFT	10	10	10	10	10	21	10	10
CSD	10	10	10	10	10	10	10	10
3PT	33	32	36	29	34	34	34	32
P2T	13	11	10	10	13	14	10	15
capno18 (ref)	39	38	37	37	36	35	35	33
DFT	38	37	36	35	35	34	32	30
CSD	38	37	36	36	35	34	32	30
3PT	42	40	40	41	40	44	40	36
P2T	38	37	35	36	35	33	32	30
capno23 (ref)	23	24	22	22	21	21	21	21
DFT	22	23	21	22	21	21	21	22
CSD	22	23	22	22	21	21	21	22
3PT	31	36	38	37	36	36	36	37
P2T	23	23	22	22	21	22	22	22
capno32 (ref)	11	12	12	15	11	10	14	14
DFT	9	12	12	15	13	11	12	29
CSD	1	12	12	15	14	11	11	14
3PT	32	33	29	30	30	32	32	33
P2T	17	17	16	16	18	21	15	16
capno35	24	23	24	23	25	25	32	
DFT	26	22	24	23	24	23	25	

CSD	26	22	24	23	23	23	25	
3PT	45	38	37	38	40	41	34	
P2T	27	24	24	23	24	27	25	
capno38 (ref)	18	18	19	18	18	22	23	22
DFT	19	19	20	19	19	19	29	19
CSD	19	19	20	19	19	19	20	19
3PT	36	33	33	29	23	27	25	25
P2T	20	22	23	21	20	21	20	19
capno103 (ref)	18	18	18	18	18	18	18	18
DFT	18	18	18	18	18	18	18	18
CSD	18	18	18	18	18	18	18	18
3PT	34	31	29	31	28	31	26	26
P2T	18	18	18	19	19	19	18	18
capno104 (ref)	11	11	11	11	11	11	11	11
DFT	11	11	11	11	11	11	11	11
CSD	11	11	11	11	11	11	11	11
3PT	23	21	24	19	21	21	18	24
P2T	11	11	12	12	12	12	12	13
capno105 (ref)	10	10	10	10	10	10	10	10
DFT	10	10	10	10	10	11	10	10
CSD	10	10	10	10	10	10	10	10
3PT	21	18	18	19	21	23	17	18
P2T	11	11	12	11	10	10	10	11
capno121 (ref)	9	9	9	9	9	9	9	9
DFT	9	9	9	9	9	9	9	9
CSD	9	9	9	9	9	9	9	9
3PT	15	15	17	15	16	18	15	19
P2T	9	9	9	9	10	10	10	10
capno122 (ref)	9	9	9	9	9	9	9	9
DFT	9	9	9	9	9	9	9	8
CSD	9	9	9	9	9	9	9	8
3PT	19	17	19	16	18	18	18	20
P2T	11	9	10	10	10	10	10	9
capno125 (ref)	15	14	14	14	14	15	14	14
DFT	15	14	14	15	14	14	14	14
CSD	15	14	14	15	14	14	14	14
3PT	16	16	15	17	16	18	20	17
P2T	15	15	15	15	15	15	15	15
capno127 (ref)	18	18	18	19	18	18	17	18
DFT	19	18	18	19	18	17	17	16

CSD	19	18	18	19	18	19	17	16
3PT	25	23	22	23	25	24	21	26
P2T	21	18	19	19	19	18	17	17
capno128 (ref)	12	13	12	11	12	12	13	13
DFT	12	13	12	12	11	12	12	13
CSD	12	13	12	12	12	12	12	13
3PT	28	26	26	26	25	23	26	22
P2T	13	13	13	12	12	13	13	14
capno134 (ref)	14	14	14	14	14	14	14	14
DFT	15	15	14	14	14	21	14	9
CSD	15	15	14	14	14	3	14	1
3PT	33	29	24	24	26	25	26	25
P2T	15	15	15	14	15	15	15	15
capno142 (ref)	15	15	15	15	15	15	15	15
DFT	5	15	15	30	15	15	15	15
CSD	5	15	15	15	15	15	15	15
3PT	29	30	29	32	29	30	28	30
P2T	20	18	21	23	17	16	20	16
capno147 (ref)	11	11	11	11	11	11	11	11
DFT	12	7	31	15	17	21	28	14
CSD	2	1	2	2	2	1	2	1
3PT	24	27	30	24	26	29	27	23
P2T	15	17	21	18	14	19	22	17
capno148 (ref)	10	10	10	10	10	10	10	10
DFT	10	10	10	10	10	10	10	10
CSD	10	10	10	10	10	10	10	10
3PT	19	21	23	20	19	21	23	19
P2T	10	11	11	11	11	10	14	10
capno311 (ref)	12	12	12	12	12	12	12	12
DFT	11	11	12	12	12	12	13	12
CSD	11	12	12	12	12	12	13	12
3PT	18	18	17	16	22	20	20	21
P2T	11	12	13	13	14	13	15	13
capno312 (ref)	7	7	7	7	7	7	7	7
DFT	7	7	7	7	7	7	21	7
CSD	7	7	7	7	7	20	21	7
3PT	21	20	19	14	15	23	22	22
P2T	17	14	10	10	10	16	21	15
capno313 (ref)	10	10	10	10	10	10	10	10
DFT	10	10	10	10	10	10	10	10

CSD	10	10	10	10	10	10	10	10
3PT	19	19	21	15	17	19	29	18
P2T	13	11	11	10	11	11	10	10
capno322 (ref)	17	18	18	18	18	18	19	20
DFT	18	18	19	18	18	18	18	17
CSD	18	18	19	18	18	18	18	17
3PT	18	18	20	19	20	23	22	20
P2T	18	18	19	17	18	19	19	17
capno315 (ref)	10	10	10	10	10	10	10	10
DFT	10	10	10	10	10	10	10	4
CSD	1	10	10	10	10	10	10	1
3PT	56	28	26	27	29	27	31	66
P2T	22	12	15	14	18	15	19	17

Table A.3: PCADR method for Capnobase

ICADR method	1 min	2 min	3 min	4 min	5 min	6 min	7 min	8 min
capno9 (ref)	18	18	18	21	20	19	19	20
DFT	18	18	18	20	19	19	20	20
CSD	18	18	18	20	19	19	20	20
3PT	20	21	22	23	19	24	23	27
P2T	18	18	18	20	19	19	22	21
capno15 (ref)	29	29	29	29	29	29	29	29
DFT	29	29	29	29	29	29	29	29
CSD	29	29	29	29	29	29	29	29
3PT	29	29	30	29	29	30	29	29
P2T	29	29	29	29	29	29	29	29
capno16 (ref)	10	10	10	10	10	10	10	10
DFT	10	10	10	10	10	10	10	10
CSD	10	10	10	10	10	10	10	10
3PT	35	35	36	31	37	32	38	40
P2T	16	17	16	12	13	14	16	19
capno18 (ref)	39	38	37	37	36	35	35	33
DFT	38	37	36	35	35	34	32	31
CSD	39	37	36	36	35	31	32	2
3PT	41	42	40	42	47	50	46	43
P2T	37	37	35	38	38	39	38	33
capno23 (ref)	23	24	22	22	21	21	21	21

DFT	22	23	21	22	21	21	21	22
CSD	22	23	22	22	21	21	21	22
3PT	30	31	31	25	24	25	29	25
P2T	25	23	25	22	21	21	22	22
capno32 (ref)	11	12	12	15	11	10	14	14
DFT	11	12	12	15	12	6	11	14
CSD	11	12	3	15	1	7	9	14
3PT	30	26	25	25	27	25	27	25
P2T	20	17	15	17	18	9	18	19
capno35 (ref)	24	23	24	23	25	25	32	
DFT	26	22	24	23	24	23	25	
CSD	26	22	24	23	23	23	25	
3PT	36	37	40	42	38	38	37	
P2T	25	23	24	23	23	25	25	
capno38 (ref)	18	18	19	18	18	22	23	22
DFT	19	19	20	19	19	19	20	19
CSD	19	19	20	19	19	19	20	19
3PT	25	27	27	29	23	34	35	32
P2T	19	21	22	19	19	23	21	19
capno103 (ref)	18	18	18	18	18	18	18	18
DFT	18	18	18	18	18	18	18	18
CSD	18	18	18	18	18	18	18	18
3PT	34	25	32	33	24	28	25	24
P2T	20	18	20	18	18	19	18	18
capno104 (ref)	11	11	11	11	11	11	11	11
DFT	11	11	11	11	11	11	11	11
CSD	11	11	11	11	11	11	11	11
3PT	21	26	22	28	25	28	24	35
P2T	11	11	12	12	12	12	12	13
capno105 (ref)	10	10	10	10	10	10	10	10
DFT	10	10	10	10	10	10	10	10
CSD	10	10	10	10	10	10	10	10
3PT	21	18	21	18	17	17	14	21
P2T	12	11	14	10	10	14	11	13
capno121 (ref)	9	9	9	9	9	9	9	9
DFT	9	9	9	9	9	9	9	9
CSD	9	9	9	9	9	9	9	9
3PT	19	15	24	19	18	17	16	18
P2T	9	12	13	11	13	11	12	9

capno122 (ref)	9	9	9	9	9	9	9	9
DFT	9	9	9	9	9	9	9	9
CSD	9	9	9	9	9	9	9	8
3PT	29	23	23	25	29	25	25	26
P2T	17	17	17	19	19	19	15	17
capno125 (ref)	15	14	14	14	14	15	14	14
DFT	15	14	14	15	14	14	14	14
CSD	1	14	17	15	14	15	3	14
3PT	25	28	28	22	30	29	26	25
P2T	20	22	20	18	20	23	21	18
capno127 (ref)	18	18	18	19	18	18	17	18
DFT	19	18	18	19		17	17	16
CSD	19	18	18	19	18	19	17	16
3PT	25	25	21	23	27	21	23	28
P2T	21	18	19	19	19	18	17	17
capno128 (ref)	12	13	12	11	12	12	13	13
DFT	12	13	12	12	11	12	12	13
CSD	12	13	12	12	12	12	12	13
3PT	25	22	25	26	22	25	23	25
P2T	18	18	20	19	15	16	15	16
capno134 (ref)	14	14	14	14	14	14	14	14
DFT	15	15	14	14	14	13	14	13
CSD	15	15	14	14	14	13	14	13
3PT	27	26	25	24	24	25	25	25
P2T	18	18	18	18	19	18	20	17
capno142 (ref)	15	15	15	15	15	15	15	15
DFT	14	15	15	15	15	15	15	15
CSD	15	15	15	15	15	15	15	15
3PT	32	31	31	31	31	32	31	32
P2T	23	20	15	21	19	18	18	18
capno147 (ref)	11	11	11	11	11	11	11	11
DFT	8	28	20	10	7	4	12	10
CSD	2	4	2	6	1	4	2	1
3PT	27	31	29	31	29	28	27	29
P2T	18	23	21	15	23	19	17	22
capno148 (ref)	10	10	10	10	10	10	10	10
DFT	10	10	10	10	10	10	10	10
CSD	10	1	10	10	10	10	10	10
3PT	26	29	27	27	25	31	26	28

P2T	18	21	19	18	16	21	18	16
capno311 (ref)	12	12	12	12	12	12	12	12
DFT	11	11	12	12	12	12	14	15
CSD	11	12	12	12	12	12	13	1
3PT	27	19	24	21	24	26	24	20
P2T	17	13	14	16	18	16	18	13
capno312 (ref)	7	7	7	7	7	7	7	7
DFT	7	7	7	7	7	7	7	7
CSD	7	7	7	7	7	7	7	7
3PT	16	18	16	18	19	15	17	17
P2T	12	11	11	12	9	11	10	15
capno313 (ref)	10	10	10	10	10	10	10	10
DFT	10	10	10	10	10	10	10	10
CSD	10	10	10	10	10	10	10	10
3PT	19	19	20	15	17	18	17	18
P2T	12	11	11	10	11	10	11	10
capno322 (ref)	17	18	18	18	18	18	19	20
DFT	18	18	19	18	18	18	18	18
CSD	18	18	19	18	18	18	18	17
3PT	19	20	20	21	20	23	26	23
P2T	19	19	19	19	18	20	19	18
capno325 (ref)	10	10	10	10	10	10	10	10
DFT	10	10	10	10	10	10	10	11
CSD	10	10	10	10	10	10	10	10
3PT	26	23	28	23	25	21	27	25
P2T	24	24	18	16	15	16	17	14

Table A.4: ICADR method for Capnabase

EMDDR method	1 min	2 min	3 min	4 min	5 min	6 min	7 min	8 min
capno9 (ref)	18	18	18	21	20	19	19	20
DFT	20	18	22	13	14	20	15	20
3PT	21	21	19	18	21	25	20	18
P2T	21	21	19	17	21	25	20	17
capno15 (ref)	29	29	29	29	29	29	29	29
DFT	29	29	29	29	29	29	29	29
3PT	27	27	27	27	23	26	27	25
P2T	26	27	27	27	23	26	27	25

capno16 (ref)	10	11	11	10	11	10	14	10
DFT	10	10	10	10	10	10	10	10
3PT	15	14	14	12	10	12	16	14
P2T	10	14	13	10	10	12	16	10
capno18 (ref)	39	38	37	37	36	35	35	33
DFT	21	22	34	36	35	34	32	31
3PT	27	27	30	31	33	31	35	37
P2T	24	27	30	31	33	31	35	36
capno23 (ref)	23	24	22	22	21	21	21	21
DFT	22	28	22	22	21	21	21	23
3PT	23	25	24	22	21	21	22	21
P2T	21	25	23	22	21	21	22	21
capno32 (ref)	11	12	12	15	11	10	14	14
DFT	11	8	10	7	9	6	9	11
3PT	14	10	12	9	10	8	10	12
P2T	12	10	12	9	10	8	10	11
capno35 (ref)	24	23	24	23	25	25	32	
DFT	27	27	23	25	24	25	25	
3PT	34	27	30	28	30	29	26	
P2T	29	27	30	28	30	29	26	
capno38 (ref)	18	18	19	18	18	22	23	22
DFT	25	21	29	20	20	22	13	22
3PT	27	30	27	30	30	29	24	27
P2T	27	30	27	29	30	28	24	26
capno103 (ref)	18	18	18	18	18	18	18	18
DFT	19	18	18	29	18	20	20	18
3PT	29	27	27	27	28	27	24	26
P2T	29	26	27	27	27	27	23	26
capno104 (ref)	11	11	11	11	11	11	11	11
DFT	11	18	11	11	11	11	11	11
3PT	22	15	15	13	15	11	10	16
P2T	11	15	14	13	15	11	9	13
capno105 (ref)	10	10	10	10	10	10	10	10
DFT	5	8	5	9	8	7	6	19
3PT	8	11	7	12	8	7	8	9
P2T	6	10	7	12	8	7	8	9
capno121 (ref)	9	9	9	9	9	9	9	9
DFT	12	11	15	11	5	10	9	11
3PT	14	14	15	13	10	14	12	12

P2T	14	14	15	13	10	13	12	11
capno122 (ref)	9	9	9	9	9	9	9	9
DFT	12	11	9	12	6	9	7	10
3PT	14	13	11	12	10	11	12	14
P2T	13	12	11	12	8	11	12	12
capno125 (ref)	15	14	14	14	14	15	14	14
DFT	15	16	14	13	18	13	16	14
3PT	21	17	17	14	19	16	16	20
P2T	18	17	17	14	19	16	16	20
capno127 (ref)	18	18	18	19	18	18	17	18
DFT	13	19	17	19	14	17	14	18
3PT	18	19	19	23	18	19	19	20
P2T	17	19	19	23	18	19	19	20
capno128 (ref)	12	13	12	11	12	12	13	13
DFT	4	12	10	12	13	12	18	
3PT	35	11	12	11	11	12	12	11
P2T	11	11	11	11	11	12	9	11
capno134 (ref)	14	14	14	14	14	14	14	14
DFT	8	11	9	11	9	12	9	15
3PT	9	8	12	12	12	13	11	11
P2T	8	7	12	12	12	13	10	11
capno142 (ref)	15	15	15	15	15	15	15	15
DFT	9	12	8	9	10	8	9	15
3PT	10	11	10	13	10	9	12	17
P2T	9	11	10	12	10	9	12	13
capno147 (ref)	11	11	11	11	11	11	11	11
DFT	9	6	6	10	7	6	7	6
3PT	13	9	10	11	10	11	10	10
P2T	11	9	10	9	10	10	10	10
capno148 (ref)	10	10	10	10	10	10	10	10
DFT	12	12	12	12	12	14	13	13
3PT	16	8	10	9	9	7	8	9
P2T	9	6	8	9	9	7	8	9
capno311 (ref)	12	12	12	12	12	12	12	12
DFT	11	9	8	13	11	11	11	11
3PT	12	11	11	12	13	12	12	16
P2T	12	11	11	11	13	12	12	15
capno312 (ref)	7	7	7	7	7	7	7	7
DFT	7	6	7	6	7	7	7	6
3PT	9	7	8	9	6	7	8	8

P2T	7	6	8	7	6	7	8	7
capno313 (ref)	10	10	10	10	10	10	10	10
DFT	6	8	6	9	6	7	9	10
3PT	10	8	7	9	8	9	9	12
P2T	8	8	7	9	8	9	9	9
capno322 (ref)	17	18	18	18	18	18	19	20
DFT	13	17	16	12	19	13	5	13
3PT	16	17	20	19	17	13	13	17
P2T	14	17	20	19	17	13	13	14
capno325 (ref)	10	10	10	10	10	10	10	10
DFT	9	15	12	12	11	10	10	16
3PT	13	17	13	17	11	12	12	16
P2T	11	17	13	17	11	12	12	15

Table A.5: EMDDR method for Capnabase

Appendix B

Results related to BCH ECG database

The results on BR estimation for the BCH ECG data in Chapter 5 were summarised for easy reading, rather than being given in full. Additional result tables are now provided for completeness. The following tables illustrate the estimated BR from the EDR, RSA, PCADR and EMDDR methods. Moreover, the results from frequency and time domain analysis are also provided, along with the reference BR.

Rec	Ref	DFT				CSD		
		EDR	RSA	PCADR	EMDDR	EDR	RSA	PCADR
ecgch1	42	35	35	60	36	35	32	36
ecgch2	65	34	43	35	67	31	57	36
ecgch3	36	27	25	31	45	27	25	26
ecgch4	35	31	32	41	63	31	53	33
ecgch5	54	52	45	50	59	32	71	34
ecgch6	59	34	37	70	62	34	65	45
ecgch7	58	31	40	51	35	34	56	31
ecgch8	48	38	43	42	63	42	60	42
ecgch9	91	36	39	39	59	39	26	31
ecgch10	67	47	42	44	29	47	59	44
ecgch11	46	35	31	35	27	36	35	36
ecgch12	42	44	46	27	65	44	46	27
ecgch13	42	44	38	26	58	59	25	57
ecgch14	64	47	46	49	63	48	47	43
ecgch15	62	36	45	31	67	46	39	33
ecgch16	42	35	34	46	48	39	34	39

ecgch17	49	33	42	51	52	25	48	34
ecgch18	36	33	38	29	67	37	37	22

Table B.1: Frequency domain analysis for BCH ECG data

Rec	Ref	3PT				P2T			
		EDR	RSA	PCADR	EMDDR	EDR	RSA	PCADR	EMDDR
ecgch1	42	51	61	52	62	47	50	44	59
ecgch2	65	51	55	56	64	43	53	46	64
ecgch3	36	46	57	37	65	49	34	33	61
ecgch4	35	42	47	44	62	37	43	39	60
ecgch5	54	59	62	58	60	48	59	51	57
ecgch6	59	59	62	58	60	50	54	56	60
ecgch7	58	56	60	56	61	46	53	50	57
ecgch8	48	59	63	68	62	54	57	54	61
ecgch9	91	51	51	48	62	42	39	42	52
ecgch10	67	59	65	63	64	53	56	52	51
ecgch11	46	58	55	55	60	50	49	44	13
ecgch12	42	49	50	55	62	45	43	49	61
ecgch13	42	56	52	55	62	46	46	47	62
ecgch14	64	51	54	53	63	51	46	46	63
ecgch15	62	57	63	59	63	50	52	50	57
ecgch16	42	47	49	46	64	39	42	42	43
ecgch17	49	49	46	52	62	43	43	41	56
ecgch18	36	43	45	40	65	38	41	36	64

Table B.2: Time domain analysis for BCH ECG data

Appendix C

Results related to BCH EMG database

The results on BR estimation for the BCH EMG data in Chapter 5 were summarised for easy reading, rather than being given in full. Additional result tables are now provided for completeness. The following tables illustrate the estimated BR from the EDR, RSA and PCADR. Moreover, the results from frequency and time domain analysis are also provided, along with the reference BR for each hour.

emgch1 (ref)	54
DFT	10
CSD	28
3PT	29
P2T	21
emgch2 (ref)	28 33
DFT	30 29
CSD	30 30
3PT	37 38
P2T	33 35
emgch3 (ref)	37 34 38 42 40 45
DFT	36 38 44 33 35 34
CSD	36 38 44 34 38 36
3PT	39 40 44 42 46 42
P2T	37 38 43 38 40 39
emgch4 (ref)	84 58 43 36 41 40 53
DFT	35 34 37 37 37 33 38
CSD	36 35 36 37 36 33 32

3PT	41	40	38	37	37	39	44
P2T	38	37	36	37	36	36	41

Table C.1: EDR method for BCH EMG data

emgch1 (ref)	54						
DFT	7						
CSD	28						
3PT	57						
P2T	22						
emgch2 (ref)	28	33					
DFT	28	28					
CSD	28	29					
3PT	35	36					
P2T	31	32					
emgch3 (ref)	37	34	38	42	40	45	
DFT	29	29	31	31	39	28	
CSD	29	28	31	29	39	28	
3PT	35	38	41	40	42	39	
P2T	32	32	37	33	36	33	
emgch4 (ref)	84	58	43	36	41	40	53
DFT	29	29	27	29	28	29	28
CSD	29	29	29	30	28	28	29
3PT	39	38	34	35	34	39	40
P2T	33	33	30	33	31	33	34

Table C.2: RSA method for BCH EMG data

emgch1 (ref)	54	
DFT	18	
CSD	35	
3PT	36	
P2T	19	
emgch2 (ref)	28	33
DFT	30	35
CSD	31	32

3PT	37	39					
P2T	33	34					
emgch3 (ref)	37	34	38	42	40	45	
DFT	38	38	34	34	34	32	
CSD	38	40	39	35	34	30	
3PT	40	41	42	41	42	39	
P2T	38	39	38	37	36	35	
emgch4 (ref)	84	58	43	36	41	40	53
DFT	32	37	36	35	35	34	39
CSD	31	39	37	36	38	36	41
3PT	40	42	38	38	38	49	45
P2T	35	39	36	37	36	37	42

Table C.3: PCADR method for BCH EMG data

Appendix D

Generation of a synthetic ECG signal

The following sections explain how the synthetic ECG signal was created. Details of all the different modes generated (AM, FM and BW) are also included.

D.1 Synthetic ECG signal

In order to generate a synthetic ECG signal of a specific duration, a single ECG beat was first created (Figure D.1) using an example found in Charlton (2016), whose duration is one second. This exemplary beat for the ECG signal was acquired from a young subject (Charlton, 2017). The timestamps and amplitudes of the single beat are given in Table D.1. In order to get an ECG signal of duration T in seconds, we need to repeat the single one second beat T times. More details on the implementation can be found in the MATLAB code given in Listing D.1.

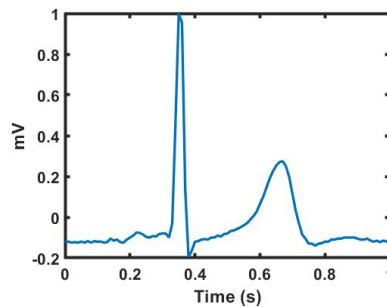


Figure D.1: A single synthetic ECG beat lasting one second

Time (s)	Amplitude (mV)	Time (s)	Amplitude (mV)	Time (s)	Amplitude (mV)
0.00	-0.1200000000000000	0.34	0.46499721063297300	0.68	0.2500002145666950
0.01	-0.1200000000000000	0.35	0.99750074502324600	0.69	0.1975002324472520
0.02	-0.1250000000000000	0.36	0.95499299082131300	0.70	0.1149997615925630
0.03	-0.1225001132570340	0.37	0.1349982117310400	0.71	0.0325003040057223
0.04	-0.1250000000000000	0.38	-0.1949984503516500	0.72	-0.0299992132354528
0.05	-0.1200000000000000	0.39	-0.1650000357611600	0.73	-0.0849997496721898
0.06	-0.1250000000000000	0.40	-0.1199988079628100	0.74	-0.1050000238407440
0.07	-0.1175000655698620	0.41	-0.11749995827372400	0.75	-0.1300000000000000
0.08	-0.1250000000000000	0.42	-0.11000020264632200	0.76	-0.1300000000000000
0.09	-0.1174999582786980	0.43	-0.10749993443795500	0.77	-0.1400000000000000
0.10	-0.1200000000000000	0.44	-0.1099992847776800	0.78	-0.1300000000000000
0.11	-0.1200000000000000	0.45	-0.1000000000000000	0.79	-0.1275001967095850
0.12	-0.12499856955370	0.46	-0.1000000000000000	0.80	-0.1200000000000000
0.13	-0.1225000059601860	0.47	-0.0900000000000000	0.81	-0.1200000000000000
0.14	-0.105000131240910	0.48	-0.09499997615925620	0.82	-0.1100000000000000
0.15	-0.1150000000000000	0.49	-0.08249983907497900	0.83	-0.1100000000000000
0.16	-0.1100000000000000	0.50	-0.0800000000000000	0.84	-0.1050000000000000
0.17	-0.1224999463583260	0.51	-0.06750016092502100	0.85	-0.1050000000000000
0.18	-0.1250000000000000	0.52	-0.06499997615925620	0.86	-0.1000000000000000
0.19	-0.109995589462390	0.53	-0.05749988675646680	0.87	-0.1000000000000000
0.20	-0.1000003576111580	0.54	-0.0500000000000000	0.88	-0.1000000000000000
0.21	-0.089996065808297	0.55	-0.0400000000000000	0.89	-0.1000000000000000
0.22	-0.0750000000000000	0.56	-0.0300000000000000	0.90	-0.104998211944210
0.23	-0.0775001728453928	0.57	-0.01249993443795450	0.91	-0.1100000000000000
0.24	-0.0850000000000000	0.58	0.00500020264632248	0.92	-0.1100000000000000
0.25	-0.0975001490224131	0.59	0.02750004172627550	0.93	-0.1050000000000000
0.26	-0.1000000000000000	0.60	0.06499976159256150	0.94	-0.1149997735129340
0.27	-0.0925001251639052	0.61	0.10000003576111500	0.95	-0.1200000000000000
0.28	-0.094999737518178	0.62	0.14500030992967000	0.96	-0.1150000000000000
0.29	-0.0824998986647591	0.63	0.18999998807820700	0.97	-0.1225001132370340
0.30	-0.0800000000000000	0.64	0.2249996622958600	0.98	-0.1150000000000000
0.31	-0.0800000000000000	0.65	0.25249997019907000	0.99	-0.1200000000000000
0.32	-0.1000004291333890	0.66	0.2700000000000000	1.00	-0.1100000000000000
0.33	-0.0299993562231754	0.67	0.2750000000000000		

Table D.1: ECG beat values

Listing D.1: Synthetic ECG signal generation

```

1 function ecg = syntheticECG(beat, hr, fs, dur)
2 %% INPUTS
3 % beat.v : amplitudes of ecg beat (mV)
4 % beat.t : timestamps of ecg beat (s)
5 % hr      : heart rate in beats per minute
6 % fs      : sampling frequency in Hz
7 % dur     : desired signal duration in seconds
8 %% OUTPUT
9 % ecg.v   : ecg amplitudes
10 % ecg.t   : ecg timestamps in seconds
11
12 beat_duration = 60/hr;           % duration of a single beat
13 beat_nsamples = beat_duration * fs; % number of samples in a ...
    single beat
14
15 sampling_int = 1/(beat_nsamples - 1); % resample to the desired ...
    sampling rate
16 ts_old = beat.t;                 % old timestamps
17 ts_new = 0:sampling_int:1;       % new timestamps
18 beat_new.v = interp1(ts_old(1:(end-1)), beat.v(1:(end-1)), ts_new, ...
    'pchip');
19 beat_new.t = ts_new;
20
21 total_nsamples = dur * fs         % total number of ...
    samples
22 nrepet = ceil(total_nsamples/length(beat_new.t)); % number of ...
    beat repetitions
23 ecg.v = repmat(beat_new.v, [1, nrepet]);
24 ecg.v = ecg.v(1:total_nsamples);
25 beat_nsamples = length(beat_new.t);
26 ecg.t = [0:(total_nsamples-1)]*(1/beat_nsamples)*(beat_nsamples/fs);

```

D.2 Respiratory-induced Modulations

Following the generation of a synthetic ECG signal of desired duration, we can generate signals that show the effects of the respiratory-induced modulations. The BW modulation of the ECG signal can be modelled by assuming a superimposed sinusoidal modulation, at a constant respiration frequency and constant amplitude. The manifestation of AM can be modelled through time domain multiplication of the amplitude of the ECG signal by a respiratory modulation, which is characterised by an amplitude and respiration frequency. Finally, the FM modulation can be modelled as a superimposed sinusoidal modulation of the ECG timings. The MATLAB code presented in Listing D.2 gives more details on the methods used.

Listing D.2: Modulated ECG signal generation

```
1 function mod_ecg = modulatedECG(ecg, rr, mod, mod_ampl)
2 %% INPUTS
3 % ecg.v      : unmodulated ecg amplitudes
4 % ecg.t      : unmodulated ecg timestamps in seconds
5 % rr        : br in bpm
6 % mod       : type of modulation ('BW', 'AM', 'FM')
7 % mod_ampl  : amplitude of modulation
8 %% OUTPUT
9 % mod_ecg.v : modulated ecg amplitudes
10 % mod_ecg.t : modulated ecg timestamps in seconds
11
12 f = 2*pi*(rr/60);
13 switch mod
14     case 'BW'
15         mod_ecg.v = ecg.v + mod_ampl*sin(f*ecg.t);
16         mod_ecg.t = ecg.t;
17     case 'AM'
18         mod_ecg.v = detrend(ecg.v).*(1+(mod_ampl*cos(f*ecg.t)));
19         mod_ecg.t = ecg.t;
20     case 'FM'
21         mod_ecg.t = ecg.t + (mod_ampl/2)*sin(f*ecg.t);
22         mod_ecg.v = ecg.v;
23 end
24
25 mod_ecg.t = mod_ecg.t(~isnan(mod_ecg.t));
26 mod_ecg.v = mod_ecg.v(~isnan(mod_ecg.v));
27
28 end
```

Appendix E

Additional information related to Chapter 3

E.1 Additional information related to Chapter 3

The following sections discuss in detail the Blind Source Separation (BSS) problem and the Principal Component Analysis (PCA) which are stated in Chapter 3.

E.1.1 BSS Model

BSS represents a model where a set of unobserved source signals is been recovered from a set of observed mixtures (Cardose, 1998; Jutten & Herault, 1991). In other words BSS is the separation of a set of source signals, $\mathbf{S} = [\mathbf{s}_1, \mathbf{s}_2 \dots, \mathbf{s}_n]$, from a set of mixed signals, $\mathbf{X} = [\mathbf{x}_1, \mathbf{x}_2 \dots, \mathbf{x}_n]$. The word blind emphasises the fact that no information is provided about the source signal and the mixture, and that the source signals are unobserved. For example, imagine a room containing three microphones and three people who are speaking simultaneously. The microphones record three time signals, $x_1(t)$, $x_2(t)$ and $x_3(t)$. Each of these signals is a superimposition of the source speech signals, $s_1(t)$, $s_2(t)$ and $s_3(t)$, emitted by the three speakers. The connection of the speech and recorded signals can be expressed as follows:

$$x_1(t) = a_{11}s_1(t) + a_{12}s_2(t) + a_{13}s_3(t), \quad (\text{E.1})$$

$$x_2(t) = a_{21}s_1(t) + a_{22}s_2(t) + a_{23}s_3(t), \quad (\text{E.2})$$

$$x_3(t) = a_{31}s_1(t) + a_{32}s_2(t) + a_{33}s_3(t), \quad (\text{E.3})$$

where a_{11} , a_{12} , a_{13} , a_{21} , a_{22} , a_{23} , a_{31} , a_{32} and a_{33} are some parameters which will be defined later. The problem of signal separation points out the importance of estimat-

ing the three original speech signals using only the recorded signals (Hyvärinen & Oja, 2000). The simplest BSS model assumes $m = n$, i.e. the number of observations is equal to the number of source signals, thus the model can be expressed by the mixing equation:

$$x_i(t) = \sum_{j=1}^m a_{ij}s_j(t), \quad (\text{E.4})$$

where $i = 1, \dots, n$. Using matrix notation and supposing that each observation and source signal is a time series of length m , the above mixing equation is written as:

$$\mathbf{X} = \mathbf{A}\mathbf{S}, \quad (\text{E.5})$$

where \mathbf{S} is an $m \times m$ matrix containing the m source signals of length m , and \mathbf{X} is a $n \times m$ containing n observations of length m , and the $n \times m$ matrix \mathbf{A} contains the mixture coefficients and which is called the mixing matrix.

Figure E.1 shows a schematic representation of the BSS model and its application in ECG signal processing, where the sources are mixed by the mixing matrix \mathbf{A} and produce the observations. It is also shown that in order to estimate the sources, a separating matrix \mathbf{W} is required, which actually corresponds to \mathbf{A}^{-1} (when $m = n$, thus \mathbf{A} is a square matrix).

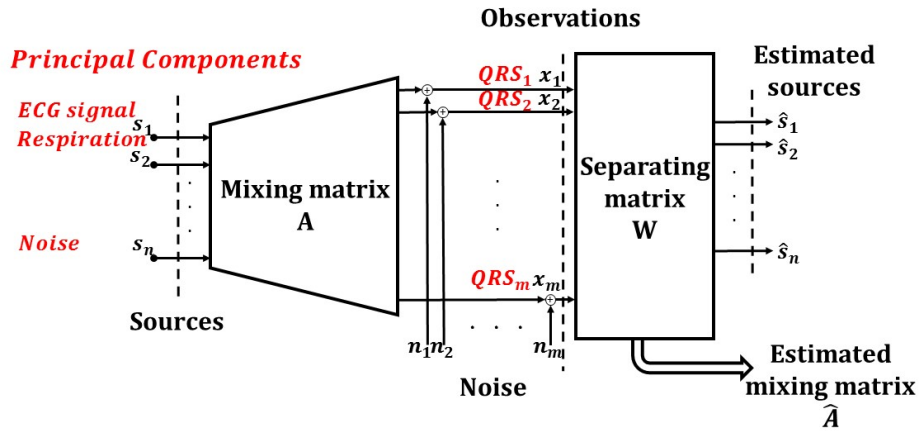


Figure E.1: Schematic representation of the BSS model application in ECG signal processing.

E.1.2 Principal Component Analysis

PCA is a statistical technique whose purpose is the dimensionality reduction by preserving as much of the relevant information as possible (Bishop, 1995; Jolliffe, 1986). The key assumption of PCA is that the principal components (PCs), i.e. source signals, are a linear combination of the data set (observations), with weights (mixing matrix) chosen so that the PCs become mutually uncorrelated. Each PC is estimated in such a way that inherits the maximum possible variance from the observations. Assume that each observation, as well as each PC is a random variable. Therefore the observations are defined as a matrix, \mathbf{X} of n random variables of length m . The procedure of estimating the PCs is described as follows: the data are first centred by removing the mean and then the auto-covariance matrix $\mathbf{R}_\mathbf{X}$ is computed for the observations \mathbf{X} :

$$\mathbf{R}_{\mathbf{X}_i\mathbf{X}_j} = \text{cov}(\mathbf{X}_i, \mathbf{X}_j) = E[(\mathbf{X}_i - \mu_{\mathbf{X}_i})(\mathbf{X}_j - \mu_{\mathbf{X}_j})^T], \quad (\text{E.6})$$

where $i, j = 1, \dots, n$ and $\mu_{x_i} = E[\mathbf{X}_i] = \frac{1}{m} \sum_{k=1}^m x_{i,k}$. Then, the $n \times n$ auto-covariance matrix $\mathbf{R}_\mathbf{X}$ is factorised using the Singular Value Decomposition (SVD), such that:

$$\mathbf{R}_\mathbf{X} = \mathbf{U}\mathbf{\Sigma}\mathbf{V}^*. \quad (\text{E.7})$$

Assuming that $\mathbf{R}_\mathbf{X}$ is a real matrix, Equation E.7 can be written as:

$$\mathbf{R}_\mathbf{X} = \mathbf{U}\mathbf{\Sigma}\mathbf{V}^T. \quad (\text{E.8})$$

The left singular vectors of $\mathbf{R}_\mathbf{X}$ are stored in matrix \mathbf{U} and the right singular vectors in matrix \mathbf{V} . The non-zero singular values of $\mathbf{R}_\mathbf{X}$ are the square root of the non-zero eigenvalues and can be found at the diagonal of matrix $\mathbf{\Sigma}$. Matrix \mathbf{V} is arranged in a decreasing order of eigenvalue magnitudes, and PCs are finally obtained by:

$$\mathbf{S} = \mathbf{V}\mathbf{X}. \quad (\text{E.9})$$

To conclude, PCA is a statistical technique facilitating dimensionality reduction which makes use of second-order statistics. The observation covariance matrix can be decomposed into a set of statistically uncorrelated source signals with the fundamental restriction of having an orthogonal mixing matrix. The main advantage of PCA is that it makes use of matrix decompositions, such as SVD, thus the computational cost can be reduced. However the restriction of the mixing matrix columns to be orthogonal remains a serious limitation of PCA.

Appendix F

Additional information related to Chapter 7

F.1 BCH data and reference WOB

Chapter 7 explored the correlation between the R-peak variability and the WOB for the first time. The developed measures were evaluated using the BCH ECG and EMG children data. The reference WOB for the 18 children from the BCH ECG database (`ecgch`) is provided for each minute and the highest WOB score observed is 3. For the 4 children recordings from the BCH EMG database (`emgch`), there is a reference WOB for each hour and the highest observed score is 1. The total number of reference hours is 16.

F.2 Pearson's correlation coefficient

The correlation coefficient of two sample sets x and y is a measure of their dependence (J. Li, Jin, Chen, Sun, & Guo, 2010; Stuart, Kendall, et al., 1963). If each set has n samples, then the Pearson's correlation coefficient is defined as:

$$r_{xy} = \frac{\sum_{i=1}^n (x_i - \bar{x})(y_i - \bar{y})}{(n-1)s_x s_y}, \quad (\text{F.1})$$

where \bar{x} and \bar{y} are the means of the sample sets x and y , and s_x and s_y are the standard deviations of x and y , respectively.

F.3 K -means clustering

This appendix brings together the theoretical bases behind the k -means classification algorithm used in Chapter 7. Suppose that there are N data points, x_i , where $i = 1, \dots, N$ that we wish to classify into K clusters. The k -means algorithm seeks to partition the data points into K disjoint subsets S_j , where $j = 1, \dots, K$. Each subset (cluster) contains N_j data points (Bishop, 1995). The basis of the partition is a minimisation problem where the algorithm attempts to minimise the sum-of-squares clustering function defined as follows:

$$F = \sum_{j=1}^K \sum_{i \in S_j} \|x_i - \mu_j\|^2, \quad (\text{F.2})$$

where μ_j is the mean of the data points in set S_j and is defined as:

$$\mu_j = \frac{1}{N_j} \sum_{i \in S_j} x_i. \quad (\text{F.3})$$

The algorithm first assigns the points randomly to the K clusters and then it computes the mean of the points in each set. Each point is then re-allocated to a new set according to the cost function F and the mean of each set are updated. This process is repeated until there is no further change in the classification of the data points.